



UNIVERSITAT POLITÈCNICA
DE CATALUNYA
BARCELONATECH

Hydro-mechanical behaviour of compacted binary mixtures : an experimental study

Sajjad Mirsalehi

ADVERTIMENT La consulta d'aquesta tesi queda condicionada a l'acceptació de les següents condicions d'ús: La difusió d'aquesta tesi per mitjà del repositori institucional UPCommons (<http://upcommons.upc.edu/tesis>) i el repositori cooperatiu TDX (<http://www.tdx.cat/>) ha estat autoritzada pels titulars dels drets de propietat intel·lectual **únicament per a usos privats** emmarcats en activitats d'investigació i docència. No s'autoritza la seva reproducció amb finalitats de lucre ni la seva difusió i posada a disposició des d'un lloc aliè al servei UPCommons o TDX. No s'autoritza la presentació del seu contingut en una finestra o marc aliè a UPCommons (*framing*). Aquesta reserva de drets afecta tant al resum de presentació de la tesi com als seus continguts. En la utilització o cita de parts de la tesi és obligat indicar el nom de la persona autora.

ADVERTENCIA La consulta de esta tesis queda condicionada a la aceptación de las siguientes condiciones de uso: La difusión de esta tesis por medio del repositorio institucional UPCommons (<http://upcommons.upc.edu/tesis>) y el repositorio cooperativo TDR (<http://www.tdx.cat/?locale-attribute=es>) ha sido autorizada por los titulares de los derechos de propiedad intelectual **únicamente para usos privados enmarcados** en actividades de investigación y docencia. No se autoriza su reproducción con finalidades de lucro ni su difusión y puesta a disposición desde un sitio ajeno al servicio UPCommons. No se autoriza la presentación de su contenido en una ventana o marco ajeno a UPCommons (*framing*). Esta reserva de derechos afecta tanto al resumen de presentación de la tesis como a sus contenidos. En la utilización o cita de partes de la tesis es obligado indicar el nombre de la persona autora.

WARNING On having consulted this thesis you're accepting the following use conditions: Spreading this thesis by the institutional repository UPCommons (<http://upcommons.upc.edu/tesis>) and the cooperative repository TDX (<http://www.tdx.cat/?locale-attribute=en>) has been authorized by the titular of the intellectual property rights **only for private uses** placed in investigation and teaching activities. Reproduction with lucrative aims is not authorized neither its spreading nor availability from a site foreign to the UPCommons service. Introducing its content in a window or frame foreign to the UPCommons service is not authorized (*framing*). These rights affect to the presentation summary of the thesis as well as to its contents. In the using or citation of parts of the thesis it's obliged to indicate the name of the author.



UNIVERSITAT POLITÈCNICA DE CATALUNYA
BARCELONATECH

Hydro-mechanical behaviour of compacted binary mixtures. An experimental study

PhD Thesis

Department of Civil and Environmental Engineering
Universitat Politècnica de Catalunya

Sajjad Mirsalehi

Supervised by: Prof. Antonio Lloret Morancho

Prof. Enrique Romero Morales

Barcelona, February 2018

Abstract

This research focusses on an experimental investigation on the hydro-mechanical behaviour of binary ‘all-one’ mixtures. These mixtures –originated from the excavation of selected materials during earthwork constructions– are basically constituted by large rock fragments immersed in a matrix with dominant finer soil fraction. These materials, which bridge the gap between coarser rockfill materials and soils, are widely accepted in different national standards for earthworks, such as dams, levees, railway and road embankments. Despite their practical interest, these mixtures have not been widely studied. The emphasis of the current study has been mainly placed on the influence of the properties of the fragments (unconfined shear strength) and the void ratio of the finer matrix to explain the hydro-mechanical behaviour of these mixtures along different stress paths, as well as to better assess the role played by fragment breakage aspects. Different mass ratios of fragments have been initially studied, which allowed selecting a matrix proportion able to fill nearly all inter-fragments voids (interactive-underfilled packing), as well as still ensuring good compaction properties (close to minimum dry density for specified water content). A constant fragment mass ratio of 40% with particles between 19 mm and 38.5 mm has been finally selected to perform a systematic experimental campaign with fragments of different uniaxial compressive strengths, ranging from natural carbonated and low-strength aggregates to high-strength slate fragments. This fixed fragment ratio has ensured reaching a mixture, in which both the density of the fine matrix and the strength of large fragments are controlling the coupled hydro-mechanical response. A procedure for fabricating artificial and cement-based fragments has been also proposed to allow obtaining an intermediate uniaxial compressive strength and thus to better fill the gap between these extreme low-strength and high-strength fragments. A real ‘all-one’ mixture retrieved under as-compacted conditions during the construction of Albagés dam (Lleida, Spain) has been also considered to compare main hydro-mechanical features with the mixtures prepared under laboratory conditions. The experimental campaign using a large-oedometer cell has included loading / unloading cycles under saturated and unsaturated conditions, as well as soaking tests at constant vertical stress. The study with different fragment strengths has been mainly focused on analysing the compressibility of the mixture on loading at different hydraulic states, the collapsible response on soaking at constant vertical stress, as well as the water retention and saturated

permeability properties. These macroscopic phenomenological results have been complemented by a microstructural description that included aspects of fragment breakage, fractal dimension changes of the particle size distribution, as well as energy transfer aspects (work input per unit volume used to densify the matrix and to break large fragments). The results have shown the important role played by the strength of the fragments to achieve better compaction properties when using high-strength fragments, which allowed reducing the compressibility on loading and the collapsibility on soaking, as well as ensuring a more efficient transfer of the work input to densify the matrix (instead of breaking particles).

Resumen

Esta investigación se centra en el estudio experimental del comportamiento hidromecánico de mezclas binarias de ‘todo-uno’. Estas mezclas -originadas a partir de la excavación de materiales seleccionados durante las construcciones de movimiento de tierras- están básicamente constituidas por grandes fragmentos de roca inmersos en una matriz con una fracción de suelo dominante. Estos materiales, que cubren la brecha entre los materiales de escolleras más gruesos y los suelos, son ampliamente aceptados en diferentes normas nacionales para estructuras de tierras, como presas, diques, y terraplenes para ferrocarriles y carreteras. A pesar de su interés práctico, estas mezclas no han sido ampliamente estudiadas. El énfasis del presente estudio se ha centrado principalmente en la influencia de las propiedades de los fragmentos (resistencia a la compresión uniaxial) y la relación de poros de la matriz más fina para explicar el comportamiento hidromecánico de estas mezclas a lo largo de diferentes trayectorias de tensión, así como para evaluar mejor el papel desempeñado por la rotura de fragmentos. Se han estudiado inicialmente diferentes proporciones másicas de fragmentos, lo que ha permitido seleccionar una proporción de matriz capaz de llenar casi todos los vacíos entre fragmentos (empaquetamiento interactivo casi lleno) e incluso garantizar buenas propiedades de compactación (cercano a la densidad seca mínima para un contenido de agua específico). Se seleccionó finalmente una relación de masa de fragmentos constante del 40% con partículas entre 19 mm y 38.5 mm para realizar una campaña experimental sistemática con fragmentos de diferentes resistencias a la compresión uniaxial, que van desde agregados carbonatados naturalmente y de baja resistencia hasta fragmentos de pizarra de elevada resistencia. Esta proporción de fragmentos prefijada ha permitido alcanzar una mezcla, en la que tanto la densidad de la matriz fina como la resistencia de los fragmentos controlen la respuesta hidromecánica acoplada. También se ha propuesto un procedimiento para fabricar fragmentos artificiales a base de cemento para permitir la obtención de una resistencia a la compresión uniaxial intermedia y así rellenar mejor el rango entre estos fragmentos de baja y elevada resistencia. También se ha considerado una mezcla real de ‘todo uno’ extraída después de compactación durante la construcción de la presa de Albagés (Lleida, España) para comparar sus principales características hidromecánicas con las mezclas preparadas en condiciones de laboratorio. La campaña experimental que utiliza una célula edométrica de grandes dimensiones ha incluido ciclos de carga/descarga en condiciones saturadas y parcialmente saturadas, así como ensayos de inundación a tensión vertical constante. El estudio con fragmentos de diferentes resistencias se ha centrado principalmente en analizar la compresibilidad de la mezcla ante carga a diferentes estados hidráulicos, la respuesta al colapso durante inundación a tensión vertical constante, así como la retención de agua y las propiedades de permeabilidad saturada. Estos

resultados fenomenológicos macroscópicos se han complementado con una descripción microestructural que incluye aspectos de rotura de fragmentos, cambios de dimensiones fractales de la distribución de tamaños de partículas, así como aspectos de transferencia de energía (trabajo por unidad de volumen aportado para densificar la matriz y consumido para romper los fragmentos grandes). Los resultados han demostrado el importante papel desempeñado por la resistencia de los fragmentos para lograr mejores propiedades de compactación al usar fragmentos de alta resistencia, que permiten reducir la compresibilidad ante carga y el colapso durante inundación, así como asegurar una transferencia de energía más eficiente para densificar la matriz (en lugar de romper partículas).

Acknowledgements

First, the author wants to express special thanks to his thesis supervisors, Prof. Antonio Lloret Morancho and Prof. Enriquir Romero Morales, without whose valuable guidance and encouragement, this thesis work would not have been accomplished. From whom, the author learned how to do research and fulfil scientific collaboration.

Besides my advisor, I would like to thank to Prof. Jean Vaunat for his valuable support and encouragement.

My sincere thanks also goes to rest of my thesis committee: Prof. Cristina Jommi and Prof. Vicente Navarro Gàmir for their insightful comments and encouragement.

Last but not the least, I would like to thank my family: my wife and my parents for supporting me spiritually throughout writing this thesis and also to my friend Dr. Alireza Kharazian for his useful guidance during my PhD work.

TABLE OF CONTENTS

Abstract.....	i
Resumen	iii
Acknowledgements	v
1 Introduction	1
1.1 Motivation of the study	1
1.2 Objectives of the study	2
1.3 Thesis outline	3
2 State of the art	6
2.1 Origin of partially saturated soils	6
2.2 Compacted soil.....	6
2.2.1 Introduction	6
2.2.2 Compaction theory	6
2.2.3 The structure of compacted soil	7
2.2.4 Influence of water content in compacted soil structure.....	8
2.3 Introduction of ‘all-one’ material as a binary granular mixtures	13
2.3.1 Introduction of ‘all-one’ mixtures	13
2.3.2 Fill and under-filled packing structure	14
2.4 Transitional zone between shielding skeleton and matrix on binary granular mixtures	17
2.4.1 Introduction	17
2.4.2 Criteria of Transitional Zone	18
2.5 Particle breakage and fractal analysis	20
2.5.1 Introduction	20
2.5.2 Method to determine particle breakage coefficient	21
2.5.3 Method to determine fractal dimension.....	24
2.5.4 Particle breakage of granular binary mixtures with fine contents	24
3 Methodology	28
3.1 Introduction	28
3.2 Description of different types of material used in the investigation	28
3.3 Material properties	31
3.3.1 Barcelona silty clay	31
3.3.2 Rigid fragments of quartzitic slate	35
3.3.3 Artificial fragments	36

3.4	Reference grain size distribution curve	37
3.4.1	Introduction	37
3.4.2	Fuller curve	37
3.4.3	Modified fuller curve	40
3.5	Compaction procedure	41
3.5.1	Introduction	41
3.5.2	Compaction procedure for ‘all-one’ material mixtures	42
3.5.3	Compaction procedure for fabricate artificial fragment	45
3.6	Equipment description and test procedure	45
3.6.1	Grain size distribution analysis (GSD).....	46
3.6.2	Suction measurements.....	46
3.6.3	Density by paraffin.....	48
3.6.4	Mercury intrusion porosimetry (MIP).....	49
3.6.5	Continuous loding/unloading oedometer tests	50
3.6.6	Soaking test	51
3.6.7	Water permeability test using oedometer cell	51
3.7	Testing program	52
4	Exploring binary mixture properties. Effect of matrix content and fragment strength	56
4.1	Exploring mixture properties on a single material with different proportions of carbonated fragments	56
4.1.1	Introduction	56
4.1.2	Binary granular mixtures with different proportions of fines	56
4.1.3	Selected proportion for the experimental study.....	58
4.2	Exploring mixture properties with different fragment strengths.....	62
4.2.1	Compaction curve of the matrix.....	62
4.2.2	Method to calculate the matrix void ratio in the mixtures.....	63
4.2.3	Influence of different materials (fragments) on the density of the compacted mixtures	64
4.2.4	Influence of compaction energy and water content on the properties of the mixtures	66
5	Hydro-mechanical characterisation of a compacted all-one material used in the construction of Albagés dam (Spain)	70
5.1	Introduction	70
5.2	Brief description of the Albagés dam.....	70
5.3	Basic properties of Albagés ‘all-one’ material.....	73

5.3.1	Atterberg limits	75
5.3.2	Grain size distribution curves.....	75
5.3.3	Standard and modified compaction curves	76
5.4	Consolidation, compressibility and collapse analysis under oedometer conditions....	77
5.4.1	Results of sample loaded up to 1 MPa and saturated	79
5.4.2	Result of sample loaded up to 2 MPa and unloaded up to 1 MPa and then saturated	81
5.4.3	Results of sample loaded up to 2 MPa and unloaded up to 0.6 MPa and then saturated	85
5.4.4	Comparison of results of the three oedometer tests as well as with some previous work	88
5.5	Permeability tests	92
5.6	Water retention curve.....	92
5.7	Numerical simulations.....	93
6	Soil-cemented artificial aggregates	96
6.1	Introduction.....	96
6.2	Cementation of soil	96
6.2.1	Types of cement composition.....	97
6.2.2	Volumetric characterization of cement hydration	98
6.2.3	Effect of cementation on mechanical behaviours of soil-cement mixtures.....	100
6.3	Artificial samples preparation method and available equipment	102
6.3.1	Materials and equipment used.....	102
6.3.2	Method to prepare artificial soil-cemented samples.....	106
6.3.3	Selection of samples for experimental work	106
6.4	Fabric of soil cemented fragments	111
6.4.1	Volumetric phases of samples before and after of cement hydration	111
6.4.2	Determination of specific densities by paraffin method.....	114
6.4.3	Microphotography of fragments.....	115
6.4.4	Pore size distributions	116
6.5	Mechanical behaviour of artificial samples.....	118
6.5.1	Introduction	118
6.5.2	Unconfined compression strength.....	118
6.5.3	Elastic modulus	119
6.5.4	Tensile strength	120
6.6	Water retention curves	121
7	Hydro-mechanical tests	124

7.1	Oedometer test in dry condition	124
7.1.1	Introduction	124
7.1.2	Compressibility, preconsolidation pressure, and elastic modulus analysis	124
7.1.3	Particle braking mechanism	129
7.1.4	Fractal analysis	142
7.1.5	Energy dissipation during dynamic compaction and static loading-unloading oedometer test	144
7.2	Oedometer tests with saturation process at different vertical stresses	152
7.2.1	Introduction	152
7.2.2	Compressibility analysis	152
7.2.3	Collapse deformation analysis.....	158
7.2.4	Odometric modulus analysis	164
7.2.5	Creep analysis	165
7.2.6	Direct and indirect permeability measurements	167
7.3	Water retention curve and suction equalization	173
7.4	Collapse comparison	175
8	Summary, concluding remarks and future investigations	178
8.1	Summary	178
8.2	Concluding remarks	178
8.3	Future investigations	184
9	References	186

LIST OF FIGURES

Figure 2-1: Distribution of elementary particles, aggregates, and pores (Alonso et al., 1987).....	8
Figure 2-2: Unimodal and bimodal structure and pore size distribution of compacted soil (Satyanaga et al., 2013).....	9
Figure 2-3: Scanning electron microscopic results at the dry and wet side of the optimum content (Delage et al., 1996).	10
Figure 2-4: The ESEM observations of compacted Barcelona silty clay (Buenfil et al., 2004).....	10
Figure 2-5: Statically compacted Barcelona silty clay: (a) compaction state of sample DD and WD; (b) collapse after wetting under vertical stress for samples with the same dry density and water content but compacted at different conditions (Suriol et al., 1998 and Suriol & Lloret 2007).	11
Figure 2-6: Compacted Boom clay: (a) stress path and wetting and drying cycle, (b) mercury intrusion porosimetry results (Romero et al., 2011).	12
Figure 2-7: Effects of “ S_r at compacted state” on the micro-structure of compacted soil (Tatsuoka, 2015).....	13
Figure 2-8: Particle size distribution of ‘all-one’ mixture.....	14
Figure 2-9: Under filled and filled packing by (Vaughan, 1994).....	15
Figure 2-10: Schematic representation of various structures of binary granular mixtures: (a) case A/A-1, (b) case B, (c) case C and (d) case D (Lopez et al., 2016).....	16
Figure 2-11: Effect of fine content in binary granular mixtures (Vallejo, 2001).....	17
Figure 2-12: Initial void ratio versus fine content (Mekkiyah & Al Khazragie, 2015)..	19
Figure 2-13: Porosity versus amount of fine content (Vallejo, 2011).....	20
Figure 2-14: Marsal breakage index- B_g (Marsal, 1967).	22
Figure 2-15: Hardin breakage index- B_r (Hardin, 1978).....	23
Figure 2-16: Modification definition of Hardin’s degradation factor (B_r) (Einav, 2007).	23
Figure 2-17: Particle breakage versus fine content (Zhang & Baudet, 2013).	25
Figure 2-18: The amount of particle breakage in overall, small, and large fragments- (SG = fine grain content, R = diameter of large /diameter of small particles) (Zhang & Baudet, 2013).	25
Figure 3-1: Particle mixtures according to grain size distribution curve (Funk and Dinger, 1980).....	29

Figure 3-2: Different types of materials (FN: Natural fragments, FS: Slate fragments, FA: Artificial fragments).	30
Figure 3-3: Strength behaviour of various materials for particles bigger than 19 mm. .	31
Figure 3-4: Procedure to collect Barcelona silty clay material.	31
Figure 3-5: Location of building B1 project at Universitat Politècnica de Catalunya - UPC campus nord (Google map, 2016).	32
Figure 3-6: Plasticity chart for Barcelona silty clay.	32
Figure 3-7: Particle size distribution of Barcelona silty clay.	33
Figure 3-8: Electronic Microscopic Image analyses of Barcelona silty clay (Compacted soil passing sieve 4.75 mm, W=11% and density of 1.63 Mg/m ³).	33
Figure 3-9: Compaction curves of Barcelona Silty clay.	34
Figure 3-10: Large carbonated fragments of Barcelona silty clay.	34
Figure 3-11: Mercury intrusion porosimetry test for large carbonated fragments of Barcelona silty clay.	35
Figure 3-12: Particles of quartzitic cambrian slate.	36
Figure 3-13: The characterization and specifications of Superdragon cement of the company Cements Molins (www.cmi.cemolins.es/en/productos/super-dragon).	37
Figure 3-14: Various particles sizes according to Fuller curve.	38
Figure 3-15: Dry sieve analysis of FN after compaction test.	39
Figure 3-16: Funk and Dinger GSD curve with various values of q.	41
Figure 3-17: Various methods of dynamic compaction equipment available at Geotechnical Laboratory of UPC.	43
Figure 3-18: Dynamic compaction test equipment available at Geotechnical Laboratory of UPC.	44
Figure 3-19: Sieve analysis equipment.	46
Figure 3-20: WP4 Dew Point Psychrometer and sample.	47
Figure 3-21: Procedure of paraffin density test; (a) warping sample in a heated oven of liquid paraffin, (b) weighing of samples with paraffin immersed in water.	48
Figure 3-22: Mercury intrusion porosimetry test equipment available at Geotechnical Laboratory of UPC.	49
Figure 3-23: Oedometer cell provided at UPC Geotechnical Laboratory.	50
Figure 3-24: Design details of the load plate and rod for drainage and measurement of vertical movement of the oedometer (Grimal, 2010).	51
Figure 3-25: Set-up of the equipment used to measure water permeability.	52

Figure 4-1: FN material with different proportions based on Funk and Dinger grain size distribution.....	57
Figure 4-2: Grain size distributions of various proportions of the mixtures, (a) 80% matrix+20% granular (FC=80), (b) 60% matrix+40% granular (FC=60), (c) 40% matrix+60% granular (FC=40), (d) 20% matrix+80% granular (FC=20).....	58
Figure 4-3: Void ratio and porosity of the mixtures versus fine content.....	59
Figure 4-4: The four packing states in binary granular mixtures.	60
Figure 4-5: Grain size distributions before and after compaction for various types of mixtures.	61
Figure 4-6: Procedure of pure matrix compaction.....	62
Figure 4-7: Compaction curves of Barcelona silty clay and the pure matrix.....	63
Figure 4-8: Densification of the matrix in the different mixtures (fragments with different strengths).....	65
Figure 4-9: Densification of the matrix versus the unconfined compression strength of the fragments.	65
Figure 4-10: The density of the mixture compared to reference pure matrix.....	66
Figure 4-11: Sieve analysis after compaction for various energies and water contents. 67	
Figure 4-12: The compaction energy versus particle breakage.....	67
Figure 5-1: Geographical location of the Albagés dam.....	71
Figure 5-2: Location of the Albagés dam on the river Set valley.	71
Figure 5-3: (a) General view of the Albagés dam under construction. (b) Compaction procedure of the core material. (c) ‘All-one’ shoulder and drain filter area. (d) Placement of total stress cells. (Alonso et al., 2016).....	72
Figure 5-4: A modified section with the materials included in the numerical model. (Alonso et al., 2016).	73
Figure 5-5: The ‘all-one’ material before excavation. Outcrop of argillite / sandstone. 74	
Figure 5-6: The ‘all-one’ material after excavation and during compaction.....	74
Figure 5-7: Atterberg limits of all-one material and previous results of other researchers.	75
Figure 5-8: Grain size distribution of in situ all-one material before and after compaction.	76
Figure 5-9: The compaction curves of the Standard Proctor and Modified Proctor from UPC laboratory test and previous reports, and the degree saturation curves of 60%, 80%, 90% and 100% for the all-one material.....	77
Figure 5-10: Void ratio versus vertical stress for sample loaded up to 1 MPa and then saturated at constant vertical stress.....	80

Figure 5-11: Time evolution of void ratio during soaking.	80
Figure 5-12: The variation of void ratio versus time for different loading steps.	81
Figure 5-13: The coefficient of secondary compression for different vertical stresses..	81
Figure 5-14: Void ratio versus vertical stress for sample loaded up to 2 MPa and unloaded up to 1 MPa and then saturated at constant vertical stress.....	83
Figure 5-15: The variation of the void ratio in time during saturation at 1 MPa.	83
Figure 5-16: Evolution of the oedometer modulus of stiffness.	84
Figure 5-17: The variation of void ratio versus time for different loading steps.	84
Figure 5-18: The coefficient of secondary compression for different vertical stresses..	85
Figure 5-19: Void ratio versus vertical stress for sample loaded up to 2 MPa and unloaded up to 0.6 MPa and then saturated at constant vertical stress.....	86
Figure 5-20: The variation of void ratio in time increment in saturation at 0.6 MPa....	87
Figure 5-21: The oedometer modulus in load increment.	87
Figure 5-22: The variation of void ratio versus time for different loading steps.	88
Figure 5-23: Comparisons of three samples with various stress paths under oedometer conditions.	89
Figure 5-24: collapse strain versus normalized stress	90
Figure 5-25: Normalised collapse versus void ratio for various materials of the dam...	91
Figure 5-26: Water retention curve for ‘all-one’ material both drying and wetting paths.	93
Figure 5-27: Vertical displacement analysis of the Albagés dam both numerical and in situ measurements for (a) central profile and (b) downstream profile (Pinyol and Alonso, 2017)	94
Figure 6-1: Volumetric quantities of water and cement, before and after hydration (Neville, 1995).....	99
Figure 6-2: The progress of hydration regarding different stages of hydration and water/cement ratios (Neville, 1995).	99
Figure 6-3: Effect of cement content on compression strength for several types of soils stabilized by Portland cement and cured for 7 days at 25 ° C and constant humidity (Ingles & Metcalf 1972).	101
Figure 6-4: Effect of the dry density of mixtures on the resistance compression of stabilized clay with a cement content of 10% (Ingles & Metcalf 1972).	101
Figure 6-5: The relation between the strength of concrete at different ages and fineness of cement (Neville, 1995).....	102

Figure 6-6: Available static compaction equipment at UPC Geotechnical Laboratory, (a) Tritest 100 press with a capacity of 5 tons, (b) Wykeham France press with a capacity of 5 tons, (c) hydraulic press with a capacity of 50 tons.	103
Figure 6-7: Provided cells and moulds to compact artificial fragments at UPC Geotechnical Laboratory.	104
Figure 6-8: Compaction loads versus time for different dry densities of samples.	105
Figure 6-9: Specimens with several cement and water contents after the compression.	107
Figure 6-10: The relationship between resistance and available water for hydration of cement-samples with dry density of 17 kN/m^3	108
Figure 6-11: Compressive strength of mixtures with a Sr of 85% and different mass ratios between cement and dry soil.	109
Figure 6-12: Volumetric properties of samples with a density of 17 kN/m^3 before hydration.	112
Figure 6-13: Volumetric properties of samples with a density of 17 kN/m^3 after hydration.	112
Figure 6-14: Volumetric properties of samples with a density of 21 kN/m^3 before hydration.	113
Figure 6-15: Volumetric properties of samples with a density of 21 kN/m^3 after hydration.	113
Figure 6-16: Comparison between the dry densities obtained experimentally and the design values proposed.	114
Figure 6-17: Available microphotography devices available at UPC Geotechnical Laboratory.	115
Figure 6-18: Microphotography of samples with density of 17 kN/m^3	115
Figure 6-19: Microphotography of samples with density of 21 kN/m^3	116
Figure 6-20: MIP results of two samples and comparison with Barcelona fragments.	117
Figure 6-21: MIP results of two samples.	117
Figure 6-22: Compressive strength versus curing time for different samples.	118
Figure 6-23: relationship between of water contents and degree of saturation with compressive strength.	119
Figure 6-24: The relationship between compression resistance and deformation modulus.	119
Figure 6-25: Relationship between indirect tensile strength and compressive strength.	120

Figure 6-26: Tensile and compressive resistance in case of several cement/soil ratios.	121
Figure 6-27: Retention curves on drying at different densities and cement/soil ratio..	121
Figure 6-28: Water retention curve by WP4 and logarithmic fitting.	123
Figure 6-29: Water retention curve by WP4 and van Genuchten fitting.	123
Figure 7-1: Variation of total void ratio in relation to vertical stress (samples loaded up to 1.9 MPa and unloaded up to 0.05 MPa for different types of the mixtures in as compacted conditions).	125
Figure 7-2: Variation of matrix void ratio in relation to vertical stress (samples loaded up to 1.9 MPa and unloaded up to 0.05 MPa for different types of the mixtures in as compacted conditions).	125
Figure 7-3: Effect of particles' strength on preconsolidation pressure.	126
Figure 7-4: Influence of particles' strength on compression (C_c) and swell (C_s) indices.	127
Figure 7-5: Changing of the elastic modulus versus effective vertical stress for different types of the mixtures.	128
Figure 7-6: Changing of the elastic modulus versus void ratio for different types of the mixtures.	128
Figure 7-7: Grain size distributions of FN, FA, and FS mixtures after dynamic compaction (A-C) and static compaction under loading-unloading oedometer (L-U) test.	130
Figure 7-8: Breakage indices versus density of the mixture.	132
Figure 7-9: Breakage indices versus unconfined strength of fragments.	132
Figure 7-10: Breakage indices versus volumetric strain during L-U process of the samples.	132
Figure 7-11: Breakage indices versus area of the particles over mass of the samples.	133
Figure 7-12: Breakage indices versus plastic work.	133
Figure 7-13: Comparison of breakage results for slate aggregates as a function of plastic work.	135
Figure 7-14: Distribution of retained weight at a given sieve size (Tapias et al., 2016).	136
Figure 7-15: The distribution of fine and large particles with various diameters resulting from particles with a diameter D_i	137
Figure 7-16: Schema of the breakage mechanism considering splitting and comminution crushing.	137

Figure 7-17: Comparison of GSD curve achieved in the experimental and theoretical method.	139
Figure 7-18: Schema of the breakage mechanism without considering comminution.	140
Figure 7-19: Variation of the value A0, A1, and A2 for all mixtures type after compaction and loading-unloading oedometer test.	141
Figure 7-20: Influence of particle size range on the fractal dimension for different mixtures after dynamic compaction test.	142
Figure 7-21: Influence of particle size range on the fractal dimension for different mixtures after Loading- unloading oedometer test.	143
Figure 7-22: Fractal number (DFr) versus unconfined strength of fragments.	144
Figure 7-23: Dry density achieved related to different blow numbers in pure matrix.	145
Figure 7-24: Relationship between energy of compaction and the dry density of matrix.	146
Figure 7-25: Scheme of deformation in the case of rigid fragments ($\Delta H = \Delta H_M$).	148
Figure 7-26: Global work and work that goes to the matrix for the oedometric test on FS sample (hypothesis of rigid fragments).	149
Figure 7-27: Global work and work that goes to the matrix for the oedometric test on FS sample (hypothesis of same strain in matrix and global mixture).	150
Figure 7-28: Relationship between Hardin breakage index and accumulated energy goes to fragments for various types of mixture.	151
Figure 7-29: Ratio of breakage/energy to fragments as a function of accumulated strain.	151
Figure 7-30: Volumetric strain versus vertical effective stress in all mixtures.	153
Figure 7-31: Structural changes of various samples under dry and wet conditions after	154
Figure 7-32: Results of the oedometric tests performed for all the materials in global mixtures (saturation under 0.075 MPa).	155
Figure 7-33: Results of the oedometric tests performed for all the materials in global mixtures (saturation under 1 MPa).	155
Figure 7-34: Results of the oedometric tests performed for all the materials in matrix part (saturation under 0.075 MPa).	156
Figure 7-35: Results of the oedometric tests performed for all the materials in matrix part (saturation under 1 MPa).	156
. Figure 7-36: Comparison of compressibility index in respect to unconfined strength of the fragments.	157

Figure 7-37: Comparison of compressibility index in respect to unconfined strength of the fragments	157
Figure 7-38: Comparison of measured and calculated collapse.	162
Figure 7-39: Evolution of collapse strain dealing with unconfined strength of fragments for various void ratio and saturation oedometer conditions.	162
Figure 7-40: Evolution of collapse strain dealing with void ratio for various fragments' strength and saturation loads.	163
Figure 7-41: Oedometric modulus vs vertical stress in dry and saturated conditions..	164
Figure 7-42: Oedometric modulus vs vertical stress in saturated conditions.	165
Figure 7-43: Secondary consolidation coefficient C_{α} versus vertical stress. Samples are saturated at 1 MPa.	166
Figure 7-44: Secondary consolidation coefficient C_{α} versus vertical stress. Samples are saturated at 0.075 MPa.	166
Figure 7-45: Fitted consolidation curves for vertical stress between 1.7 to 2 MPa for all samples.	168
Figure 7-46: Permeability vs vertical stress. Samples saturated at 0.075 MPa.	169
Figure 7-47: Permeability vs vertical stress. Samples saturated at 1 MPa.	169
Figure 7-48: The permeability in respect to the variation of void ratio under to saturation condition for all types of mixtures.	171
Figure 7-49: The permeability in respect to the variation of matrix void ratio under to saturation condition for all types of mixtures.	172
Figure 7-50: Water retention curve of the fragments dealing with the degree of saturation, drying paths.	173
Figure 7-51: Suction equilibration during oedometer saturation condition.	174
Figure 7-52: Results of compression test versus degree of saturation for sandstone and argillite with various void ratios.	175
Figure 7-53: The results of normalized collapse strain for various material with different strengths are plotted versus the void ratio before collapse.	177

LIST OF TABLES

Table 2-1: Description of various types of binary granular mixtures by (Lopez et al., 2016).....	16
Table 2-2: Percentage of gravel in mixtures conducting to different types of structures (Vallejo, 2011).....	18
Table 2-3: Different structures of binary mixture according to fine content, (FC (the ratio of the weight of fine to the total weight of the binary mixtures).	18
Table 3-1: Different types of mixture (M, FN, FA, and FS).	29
Table 3-2 : Properties of the quartzitic slate (Romero et al., 2013).	35
Table 3-3: Physical and chemical properties of Superdragon cement (www.cmi.cemolins.es/en/productos/super-dragon).	36
Table 3-4: Calculations for a 0.5 power gradation curve using 40 mm maximum aggregate sizes.	38
Table 3-5: Experimental program of Albagés dam material for both core and ‘all-one’ material.	53
Table 3-6: Experimental program of ‘all-one’ mixtures.	53
Table 3-7: Different H-M paths for various ‘all-one’ material	54
Table 4-1: Various proportions of matrix and fragments.	57
Table 4-2: Breakage potential for various fine contents in the binary granular mixtures.	60
Table 4-3: Dry density of the matrix and the compacted mixtures.	64
Table 4-4: Dry density values for various energies and water contents.	68
Table 5-1: The coefficient of secondary compression (C_∞), the oedometer modulus of stiffness (E_m), the compressibility index (λ and k), and the collapse deformation expressions.	78
Table 5-2: The evolution of the sample state during the loading-unloading and wetting processes.	79
Table 5-3: The evolution of the sample state during the loading-unloading and wetting process (loaded up to 2 MPa unloaded up to 0.6 MPa and saturated).....	82
Table 5-4: The evolution of the sample state during the loading-unloading and wetting process (loaded up to 2 MPa unloaded up to 0.6 MPa and saturated).....	86
Table 5-5: The coefficient of secondary compression for different vertical stresses.	88
Table 5-6: Permeability test for all-one samples in tow normally and over consolidated states.	92

Table 6-1: Various oxide of cement generated by the different materials (Neville, 1995).	97
Table 6-2: Main compounds of cement (Neville, 1995).	97
Table 6-3: Mass properties of cement and water before and after of hydration process (Neville, 1995).....	98
Table 6-4: The amount of available water for hydration of various specimens.	108
Table 6-5: Selected samples regarding the types of experimental program and equipment to compact samples.....	110
Table 7-1: Data summary of compression index (C_c), swelling index (C_s), preconsolidation pressure (σ_{pc}) for different mixtures.	126
Table 7-2: Data summarizing for breakage indices after dynamic compaction and static loading-unloading oedometer tests.....	131
Table 7-3: Parameters of breakage model and average errors obtained by curve fitting of the experimental results	138
Table 7-4: The value of A_0 , A_1 , and A_2 for all specimens after dynamic compaction(A- C) and static loading unloading oedometer (L-U) test.	141
Table 7-5: The value of fractal number for various mixtures.....	143
Table 7-6: Energy (kPa) distribution through matrix and breakage of the particles in dynamic compaction.....	147
Table 7-7: Energy (kPa) distribution through matrix and breakage of the particles in static loading oedometer compaction.	150
Table 7-8: The evolution of the pure matrix during the loading and wetting process at 0.075 MPa.....	158
Table 7-9: The evolution of the FN mixture during the loading and wetting process at 0.075 MPa.....	158
Table 7-10: The evolution of the FA mixture during the loading and wetting process at 0.075 MPa.....	158
Table 7-11: The evolution of the FS during the loading and wetting process at 0.075 MPa.....	159
Table 7-12: The evolution of the pure matrix during the loading and wetting process at 1 MPa.....	159
Table 7-13: The evolution of the FN mixture during the loading and wetting process at 1 MPa.....	159
Table 7-14: The evolution of the FA mixture during the loading and wetting process at 1 MPa.....	159
Table 7-15: The evolution of the FS mixture during the loading and wetting process at 1 MPa.....	160

Table 7-16: Summary of the collapse deformation in both matrix and global part of the various mixtures. 160

Table 7-17: Parameters related to collapse deformation under two vertical loads..... 161

1 Introduction

1.1 Motivation of the study

The soils that are available on site for earthworks structures, such as dams, levees, railway and road embankments, often need improvements to satisfy deformation and strength requirements. These improvements require using optimised compaction techniques and adequate materials, to reduce costs and environmental impact to a minimum. This is the case of reducing water demand for compaction, particularly in arid climate countries (unsaturated state), or using energy input per unit volume of soil as low as possible to achieve an adequate densification of the material. In fact, it is well known that applying a modified Proctor energy of compaction ($2700 \text{ kN}\cdot\text{m}/\text{m}^3$) only induces a small increase in dry density -of the order of 11% - compared to the lower standard Proctor energy of compaction ($596 \text{ kN}\cdot\text{m}/\text{m}^3$).

The need for using materials that are available within the surroundings of the construction, have promoted the use of different ranges of particle sizes and mixtures of soils. A particular case is the use of 'all-one' materials formed during excavation, widely accepted in national standards for earthworks, which are mixtures with particles sizes covering the range between rockfill and soils. The advantage of using this type of mixture with large fragments immersed in a finer fraction matrix is that it usually requires lower amounts of water for compaction. These large fragments display a low porosity, which makes difficult absorbing the optimum and larger amount of water determined under laboratory conditions (conventional compaction tests use the fine fraction $< 4.76 \text{ mm}$). In addition, these oversized fragments with high dry density are expected to induce an increase in the dry density of the mixture compared to that obtained with the finer fraction used in laboratory compaction. This is the case if the fine fraction is adequately compacted and the compaction energy is not mainly used to break the coarse fragments.

Previous studies in the Geotechnical Laboratory at the Universitat Politècnica de Catalunya have mainly focused on studying the behaviour of coarse granular fragments (rockfill), in which contacts between particles are largely stressed and the compressibility of the material is mainly controlled by particle breakage and their subsequent rearrangement (Oldecop & Alonso 2001). Particle breakage, which is highly affected in water-driven environments, involves grain crushing and spalling of stressed contact zones, particle splitting or both mechanisms. In addition, studies have been done on fill materials formed by fragments with highly degradable and evolving microstructure (Cardoso et al. 2012). Nevertheless, 'all-one' mixtures with relatively 'stable' fragments and with an 'interactive-underfilled' structure (Lopez, 2016) conformed by excess of fines and many low stressed particle contacts- have been less studied. These mixtures are

anticipated to behave as materials in the transition between rockfill and soils. In fact, the hydro-mechanical behaviour of these mixtures is expected to be ruled by the strength of large fragments (unconfined compression strength) and the void ratio of the finer matrix.

On the other hand, a major consideration for a technical professional dealing with unsaturated soils is related to the effect of wetting on engineering performance. In fact, the estimation of collapse deformation and the effect of water is an important issues to the design of many engineering structures during and after the construction.

Thus, there is a need for experimentally studying in a systematic way these ‘all-one’ mixtures: their compaction properties, their compressibility on loading at different hydraulic sates, their collapse on soaking, the breakage of large fragments, as well as their hydraulic properties. To simplify the study, only a proportion of 40% (mass basis) of fragments (up to 39 mm in size) have been considered immersed in a matrix (60%) with large sizes of particles (up to 19 mm in size). This proportion of binary mixture provides a good framework to characterise the couple hydro-mechanical behaviour of ‘all-one’ materials, since it is associated with an interactive-underfilled configuration (matrix nearly filling all inter-fragments voids) and close to a minimum void ratio of the mixture during compaction (to ensure good compaction properties).

Experimental efforts have been placed on studying the impact of having different qualities of fragments. This quality assessment has been based on selecting fragments of different unconfined compression strengths (carbonated natural fragments to higher quality slate fragments). In between, a preparation procedure has been followed to create artificial fragments with intermediate unconfined strength. This way, aspects related to breakage of particles (how compaction and compression work input is used to break particles and densify the matrix) could be better assessed.

1.2 Objectives of the study

The general objective of this Thesis is to advance in the knowledge of ‘all-one’ mixtures subjected to hydro-mechanical actions. A constant proportion of fragments (40% in mass basis) has been used with different strength properties of the fragments (carbonated natural fragments, artificially prepared fragments and slate fragments).

To achieve this main goal, the following objectives have been addressed:

- To define the best proportion (mass basis) of matrix component to ensure good compaction properties and a good filling of the inter-fragment voids.

- To better assess the impact of particle strength and dry density of the matrix on the overall hydro-mechanical response of the mixture with a fixed proportion of matrix (60%) and varying strengths of fragments.
- To fabricate artificial fragments to bridge the gap between low-strength natural carbonated aggregates and high-strength slate fragments.
- To assess a real case study of compacted all-one material associated with a dam construction and compare the experimental results with tests performed along the Thesis with a fixed proportion of matrix.
- To perform hydro-mechanical tests on ‘all one’ binary mixtures to better characterise the following aspects: compaction properties, compressibility on loading at different hydraulic sates, collapse on soaking, changes in the particle size distribution (breakage of large fragments), as well as water permeability.
- To compare selected hydro-mechanical results with the same compacted matrix with null content of fragments (100% matrix content).

1.3 Thesis outline

The Thesis is organized in nine Chapters. The contents of each chapter are listed below:

- Chapter 1 provides a background and the motivation of the study, research objectives, and the organization of the Thesis.
- Chapter 2 presents a literature study on the hydro-mechanical behaviour of compacted soils, as well as on the behaviour of binary mixtures.
- In chapter 3, the properties of the studied materials are described. The experimental equipment and protocols used in the test programme are presented. The methodologies to evaluate the hydro-mechanical behaviour are specified.
- In chapter 4, the compaction properties of binary mixtures are assessed by considering different matrix proportions and fragments with different unconfined compression strengths.
- Chapter 5 is associated with a real case study of compacted all-one material in the construction of a dam. The experimental results are focused on compressibility on loading and collapsibility on soaking under various loading-unloading and wetting paths.
- In chapter 6, the fabrication procedure of artificial soil-cement aggregates are presented. The mechanical properties of aggregates are provided to bridge the gap of fragments with different strengths.

- In chapter 7, the hydro-mechanical behaviour of different all-one mixtures under oedometer conditions is presented. Experimental results are focused on compressibility on loading, collapsibility on wetting, as well as on fragment breakage.
- Chapter 8 summarises the main conclusions of the investigation and outlooks for future work.
- Chapter 9 presents the list of the quoted references.

2 State of the art

2.1 Origin of partially saturated soils

Whilst the mechanics of saturated soils is well understood, the topic of partially saturated or unsaturated soils has been much less comprehensively investigated. The origin of partially saturated soils can understand the behaviour of this type of soils. The partially saturated soil can be found as a natural or artificial form. The natural soil such as sedimentary type usually presents initially a saturated condition but then it moves to partially saturated condition by drying as an environmental changing condition and can be found more in the arid and semi-arid area. For instant, some of the tropical soils such as laterite or saprolite are found in unsaturated state due to high permeability and climate change conditions are originated by decomposition of the parent rock (Vaughan, 1985). The artificial soils are compacted soils with unsaturated nature condition, which are widely used in dams, embankments and earth fills. Also, according to Barden (1995) it is reasonable to accept similarity between the natural soils and compacted soils.

2.2 Compacted soil

2.2.1 Introduction

Compacted soils are used for a variety of engineering structures such as dams, canals, roads and railway embankments, dikes, and etc. So, the study of the fundamental behaviour of these types of soils is very important for civil engineering. The main objective of soil compaction is to provide a new material with a better structure to improve the properties of the soil. Therefore, it is important to understand the hydro-mechanical behaviour of compacted soils. Several researchers conclude that the behaviour of compacted soils that is characterized by its collapsibility, swelling, permeability and others is, in fact, basically controlled by the stress variables, dry density, degree of saturation and microstructure (Barden and Sides, 1970; Cox, 1978; Lawton et al., 1989; Gens et al., 1995; Tatsuoka, 2015).

2.2.2 Compaction theory

Densification of soil mainly consists in applying mechanical energy for the improvement of geotechnical properties. The idea is to impact an increase in shear strength, decrease permeability and future settlements. The base of compaction theory comprises of two

sections, (i) the interaction between particles and (ii) the structure of compacted soils. The interaction between particles depends on the nature of soils. In the case of granular particles, interaction occurs as a direct contact between particles, while in presence of colloidal soils this interaction happens by means of the electromagnetic forces (Carvalho et al, 1987). Likewise, the evaluation of compacted soil behaviour is related to understanding the structure of the compacted soil. Therefore, the different types of compacted soil structure and the influence of various parameters on this structure are described in the next sections.

2.2.3 The structure of compacted soil

Collins and McGown (1974) published one of the early studies in the structure of compacted soil and recommended three concepts to describe the structure of compacted soils: 1) the arrangement of elementary particles (platelets); 2) the assembly of particles (aggregates); and 3) empty spaces. Alonso et al. (1987) in their research conducted the microstructural analysis on compacted soil. They pointed out that the microstructure of compacted clay soil is comprised of three elements: Size of the individual particles, aggregates of particles, and pores. By a combination of these three components, three types of basic structures can be determined as follows:

- Matrix type which is made by homogeneously distributed of particles.
- Basic particle aggregates that are related to elementary particles into greater grains and larger pore between them.
- Sand or clay grains between large grains or direct contacts between clay particles without connectors.

Figure 2-1 shows the combination of these three elements by (Alonso et al., 1987). According to their dissertation, the factors which are having influence on arrangement of compacted soil particles can be classified as internal and external. The internal factors consist of mineralogy, shape, size of the particles, and water content. External factors are included the technique of compaction method and the magnitude of the energy used during compaction procedure. Thus, the compaction of the soil as an external factor changed the arrangement of particles, the initial structure, and the pores structure.

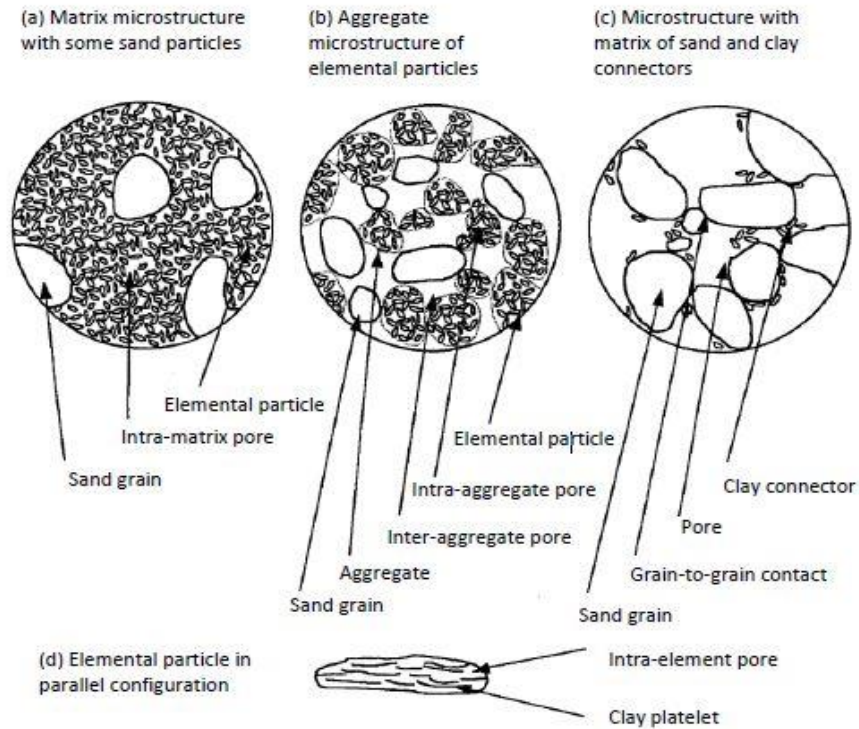


Figure 2-1: Distribution of elementary particles, aggregates, and pores (Alonso et al., 1987).

The structure of compacted soil is highly affected by microstructure composition. Therefore, microstructure analysis has been played an important role to determine mechanical and hydraulic behaviour of compacted soils.

2.2.4 Influence of water content in compacted soil structure

The capillary air-water and water–solid adsorption happens between water and the soil particles at a microscopic level. Consequently, extraordinary focusing is required to understand this microstructural behaviour. Some of the early works on microstructure analysis of compacted soil based on the concepts of flocculated (dry side of optimum) and dispersed structure (wet side of optimum) have been published by Lambe, (1958); Seed & Chan, (1959); Lambe & Whiteman, (1969).

Barden (1974) emphasises the importance of optimum water content as a dividing line between wet and dry consolidation processes.

Alonso et al. (1987) found that the compacted soil on wet side of optimum water content has matrix microstructure. Also, in dry side of the optimum, collapsibility behaviour are predominant in the microstructure of aggregates or fragments connectors.

Lawton et al. (1989) realized the effect of compacted soil structure on dry and wet side of optimum. They observed that samples compacted on dry side, due to an open initial structure (flocculated), exhibit collapse behaviour when getting saturated. In some case of very compacted condition, swelling behaviour can be happened. However, there is not any changing occurred in volume by compacted on wet side after saturation.

The bimodal and unimodal structure of compacted soil are described by (Gens et al., 1995; Satyanaga et al., 2013). Generally, samples compacted on the dry side show a “bimodal” pore size distribution (PSD) with two distinct peaks for fines and aggregates; whereas, those compacted on wet side show a PSD with a single, wider peak. The structure of bimodal and unimodal on dry and wet side of compacted soil are shown in Figure 2-2 (Satyanaga et al. 2013).

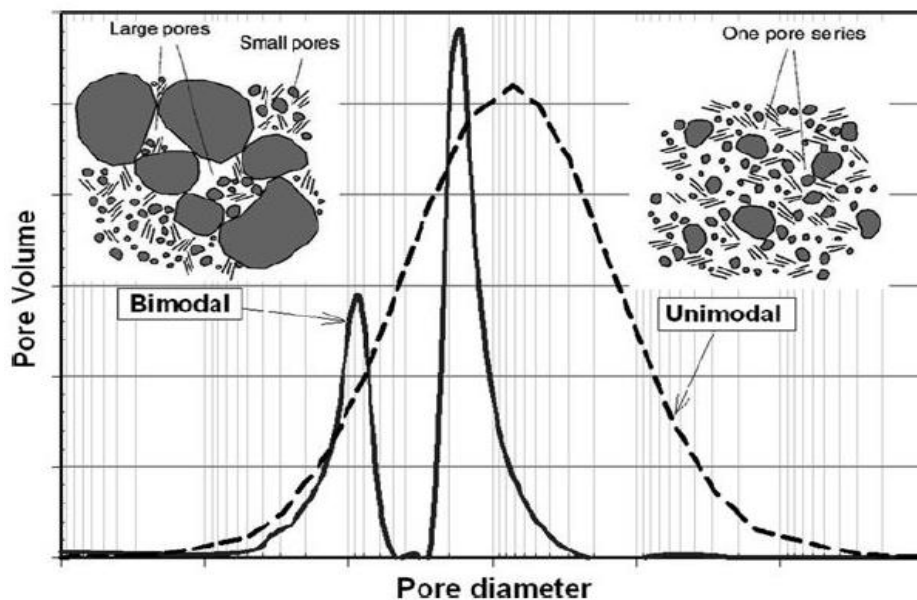


Figure 2-2: Unimodal and bimodal structure and pore size distribution of compacted soil (Satyanaga et al., 2013).

Delage et al. (1996) studied on the microstructure of a laboratory statically compacted silt at different densities and water contents, at various points of the Proctor curve. The techniques were assessed to study of microstructure analysis are scanning electron microscopic (SEM) as a qualitative method and mercury intrusion pore size distribution (PSD) as a quantitative method. Soils compacted at the dry side of optimum demonstrate open structure formed by aggregates of particles, while soil compacted at wet side presented a more homogeneous structure without the presence of large pores. Figure 2-3

represents the scanning electron microscope results at the dry and wet side of the optimum content.

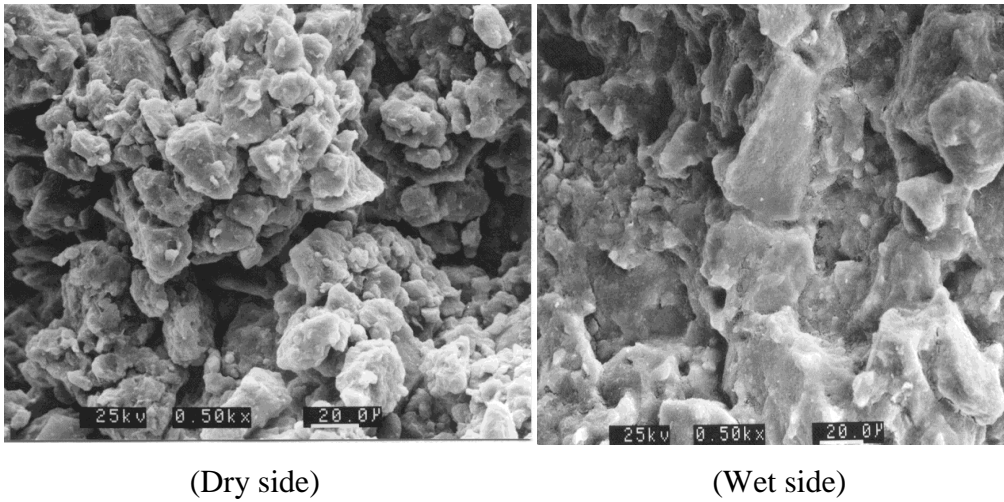


Figure 2-3: Scanning electron microscopic results at the dry and wet side of the optimum content (Delage et al., 1996).

Buenfil et al. (2004) analyzed the microstructural behaviour of compacted Barcelona silty clay under isotropically load in triaxial cell. Sample were compacted statically at high void ratio ($e=0.82$) and then loaded under isotropic conditions until reach a lower void ratio ($e=0.57$). The ESEM observations are shown in Figure 2-4. The clay aggregates are clearly observed in case of high void ratio (Figure 2-4,(a)), afterwards, a significant reduction occurred at size and volume of the macropores in lower void ratio conditions upon isotropic loading (Figure 2-4,(b)).

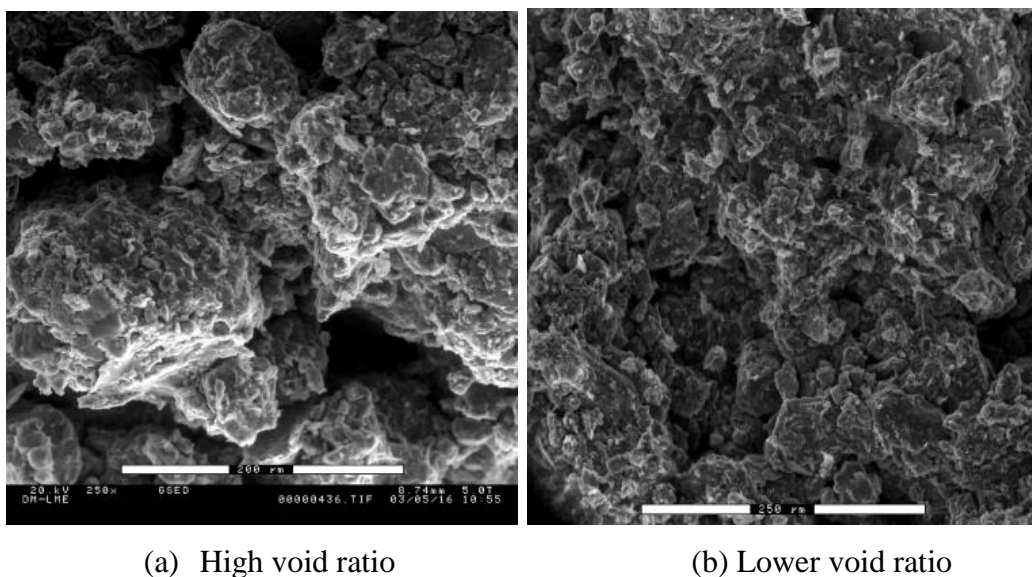


Figure 2-4: The ESEM observations of compacted Barcelona silty clay (Buenfil et al., 2004).

Some studies (Romero & Simms, 2008; Lee & Zhang, 2009; Monroy et al. 2010) represented that, when soil is compacted on dry side, water is confined in clay aggregates and trended to build aggregates structures that behave as much larger particles.

Suriol et al. (1998) and Suriol & Lloret (2007) evaluated microstructural effects on both wet and dry side of optimum in compacted Barcelona silty clay ($W_L=30.5\%$, $IP=11.8\%$). For same vertical compaction stress of 0.6 MPa, points D and W in Figure 2-5 (a) were selected to represent the dry and wet sides of optimum, respectively. After compaction, the specimen on point W was dried under suction controlled oedometer conditions until reach the same water content, dry density and suction that the specimen compacted at dry conditions (point WD), then, two samples were selected as WD and DD, to evaluate collapse potential in soaking under constant vertical stress. It can be seen that, under the same dry density, suction and water content the microstructure effect causes more collapsibility on sample DD in compare with sample WD. after drying, the structure of the specimen compacted at wet conditions is not the same that the structure of the sample compacted at dry conditions.

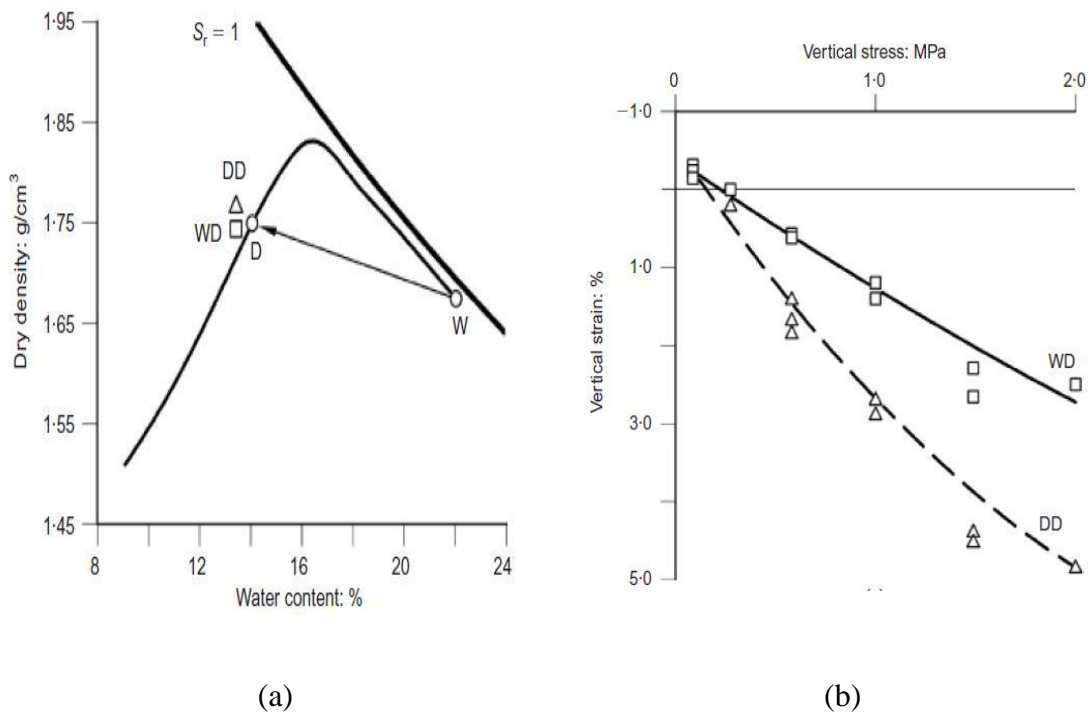


Figure 2-5: Statically compacted Barcelona silty clay: (a) compaction state of sample DD and WD; (b) collapse after wetting under vertical stress for samples with the same dry density and water content but compacted at different conditions (Suriol et al., 1998 and Suriol & Lloret 2007).

Romero et al. (2011) studied the effect of loading and suction changing in compacted Boom clay under oedometer conditions. The scheme of stress and wetting is represented in Figure 2-6 (a). Additionally, the results of pore size distribution tests are plotted in Figure 2-6 (b). It can be seen from Figure 2-6 (b) that, the first loading-wetting path under overall constant volume causes remarkable reduction in macropores sizes, and increasing in volume sizes, after that, the volume decreased during the drying path. In contrast point, the microporosity remains unchanged during wetting–drying cycle.

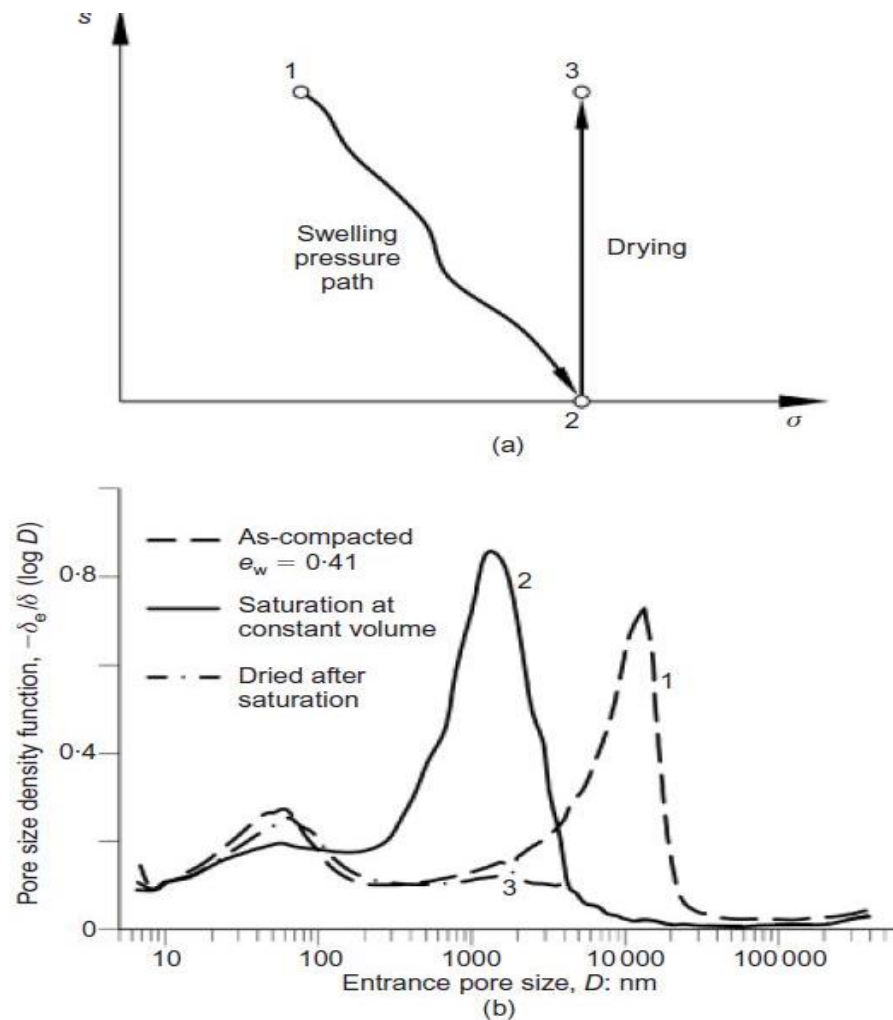


Figure 2-6: Compacted Boom clay: (a) stress path and wetting and drying cycle, (b) mercury intrusion porosimetry results (Romero et al., 2011).

Tatsuoka (2015) reviewed the influence of degree of saturation on both dry and wet side of compacted soil, he revealed that, in case of degree of saturation less than a certain optimum amount ($S_r < S_{r\text{opt}}$), due to high matric suction and lower water content, the fine particle sticking to large fragments and causes coherent micro-structure. From the opposite position, when, the degree of saturation is higher than optimum one ($S_r > S_{r\text{opt}}$)

due to low matric suction and higher degree of saturation, the fine particle filled the void between large fragments and causes dispersive micro-structure. In coherent micro-structure the structure is more stable than dispersive structure because of contribution of fine particle in stability of large fragments. Figure 2-7 illustrates the effect of degree of saturation as compacted state on micro-structure.

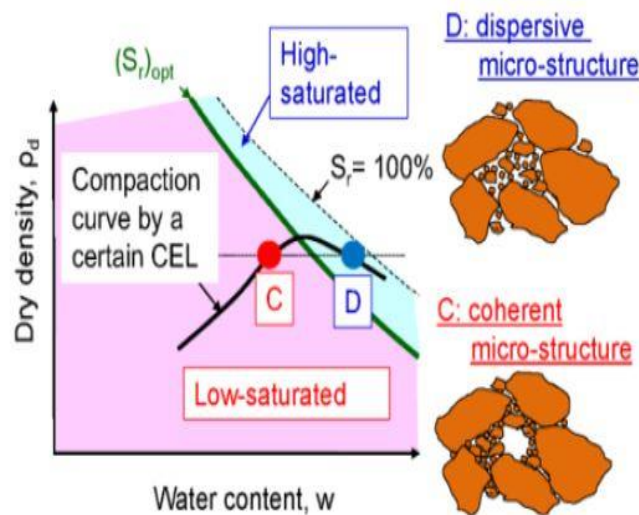


Figure 2-7: Effects of “ S_r at compacted state” on the micro-structure of compacted soil (Tatsuoka, 2015).

2.3 Introduction of ‘all-one’ material as a binary granular mixtures

2.3.1 Introduction of ‘all-one’ mixtures

The need for using materials that are available within the surroundings of the construction, have promoted the use of different ranges of particle sizes and mixtures of soils. The ‘all-one’ is a materials formed during excavation, widely accepted in national standards (For example, PG3=Spanish standard for road construction for earthworks), which is a mixtures with particles sizes covering the range between rockfill and soils. Figure 2-8 depicts the area of grain size distribution curve for all-one mixture as binary granular mixtures.

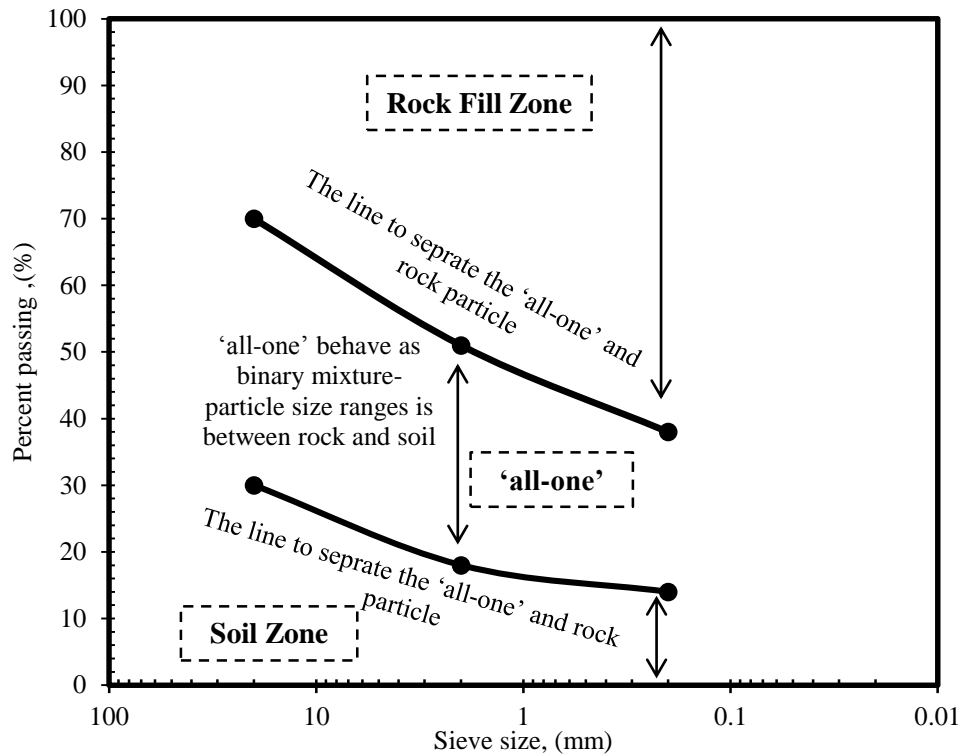
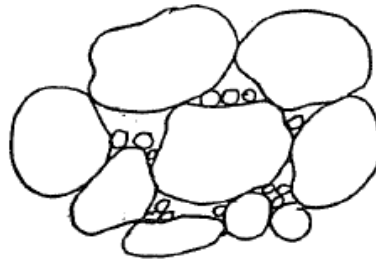


Figure 2-8: Particle size distribution of 'all-one' mixture.

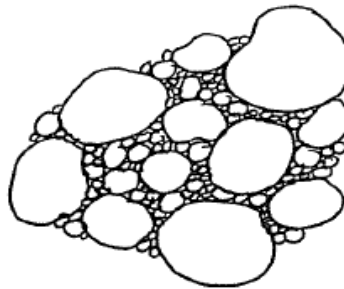
The advantage of using this type of mixture with large fragments immersed in a finer fraction matrix is that it usually requires lower amounts of water for compaction. These large fragments display a low porosity, which makes difficult absorbing the optimum and larger amount of water determined under laboratory conditions (conventional compaction tests use the fine fraction < 4.76 mm). In addition, these oversized fragments with high dry density induce certain increase in the dry density of the mixture compared to that obtained with the finer fraction used in laboratory compaction.

2.3.2 Fill and under-filled packing structure

One of the methods to preparation material for granular fill is the excavation of rock. The procedure of blasting rock during excavation causes new types of structures named filled and under –filled packing. The Figure 2-9 shows two types of packing by blasting the rock surroundings of the construction (Vaughan, 1994).



UNDER-FILLED PACKING
[SHORTAGE OF FINES - FEW HIGHLY STRESSED PARTICLE CONTACTS]



FILLED PACKING
[EXCESS OF FINES - MANY LOW STRESSED PARTICLE CONTACTS]

Figure 2-9: Under filled and filled packing by (Vaughan, 1994).

It can be shown that from Figure 2-9, in under-filled packing structure large particles have direct contact to other large particles with small amount of fine particles between the voids. The few amounts of fine particles are insufficient to fill all the pores. Therefore, the few contacts between large fragments became highly stress by increasing the amount of load. By increasing the amount of load, grain breakage will occur at large particles in contact surface. By breaking the large particles the amount of fine content increased. On the other hand, in filled packing structure, fine particles fill the voids between coarse particles, due to increasing in particles contacts, the stress getting lighter, but particle breakage will be restricted by increasing the amount of load (Vaughan, 1994).

According to study of Lopez et al. (2016), the binary granular mixture can be divided to five zone areas based on fine content concentration in the mixtures. The description of each zone and schematic structure are represented in Table 2-1 and Figure 2-10, respectively.

Table 2-1: Description of various types of binary granular mixtures by (Lopez et al., 2016).

Types of structure	Description
(A) Underfilled (A-1) Underfilled-unstable	None or small amount of fines underfilling the voids between coarse grains with little contribution to the load-bearing skeleton
(B) Interactive-underfilled	Strong interaction between fractions; coarse grains still responsible for the main load-bearing skeleton, whereas the fines optimally fill their voids
(C) Interactive-overfilled	Fine particles start overfilling the voids between coarse grains, significantly disrupting their contact network and starting to form a load-bearing skeleton
(D) Overfilled	None or small amount of coarse grains floating in a matrix of fine grains

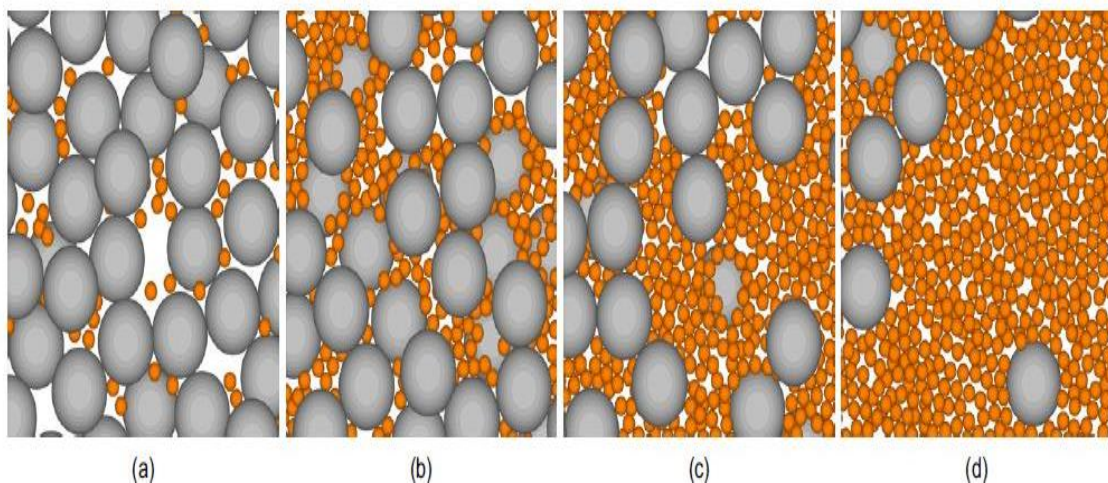


Figure 2-10: Schematic representation of various structures of binary granular mixtures: (a) case A/A-1, (b) case B, (c) case C and (d) case D (Lopez et al., 2016).

2.4 Transitional zone between shielding skeleton and matrix on binary granular mixtures

2.4.1 Introduction

Generally, in binary granular mixture, the structure properties of mixture, depends on the amount of coarse or fine particles. The structure of mixtures is changing by increasing the amount of fines. This changing behaviour of structure in binary granular mixture is shown in Figure 2-11 as presented by Vallejo (2001).

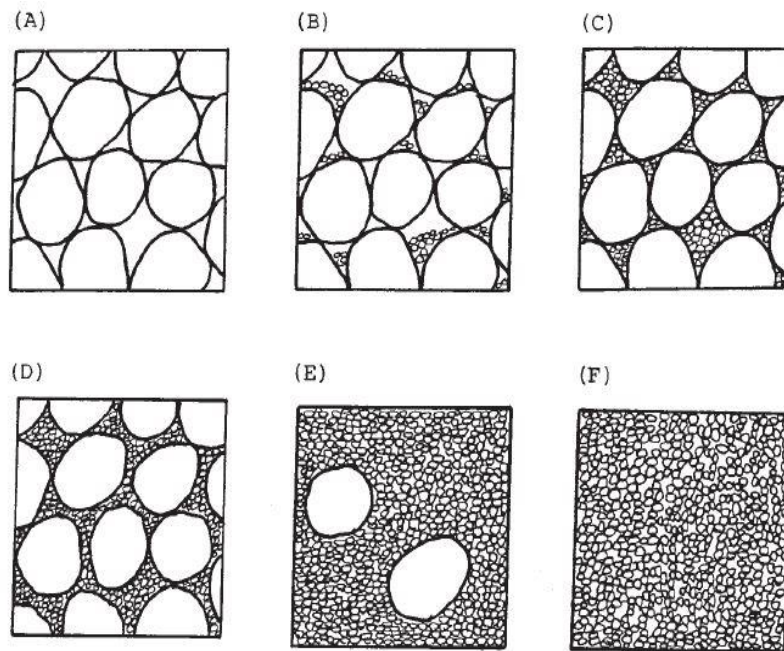


Figure 2-11: Effect of fine content in binary granular mixtures (Vallejo, 2001).

When, there is not any fine particles or a very small amounts of fine content exists between granular fragments, the properties of structure are supported by coarse grain material which is represented in Figure 2-11 (A) and (B) (coarse grain concentration is between 80 to 100 %). The transitional coarse grain supported structure is shown in Figure 2-11 (C) (coarse range between 70 to 80%). Also, the transitional fine grain supported structure is presented in Figure 2-11 (D). (Coarse range between 40 to 70%). Finally, the fine grain supported structure has not any or very small amount of coarse grain is presented in Figure 2-11 (E) (F) (coarse range between 0 to 40%).

2.4.2 Criteria of Transitional Zone

Table 2-2 shows some limit of percentage of gravel in binary mixtures which controlled the shear resistance of mixtures by various researchers.

Table 2-2: Percentage of gravel in mixtures conducting to different types of structures (Vallejo, 2011).

Percentage of gravel in mixtures				
Gravel supported shear resistance	Gravel and sand supported shear resistance	Sand supported shear resistance	References	
>65	65-40	<40	Fragaszy et al. 1992 Marsal and Fuentes de la Rosa 1976 Vasileva et al. 1971 Doddiah et al. 1969 Holtz and Gibbs 1956	
>70	70-50	<50		
>80	80-55	<55		
>70	70-50	<50		
>65	65-50	<50		
Average	>70	70-49	<49	

Also Minh et al. (2014) and Lopez et al. (2016), they characterized the structure type of binary mixtures by the amount of fine content in the mixtures. The limits obtained in their investigations are shown in table 2-3.

Table 2-3: Different structures of binary mixture according to fine content, (FC (the ratio of the weight of fine to the total weight of the binary mixtures)).

Type of mixtures	Minh et al. (2014)	Lopez et al. (2016)
Underfilled	FC < 32%	FC < 25%
Interactive-underfilled	32 < FC > 44 %	25 < FC > 40 %
Interactive-overfilled	44 < FC > 55 %	40 < FC > 55 %
Overfilled	FC > 55 %	FC > 55 %

Based on previous studies (Vallejo, 2001; Mekkiyah & Al Khazragie, 2015) on the effects of grain size on porosity, it can be seen that, fine particles filled the voids between granular fragments and causes decreasing in void ratio until they occupied all voids. Afterwards, void ratio started to increase by increasing in amount of fine particles. Figure

2-12 presents the void ratio versus fine sand contents according to study of Mekkiyah & Al Khazragie, (2015). They understood that, the TFSC (Transitional fine soil content) occurred at range of 55 to 70 % of fine sand content (the point of changing in void ratio) which is similar to study of (Belkhatir et al., (2011); Kuebris et al., (1998); Mitchel, (1993).

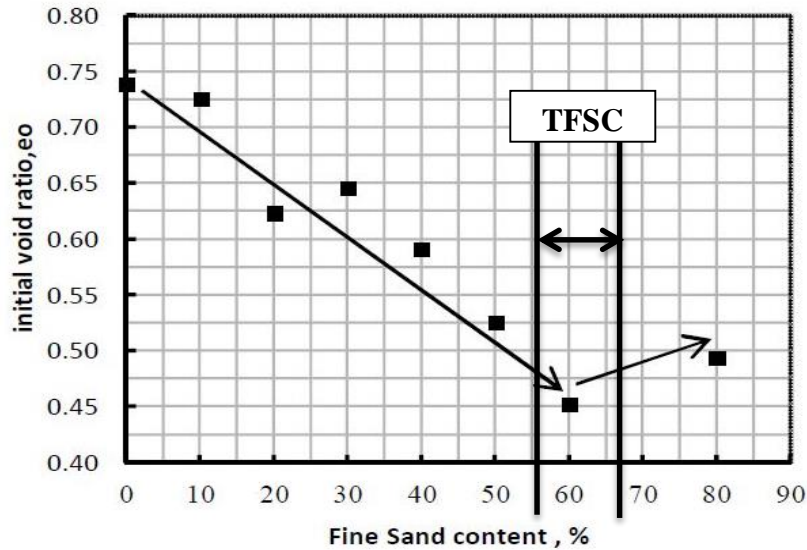


Figure 2-12: Initial void ratio versus fine content (Mekkiyah & Al Khazragie, 2015).

The porosity of granular mixtures (n_{mix}) can be determined by following equation 2-1 according to Vallejo (2011).

$$n_{mix} = \frac{V_0 - \left[\frac{W_c}{\gamma_c} + \frac{W_f}{\gamma_f} \right]}{V_0} \quad \text{Equation 2-1}$$

Where,

n_{mix} = Porosity of binary granular mixtures.

W_c = Weight of the coarse particles.

W_f = Weight of fine particles.

γ_c = Unit weight of coarse fragments.

γ_f = Unit weight of fine particles.

V_0 = Bulk volume.

The effect of fine content on the porosity of binary mixtures based on Vallejo (2011) is provided in Figure 213. The changing point in porosity describes the transitional zone.

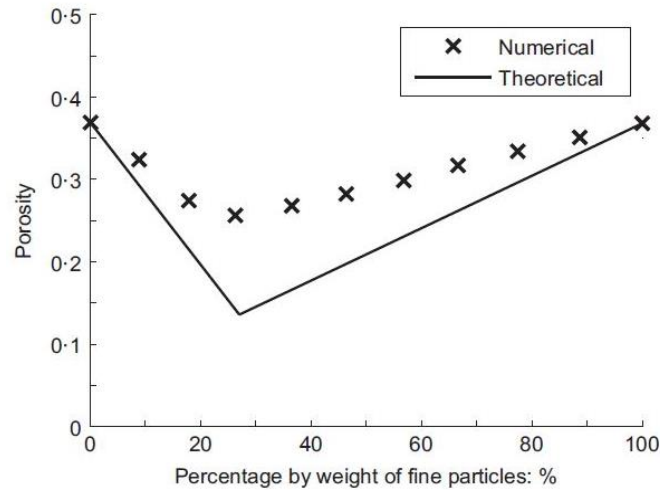


Figure 2-13: Porosity versus amount of fine content (Vallejo, 2011).

To sum up, the experimental data are rather controversial, and there is no general agreement about exactly a specific ratio for transitional zone in binary granular mixtures. Consequently, it can be seen that, some parameters such as particle mineralogy, strength, particle breakage, and grading would have effect to change the transitional zone. Therefore, each binary mixture depends on coarse and fine fragments types, strength, grading and breakage potential will have own criteria of transitional zone. In this dissertation, the transitional zone will discuss for ‘all-one’ mixtures in chapter 4.

2.5 Particle breakage and fractal analysis

2.5.1 Introduction

In geotechnical engineering structures such as earth structures or rock fill dams, due to high stress level, the particle breakage acts as an important function in the mechanical behaviour of the soil. Various Scientifics understood that the grain breakage can play a fundamental role in mechanical behaviour of variety of soil structures. A number of researchers tried to assess this behaviour either in field (Lee & Farhoomand, 1967; Coop & lee, 1993; Lade et al., 1996) or laboratory conditions (Blackwelder, 1920; Rowe, 1954; Hagerty et al., 1993; Lade & yamamuro, 1996, Vallejo, 2005; McDowell & De Bono, 2013).

Totally, based on analysis of previous researchers the following parameters affected to the amount of particle breakage:

- Particle shape.
- Particle strength.
- Particle size distribution.
- Void ratio.
- Amount of water in particle.
- Effective stress path.
- Contact forces between grains.

The breakage of material is detected by doing the sieve analysis before and after each test. Several indices are introduced to discover the changing in grain size distribution curve. Another important characterization procedure which is related to size and fragmentation of particles is fractal analysis. The description of these breakage parameters in mechanical points of soil will be included in next section. The methods of quantification developed by various researchers and previous studies are described.

2.5.2 Method to determine particle breakage coefficient

Several studies have been performed to identify particle breakage index. (Hazan, 1911; Shergold, 1954; Leslie, 1963; Marsal, 1967; Lee and Farhoomand, 1967; Hardin, 1978; Indraratna et al. 2005; Einav, 2007).

One of the seminal researches to evaluate considerable amount of particle breakage in rockfill material during large-scale triaxial tests was made by Marsal (1967). The Marsal breakage factor (Bg) presented as an amount of percentage differences in grain size distribution curve before and after loading. In order to calculate the Bg index, the percentage differences of remain material for each different sieve size before and after test is evaluated by following equation:

$$\Delta W_k = \Delta W_{ki} - \Delta W_{kf} \quad \text{Equation 2-2}$$

Where,

ΔW_k = The percentage differences of remain material before and after test on the same sieve size.

ΔW_{ki} = The percentage retained on sieve size k before the test.

ΔW_{kf} = The percentage retained on the same sieve size after the test.

He observed the positive and negative value of differences and finally he decided to specify Bg as a sum of the positive value of ΔW_k in percentage amount. This method implies that Bg could change if a different set of sieves was used. Figure 2-14 shows procedure of Marsal breakage index calculation.

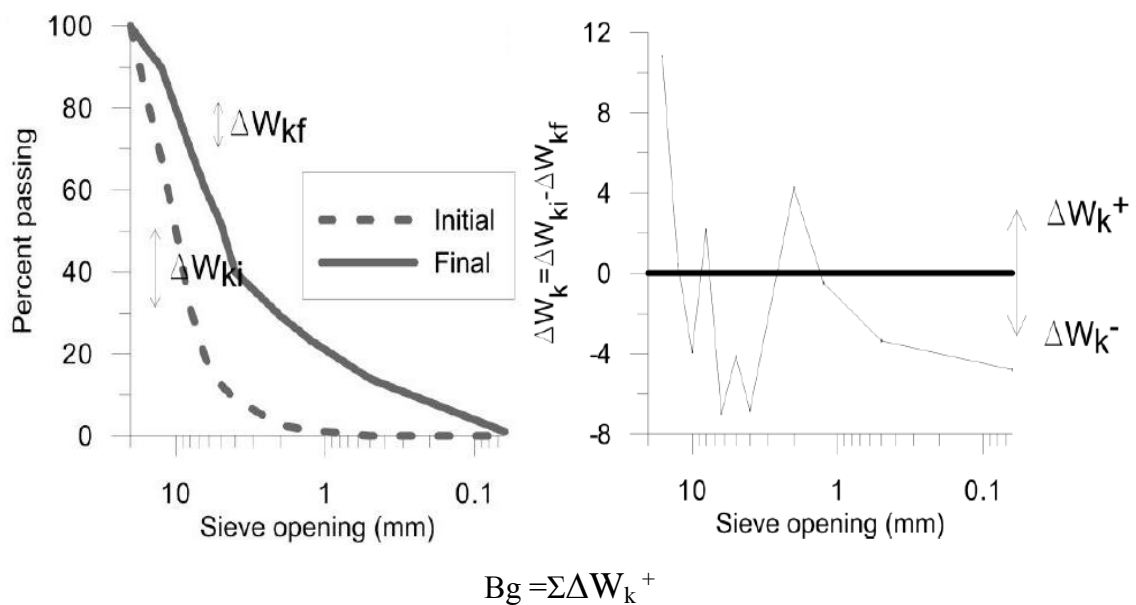


Figure 2-14: Marsal breakage index-Bg (Marsal, 1967).

The difference between the area of grain size distribution curve before and after test as a new important particle breakage index Br was proposed by Hardin (1985). He indicated particle degradation in a ratio of $Br = Bt/Bp$, where Bt and Bp, are breakage potential and total breakage area base on GSD curve, respectively. It has to be considered that the area between curves can be calculated by planimeter or numerical integration method. The area between curves is shown in Figure 2-15.

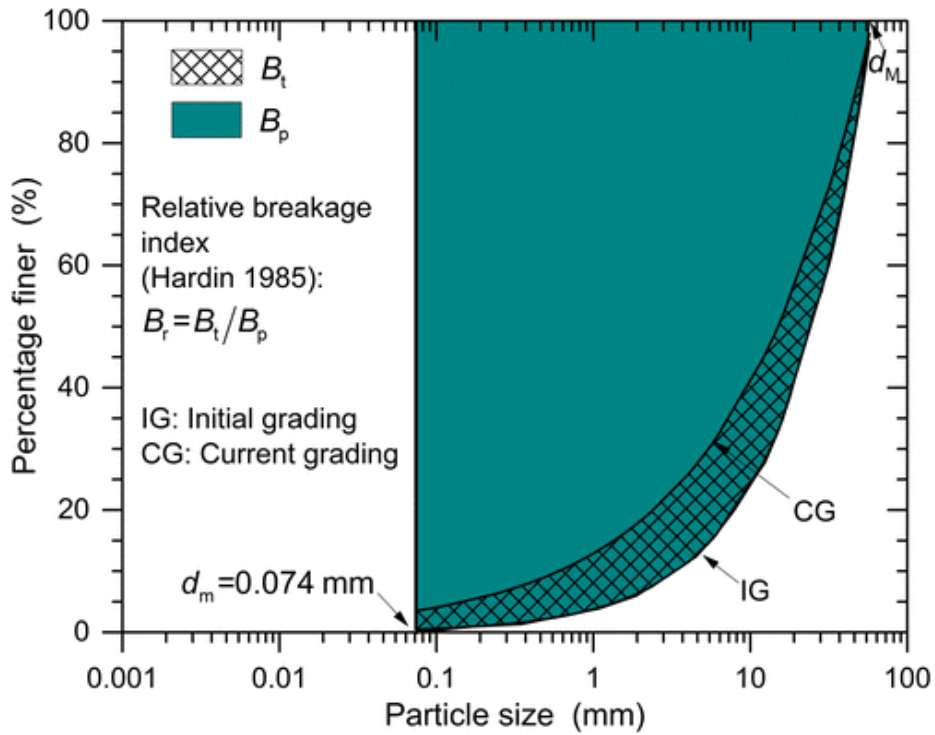


Figure 2-15: Hardin breakage index-Br (Hardin, 1978).

One of the most interesting approaches to this issue has been proposed by Einav (2007). He modified the Hardin breakage index (Br). The conception of reformed index by Einav is shown in Figure 2-16.

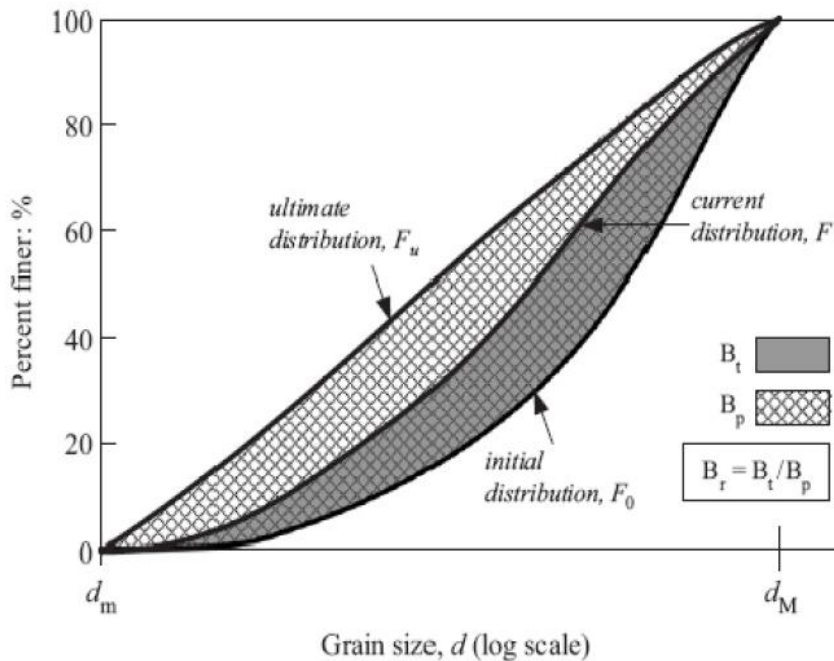


Figure 2-16: Modification definition of Hardin's degradation factor (Br) (Einav, 2007).

2.5.3 Method to determine fractal dimension

Tyler Wheatcraft (1992) developed a formula using particle size analysis for calculating the fractal dimension of fragmentation (DF_R). This calculation uses the retaining sieve mass and its corresponding diameter. This equation is defined as follows:

$$\frac{M(R < r)}{M_T} = \frac{r^{3-DF_R}}{r_L^{3-DF_R}} \quad \text{Equation 2-3}$$

Where,

$M(R < r)$ = Cumulative mass of particles with size R smaller than a given comparative size r.

M_T : Total mass of particles.

r_L : Maximum particle size defined by the largest sieve size opening.

DF_R : Fragmentation fractal dimension ($DF_R = 3 - m$).

Where m is the slope coefficient of the best line suited applied to the equation that can be determined from the plot of $M(R < r)/M_T$ versus r/r_L in a log-log scale.

The fractal dimension, by masses method, is determined depending on the particle size, the type of material selected, and the sample mass.

2.5.4 Particle breakage of granular binary mixtures with fine contents

Most published studies on particle breakage as mentioned in previous sections have focused on behaviour of particle index in well graded soil (uniform), otherwise, in case of binary granular mixtures, the amount of fine and coarse grain can have some effects on particle breakage.

According to study of Zhang & Baudet (2013) on the behaviour of particle breakage under 1-D oedomeer condition, the particle breakage decreased when fine grain content increased. Figure 2-17 shows the result of Zhang & Baudet (2013) on various size of the particles and different load conditions and with different fine contents.

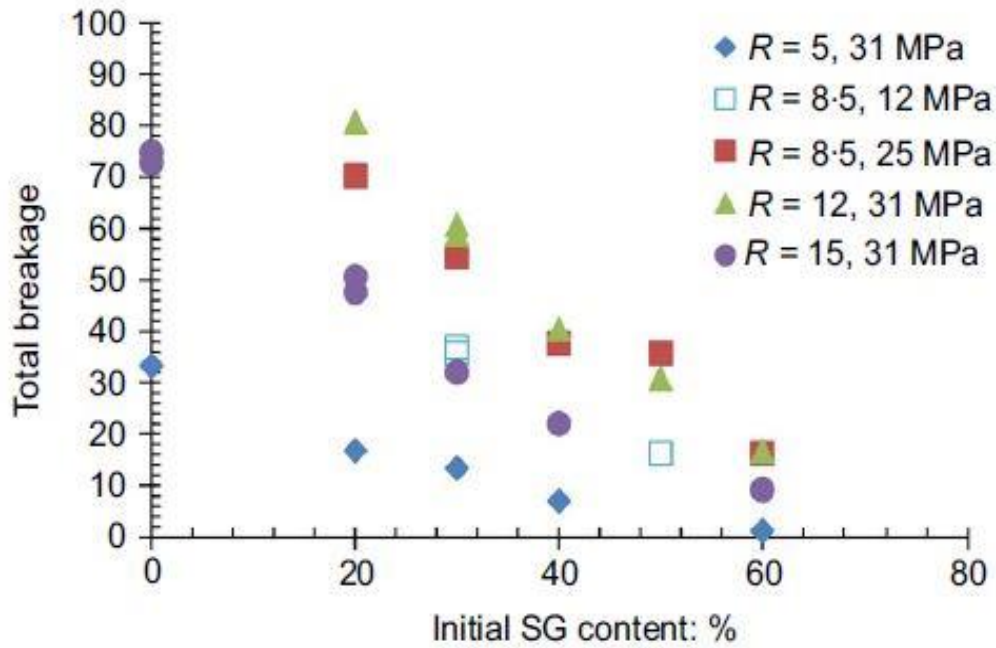


Figure 2-17: Particle breakage versus fine content (Zhang & Baudet, 2013).

Figure 2-18 illustrates the amount of particle breakage obtained by Hardin method in total and in small and large fragments separately.

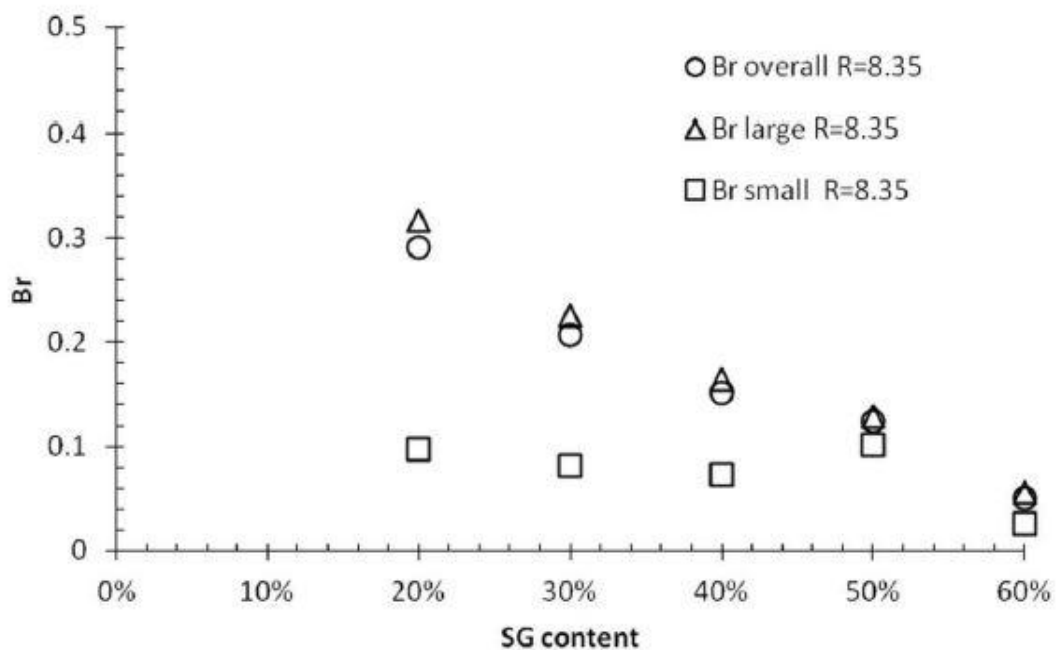


Figure 2-18: The amount of particle breakage in overall, small, and large fragments-(SG= fine grain content, R = diameter of large /diameter of small particles) (Zhang & Baudet, 2013).

It can be seen from Figure 2-18 , by increasing the fine content, the amount of breakage in small particle increased slightly, while this amount is significantly reduced in case of large fragments. In overall, it can be conclude that the breakage of mixtures is controlled by large fragments. Therefore, in binary granular mixture the size of large fragments plays an important role to control the breakage of the mixtures.

Generally, by decreasing the amount of fine content and in presence of more large particles, the amount of breakage will be raised according to studies of (Vallejo et al., (2005), Vallejo & Lobo-Guerrero, (2012)). They pointed out that by increasing the amount of large particles in granular mixtures, particles attract more forces and tends to break.

Einav (2007) carried out a series of numerical simulation by using the DEM software on bi-modal poorly graded specimens, and observed that the bigger particles attract more force chains than the smaller particles which is because the large particles having larger surface area and more contact points.

3 Methodology

3.1 Introduction

The present dissertation was designed to investigate the hydro-mechanical behaviour of ‘all-one’ mixtures. The behaviour are evaluated as a real case study on the construction of Albagés dam. As well as, at laboratory condition the experimental results of ‘all-one’ mixture prepared with different grain sizes and material are evaluated. The methodological approach taken into account in this study is provided with the experimental data. The following approaches such as: Compressibility, elastic modulus, collapsibility, water retention curve, and permeability are taken in to account to analysis the hydro-mechanical (H-M) behaviour of compacted ‘all-one’ mixtures. Also, microstructural changes (particle size distribution changes) under various H-M paths were selected to understand the breakage behaviour of compacted material.

3.2 Description of different types of material used in the investigation

To establish the basic material for this research and to analyse the behaviour of different fragment sizes under some experimental studies, four kinds of mixture material were selected, namely FN, FS, M and FA (see Table 3-1). ‘All-one’ mixtures were prepared with different types of materials as large fragments immersed into the same type of finer particles. All types of mixtures are blended according to grain size distribution curve presented by (Funk and Dinger, 1980). The various fragments size mixtures, according to GSD curve defined by this method are represented in Figure 3-1. The idea to select this method as reference curve will be discussed later in more detail in this chapter. The key advantage of using Funk and Dinger GSD curve is that, the maximum and minimum fragment size are possible to control in mixtures. In this work, the size of 38.5 mm and 0.15 mm of particles are used in mixtures as maximum and minimum size, respectively. In addition, 60 percent of fragments smaller than 19 mm up to minimum size to 0.15 mm are combined with 40 percent of fragments size between 19 mm to 38.5 mm. Fragments with size less than 19 mm are named matrix part which are similar in all mixtures and consist of Barcelona silty clay. In addition, different types of fragments are used for particles bigger than 19 mm. Accordingly, FN contained Barcelona silty clay particles as natural fragments either in matrix or fragments bigger than 19 mm. The combination of

60 % of Barcelona silty clay fragments less than 19 mm and 40 % of quarzitic slate between 19 mm and 38.5 mm formed FS as rigid mixtures. Finally, the 60 % of Barcelona silty clay under 19 mm adding to 40 % of artificially cemented fragments comprised the FA types of mixture. Table 3-1 and Figure 3-2 provide informations for four kinds of mixture materials for next experimental study.

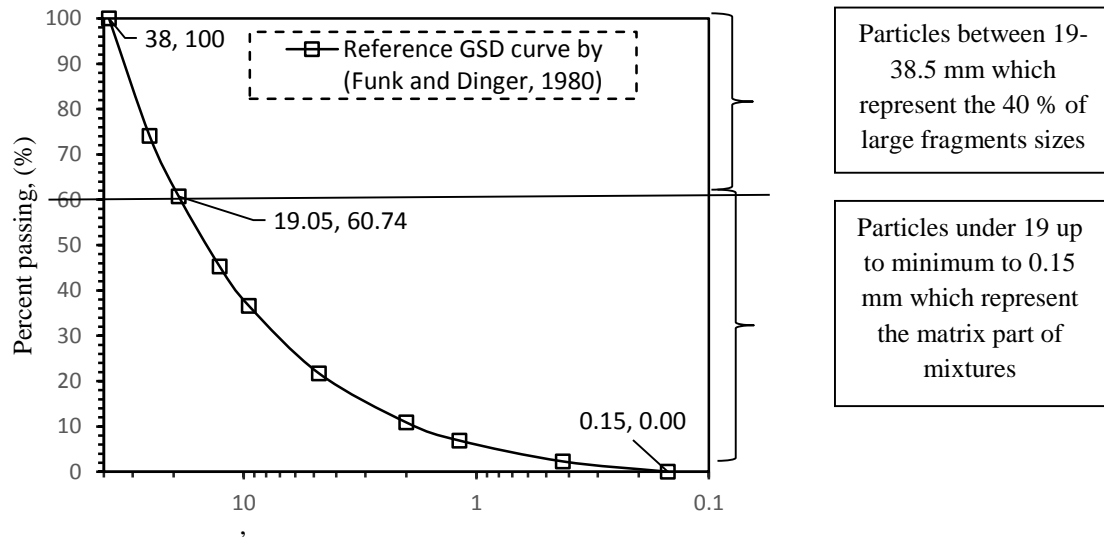


Figure 3-1: Particle mixtures according to grain size distribution curve (Funk and Dinger, 1980).

Table 3-1: Different types of mixture (M, FN, FA, and FS).

Mixture Type	Description of Mixtures
FN	Barcelona silty clay particles between 38.5-0.15mm combined according to modified Funk and Dinger GSD curve
FS	60 % Barcelona silty clay particles between 19-0.15 mm+40 % quarzitic slate between 19-38.5mm
M (Matrix form)	100 % of the particles between 19-0.15mm
FA	60 % of the particles between 19-0.15 mm + 40% of artificially cemented fragments



(a): Matrix



(b): FN



(c): FS



(d): FA

Figure 3-2: Different types of materials (FN: Natural fragments, FS: Slate fragments, FA: Artificial fragments).

As it can be seen above, For the purpose of compaction optimization, and to see how much energy goes to densify matrix part and breakage of fragments, particles larger than 19 mm was selected based on stiffness of fragments. Therefore, Barcelona silty clay and slate quartzitic are chosen as weak and rigid fragments, respectively. The artificial cemented fragments are selected to represent the strength behaviour between them. The Figure 3-3 shows the compression strength of materials for particle selected bigger than 19 mm.

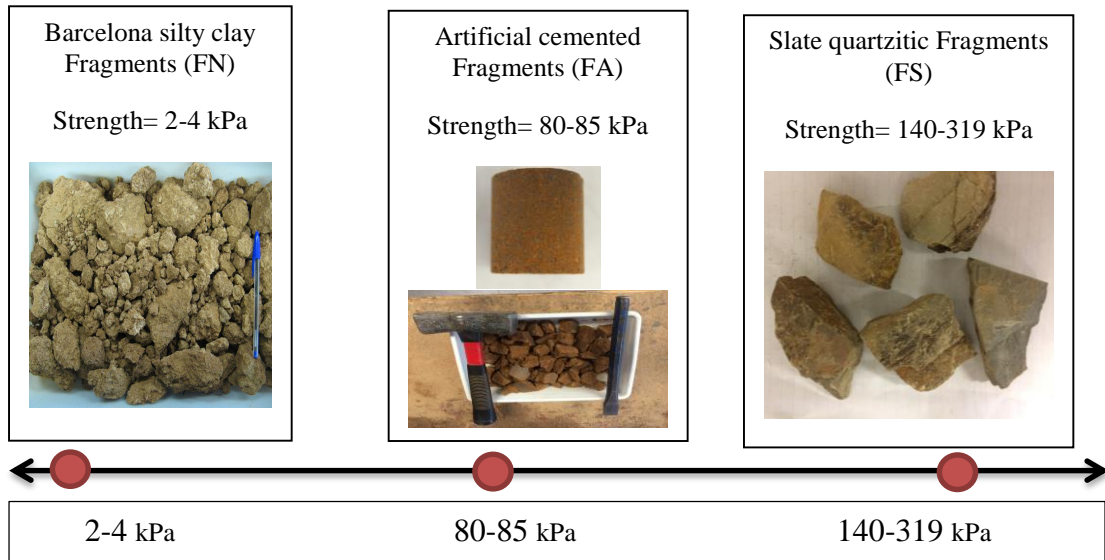


Figure 3-3: Strength behaviour of various materials for particles bigger than 19 mm.

3.3 Material properties

The basic geotechnical properties of various materials are described in this section.

3.3.1 Barcelona silty clay

Around 400 kg of Barcelona silty clay was collected from UPC Campus Nord during the excavation of the retaining wall for the building B1. The soil collected procedure and location map of Barcelona silty clay are shown in Figure 3-4 and Figure 3-5.

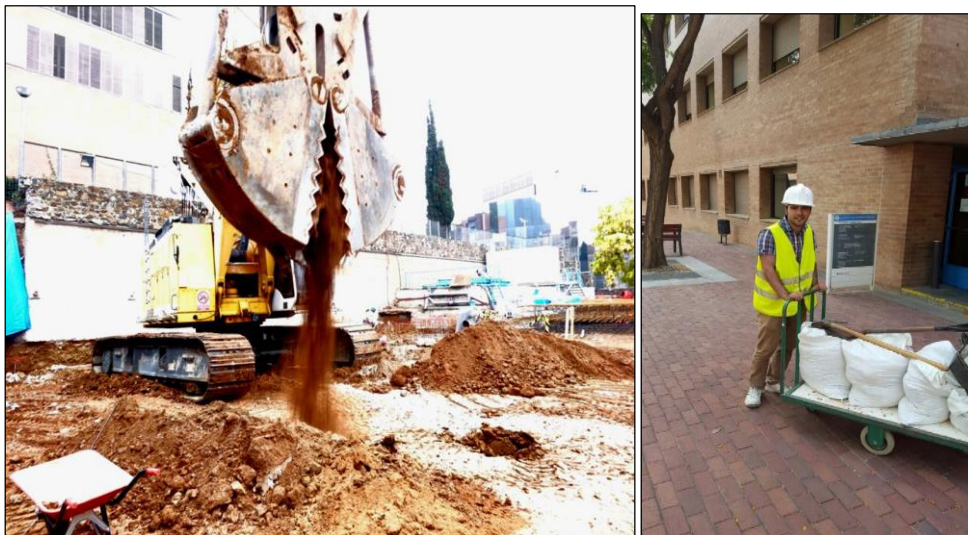


Figure 3-4: Procedure to collect Barcelona silty clay material.



Figure 3-5: Location of building B1project at Universitat Politècnica de Catalunya - UPC campus nord (Google map, 2016).

The characterization of the Barcelona silty clay for matrix and fragments includes grain size distribution, consistency limits, compaction curves, and pore size distribution. Figure 3-6 presents basic geotechnical properties, which are plotted in plasticity chart.

w_L (%)	w_p (%)	PI (%)	Sand (%)	Silt (%)	Clay (%)	ρ_s Mg/m^3
31-32	16-20	11-16	39-47%	40-45%	13-16%	2.67-2.71

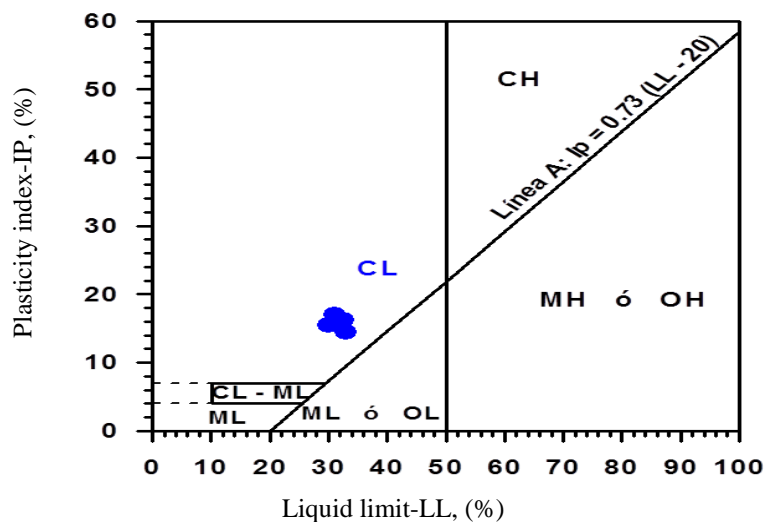


Figure 3-6: Plasticity chart for Barcelona silty clay.

The particle size distribution of Barcelona silty clay done by previous researchers at UPC Geotechnical Laboratory are shown in Figure 3-7. In addition, Figure 3-8 represents the electronic microscope image analyses of Barcelona silty clay. The compaction curves of Barcelona silty clay for matrix and particle (passing # 4 sieves) for both modified and standard method are shown in Figure 3-9. In natural Barcelona silty clay there are some large fragments cemented with carbonate which are presented in Figure 3-10.

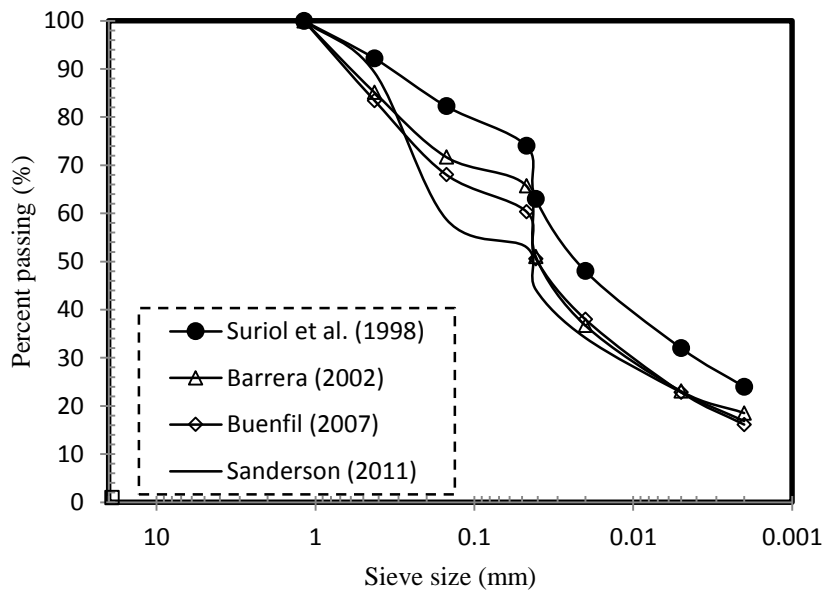


Figure 3-7: Particle size distribution of Barcelona silty clay.

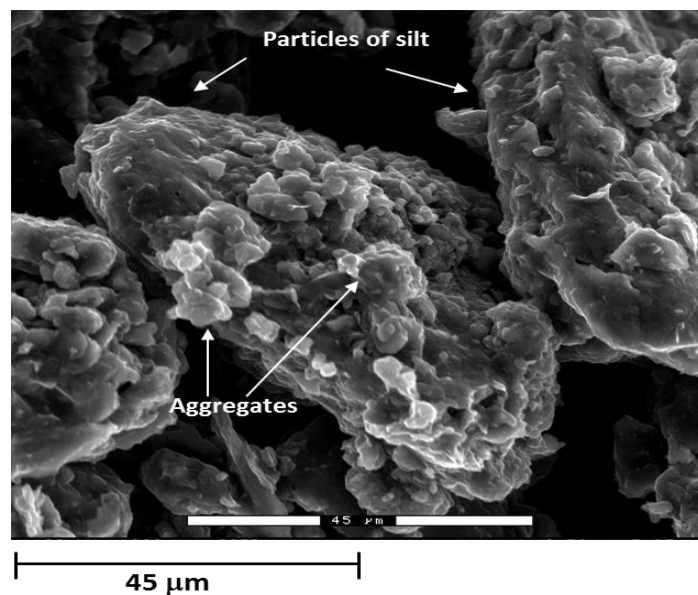


Figure 3-8: Electronic Microscopic Image analyses of Barcelona silty clay (Compacted soil passing sieve 4.75 mm, $W=11\%$ and density of 1.63 Mg/m^3).

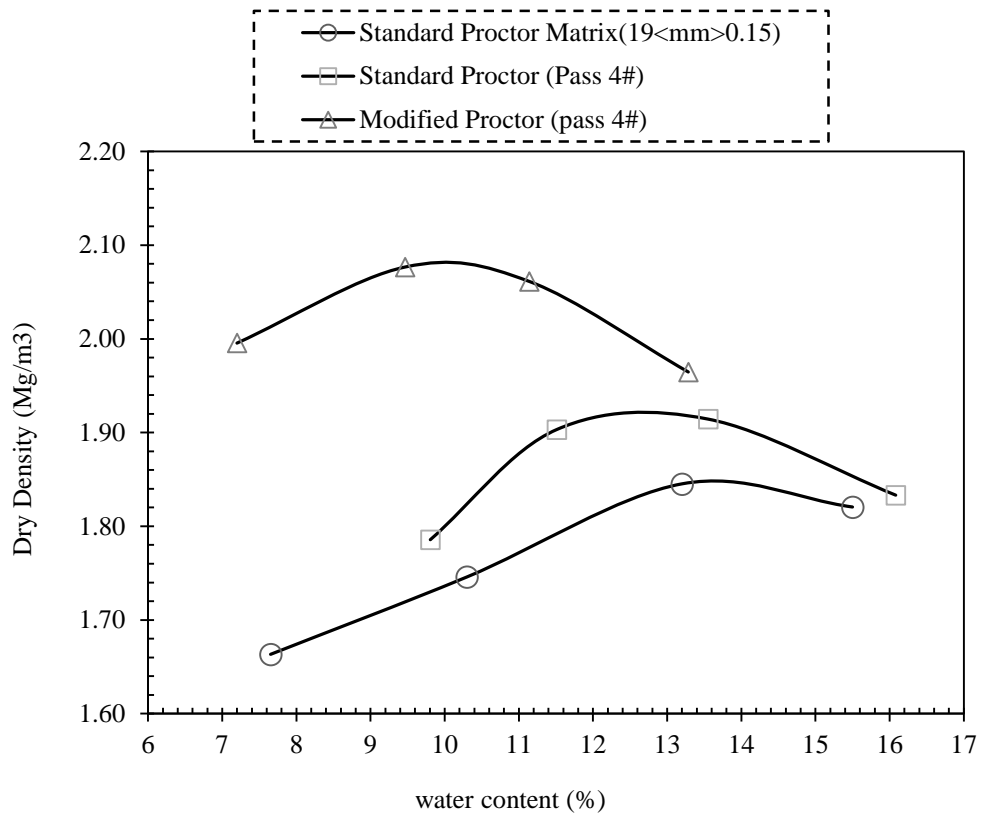


Figure 3-9: Compaction curves of Barcelona Silty clay.



Figure 3-10: Large carbonated fragments of Barcelona silty clay.

The result of mercury intrusion porosimetry test for large carbonated fragments is shown in Figure 3-11. Dry density of fragments is equal to 2.2 Mg/m³.

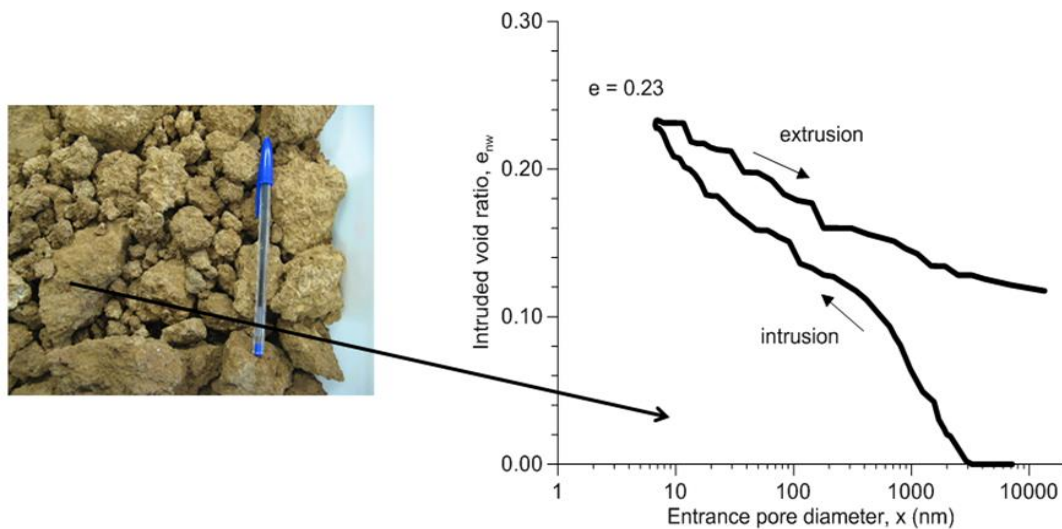


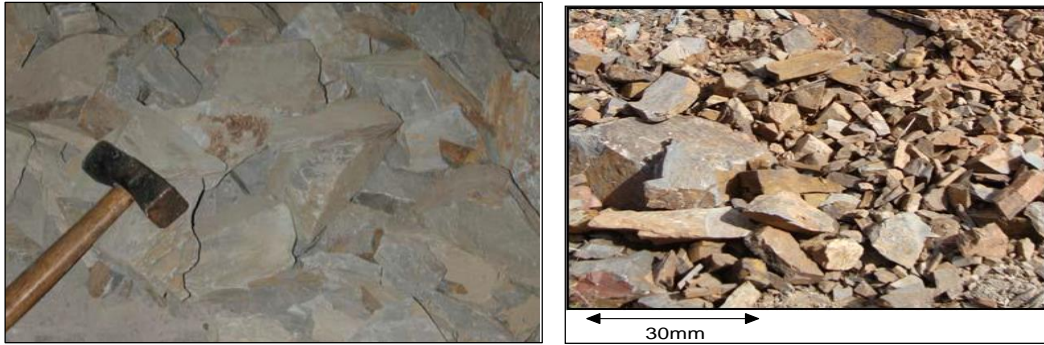
Figure 3-11: Mercury intrusion porosimetry test for large carbonated fragments of Barcelona silty clay.

3.3.2 Rigid fragments of quartzitic slate

In order to form the mixtures FS, the 40 % of quartzitic large fragments between 19 to 38.5 mm have been combined with matrix type. The large particles of quartzitic cambric slate were collected from Pancrudo river outcrop (Aragón, Spain), then they were crushed to obtain particles size between 19 to 38.5 mm for the experimental test. Some properties of the rock slate material are summarized in Table 3-2 (Romero et al. 2013). Also, the quartzitic large slate both in place and in laboratory conditions are depict in Figure 3-12.

Table 3-2 : Properties of the quartzitic slate (Romero et al., 2013).

Property	Value
Uniaxial compression strength:	14.2-31.9 MPa
Tensile strength (saturated core specimen: $\phi=50\text{mm}$; $h=25\text{mm}$)	5.97 MPa
Density of solids ·	2.75 Mg/m ³
Water absorption (saturation)	2.9%
Void ratio (mercury intrusion porosimetry)	0.081
Slake durability (5th cycle) (ASTM D4644)	96.5%
Flakiness index	19%



(a) Laboratory crushed particles

(b) Large slate at origin place

Figure 3-12: Particles of quartzitic cambrian slate.

3.3.3 Artificial fragments

As it was mentioned, the FA combined 60 percent of matrix and 40 % of artificial cemented fragments. The idea of creation artificial fragments is to fabricate particles between higher and lower amount of available strength (Barcelona carbonated = 2-4 kPa and Slate = 140-319 kPa). This artificial particles were prepared at UPC Laboratory. Samples are prepared by combining available Barcelona silty clay particles less than 2 mm with distilled water and Portland cement. Static compaction was selected to reach the dry density of 2.1 Mg/cm³ which is similar to density of natural fragments. The cement that was chosen is the Superdragon type of the company Cements Molins. It is a Portland CEM I 52.5 R, and its physical and chemical properties are presented in Table 3-3. The characterization and specifications of Superdragon cement are defined in Figure 3-13.

Table 3-3: Physical and chemical properties of Superdragon cement
(www.cmi.cemolins.es/en/productos/super-dragon).

PHYSICAL AND CHEMICAL PROPERTIES	
Physical state at 20 °C	Powder
Colour	Grey.
Odour	Odourless
pH value in distilled water	11-13.5 (20 °C)
Melting point [°C]	> 1250
Density	2.75 - 3.20 g/cm ³ (20 °C)
Bulk density	0.9 - 1.5 g/cm ³ (20 °C)
Solubility in water [mg/l]	Slight. 100 - 1500 (20 °C)

	Typical values	Specifications according to standard	
Clinker (%)	98	min. 95 - max. 100	
Minor component (%)	2	min. 0 - max. 5	
Loss of ignition (%)	2,5	max. 5,0	(1)
Sulfate, SO ₃ (%)	3,4	max. 4,0	
Chlorides, Cl ⁻ (%)	0,04	max. 0,10	
Insoluble residue (%)	0,70	max. 5,0	
Blaine specific surface (cm ² /g)	4600	-	(2)
Soundness Le Chatelier (mm)	0,5	max. 10	
Initial setting time (min)	110	min. 45	
Final setting time (min)	170	max. 720	
1 day compressive strength (MPa)	27	-	(3)
2 days compressive strength (MPa)	40	min. 30,0	
7 days compressive strength (MPa)	52	-	
28 days compressive strength (MPa)	61	min. 52,5	
(1) Chemical (2) Physical (3) Mechanical			

Figure 3-13: The characterization and specifications of Superdragon cement of the company Cements Molins (www.cmi.cemolins.es/en/productos/super-dragon).

The procedure of fabrication and main mechanical characteristic of artificial fragments will be presented in detail in chapter 6.

3.4 Reference grain size distribution curve

3.4.1 Introduction

Up to now, several attempts have been made by different researchers to find ideal grading curve for aggregates with various sizes to fill up the voids between large particles with finer particles to obtain best packing density. Taking into account this idea, the selection of the reference GSD play an important role in the development of this work.

3.4.2 Fuller curve

Among various researchers, one of the most widespread grain size distribution curve is the fuller curve presented by Fuller and Thompson (1907). Fuller grain size distribution curve was the first approach of current research, to draw possible position of ‘all-one’ mixture with different particle size. Depending on the theory of fuller curve, the cumulative GSD is shown in equation 3-1:

$$P(d) = \left(\frac{D}{D_{Max}} \right)^q \quad \text{Equation 3-1}$$

Where,

P (d): Presents the cumulative particle size distribution curve.

D: Presents a given particle size.

D_{Max}: Presents maximum particle size.

q: Parameter that ranges from 0.45 to 0.50.

The calculation procedures of particles sizes used according to Fuller are shown in Table 3-4 and Figure 3-14, respectively. It must be pointed out that an amount greater than 4% of particles are smaller than 0.075 mm.

Table 3-4: Calculations for a 0.5 power gradation curve using 40 mm maximum aggregate sizes.

Particle size (mm)	% passing	
40	$P=(40/40)^{0.5} * 100$	79.7 %
25.4	$P=(25.4/40)^{0.5} * 100$	69 %
19	$P=(19/40)^{0.5} * 100$	56.35 %
12.5	$P=(12.5/40)^{0.5} * 100$	48.75 %
9.5	$P=(9.5/40)^{0.5} * 100$	35 %
4.75	$P=(4.75/40)^{0.5} * 100$	22.4 %
2	$P=(2/40)^{0.5} * 100$	17.2 %
1.18	$P=(1.18/40)^{0.5} * 100$	10.3 %
0.425	$P=(0.425/40)^{0.5} * 100$	6.13 %
0.15	$P=(0.15/40)^{0.5} * 100$	6.12 %
0.075	$P=(0.075/40)^{0.5} * 100$	4.33 %
Pan	-	-



Figure 3-14: Various particles sizes according to Fuller curve.

Hence, firstly, ‘all-one’ material has been mixed by following the Fuller curve design. Then, compaction and oedometer tests have been performed on the different mixtures. A major problem of Fuller curve is that, the analysis of particle breakage is difficult base on grain size distribution after compaction and oedometer test.

The dry sieve analysis method was selected to see particle breakages after dynamic compaction and static loading-unloading oedometer. Figure 3-15, shows the GSD curve before and after the test of FN mixtures. As it is shown in Figure 3-15. For particles smaller than 0.7 mm, the GSD curve of new material after compaction goes to below the original one and causes problems to calculate the particle breakage index in the range of finest particles. The high amount of fine particles in these types of mixtures in presence of the water compaction and pressure of compaction after test creates new aggregates which are difficult to separate. It is beyond the scope of this study to analysis the particle breakage index. Even, in case of utilizing wet sieve analysis, the water disaggregates all particles and made it impossible to see the breakage potential. Also, the amount of fine particles based on Fuller curve is high and the binary mixtures is an over-filled packing structure that will be discussed in binary chapter.

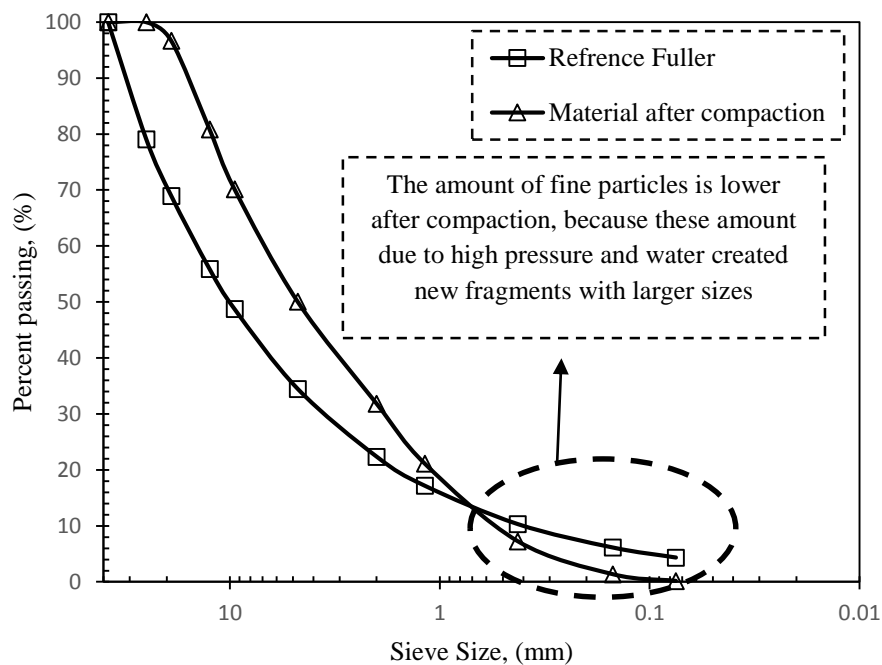


Figure 3-15: Dry sieve analysis of FN after compaction test.

3.4.3 Modified fuller curve

Furthermore, the use of a new modified curve was decided to solve the problems in the fine range of the reference Fuller curve. A number of researchers tried to modified this curve such as Andreasen and Andersen (1930), Peronius and Sweeting (1985), Kumar and Santhanam (2003). The idea of Funk and Dinger method is to create a grading curve based on both maximum and minimum particle size. This interpretation is different from that represented in Fuller curve which only pays attention to maximum fragments size. This new modified curve follows the equation 3-2:

$$P(d) = \frac{D^q - D_{Min}^q}{D_{max}^q - D_{Min}^q} \quad \text{Equation 3-2}$$

Where,

P (d): Presents the cumulative particle size distribution curve.

D: Presents a given particle size.

D_{max}: Presents maximum particle size.

D_{min}: Presents minimum particle size.

q: Parameter that ranges between 0.3 and 0.8.

Many authors attempted to optimize their packing by changing q value in Funk and Dinger equation in case of their experimental scope, such as (Kumar and Santhanam, 2003; Brouwers and Radix, 2005; Vogt and Lagerblad, 2006; Garas and Kurtis, 2008; Hunger, 2010).

By changing the q value in equation 3-2 the amount of fragments in the mixture will be altered. By using small value of q the amount of fine particles increase while by increasing the q number the quantity of finer particle decreases. Figure 3-16 presents the effect of different values of q based on Funk and Dinger modified equation.

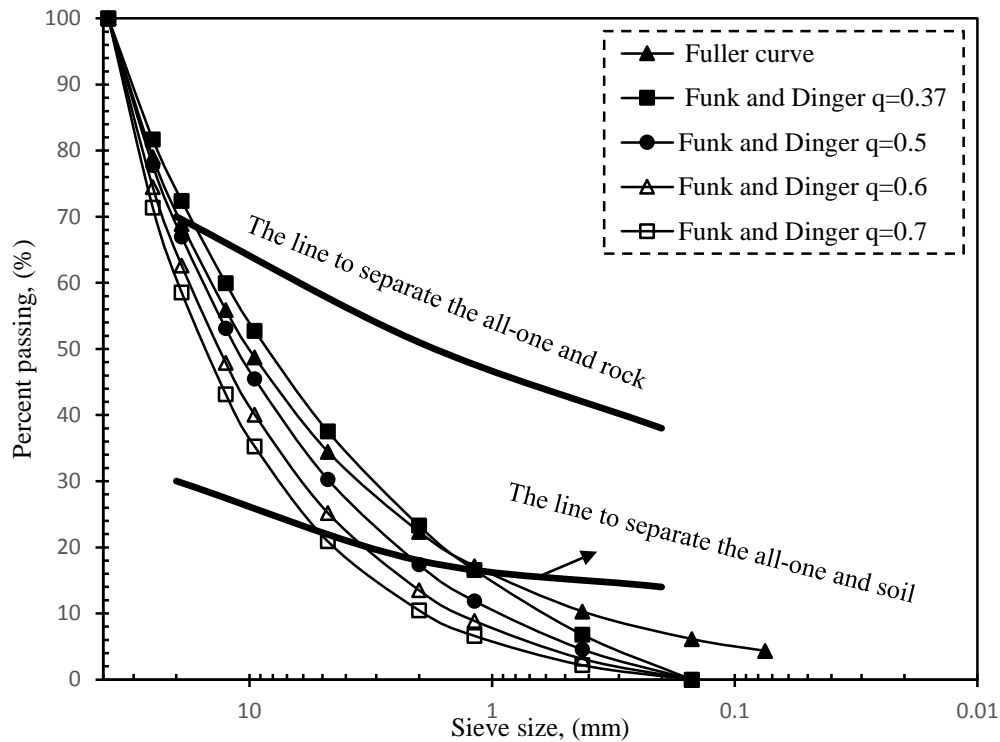


Figure 3-16: Funk and Dinger GSD curve with various values of q .

In this research thesis Funk and Dinger method with q number of 0.7 have been chosen. As it can be seen in Figure 3-16 the GSD curves covers the area between rock and soil region, also it is a suitable packing for our research purpose to represent the interactive under-filled or overfilled 'all-one' mixtures based on (Lopez, 2016). The method to select a fix proportion will be described more in detail in chapter 4.

3.5 Compaction procedure

3.5.1 Introduction

Generally, at the laboratory conditions, two types of compaction procedure are used: Dynamic compaction (standard Proctor normal, Modified proctor, Harvard miniature, Jodhpur mini compactor test, and CBR), and static compaction (can be applied by various mechanical systems). In this investigation, the dynamic compaction was carried out for all material mixtures (M, FN, FS, and FA) and static compaction was selected to fabricate artificially cemented fragments. The procedures of static and dynamic compaction are described in this section.

3.5.2 Compaction procedure for ‘all-one’ material mixtures

Typically, sheepfoot rollers as a dynamic compaction method are effective in dam and road construction projects. This type of compaction technique is useful for clay soil, and it is appropriated for material at lower water content. Therefore, at laboratory conditions it is desirable to use a compaction method which is close to sheepfoot roller compaction. The dynamic compaction procedure has been used for all material mixtures. An energy equal to 594 kJ/m^3 , as the same energy of standard Proctor normal was applied to all samples.

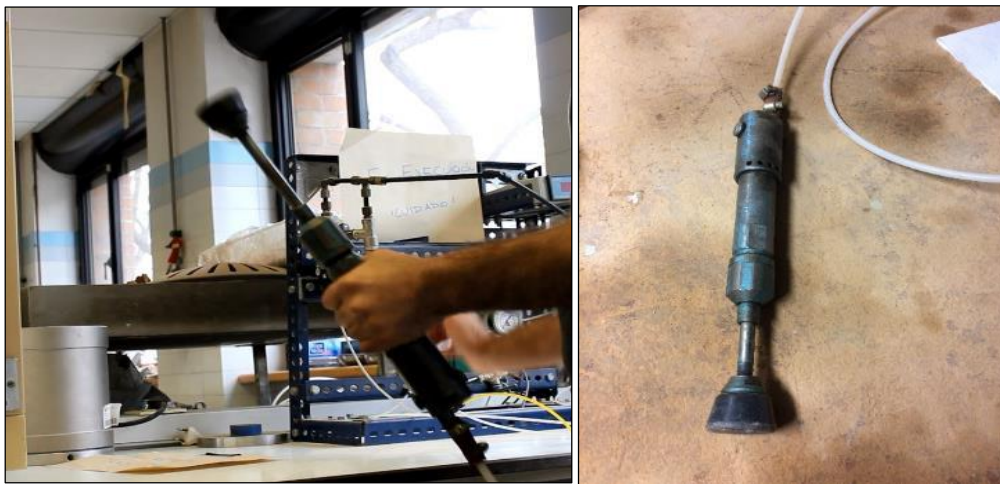
‘All-one’ material consists of fragments of various sizes and strength. In order to use appropriate equipment to compact this type of material, several attempts have been done in laboratory conditions. The procedures are described as follows:

First of all a Marshal hammer with weight of 4.357 kg and fall height of 495 mm are used to compact ‘all-one’ mixtures, Figure 3-17(a) shows the Marshall hammer equipment. The main disadvantage of this method is that, the area of hammer was too big and heavy, so applying the standard compaction energy by Marshal Procedure, considerable amount of particles were broken and it was difficult to see the breakage of fragments with various sizes and strength. Secondly, attempts were performed using the air pressure dynamic compaction method, however, there was certain drawbacks associated with the use of this method to control the number of blows and the energy of compaction. Figure 3-17(b) illustrates the air pressure compaction method hammer available at UPC Geotechnical Laboratory.

Finally, the hammer with smaller area of 30 mm and weight of 1 kg and fall height of 305 mm have been used to compact ‘all-one’ material in laboratory condition. In this case, by increasing the number of blows under the same compaction energy, it is possible to simulate the sheepfoot roller compaction idea. The new hammer is presented in Figure 3-17(c).



(a) Marshall compaction equipment.



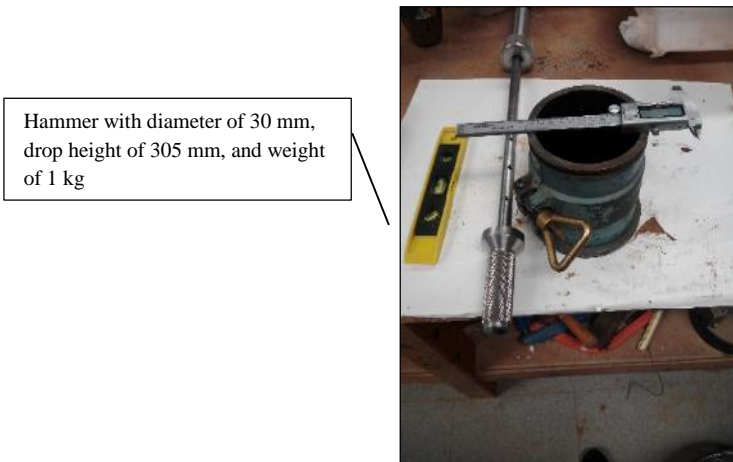
(b) Air pressure compaction.



(c) New hammer compaction.

Figure 3-17: Various methods of dynamic compaction equipment available at Geotechnical Laboratory of UPC.

For the purpose of dynamic compaction, two types of mould were utilized to compact material. The first one is the standard compaction mould to investigate changes in the GSD curves for reference matrix material of Barcelona silty clay. The second one is an oedometer cell that was used to compact different grain sizes and materials of ‘all-one’ mixtures. The available equipment’s compaction are presented in Figure 3-18(a) and 3-18(b).



(a) Compaction equipment with standard mold



(b) Compaction equipment with Oedometric cell.

Figure 3-18: Dynamic compaction test equipment available at Geotechnical Laboratory of UPC.

In order to achieve the same condition in the oedometer cell as they were obtained in the compaction mould and in case of new hammer, the same energy of 594 kJ/m^3 for standard

Proctor compaction was selected to transmit to oedometer cell. The number of blow were calculated using equation 3-3.

$$N = \frac{E*V}{W*H} \quad \text{Equation 3-3}$$

Where,

N= Number of blows.

E= Energy of compaction per unit volume of soil.

W= Weight of hammer.

H= Height of hammer.

V= Volume of mold.

3.5.3 Compaction procedure for fabricate artificial fragment

The static compaction was selected to fabricate artificial cemented fragments using various types of mould and hydraulic press equipment. In this case, during static compaction, load is controlled to obtain a fixed density value for fragments. The procedure of compaction will be discussed in chapter 6.

3.6 Equipment description and test procedure

In this study there are two main aims for experimental point of view, first one is to investigate the H-M behaviour of ‘all-one’ mixtures under oedometer conditions. The second one is to ascertain microstructure change after of each mechanical test. Thus, two major subjects have been taken into account to study the behaviour of different kinds of ‘all-one’ mixtures namely, initial characterization and the response of the soil to applied actions. The experiments to determine initial characterization of samples included grain size distribution, water retention curve, density, water permeability, suction measurements, and porosimetry analyses. The experimental program carried out to characterize the hydro-mechanical (H-M) behaviour of different types of material under study consists in the application of different types of actions on the soil. This experimental program is divided in two main parts, namely mechanical and hydraulic analyses. Firstly, the mechanical comprised vertical load-unload cycles under oedometer (1-D) conditions and the increase of the load up to 2 MPa. Secondly, the hydraulic step contained loading, soaking and unlading processes. Here, some of the equipment which are used in this thesis to coverage experiments are described.

3.6.1 Grain size distribution analysis (GSD)

To understand the microstructure changes in samples after of each test, the dry sieve analysis are selected to draw the grain size distribution curve after and before of each test. The grain size distribution test has been done by means of sieves series number 38.5, 25, 19, 12.5, 9.5, 4.75, 2, 1.18, 0.425, 0.15 mm which are provided at UPC Geotechnical Laboratory. The sieve numbers used to evaluate the microstructure changes are shown in Figure 3-19. One of the main points of grain size curves is to obtain the particle breakage and fractal number. In order to maintain the size of the natural fragments the sieving tests have been done in dry conditions. The separation of the individual fragments in the aggregations has been performed by hand without using water.

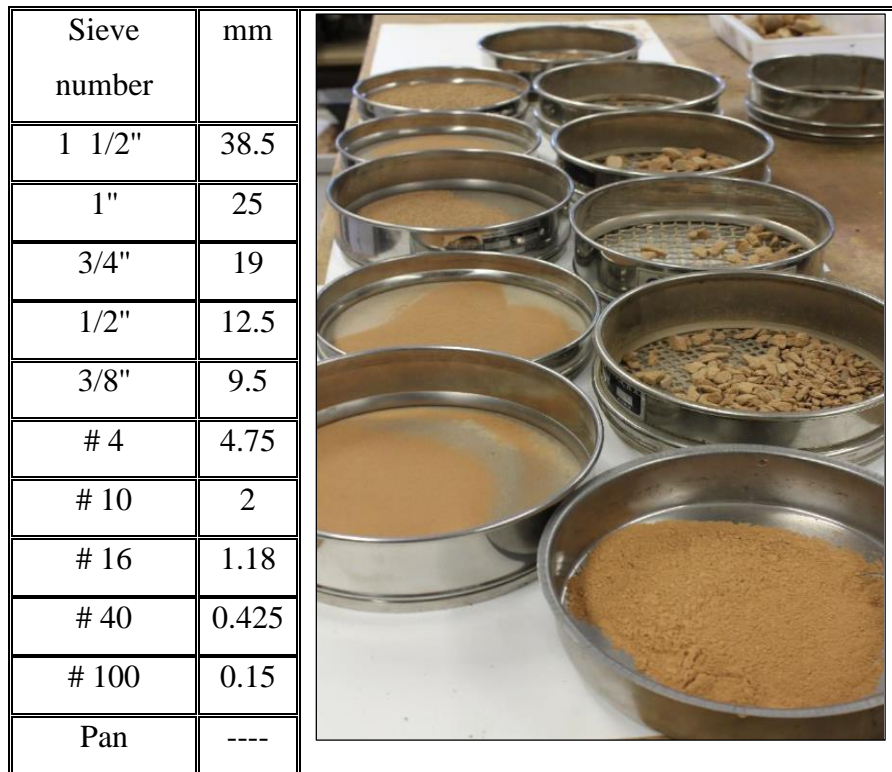


Figure 3-19: Sieve analysis equipment.

3.6.2 Suction measurements

The water retention properties and the suction value of compacted soil are fundamental aspects in compacted soils behaviour. In this research investigation the chilled-mirror Psychrometer was used for measuring total suction. The equipment used was a 'WP4-T Dew point Potentia Meter' that is shown in Figure 3-20. The accuracy of total suction

measurement using this instrument is ± 0.1 MPa from 0 to 10 MPa and 1% from 10 to 300 MPa. The range of measurement is from 0 to 300 MPa.



Figure 3-20: WP4 Dew Point Psychrometer and sample.

According to Fredlund and Rahardjo (1993) the relationship between the total suction and the relative humidity is based on the psychrometric law (equation 3-4):

$$\psi = \frac{RT\rho_w}{M_w} \ln(RH) \quad \text{Equation 3-4}$$

Where,

Ψ = Total suction.

R= Gas constant equal to 8.314 J/mol.K.

T= Absolute temperature.

M_w = The molecular mass of water equal to 18.016 kg/kmol.

ρ_w = The density of pure water equal to 998 kg/m³ at 293 K.

RH= Relative humidity value of vapor pressure equal to $RH = \rho_v / \rho_{v0}$.

ρ_v = Vapor pressure.

ρ_{v0} = Saturation vapor pressure.

The method of calibration and more information about the equipment and test procedure in detail are mentioned in Cardoso et al. (2007) and Decagon Devices, Inc. (2003).

In this method, samples were placed in chamber inside the device. The soil in the specimen chamber was permitted to reach isothermal equilibrium which was defined as

the null difference between temperature of the vapour space and the specimen. The device showed the difference in temperature between the headspace and the mirror. The chamber was closed and after reaching equilibrium, the relative humidity and the temperature of the vapour space were shown in the display screen. The measurement was achieved two times each specimen.

3.6.3 Density by paraffin

The paraffin method has been used to see the density of artificial cemented fragments after static compaction. Firstly, the samples were submerged slowly in liquid paraffin using several layers to prevent breakages. It is very important during warping in paraffin to be sure that no particles of the sample are lost, and to prevent entry or exit of water and air in the same time. For determining density, is necessary to know the mass of the samples before being waxed, after being waxed, and when paraffin is dry, immersed in water .The device and procedure are illustrated in Figure 3-21.



(a)

(b)

Figure 3-21: Procedure of paraffin density test; (a) warping sample in a heated oven of liquid paraffin, (b) weighing of samples with paraffin immersed in water.

Eventually, the density can be obtains by Equation 3-5:

$$\rho = \frac{W_1}{\left[\frac{W_2-W_3}{\rho_w}\right] - \left[\frac{W_2-W_1}{\rho_p}\right]}$$

Equation 3-5

Where,

W_1 = Weight of soil fragments,

W_2 = Weight of wax soil fragment with paraffin,

W_3 = Weight of wax soil fragment with paraffin in water,

ρ_w = Density of water,

ρ_p = Density of paraffin.

3.6.4 Mercury intrusion porosimetry (MIP)

MIP test has been selected to describe the porosimetry of fragments and compacted material. The pore size distribution (PSD) obtained from mercury intrusion porosimetry (MIP) test has been used to study the microstructure. This equipment presents two pressure-generating systems: the low-pressure system works under dry nitrogen pressure in a range between 0.0025 and 0.2 MPa, whereas the high-pressure one uses oil for pressure in the range of 0.2 to 220 MPa (Piña, 2011). The mercury intrusion porosimetry equipment is shown in Figure 3-22.

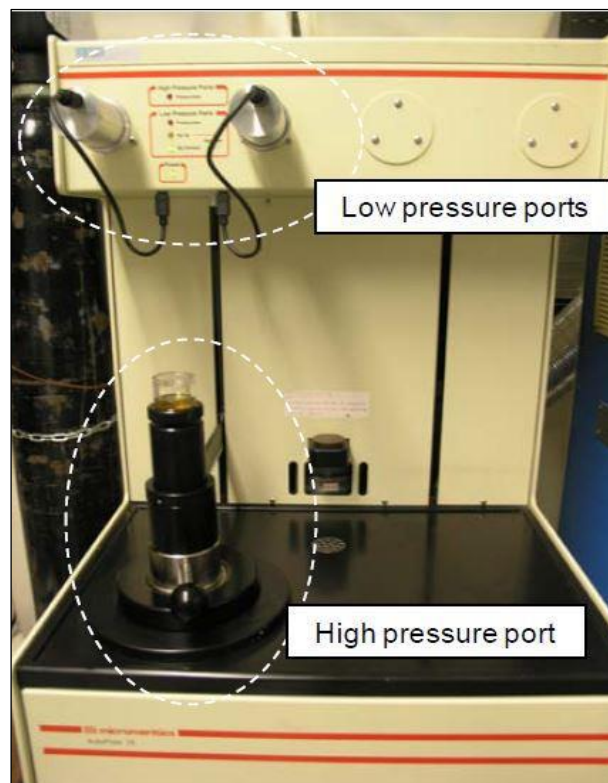


Figure 3-22: Mercury intrusion porosimetry test equipment available at Geotechnical Laboratory of UPC.

3.6.5 Continuous loading/unloading oedometer tests

The tests used to study the compressibility of the different compacted mixtures have been done in an oedometer with interior dimensions of 151 mm and an internal free height of approximately 180 mm. The load was applied through a stainless steel plate. The upper head moved with the specimen deformation while the bottom is held fixed. The movement of the upper head was measured by a vertical shaft coming out to the outside of the cell. Vertical deformation measurements were automated using a LVDT with a maximum stroke of 33 mm. LVDT mounted in stable frame formed by two rigid steel bars that support the frame. Both head have drainage system. The load was applied directly on the top by air pressure. The maximum vertical stress that can be applied is 2 MPa. The oedometer cell set up is shown in Figure 3-23.

The available air pressure system at UPC Geotechnical Laboratory is used to apply directly load top of the cell. A latex membrane are used to separate the air pressure and allowed the specimen to be compressed. A computer data acquisition system recorded the vertical displacement readings of the specimen head and the loading application by means of the air pressure. The scheme of continuous loading/unloading oedometer equipment is provided at Figure 3-24 taken form by Grimal, (2010).



Figure 3-23: Oedometer cell provided at UPC Geotechnical Laboratory.

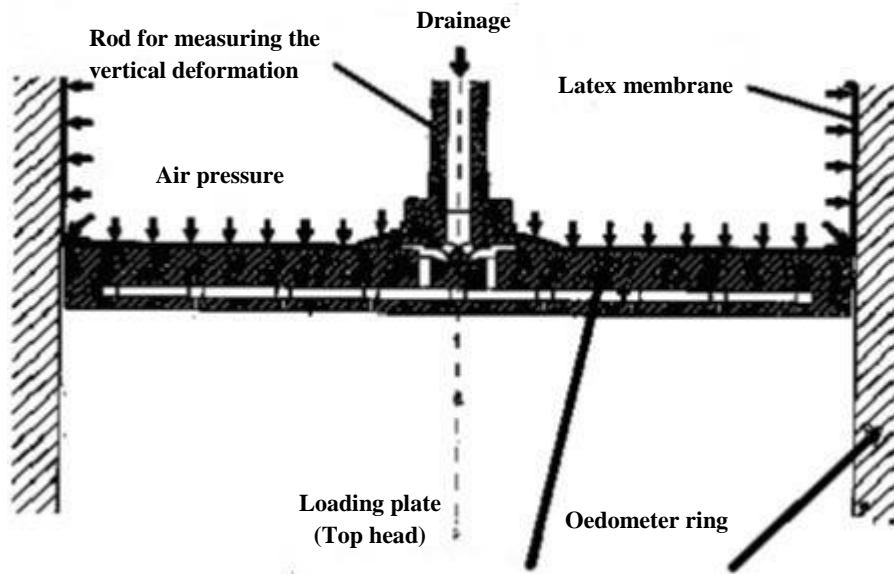


Figure 3-24: Design details of the load plate and rod for drainage and measurement of vertical movement of the oedometer (Grimal, 2010).

3.6.6 Soaking test

The volume of water necessary to saturate the samples and to study the collapsibility behaviour of various types of mixture under oedometer conditions was applied by a pressure/ volume controller (GDS). The specimen inside the same oedometer cell conditions as described before, was soaked at various vertical load conditions to realize collapse potential. The available GDS at UPC laboratory is shown in next Figure 3-25 develop with permeability test devices.

3.6.7 Water permeability test using oedometer cell

To achieve water permeability measurement beneath a constant vertical stress, the oedometer cell prepared by UPC Geotechnical Laboratory was used. Figure 3-25 depicts the experimental set-up of the equipment. A pressure volume controller (GDS) are used to apply the desire hydraulic conditions. After fully saturation of sample inside the oedometer cell the water volume that comes from the top of the cell and the volume of water that exits from the pressure/volume controller are measured at several time periods. The water permeability of sample was extracted from curve volume of water versus time.

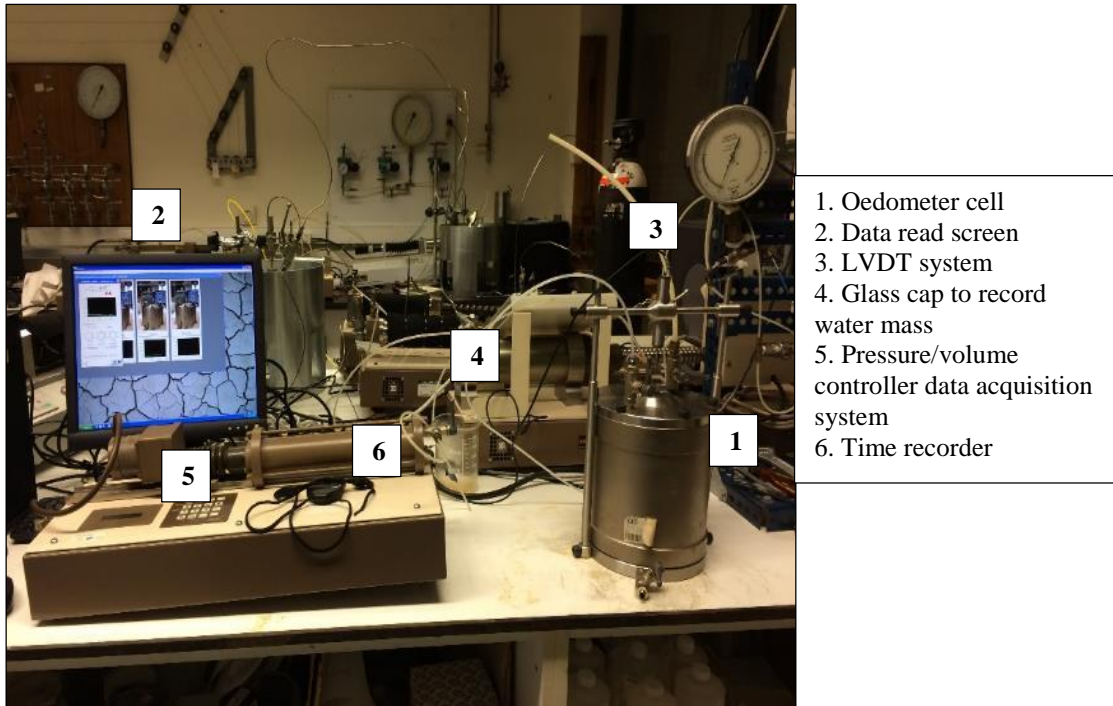


Figure 3-25: Set-up of the equipment used to measure water permeability.

3.7 Testing program

Experimental data on the hydro-mechanical behaviour of compacted ‘all-one’ mixtures with different grading size distributions and materials will be provided in this research thesis. There are two principal experimental purpose of this study: 1.To investigate behaviour of ‘all-one’ mixtures as a real case study in Albagés dam structure. 2. To ascertain ‘all-one’ mixtures on laboratory conditions with various GSD and materials.

Subsequently, following experimental program is designed to achieve main characterization of ‘all-one’ mixture under various H-M stress path.

Table 3-5 presents the experimental program of Albagés dam for ‘all-one’ mixtures. Mechanical characterization includes consistency limits, compaction curve, particle size distribution, and compressibility. On the other hand, hydraulic behaviour comprises of permeability and water retention curves.

Table 3-5: Experimental program of Albagés dam material for both core and ‘all-one’ material.

‘All-one’	
Mechanical characterization	Hydraulic characterization
Atterberg limits	Suction measurements
Compaction tests	Permeability using oedometric cell
Sieve analysis	1-D compressibility
-	Soaking test under oedometric odometer cell

To present differences in H-M phenomenological behavioural features, the compacted all-one mixtures will be compared to same compacted soil without null fragments. In addition, artificial cemented fragments will be used to see the particle breakage and pore size. Moreover, microstructural changes (particle size distribution changes) will be evaluated along the different H-M stress paths (water content and loading cycles). The experimental program of various all-one mixtures under different H-M stress paths are defined in Table 3-6 and Table 3-7, respectively.

Table 3-6: Experimental program of ‘all-one’ mixtures.

Mechanical Behaviour	
Breakage potential	Sieve analysis before and after each test
Fractal analysis	
Energy dissipation during compaction	
Compressibility index on loading/unloading	Continuous loading/unloading odometer cell
Pre-consolidation pressure	
Hydraulic Behaviour	
Compressibility index on wetting	Soaking test under constant vertical load under oedometric conditions
Collapse potential	
Permeability	Water permeability test using oedometric cell
Water retention curve	Suction measurements using WP4
Suction equilibration	

Table 3-7: Different H-M paths for various ‘all-one’ material

Stress Path				Mixtures
Loading up to 1.9 MPa	Unloading up to 0.05 MPa	-		M,FN,FS,FA
Loading up to 1 MPa	Saturated	Loading up to 2 MPa	Unloading up to 0.05 MPa	M,FN,FA,FS
Saturated	Loading up to 2 MPa	Unloading up to 0.05 MPa		M,FN,FA,FS
Saturated	Loading up to 1 MPa	-	-	Albagés dam ‘all one’
Loading up to 2 MPa	Unloading up to 1 MPa	Saturated	-	Albagés dam ‘all one’
Loading up to 2 MPa	Unloading up to 0.06 MPa	Saturated	-	Albagés dam ‘all one’

4 Exploring binary mixture properties. Effect of matrix content and fragment strength

4.1 Exploring mixture properties on a single material with different proportions of carbonated fragments

4.1.1 Introduction

Usually, it is difficult to determine a reference value for the definition of the transition fine soil content in binary granular mixtures. However, up to now, there are a number of investigations that has been carried out to identify a limit of gravel or fine content in the mixtures. Using different approaches, researchers have been able to specify at which mass proportions of fine and gravel, mixtures properties are controlled by fine, gravel or both of them. Nevertheless, there are certain problems to use the conventional limits of the investigated literature to understand the behaviour of the binary granular mixtures of this research study. One of the main limitations of the experimental approach of the previous studies refers to the small particle size used. Therefore, the effect of some parameters such as particle breakage, particle strength and particle size have not been addressed. In the current research study, granular binary mixtures of the all-one material consists of particles between 19 to 38.5 mm (Fragments with different strengths) and fine particles (Matrix) between 19 to 0.15 mm. It is clear in the matrix part there are already some large fragments. Accordingly, in order to achieve an understanding of this type of binary mixtures, some explanations should be addressed based on the strength of the fragments and the void ratio of the matrix in binary granular mixtures. The experimental study and analyses carried out are explained below.

4.1.2 Binary granular mixtures with different proportions of fines

To consider several mixture percentages in the laboratory programme of this study, various proportions of the Barcelona silty clay and carbonated fragments have been chosen (mixture with natural carbonated fragments: FN). The granular fragments and fine particles are prepared according to Funk and Dinger grain size distribution curve at different percentages. Initially, materials with different percentages of fine and granular fragments are combined by adding 10 % of water content to the matrix part. Fine content (FC) ratio as an index is selected to represent the amount of fine (particles with sizes between 19 and 0.15 mm) in the mixture. Four types of samples are prepared based on

different combinations of matrix and fragments. The different percentages are presented in Table 4-1. The material and the grain size distributions of each mixture are shown in Figure 4-1 and Figure 4-2, respectively. Later, materials were placed in 3 layers into a cylindrical cell with a diameter of 150 mm and 180 mm in height. Dynamic compaction of standard Proctor energy equal to 594 kJ/m^3 has been selected to compact the material. The sieve analysis was carried out after compaction to see particle breakage (particularly of the carbonated fragments with initial sizes between 19 mm and 38 mm). After compaction, the minimum porosity of the granular mixtures (n_{mix}) was determined according to equation 2-1 (described in chapter 2) to specify the possible transition zone.

Table 4-1: Various proportions of matrix and fragments.

Mixture Type	Matrix percent (particle sizes 0.15mm to 19mm) %	Fragment percent (particle sizes 19mm to 38mm) %
A (FC=80)	80	20
B (FC=60)	60	40
C (FC=40)	40	60
D (FC=20)	20	80

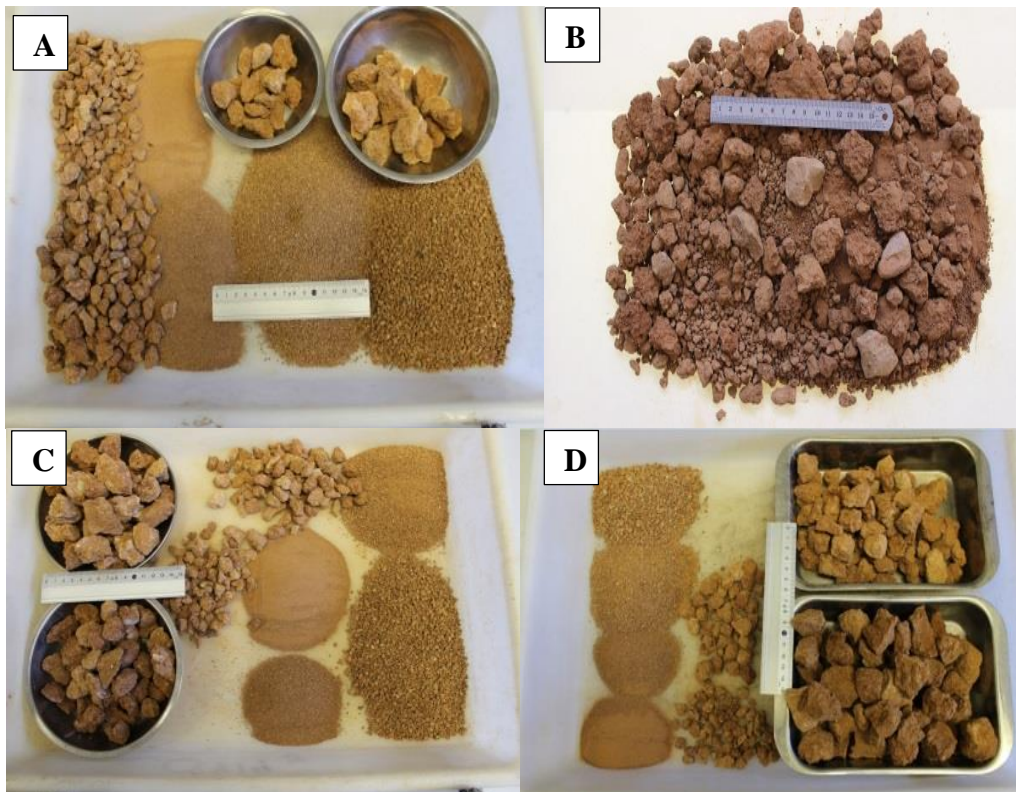


Figure 4-1: FN material with different proportions based on Funk and Dinger grain size distribution.

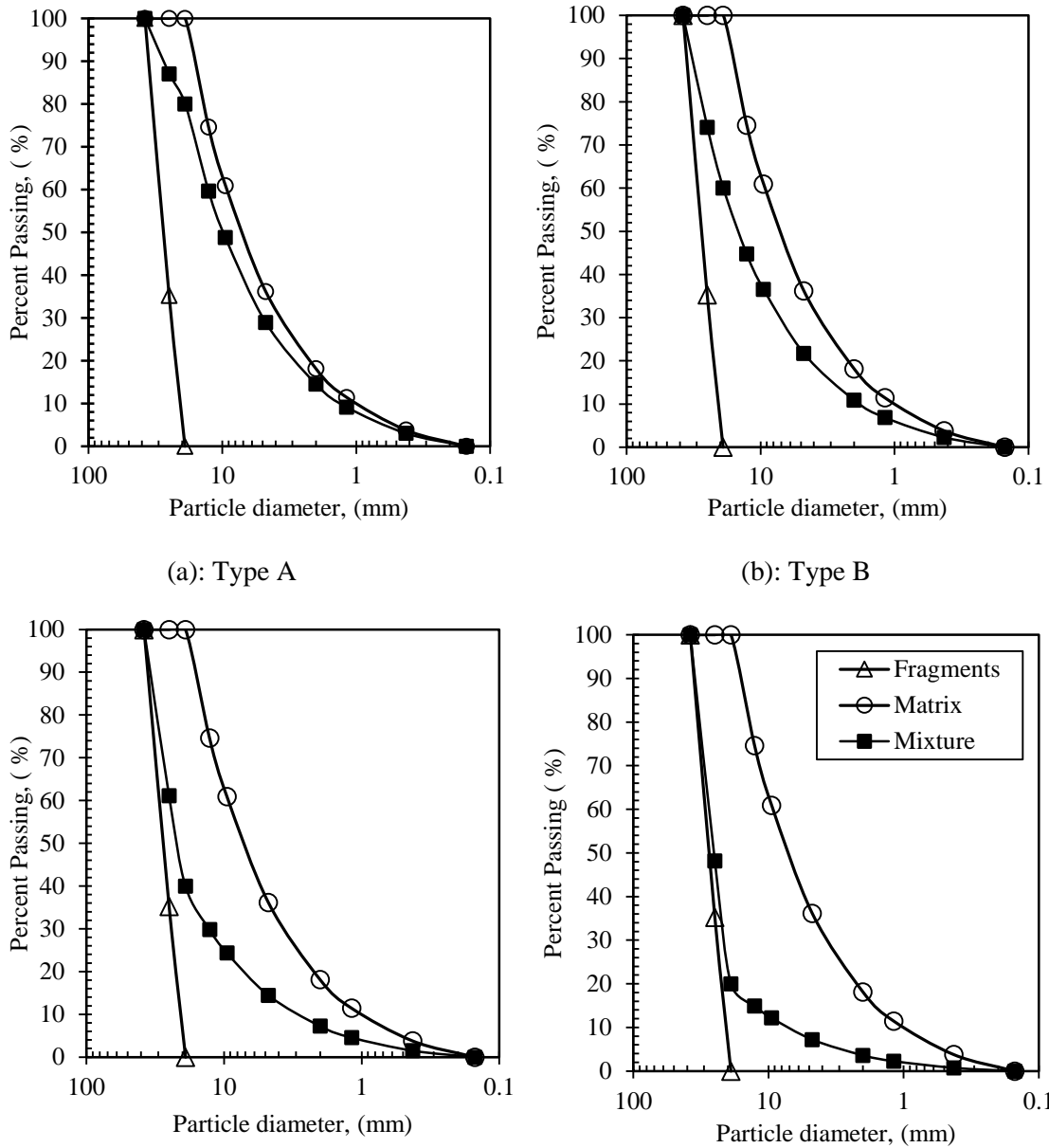


Figure 4-2: Grain size distributions of various proportions of the mixtures, (a) 80% matrix+20% granular (FC=80), (b) 60% matrix+40% granular (FC=60), (c) 40% matrix+60% granular (FC=40), (d) 20% matrix+80% granular (FC=20).

4.1.3 Selected proportion for the experimental study

The void ratio and porosity of the different granular mixtures versus fine content are plotted in Figure 4-3. It is observed that by increasing the matrix proportion in the binary mixtures, the amount of void ratio decreased due to filling of the macro voids between large fragments by the fine particles. The void ratio reduced until it reaches 80% of matrix content, and then starts to increase again by increasing the number of fine particles. The

transition of fine content occurred at a range of 75 to 85 % of the matrix content in granular mixtures. In this case, by increasing the fine content after the transition point, there is no more space between the granular fragments to be filled by fine particles, so, extra fine particles cause an increase in the void ratio as they do not fill the void between granular.

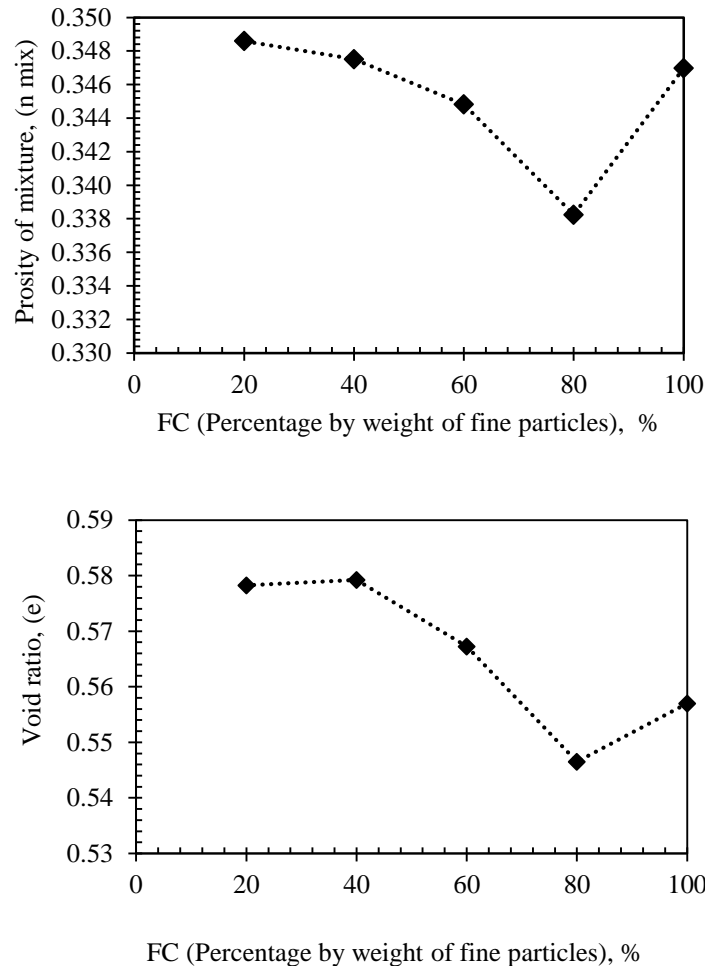


Figure 4-3: Void ratio and porosity of the mixtures versus fine content.

This concept was further used to select a binary granular mixture between underfilled and filled packing structures, in order to cover the properties of ‘all-one’ mixtures and evaluate the behavioural features of this type of materials. Thus, based on experimental findings in the behaviour of various proportions of the matrix and granular fragments, different state zones are displayed in Figure 4-4 according to Lopez et al. (2016). The state A, B, C, and D represented the underfilled, interactive-underfilled, interactive-overfilled, and overfilled structure, respectively. The properties of the binary mixtures in

states A and B are controlled by granular particles, in the state C both granular and fine particles are affecting the properties, while, only fine particles have influence on the mixtures in the state D. To assess the breakage index the sieve analysis after compaction is presented in Figure 4-5. The values of the Marsal breakage are specified in Table 4-2. It is detected that when there is a reduced content of fine, the amount of breakage increased due to the presence of large fragments.

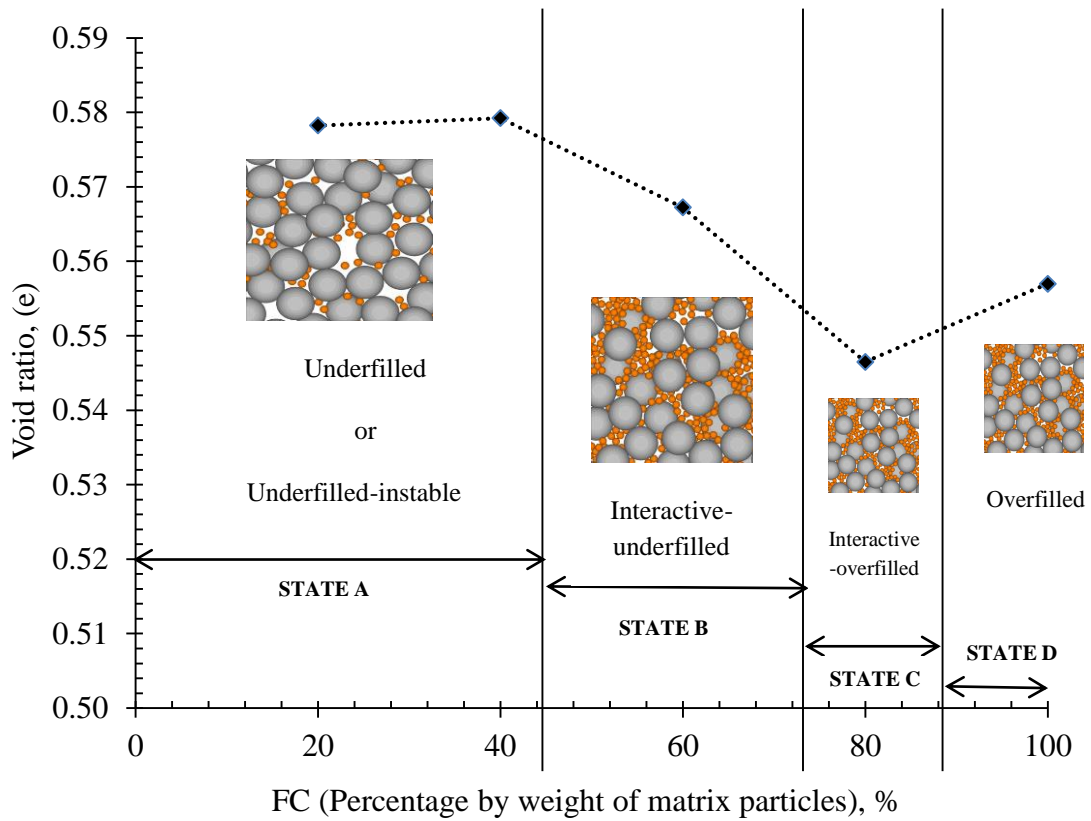
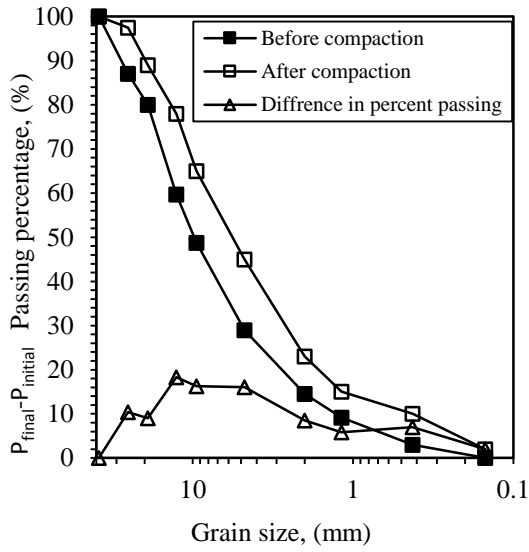


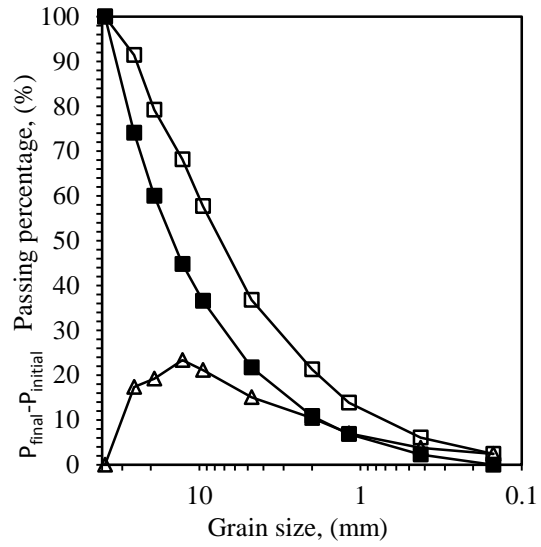
Figure 4-4: The four packing states in binary granular mixtures.

Table 4-2: Breakage potential for various fine contents in the binary granular mixtures.

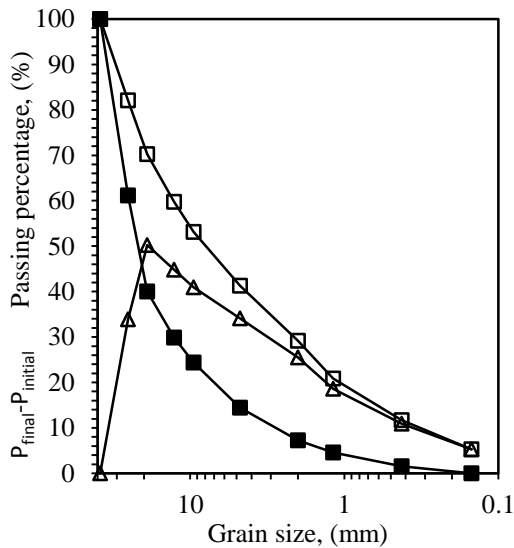
Type of Binary mixture	Breakage Potential
FC=20	50.21
FC=40	47.52
FC=60	23.37
FC=80	20.83



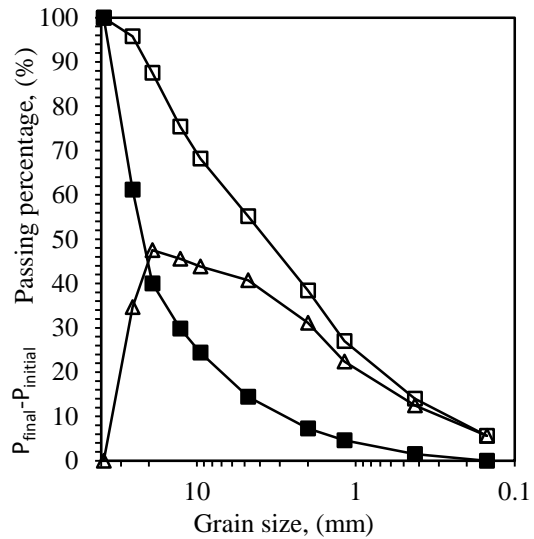
(A) FC= 80



(B) FC=60



(C) FC= 40



(D) FC= 20

Figure 4-5: Grain size distributions before and after compaction for various types of mixtures.

To sum up, by selecting 40 % of granular fragments between 19 to 38.5 mm and 60% of the fine particles (matrix) between 19 to 0.15 mm, the conditions in which the properties are controlled by both fine and aggregates (fragments) are considered. Therefore, this proportion of mixtures will be selected to explore the ‘all-one’ behaviour in the experimental programme of this research.

4.2 Exploring mixture properties with different fragment strengths

4.2.1 Compaction curve of the matrix

First of all, to have an idea of matrix and fragment behaviour in the mixtures, references compaction curve of the matrix has been studied. The matrix material has been compacted by the energy of the standard Proctor test (594 kJ/m^3). The dimensions of cylindrical metal moulds used are $102.0 \pm 0.4 \text{ mm}$ internal diameter and drop height of $122.4 \pm 0.1 \text{ mm}$ which is equivalent to a volume of 1000 cm^3 . The equipment (hammer mass of 1 kg , diameter 30 mm and height of drop of 350 mm) and sample preparation water contents are displayed in Figure 4-6.

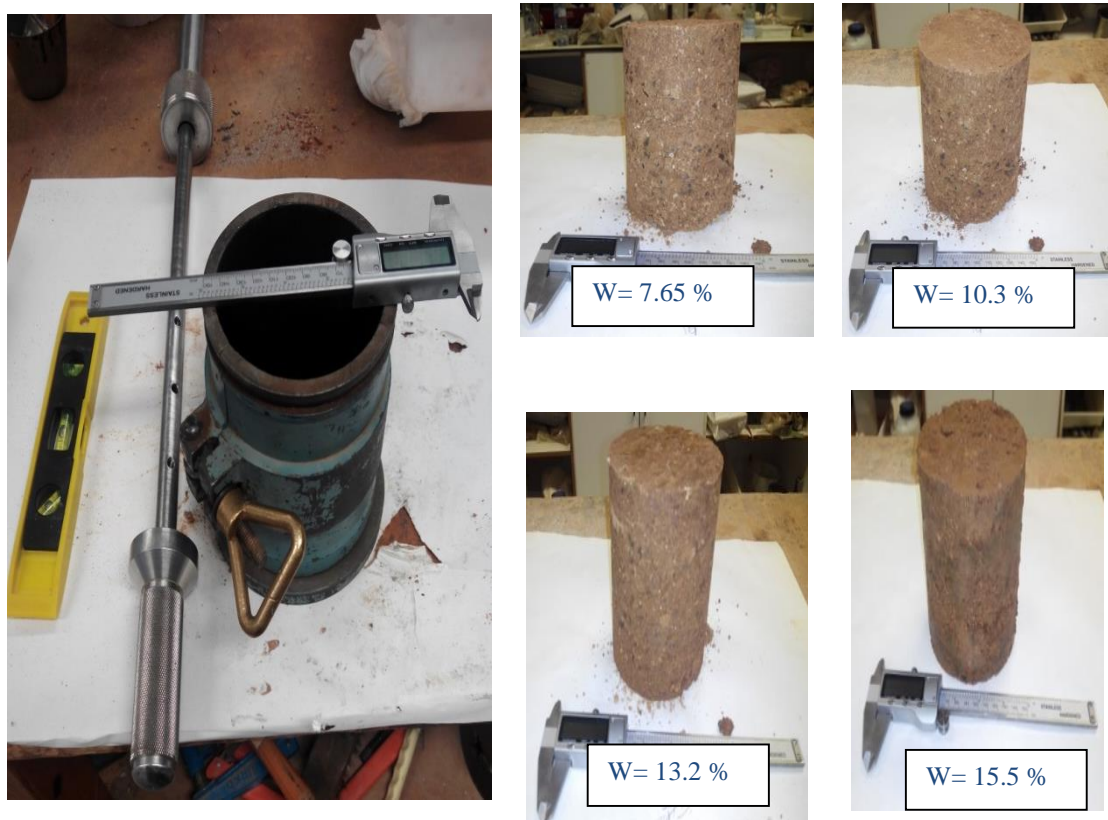


Figure 4-6: Procedure of pure matrix compaction.

The compaction curve of the matrix is plotted in Figure 4-7, together with some curves obtained by different researchers at the geotechnical laboratory UPC for material passing sieve number 4#.

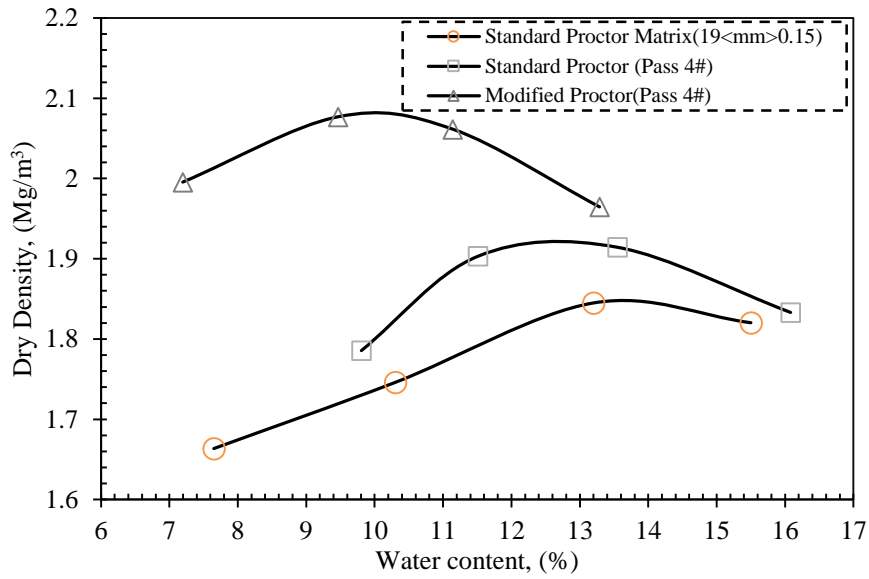


Figure 4-7: Compaction curves of Barcelona silty clay and the pure matrix.

It is observed that by increasing the size of the particles the optimum water content increased with a lower maximum dry density. This reduction in maximum dry density is associated with the transfer of some compaction energy to break large aggregates of the matrix.

4.2.2 Method to calculate the matrix void ratio in the mixtures

The behaviour of granular mixtures is ruled by the strength of the fragments and the dry density of the matrix. The following procedure has been adopted to compute the dry density in the matrix part (the matrix mass fraction represents 60%). The density of solids of the granular mixtures was determined using the following relationship:

$$\frac{1}{\rho_{sm}} = \frac{f_c}{\rho_{sM}} + \frac{(1-f_c)}{\rho_{sF}} \quad \text{Equation 4-1}$$

Where,

ρ_{sm} = Solid density of mixture.

ρ_{sM} = Solid density of matrix.

ρ_{sF} = Solid density of fragment.

f_c = Mass fraction of matrix in the mixture ($f_c = 0.60$).

Based on the solid density of the mixtures the matrix density can be obtained from following expression (equation 4-2):

$$\rho_{dM} = \frac{f_c \rho_{sm}}{e + \frac{f_c \rho_{sm}}{\rho_{sM}}} \quad \text{Equation 4-2}$$

Where,

ρ_{dM} = Dry density of matrix part.

e = Overall void ratio of the mixture.

In addition, the void ratio of the matrix (e_M) obtained from equation 4-3:

$$e_M = \frac{\rho_{sM}}{\rho_{dM}} - 1 \quad \text{Equation 4-3}$$

4.2.3 Influence of different materials (fragments) on the density of the compacted mixtures

Here, the results of matrix density for different types of fragment (natural carbonated aggregates FN, artificial fragments FA, and slate fragments FS) are shown in Table 4-3. The samples are compacted at Standard Proctor energy and the matrix density is calculated based on equation 4-1 and equation 4-2.

Table 4-3: Dry density of the matrix and the compacted mixtures.

Type	Dry Density (Mg/m ³)	Matrix Density (ρ_{dM}) (Mg/m ³)	Matrix densification with respect to pure matrix (%)
Matrix a-c	1.72	1.72	-
FN a-c	1.68	1.28	74.4
FA a-c	1.71	1.31	76.2
FS a-c	1.8	1.47	85.5

Based on data obtained in Table 4-3, the matrix densification in various mixtures with respect to the maximum dry density of the pure matrix is presented in Figure 4-8. The

strength of the fragments can be associated with the unconfined uniaxial compression strength. The relationship between the unconfined compression strength of the fragments and the densification of the matrix are shown in Figure 4-9. It can be seen that by increasing the unconfined compression strength of the fragments in the mixtures, the matrix dry density increases due to less breakage of the fragments. When the fragment strength decreases, a significant part of the compaction energy is used for particle breakage without inducing an important densification of the matrix.

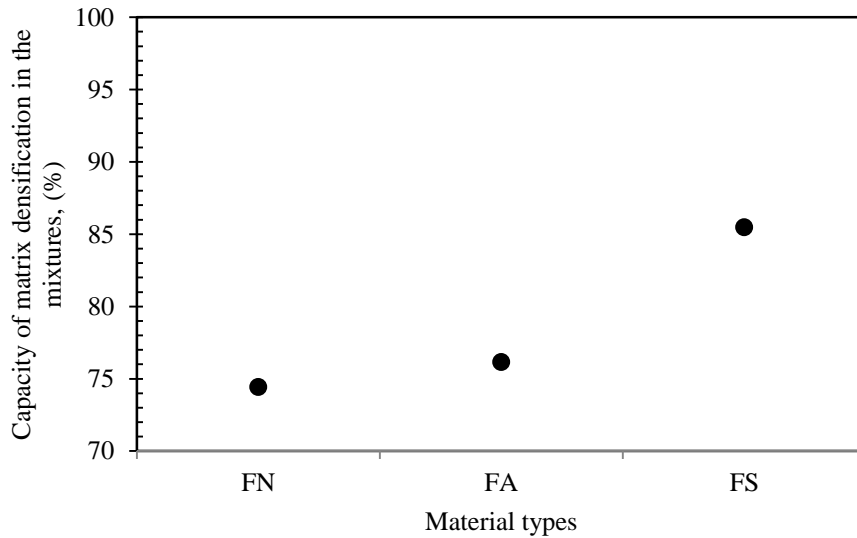


Figure 4-8: Densification of the matrix in the different mixtures (fragments with different strengths).

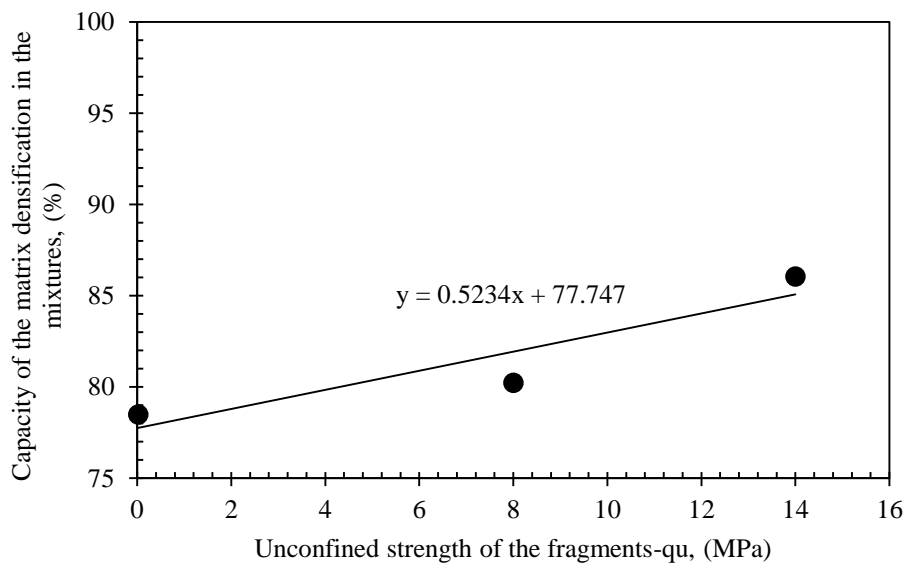


Figure 4-9: Densification of the matrix versus the unconfined compression strength of the fragments.

The total dry densities of the mixtures of various types are plotted with the compaction reference curve of the pure matrix (Figure 4-10). The highest total dry density is obtained for the mixture with highest strength of the fragments (FS with slate fragments). In this case, most of the compaction energy is transferred to densifying the matrix instead of breaking fragments. The transitions of compaction energy between densifying matrix and breakage of the fragments will be discussed in chapter 7.

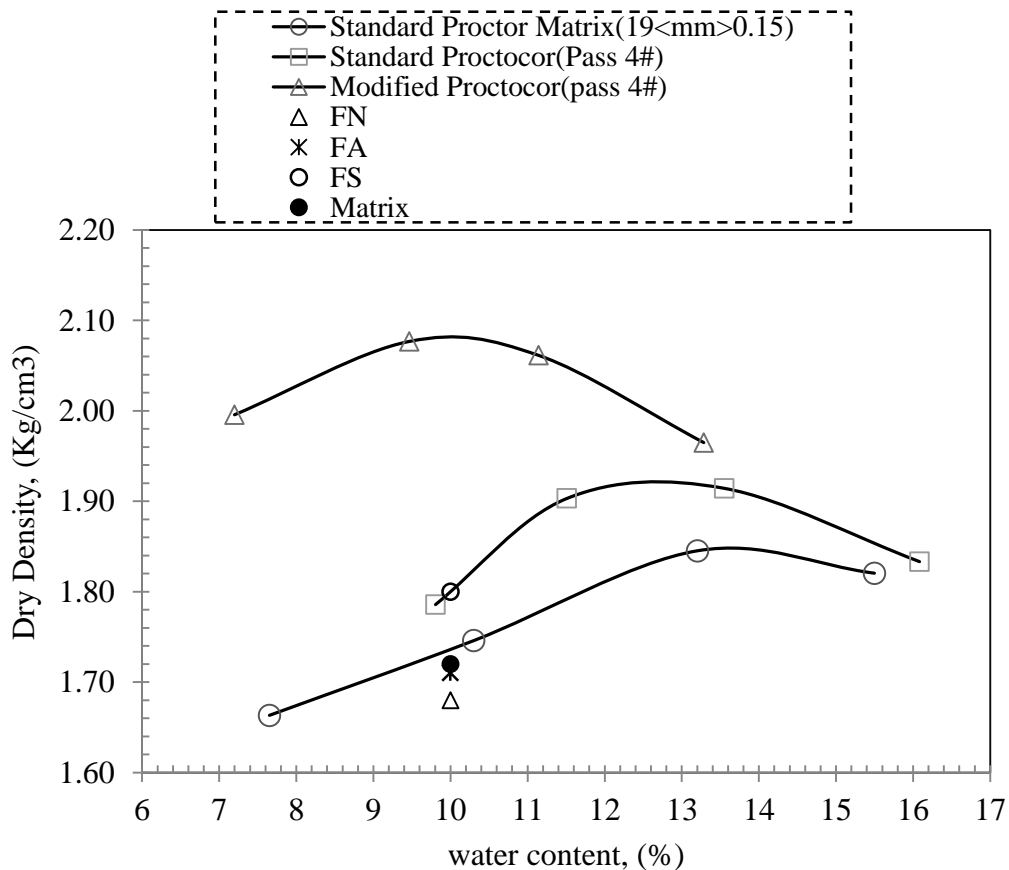


Figure 4-10: The density of the mixture compared to reference pure matrix.

4.2.4 Influence of compaction energy and water content on the properties of the mixtures

To understand the effect of compaction energy and water content, the FA mixtures with artificial fragments was selected to compact in standard Proctor (SP), double standard Proctor (SPd), and modify Proctor (MP) energy at 10 % of water content. Tests with constant SP energy but with 10 and 13 % of water content were also performed. The sieve analysis after compaction for both cases is plotted in Figure 4-11.

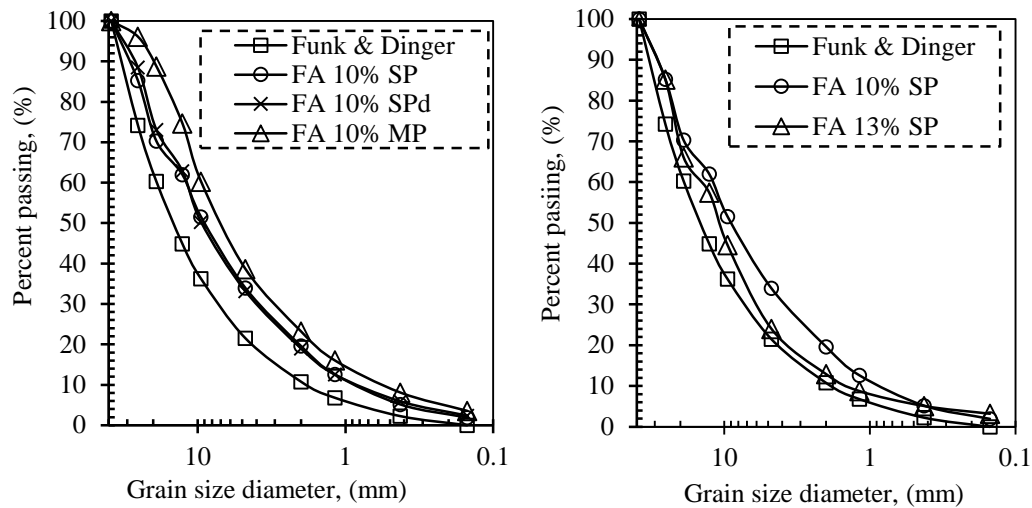


Figure 4-11: Sieve analysis after compaction for various energies and water contents.

The relationship of compaction energy and particle breakage is shown in Figure 4-12. As observed, by increasing the compaction energy the particle breakage increased. A linear tendency and the regression line equation is presented in the figure.

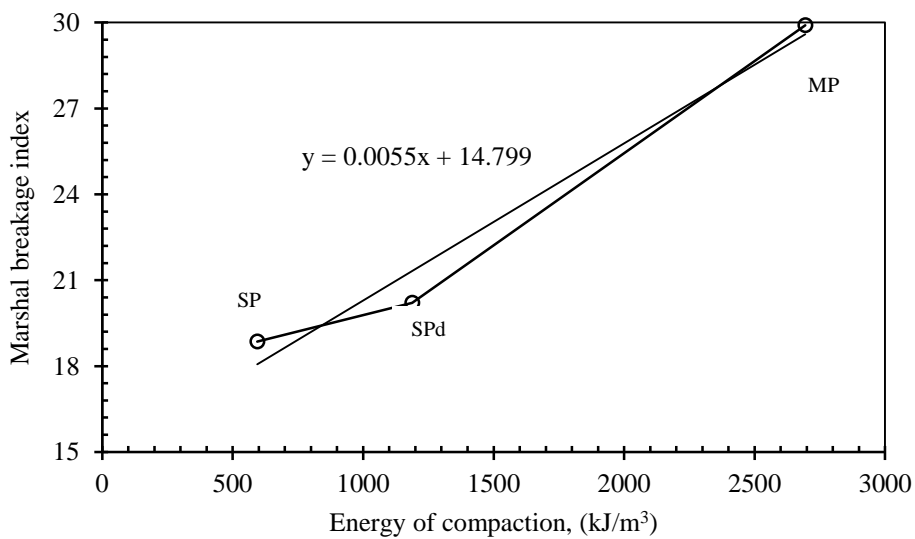


Figure 4-12: The compaction energy versus particle breakage.

Finally, Table 4-4 presents the results of the dry density for the different compaction energies. It is clear that by increasing both energy and water content the dry density of the mixtures increased. It should be considered that in case of higher water contents it is difficult to separate the material after compaction to do the sieve analysis and analyse particle breakage, since particles stick to each other.

Table 4-4: Dry density values for various energies and water contents.

Mixture type	Bulk density (Mg/m³)	Dry density (Mg/m³)
10 % water content constant		
FA SP	1.87	1.71
FA SPd	1.92	1.75
FA MP	2.05	1.87
Standard Proctor constant		
FA 10% water content	1.78	1.62
FA 13% water content	2.02	1.79

5 Hydro-mechanical characterisation of a compacted all-one material used in the construction of Albagés dam (Spain)

5.1 Introduction

This chapter aims at assessing to assess the hydro-mechanical behaviour of a real case of all-one material used in the construction of the Albagés dam which is a 85 m high zoned earth dam built in Lleida (Spain).

The compacted materials used in the Albagés dam structure comprised a clayey silt core, coarse material used in the toe drain and external upstream shoulder, and all-one material used in main shoulders, as described below. These materials have been extensively characterised by laboratory tests performed at the Geotechnical Laboratory UPC. During construction (2015 to 2018), block samples of the different materials have been retrieved for laboratory tests. Regarding the all-one material constituted by an under-filled mixture of heterogeneous argillite / sandstone, it underwent some further particle crushing during compaction affecting the large fragments (large fragments were initially > 200 mm). This compaction led to a more extended particle size distribution with more fine content (interactive-underfilled packing with maximum sizes around 50 mm).

Laboratory tests on all-one material were focused on determining compressibility parameters on loading, collapse properties on soaking and water permeability. These properties are fundamental to adequately simulate with coupled hydro-mechanical numerical codes the response of the dam along the different construction stages, reservoir impoundment and the post-construction long-term behaviour.

5.2 Brief description of the Albagés dam

The dam for irrigation activities is located in the valley of the river Set on the Segarra-Garrigues canal in the province of Lleida in Catalonia, Spain. The reservoir covers an approximate area of 5864 hectares with a storage capacity of 80 cubic hectometres. Figure 5-1 and Figure 5-2 indicate the dam's location.

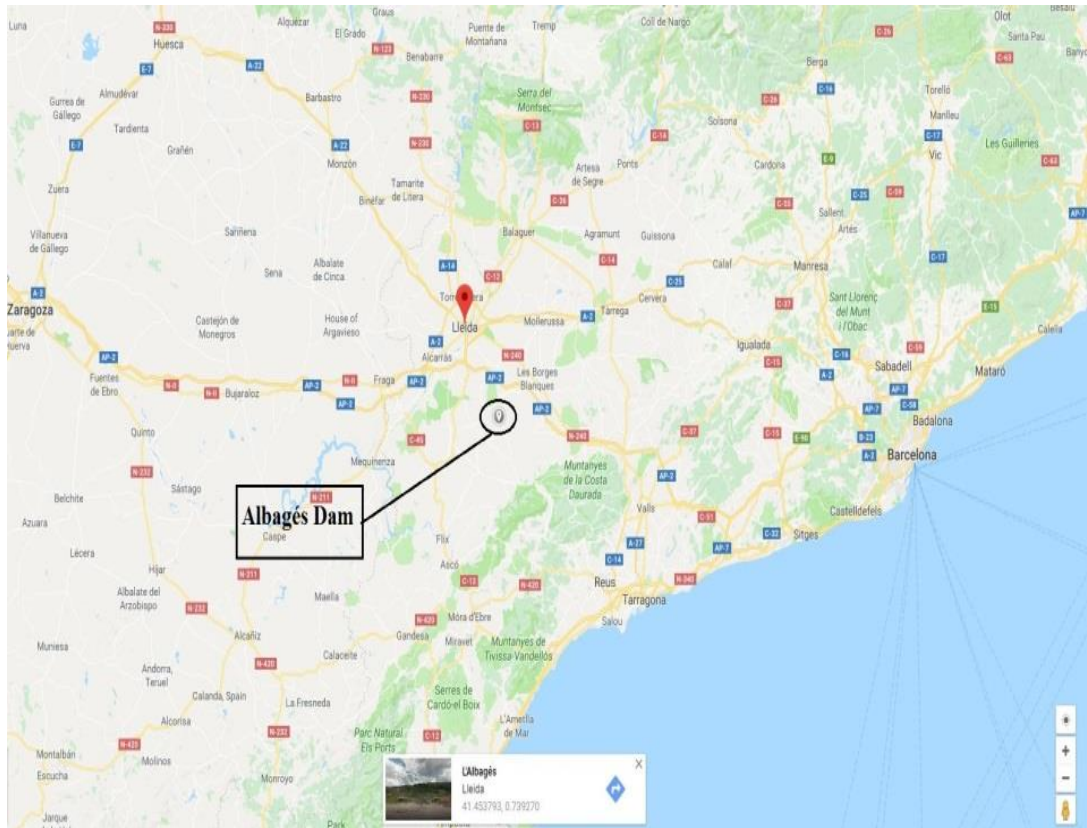


Figure 5-1: Geographical location of the Albagés dam.

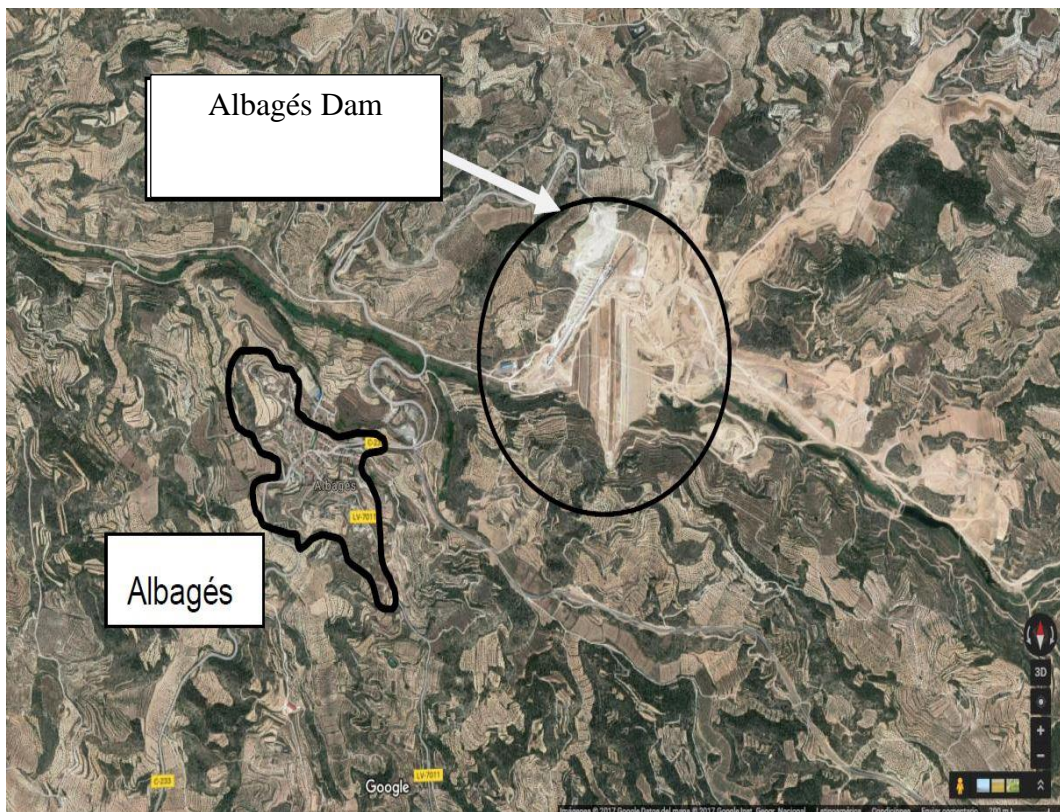


Figure 5-2: Location of the Albagés dam on the river Set valley.

The construction of the dam began at the beginning of 2015 and is currently (2018) already completed. The zoned earth dam is 85 m high, has a width at crest of 10 m and presents 3 H: 1 V upstream slopes.

The compacted materials studied consists of clayey silt core, ‘all-one’ mixture, and coarse granular materials. The ‘all-one’ mixture originated due to the excavation of argillite and sandstones from the Oligocene epoch. It forms the inner upstream shoulder and the downstream shoulder of the dam. Figure 5-3 presents the pictures obtained during the construction process, compaction of the core and ‘all-one’ materials, and the installation of total stress cells.

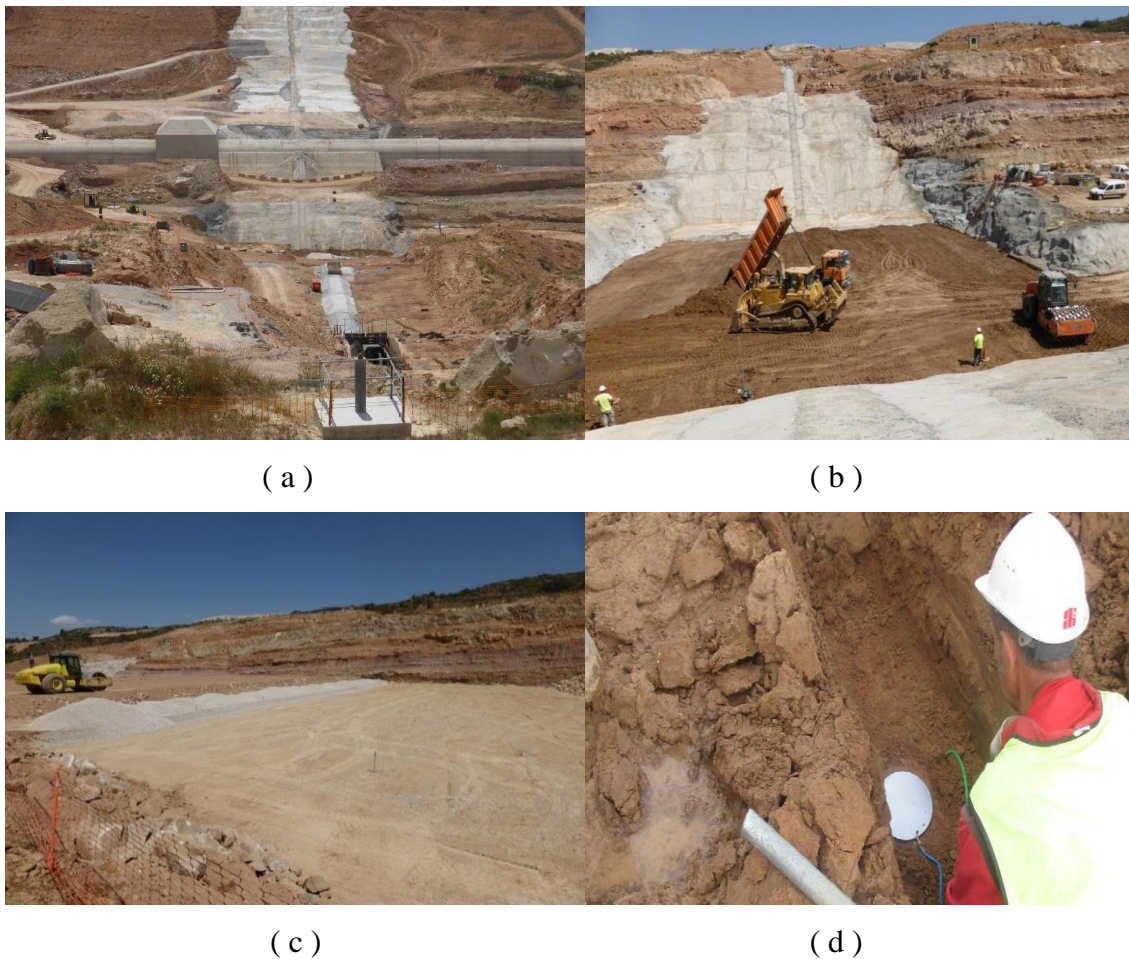


Figure 5-3: (a) General view of the Albagés dam under construction. (b) Compaction procedure of the core material. (c) ‘All-one’ shoulder and drain filter area. (d) Placement of total stress cells. (Alonso et al., 2016).

In addition, the modified section of the dam (Alonso et al., 2016) is presented in Figure 5-4, where the different materials can be observed.

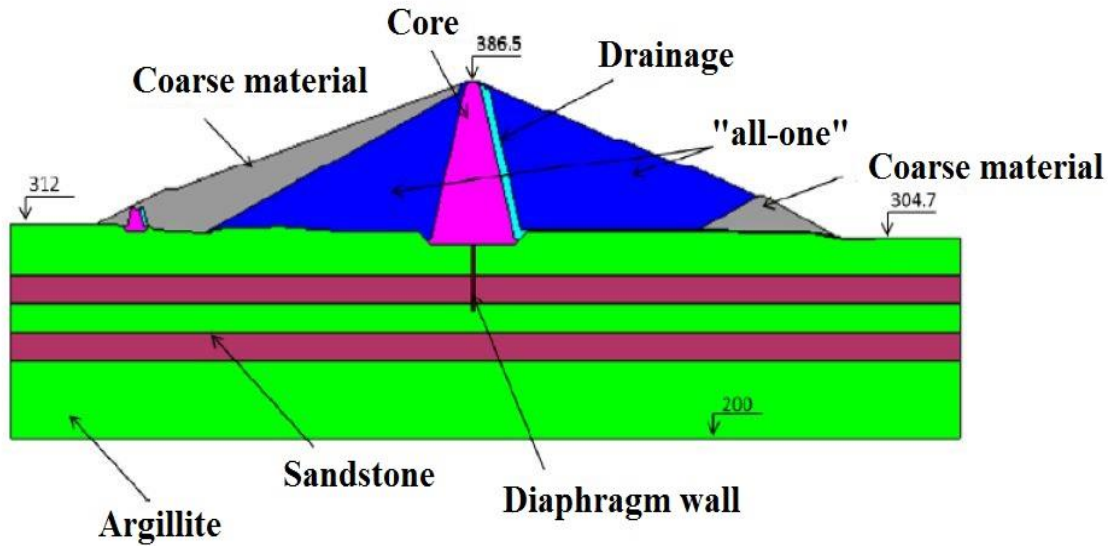


Figure 5-4: A modified section with the materials included in the numerical model. (Alonso et al., 2016).

5.3 Basic properties of Albagés ‘all-one’ material

As a construction material, the material constituted mainly by argillite and sandstone is the dominant material of the project. Figure 5-5 presents the outcrop of argillite / sandstone before excavation. In addition, Figure 5-6 shows the ‘all-one’ material that is formed after excavation and during the compaction process. The dry density of the ‘all-one’ material is around 2.1 Mg/m^3 after in situ compaction conditions with a water content of 10%. It has a liquid limit of 30% and a plasticity index of 13.6%.



Figure 5-5: The ‘all-one’ material before excavation. Outcrop of argillite / sandstone.



Figure 5-6: The ‘all-one’ material after excavation and during compaction.

In this section, the results of some basic experimental works performed on ‘all-one’ mixtures are presented. The following experimental study has been considered:

- Atterberg limits.
- Grain size distribution curves.
- Standard and modified Proctor compactions.

5.3.1 Atterberg limits

The results achieved from the Atterberg limit tests in the UPC laboratory and previous reports are shown in Figure 5-7. It has a liquid limit of 30% and a plasticity index of 13.6% (material of low plasticity).

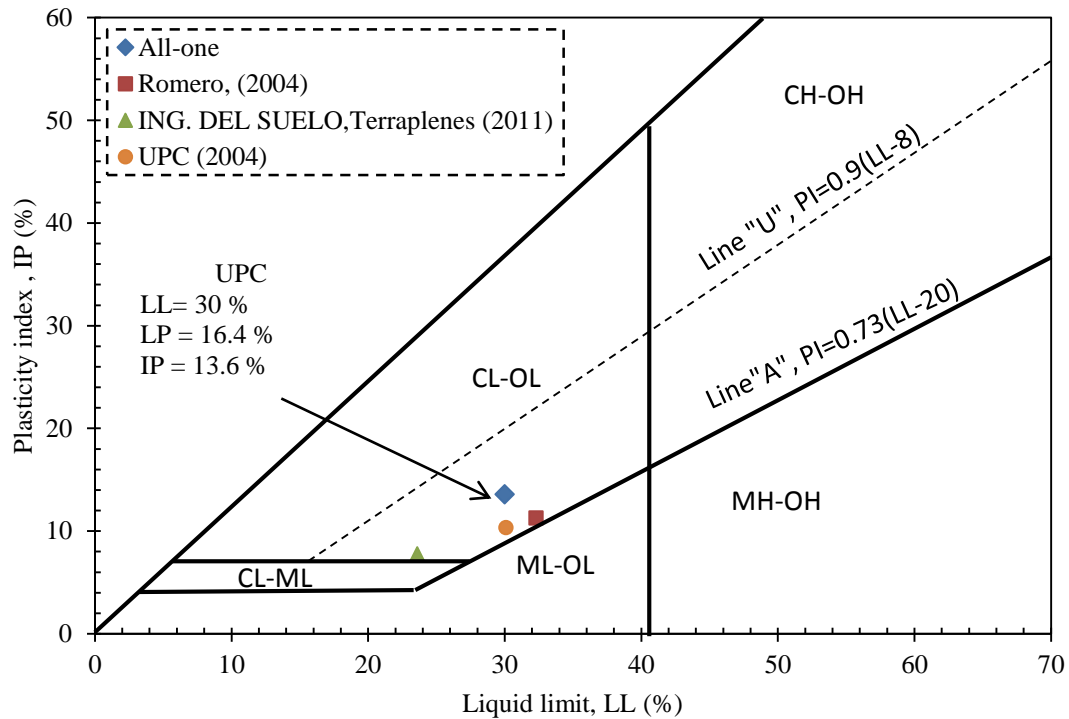


Figure 5-7: Atterberg limits of all-one material and previous results of other researchers.

5.3.2 Grain size distribution curves

Two grain size distribution curves of compacted ‘all-one’ have been determined as shown in Figure 5-8. One of them corresponds to the material extracted from the top layer of compacted in situ conditions (0_30 cm), and the other one is related to the bottom layer (30_60 cm). The changes of the two curves are not considerable; therefore, there is no difference between using material from the top layer or the bottom layer. As can be seen, 10 % of the material is smaller than 1 mm, and the rest ranges between 1 and 50 mm. This means that the fine particles are not sufficient to fill all the voids between the large particles, based on Vallejo (2011). This type of mixture is called interactive-underfilled packing, which includes the ‘all-one’ material concept. In addition, the initial GSD curve before compaction for the ‘all-one’ sample corresponding to the embankment structure is plotted. It can be observed that before compaction particle sizes greater than 250 mm are

present in the curve of sample M4. These oversized particles were crushed after compaction under in situ conditions. After in situ compaction, the samples have been sent to UPC laboratory in large boxes. Because of a random selection of material in the boxes to do GSD test in the laboratory conditions some of the fines present in the initial curve are not detected in the curves after compaction. Therefore, a modification of initial M4 curve without fines is plotted by removing the fine content. The Hardin breakage index after compaction was calculated and is equal to $B_r = 0.3$.

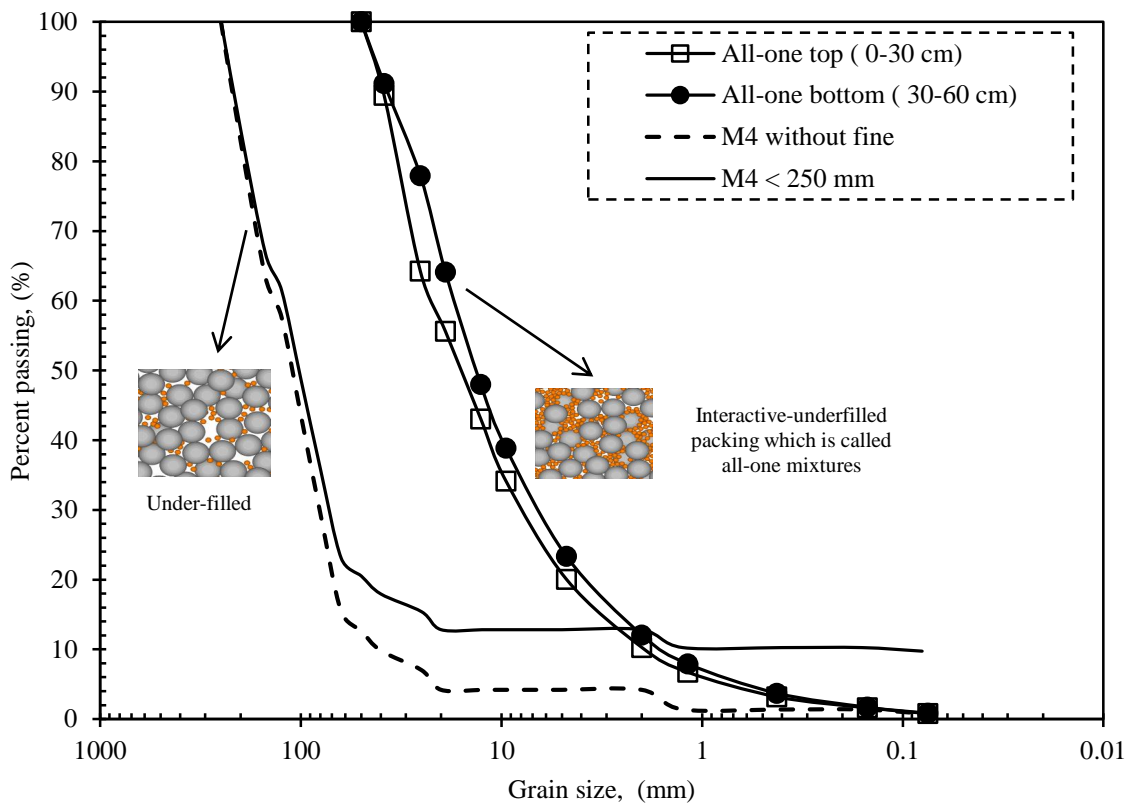


Figure 5-8: Grain size distribution of in situ all-one material before and after compaction.

5.3.3 Standard and modified compaction curves

The dry density and the optimum water content of the ‘all-one’ material have been evaluated by Standard Proctor (PN) and Modified Proctor (PM) compaction tests. The results obtained at the UPC laboratory in 2017 and in previous reports on the compaction curves are plotted in Figure 5-9. It is observed that in the tests carried out in the UPC laboratory; higher optimum density values are obtained for both the Standard Proctor (2.03 Mg/m³), and the Modified Proctor (2.21 Mg/m³) at lower water contents compared

with the results of previous reports (11.5% and 7% respectively). The in situ dry density (around 2.1 Mg/m³ at a water content around 10%) is between these Proctor values.

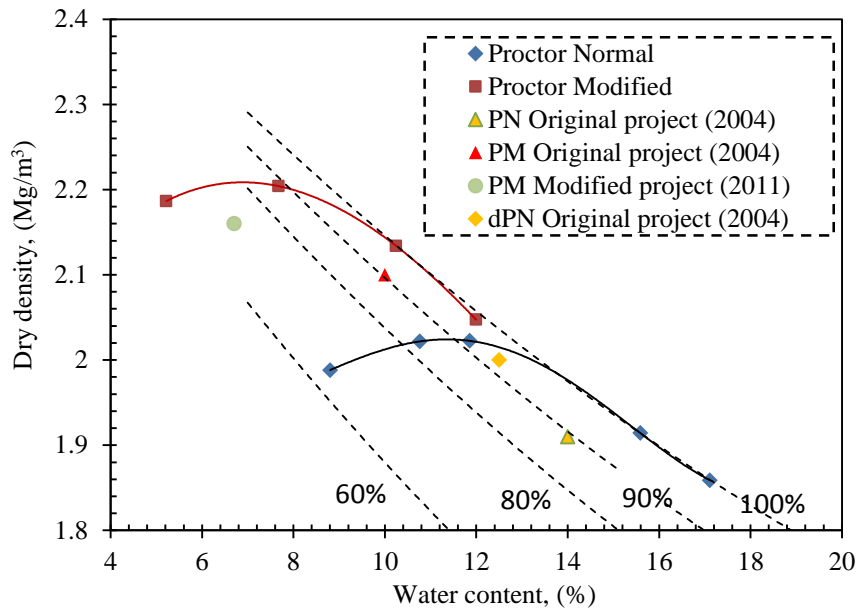


Figure 5-9: The compaction curves of the Standard Proctor and Modified Proctor from UPC laboratory test and previous reports, and the degree saturation curves of 60%, 80%, 90% and 100% for the all-one material.

5.4 Consolidation, compressibility and collapse analysis under oedometer conditions

The oedometer tests are carried out to evaluate the compressibility on loading, the secondary compressibility, and the collapse deformation on soaking of the ‘all-one’ material. Three stress paths are selected as described in the methodology. Some coarse fraction has been removed and the rest of the material has been able to be tested under oedometric conditions (diameter of the cell 150 mm). Under in situ conditions, the initial water content has a range between 7 % and 10 %. At laboratory conditions samples are prepared at 8 % of water content. Actually, a lower amount of humidity has been chosen to evaluate the maximum potential for collapse on soaking. The coefficient of secondary consolidation (C_{α}), the oedometer modulus of stiffness (E_m), the compressibility index (λ and k), and the collapse deformation are evaluated. Some of the general and fitting expressions to calculate the coefficients are presented in Table 5-1.

Table 5-1: The coefficient of secondary compression (C_{α}), the oedometer modulus of stiffness (E_m), the compressibility index (λ and k), and the collapse deformation expressions.

Expression	Symbols	Equation number
$\lambda = -\frac{\Delta e}{\Delta \ln \sigma'_v}$	Δe : Change in void ratio () σ'_v : Vertical effective stress. (kPa)	5-1
$\text{Collapse deformation} = -\left[\frac{\Delta e}{1+e_0}\right]$	Δe : Change in void ratio resulting from wetting () e_0 : Initial void ratio ()	5-2
$E_m = \frac{\Delta \sigma'_v}{\Delta \varepsilon_v}$	$\Delta \sigma'_v$: Change of vertical effective stress. (MPa) $\Delta \varepsilon_v$: Variation of deformation. () E_m : Oedometer modulus of stiffness (MPa)	5-3
$E_m = x * e^{y * \sigma'_v}$	E_m : Oedometric modulus. (MPa) σ'_v : Vertical effective stress. (kPa) x: Parameter. (MPa) y: Parameter. (1/kPa)	5-4
$C_{\alpha} = -\frac{\Delta e}{\log\left(\frac{t_2}{t_1}\right)}$	C_{α} : Coefficient of secondary compression. () Δe : Change in void ratio () in time period t_1 to t_2	5-5
$C_{\alpha} = \frac{\sigma'_v}{m + n * \sigma'_v}$	C_{α} : Coefficient of secondary compression. () σ'_v : Vertical effective stress. (kPa) m: Parameter. (kPa) n: Parameter. ()	5-6

5.4.1 Results of sample loaded up to 1 MPa and saturated

The ‘all-one’ material is compacted statically to the vertical stress of 1 MPa with a dry density of 1.9 Mg/m³ and then saturated at the constant stress of 1 MPa. The evolution of the sample state during the loading and wetting processes is presented in Table 5-2. The low initial value of the degree of saturation increases from 0.26 to 0.51 up to the maximum applied vertical stress. The in situ average value of the degree of saturation is 0.85. Consequently, the collapse deformation under laboratory condition is expected to be greater than the in situ compacted material.

Table 5-2: The evolution of the sample state during the loading-unloading and wetting processes.

Condition	σ'_v (MPa)	ε_v (%)	e	ω	S_r	ρ_d (Mg/m ³)	E_m (MPa)
Initial	0	0	0.814	0.08	0.265	1.49	
Loading	0.075	1.88	0.780	0.08	0.277	1.52	
Loading	0.2	4.21	0.738	0.08	0.293	1.55	
Loading	0.5	14.43	0.552	0.08	0.391	1.74	
Loading	1	21.65	0.421	0.08	0.513	1.90	6.92
Saturation	1	29.11	0.286	0.116	1	2.10	

The loading results in terms of void ratio versus vertical total / effective stress are shown in Figure 5-10. In addition, the time evolution of the void ratio on the wetting process at the vertical constant stress (1 MPa) is presented in Figure 5-11. A collapse of around 7.5 % (volumetric deformation) is observed. The maximum compressibility index is equal to $\lambda = 0.196$. The variation of the void ratio in time for various loading steps is shown in Figure 5-12. Also, the evolution of the secondary compression parameter with stress is presented in Figure 5-13.

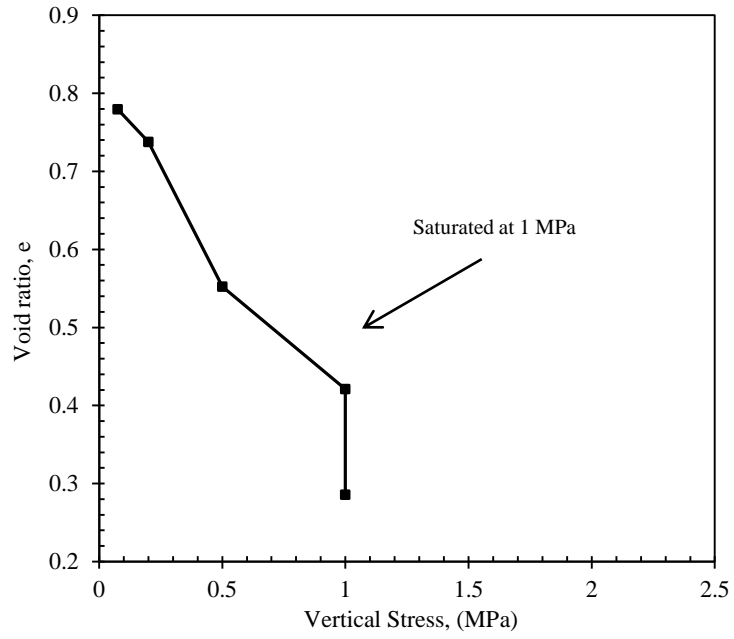


Figure 5-10: Void ratio versus vertical stress for sample loaded up to 1 MPa and then saturated at constant vertical stress.

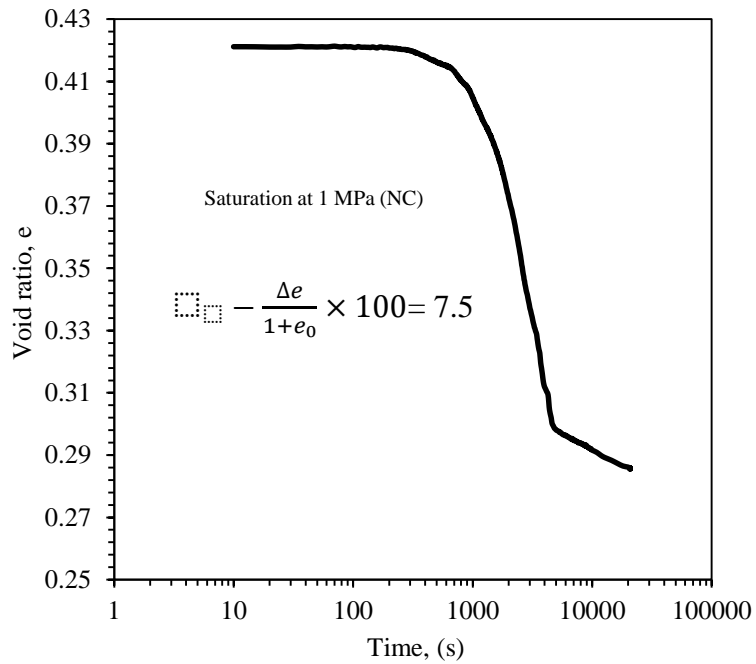


Figure 5-11: Time evolution of void ratio during soaking.

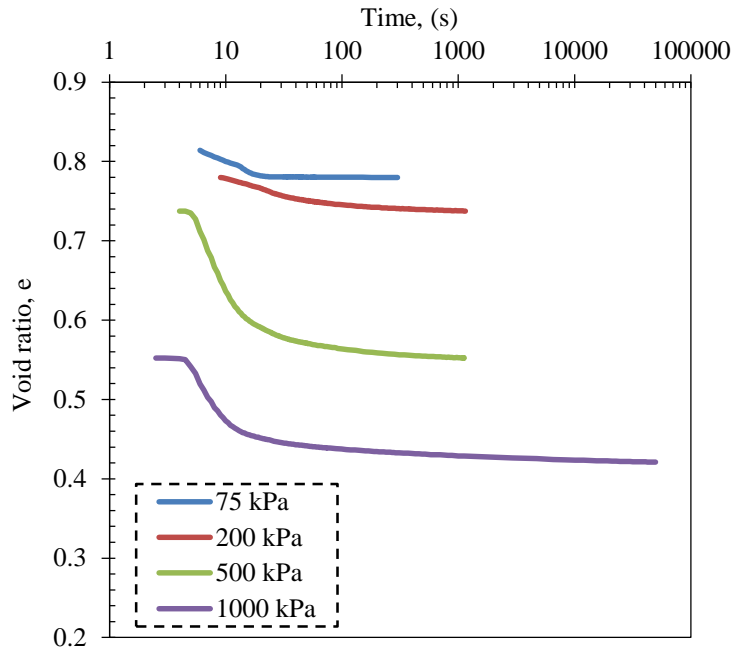


Figure 5-12: The variation of void ratio versus time for different loading steps.

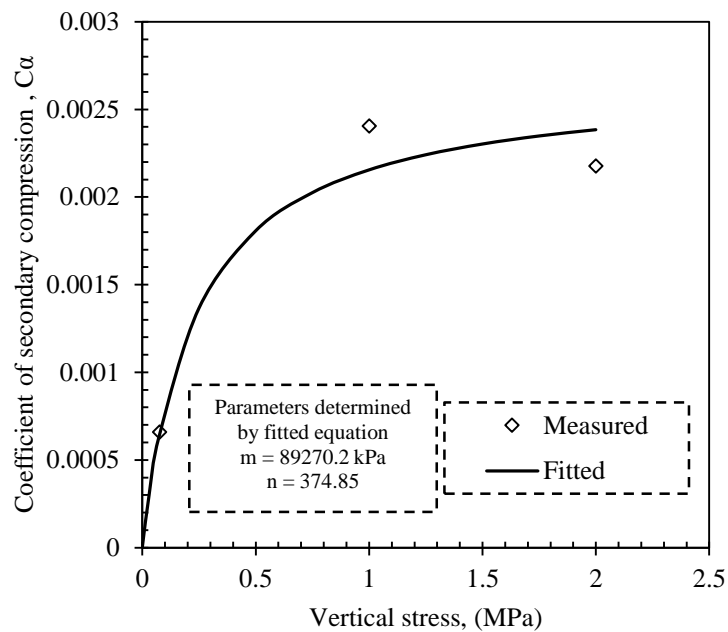


Figure 5-13: The coefficient of secondary compression for different vertical stresses.

5.4.2 Result of sample loaded up to 2 MPa and unloaded up to 1 MPa and then saturated

The ‘all-one’ material is compacted statically to a vertical stress of 2 MPa with a dry density of 2.06 Mg/m³, which approximately corresponds to in situ conditions. Then, the

sample is unloaded up to 1 MPa and afterwards saturated. The evolution of the sample state during the loading-unloading and wetting process is presented in Table 5-3. The low initial value of the degree of saturation increases from 0.26 to 0.69 at the maximum applied vertical load. The in situ average value of the degree of saturation is 0.85. So, the collapse strain under laboratory conditions is still expected to be higher than the in situ compacted material. Step loading-unloading results in terms of void ratio versus vertical total / effective stress are shown in Figure 5-14. Values of the compressibility parameter for both loading and unloading (based on equation 5-1) were measured ($\lambda = 0.156$ and $\kappa = 0.002$). In addition, the time evolution of the change in void ratio on the wetting process at the vertical constant stress (1 MPa) is presented in Figure 5-15. The collapse deformation was calculated based on equation 5-2. A collapse of around 2.0% (volumetric deformation) is observed. Figure 5-16 presents the calculated oedometer modulus of stiffness based on equation 5-3 and 5-4, respectively. The varying of modulus is evaluated in different loading steps. The variation of the void ratio in time for various loading steps is shown in Figure 5-17. The secondary compression coefficients are determined by equation 5-5.

Table 5-3: The evolution of the sample state during the loading-unloading and wetting process (loaded up to 2 MPa unloaded up to 0.6 MPa and saturated).

Condition	σ'_v (MPa)	ε_v (%)	e	ω	S_r	ρ_d (Mg/m³)	E_m (MPa)
Initial	0	0	0.814	0.08	0.265	1.49	
Loading	0.075	1.789	0.8084	0.08	0.267	1.49	
Loading	0.2	4.470	0.7119	0.08	0.303	1.58	
Loading	0.5	14.199	0.5303	0.08	0.407	1.76	
Loading	1	21.147	0.4125	0.08	0.524	1.91	7.70
Loading	1.2	22.700	0.3911	0.08	0.552	1.94	16.81
Loading	1.5	24.752	0.3554	0.08	0.608	1.99	15.31
Loading	1.7	27.698	0.3390	0.08	0.637	2.02	21.98
Loading	2	27.671	0.3134	0.08	0.689	2.06	21.28
Unloading	1.5	27.602	0.314	0.08	0.688	2.05	
Unloading	1	27.499	0.3150	0.08	0.686	2.05	
Saturation	1	27.937	0.288	0.107	1.000	2.10	

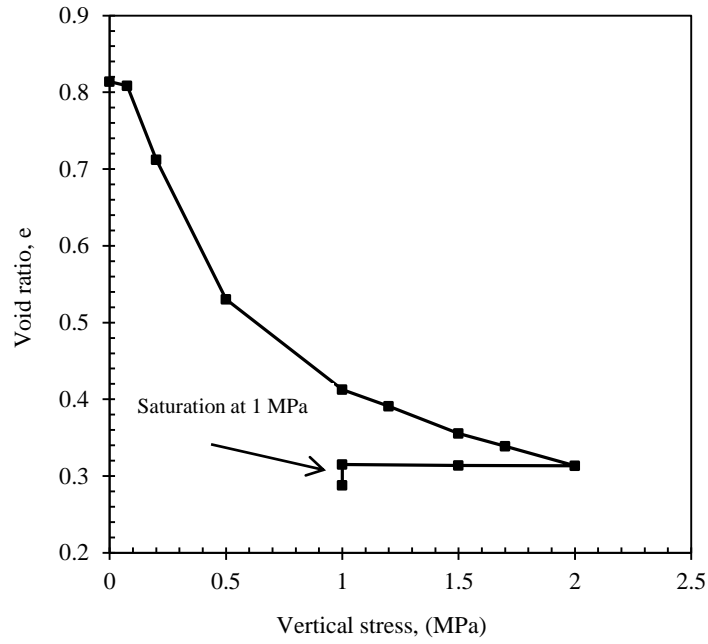


Figure 5-14: Void ratio versus vertical stress for sample loaded up to 2 MPa and unloaded up to 1 MPa and then saturated at constant vertical stress.

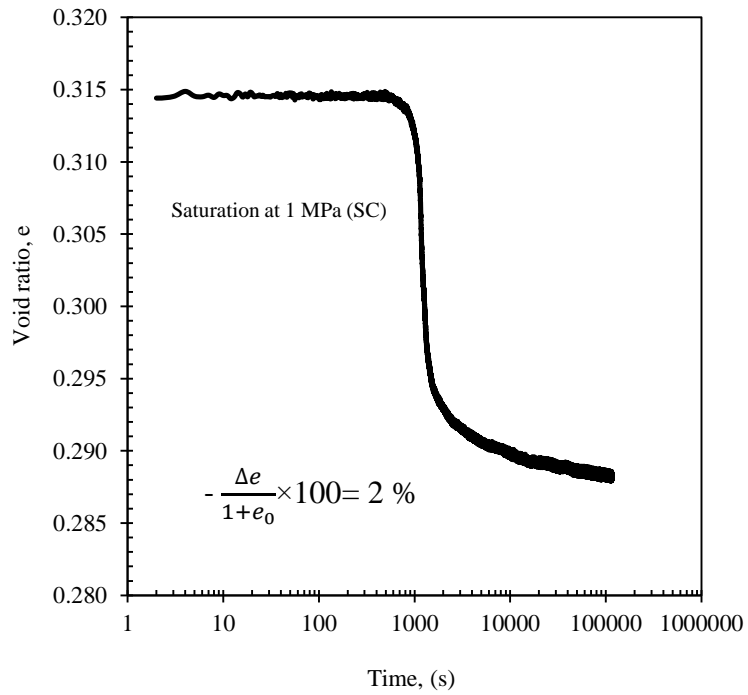


Figure 5-15: The variation of the void ratio in time during saturation at 1 MPa.

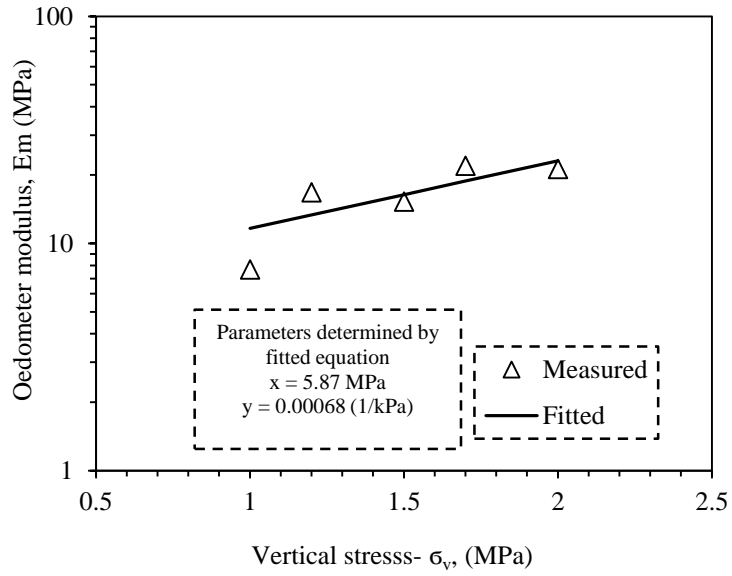


Figure 5-16: Evolution of the oedometer modulus of stiffness.

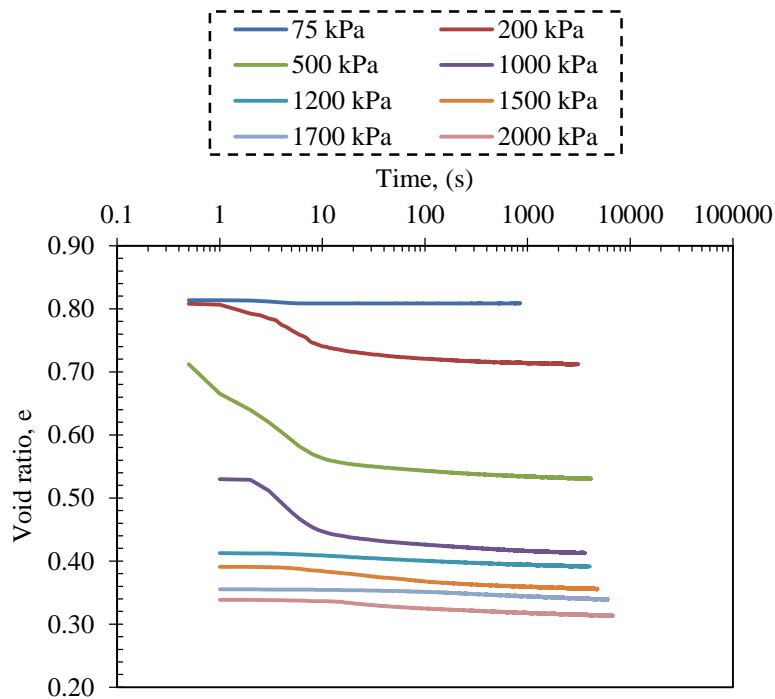


Figure 5-17: The variation of void ratio versus time for different loading steps.

The secondary compression coefficients for the different loading steps are presented in Figure 5-18. In addition, the fitting parameters are calculated according to equation 5-6.

The average value of secondary compression coefficient is around 0.0035 under in situ stress states.

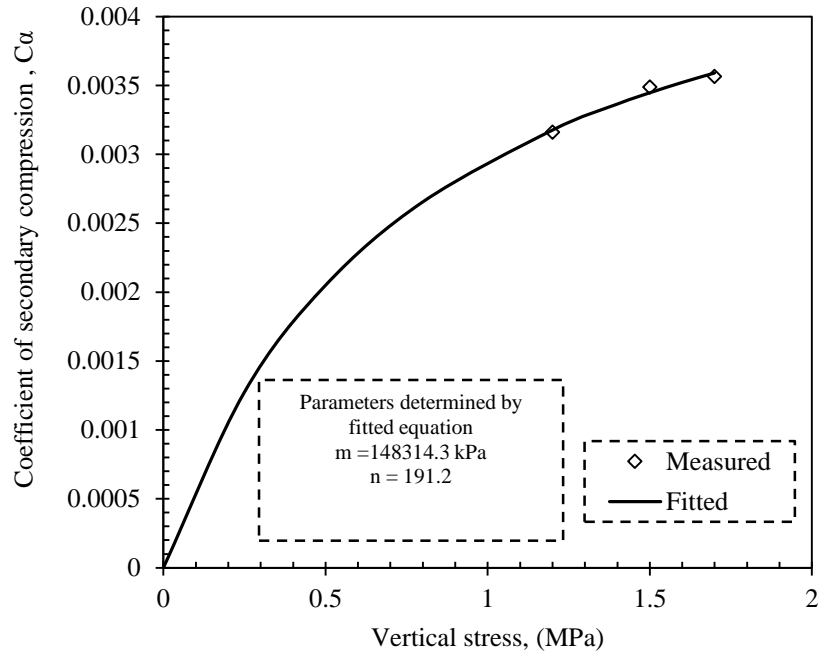


Figure 5-18: The coefficient of secondary compression for different vertical stresses.

5.4.3 Results of sample loaded up to 2 MPa and unloaded up to 0.6 MPa and then saturated

The ‘all-one’ material is compacted statically to the vertical stress of 2 MPa with a dry density of 2.06 Mg/m³, which corresponds to in situ conditions. Then unloaded up to 0.6 MPa and saturated. The evolution of the sample state during the loading-unloading and wetting process are presented in Table 5-4. The low initial value of the degree of saturation increases from 0.265 to 0.69 up to the maximum applied vertical load. The compressibility index values (post-yield and pre-yield, respectively) are as follows:

$$\lambda = 0.176, \kappa = 0.003.$$

Table 5-4: The evolution of the sample state during the loading-unloading and wetting process (loaded up to 2 MPa unloaded up to 0.6 MPa and saturated).

Condition	σ'_v (MPa)	ε_v (%)	e	ω	S_r	ρ_d (Mg/m ³)	E_m (MPa)
Initial	0	0	0.814	0.08	0.265	1.49	
Loading	0.075	1.79	0.782	0.08	0.276	1.52	
Loading	0.2	4.47	0.733	0.08	0.295	1.56	
Loading	0.5	14.120	0.556	0.08	0.388	1.73	
Loading	1	21.15	0.430	0.08	0.502	1.89	7.20
Loading	1.2	22.70	0.402	0.08	0.537	1.93	12.88
Loading	1.5	24.75	0.365	0.08	0.592	1.98	14.62
Loading	2	27.70	0.312	0.08	0.693	2.06	16.97
Unloading	1.5	27.67	0.312	0.08	0.692	2.06	
Unloading	1	27.60	0.313	0.08	0.689	2.06	
Unloading	0.6	27.50	0.315	0.08	0.685	2.05	
Saturation	0.6	27.94	0.307	0.114	1	2.07	

Step-loading-unloading results in terms of void ratio versus vertical total / effective stress are shown in Figure 5-19. In addition, the time evolution of the change in the void ratio on the wetting process at the vertical constant stress (0.6 MPa) is presented in Figure 5-20. A collapse of around 0.43 % (volumetric deformation) is observed, which is lower than the previous value at 1 MPa, as a consequence of the lower applied stress.

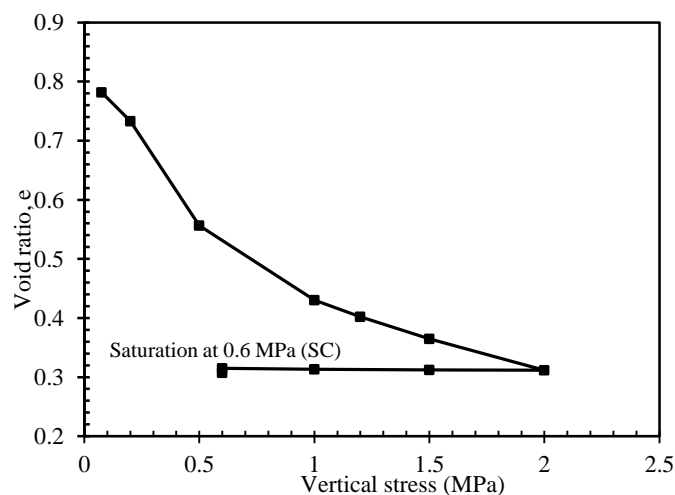


Figure 5-19: Void ratio versus vertical stress for sample loaded up to 2 MPa and unloaded up to 0.6 MPa and then saturated at constant vertical stress.

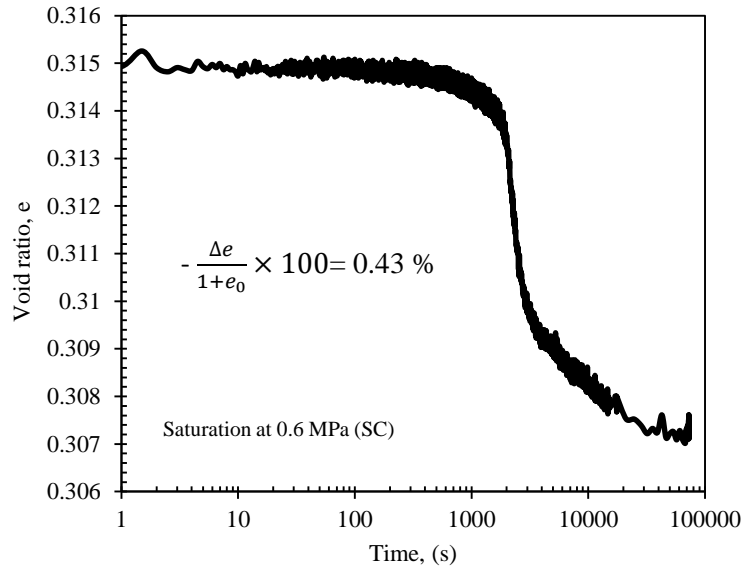


Figure 5-20: The variation of void ratio in time increment in saturation at 0.6 MPa

Figure 5-21 depicts the calculated and fitted oedometer modulus of stiffness. The modulus is evaluated at different loading steps.

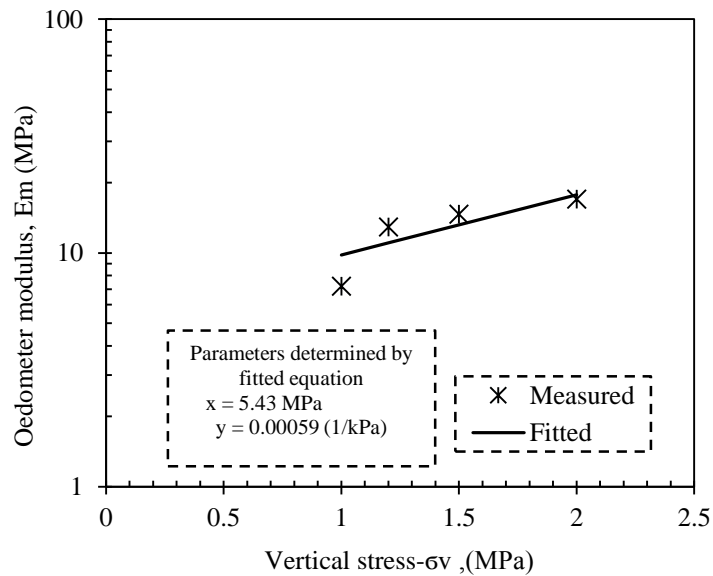


Figure 5-21: The oedometer modulus in load increment.

The time evolution of the void ratio for various loading steps is shown in Figure 5-22.

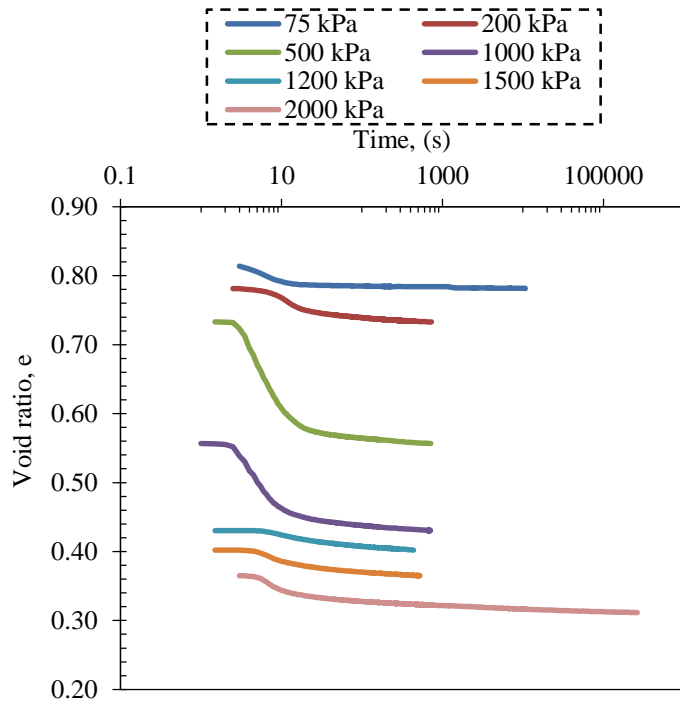


Figure 5-22: The variation of void ratio versus time for different loading steps.

The secondary compression coefficient is presented in Table 5-5. The coefficient is determined for the maximum load of 2 MPa and for the saturation load at 0.6 MPa, considering the post-saturation stage of 4 days.

Table 5-5: The coefficient of secondary compression for different vertical stresses.

Load (MPa)	Coefficient of secondary compression	
	C_{α}	
0.075	0.00066	
2	0.00218	
0.6 (creep)	0.0003	

5.4.4 Comparison of results of the three oedometer tests as well as with some previous work

In order to assess the collapse deformation of three samples with various stress paths, the variation of void ratio versus logarithmic effective stress is presented in Figure 5-23 for the three cases. The specimens are classified as follows:

- Group A: Loaded up to 1 MPa and saturated at constant vertical stress.
- Group B: Loaded up to 2 MPa and unloaded up to 1 MPa and saturated at constant vertical stress.
- Group C: Loaded up to 2 MPa and unloaded up to 0.6 MPa and saturated at constant vertical stress.

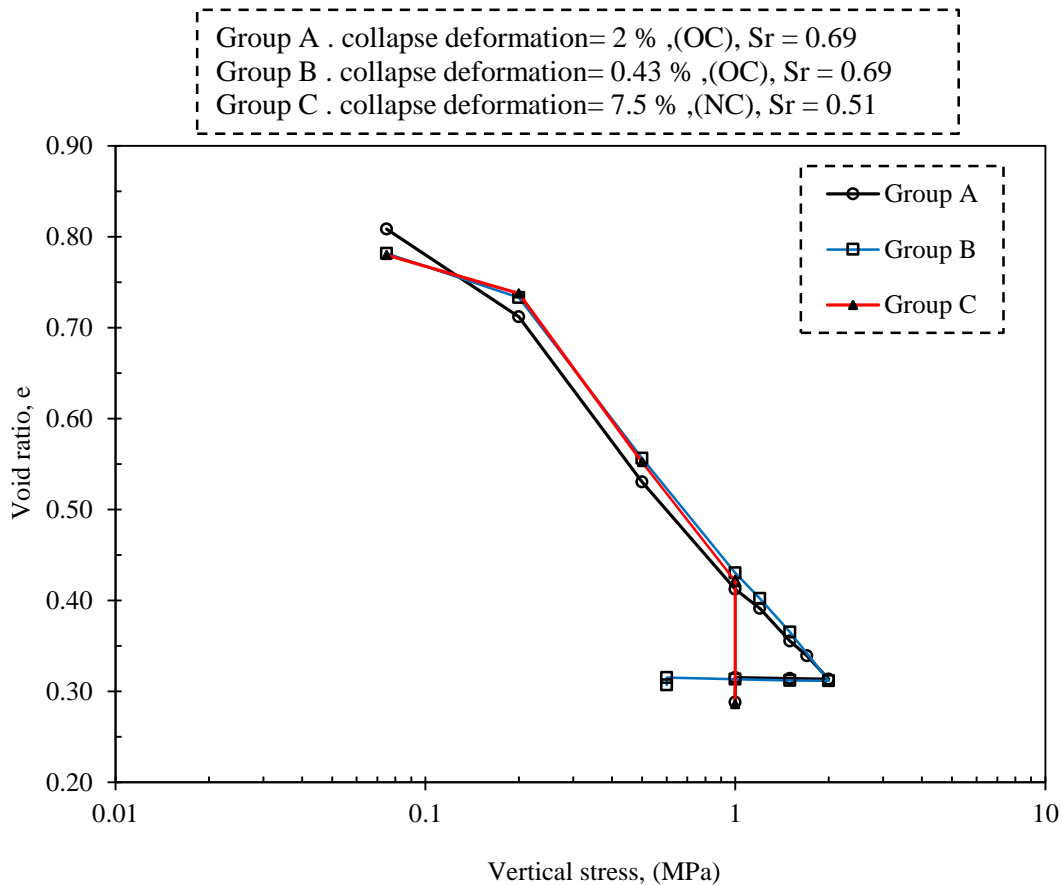


Figure 5-23: Comparisons of three samples with various stress paths under oedometer conditions.

It is observed that the highest collapse deformation occurs in the group A where the sample saturated at 1 MPa in a normally consolidated state and lower degree of saturation ($S_r = 0.51$, and collapse strain = 7.5%). The collapse in samples group B and group C occurs under over consolidated states (maximum stress of 2 MPa) and reaches collapse values of 2 % and 0.43 %, respectively. Based on results obtained in group B and group C the collapse depends not only on the initial degree of saturation but also on the current stress applied and the history of stresses.

To assess and compare the collapse of the three samples, the term "normalized stress" is defined as the vertical stress at collapse divided by the maximum vertical stress applied (σ^*). The results are shown in Figure 5-24. It can be observed that when the saturation reaches the maximum stress history of the soil the amount of collapse increases (normally consolidated condition).

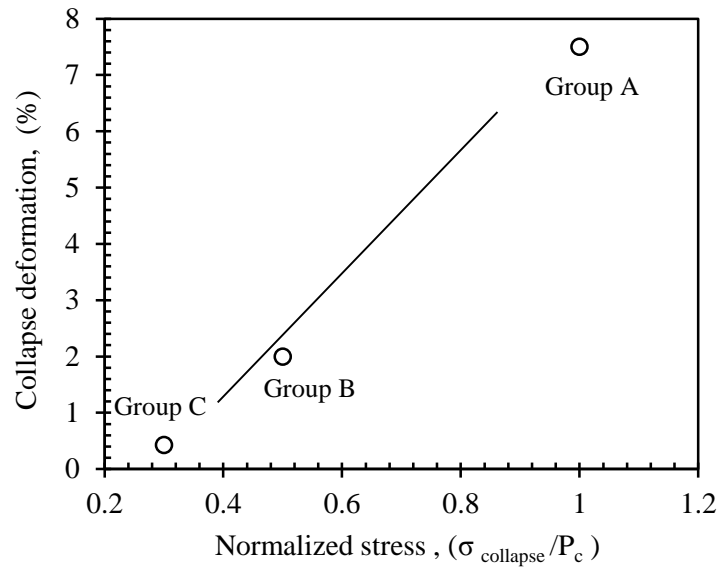


Figure 5-24: collapse strain versus normalized stress

To evaluate and compare the collapse of ‘all the’ materials in the dam (core, ‘all-one’, and coarse materials), the term "normalized collapse" is defined in equation 5-7.

$$\text{Normalised collapse} = \frac{\text{Volumetric deformation of collapse}(\%)}{\text{Vertical stress at collapse (kPa)}} \quad 5-7$$

To analyse in a more objective way the normalised results are evaluated based on the initial void ratio before collapse. The collapse obtained during saturation condition for different tests are plotted in Figure 5-25. It is clear that the amount of collapse increases with higher void ratios. Moreover, in the case of the same void ratio specially around 0.5 at the same vertical stress, the ‘all-one’ and coarse materials display more collapse compared to the core material, which can be related to the effect of the initial degree of saturation (higher in the wet core material).

The collapse deformations obtained with this in situ compacted ‘all-one’ material will be compared to experimental results using artificial fragments when discussing the hydro-mechanical behaviour.

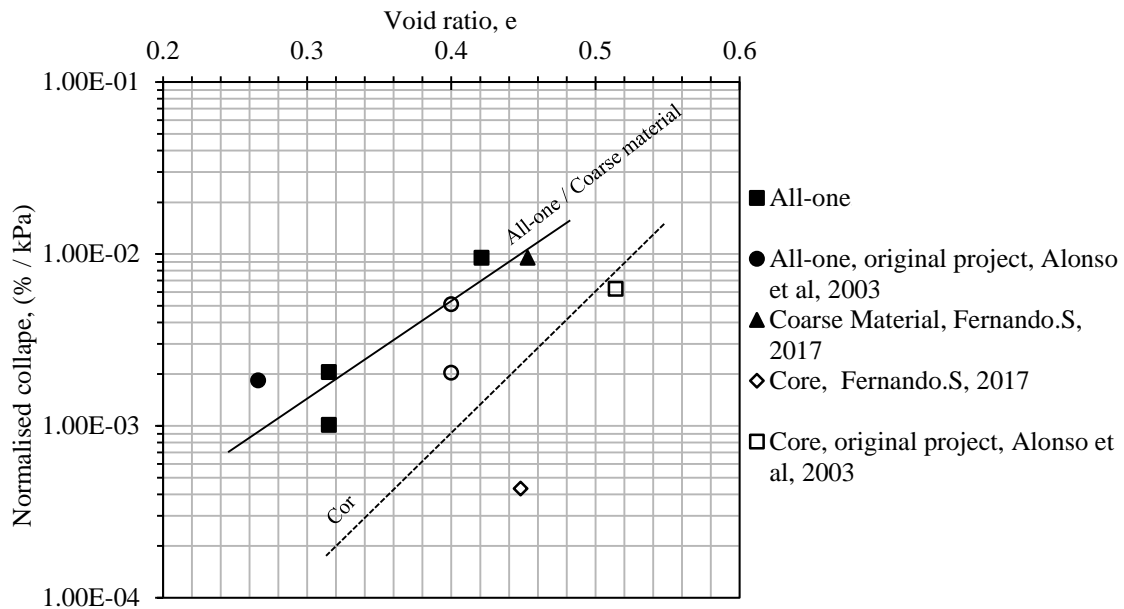


Figure 5-25: Normalised collapse versus void ratio for various materials of the dam.

In addition, the parameters obtained from these three oedometer tests are summarized in Table 5-7.

Table 5 7: Parameters obtained from oedometer tests for three group of samples.

Group	E_m (MPa)	Compressibility index	Swell index
		(λ)	(κ)
A: Saturation at 1 MPa (OC)	21.3	0.156	0.002
B: Saturation at 0.6 MPa (OC)	17	0.176	0.003
C: Saturation at 1 MPa (NC)	6.9	0.196	-

In normally consolidated state the modulus of stiffness shows the smaller value compared to over consolidated states (the post-yield compressibility is also higher for the normally consolidated). This is a consequence of the higher void ratio attained on the normally consolidated sample at a maximum vertical stress of 1MPa.

5.5 Permeability tests

The permeability using controlled gradient for the ‘all-one’ material is measured in groups A and B under oedometer conditions. In the first case, the permeability is measured by a saturation load of 1 MPa in normally consolidated state (NC) and in the second case, the permeability is measured at saturation load of 1 MPa in over consolidated state (OC). In both cases the void ratio is approximately the same (around 0.29). The results are shown in Table 5-8. As observed, an important difference is obtained, which cannot be easily explained, unless some localised flow conditions are accepted for test A. Nevertheless, one of the tests indicates a very low permeability of the ‘all-one’ material, which justified the decision of using a different external upstream shoulder material (coarse material). Previous experimental results on ‘all-one’ material at equivalent void ratio indicated values not exceeding 10^{-9} m/s.

Table 5-6: Permeability test for all-one samples in tow normally and over consolidated states.

Group	Void ratio (e)	Permeability, k (m/s)
A: Saturation at 1 MPa (OC)	0.288	5.6×10^{-7} m/s
C: Saturation at 1 MPa (NC)	0.286	6.9×10^{-10} m/s

5.6 Water retention curve

In order to assess the partially saturated behaviour, the samples were compacted to standard Proctor (SP). Suction was determined by dew point psychrometers and tensiometers were used in the case of values close to saturation conditions. The drying and wetting cycles were fitted to van Genuchten model and parameters are included in Figure 5-26. A 12.5 % of water content was observed at the beginning of drying path, while this value due to hysteretic behaviour shows 11.3 % at the end of the wetting path.

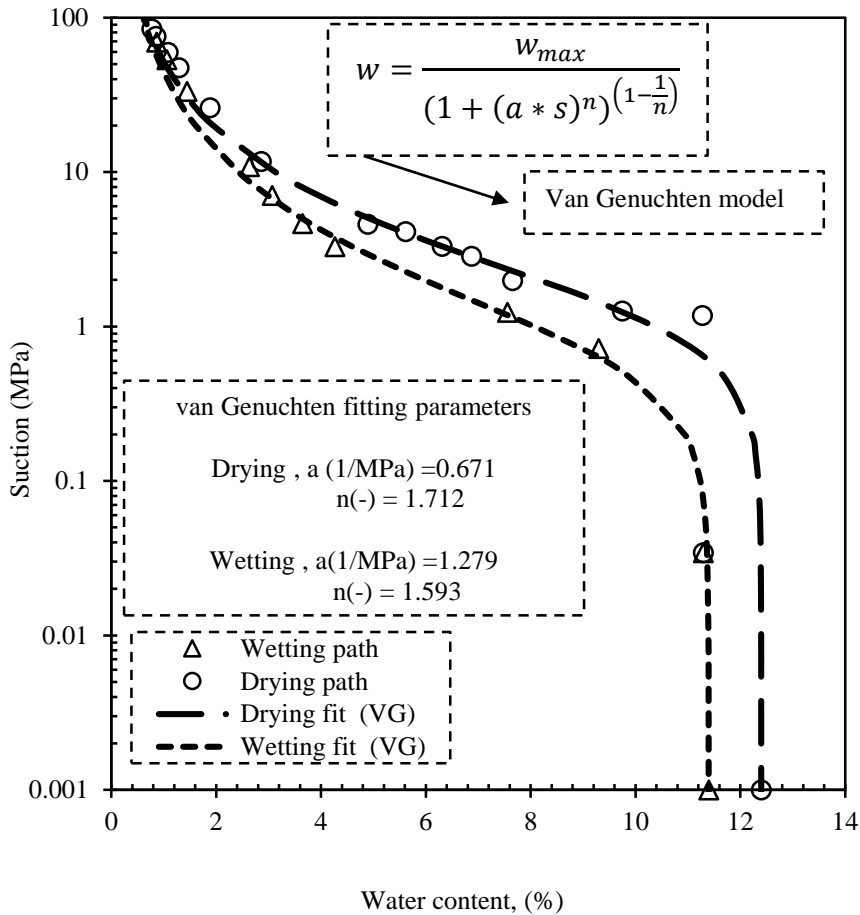
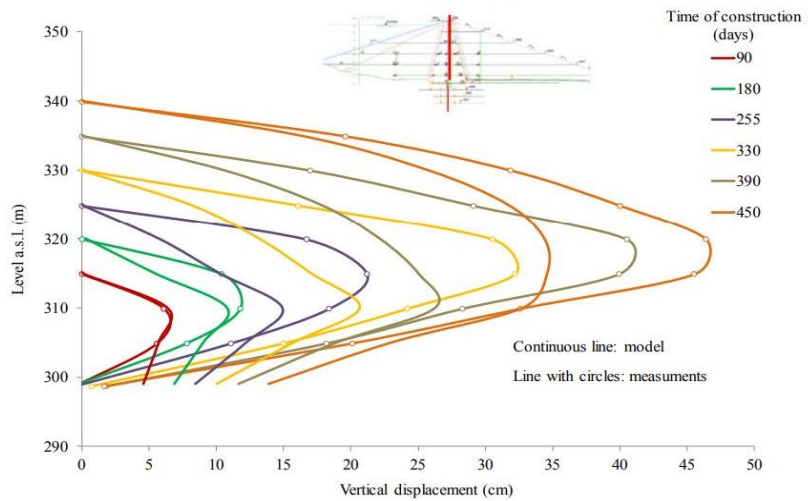


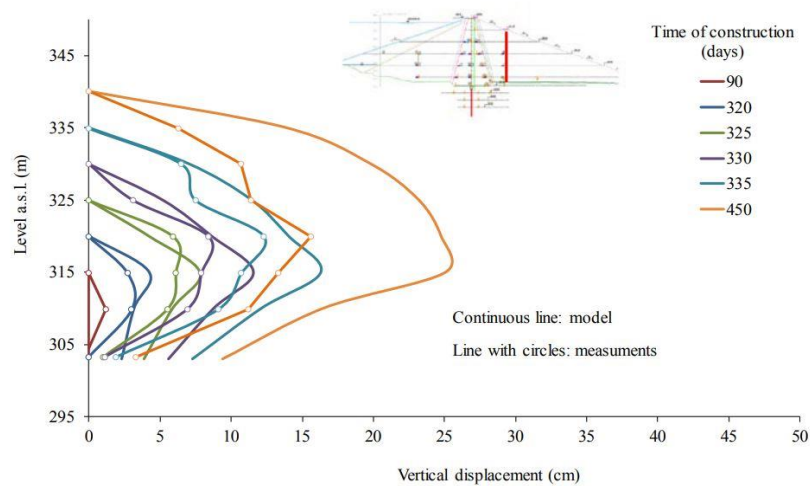
Figure 5-26: Water retention curve for ‘all-one’ material both drying and wetting paths.

5.7 Numerical simulations

Finally, these results will provide useful information for the different hydro-mechanical parameters of the ‘all-one’ material for a ‘class A’ modelling of the Albagés dam. Pinyol and Alonso (2017) simulated the Albagés dam using Code_Bright based on laboratory tests and compared the ‘class A’ modelling results to field test results. The results of settlements in a central profile and downstream are shown in Figure 5-27 from Pinyol and Alonso (2017).



(a)



(b)

Figure 5-27: Vertical displacement analysis of the Albagés dam both numerical and in situ measurements for (a) central profile and (b) downstream profile (Pinyol and Alonso, 2017)

It can be seen from Figure 5-27, significant differences observed between modelling results based on laboratory data and in situ measurements. The model calculates settlement greater than those recorded in the downstream shoulder of the ‘all-one’ material. These differences could be related to incorrect estimation of some parameters such as initial preconsolidation stress, compressibility (higher in laboratory tests than expected under in situ conditions), and the evolution of the suction due to the hydraulic and mechanical behaviour.

6 Soil-cemented artificial aggregates

6.1 Introduction

Cement is one of the most used building materials for all types of infrastructure, due to its low economic cost and the resistant characteristics. For some of these characteristics, it is not only used in structural applications but also, in the last few decades, there has been a surge of interest to use in geotechnical aspects. The cementation may be ascertained as a precipitation of microcrystals in the pore spaces of soils, creating a strong and rigid structure by binding the grains together. This will increase the soil stability against disaggregation. A number of researchers investigated the effect of hydro-mechanical characteristics of artificial soil-cemented samples by using various cement agents with different grain size distribution and density (Cuccovillo & Coop, 1999; Feda, 2022; Rotta et al., 2003; Yun & Santamarina, 2005; Kamruzzaman et al., 2009).

In this section of the dissertation, the main idea is to create clates in laboratory conditions by mixing of cement, with the natural soil obtained in the Campus Nord, UPC. The aim is to obtain fragments with different particles strength. It is difficult to find a particle by different ranges of stiffness in nature. Therefore, the artificial soil-cemented fragments were prepared to provide fragments strength between the ranges of rock and natural aggregates strength. Unconfined compressive strength tests, indirect tensile strength tests, determination of specific densities by paraffin, determination of the retention curve (WP4), and pore size distribution (MIP) test was carried out to characterize some of the main hydro-mechanical behaviours of artificial samples. It should be considered that the tests of this chapter have been done parallel with a master student Xavi Nonell Arellano (2015). To conclude, by understanding the perfect knowledge of these artificial fragments, the possible next use and future line of investigation especially as compacted material are described.

6.2 Cementation of soil

This section considers a brief clarity about cement composition and effect on soil cemented aggregates without extensively focusing on chemical issues.

6.2.1 Types of cement composition

By crushing, proportioning and milling of the materials that are shown in Table 6-1, cement is manufactured and cusses different oxides. The different types of cement oxide generated by the some materials are represented in Table 6-1. Moreover, the Portland cement as a cement type used in this investigation is made by blending an applicable mixture of limestone and clay or shale together, and by heating them to 1450°C in a rotary kiln.

Table 6-1: Various oxide of cement generated by the different materials (Neville, 1995).

Name	Material
Calcium oxide (CaO) (C)	limestone, chalk, shells, shale or calcareous rock
Silicon oxide (SiO ₂) (S)	sand, old bottles, clay or argillaceous rock
Aluminium oxide (Al ₂ O ₃) (A)	bauxite, recycled aluminium, clay
Iron oxide (Fe ₂ O ₃) (F)	clay, iron ore, scrap iron and fly ash
Gypsum, CaSO ₄ .2H ₂ O	found together with limestone

Regarding to typical oxides composition as follows: Calcium oxide (lime) CaO, silicon dioxide (silica) SiO₂, aluminium oxide (alumina) Al₂O₃, iron oxide Fe₂O₃, water H₂O, and sulphate SO₃. The basic components of cement are summarised in Table 6-2.

Table 6-2: Main compounds of cement (Neville, 1995).

Name of compound	Oxide composition	Abbreviation
Tricalcium silicate	3CaO.SiO ₂	(C3S)
Dicalcium silicate (the belita)	2CaO.SiO ₂	(C2S)
Dicalcium silicate	3CaO.Al ₂ O ₃	(C3A)
Tetracalcium aluminoferrite (or ferrite)	4CaO. Al ₂ O ₃ .Fe ₂ O ₃	(C4AF)

6.2.2 Volumetric characterization of cement hydration

By the addition of Portland cement several chemical reactions causing immediate and long-term changes to the soil. The most important are hydration and pozzolanic reactions. The hydration process is a complicated set of reactions between cement and water. With a hydration of the cement, the resistance increases, although its value depends on the size of the cement and the percentage of cement. According to the study of Neville (1995), the hydration of 100 gr mass of cement and volumetric processes are investigated.

Based on the following estimation the mass properties and diagram of the volumetric changes before and after hydration are presented in Table 6-3 and Figure 6-1, respectively. Some of the main conclusion are as follows:

- The specific gravity of dry cement is $31.5 \text{ kN} / \text{m}^3$.
- The specific gravity of the products of hydration in saturated condition is $21.6 \text{ kN} / \text{m}^3$.
- The mass of non-evaporable water is 23% of the mass of the dry cement.

Table 6-3: Mass properties of cement and water before and after of hydration process (Neville, 1995).

Mass of dry cement	100 g
Absolute volume of dry cement	31.8 ml
Weight of combined water	23 g
Volume of gel water	19 ml
Total water in the mix	42 ml
Water/cement ratio by mass	0.42
Water/cement ratio by volume	1.32
Volume of hydrated cement	67.9 ml
Original volume of cement and water	73.8 ml
Decrease in volume due to hydration	5.9 ml
Volume of products of hydration of 1 ml of dry cement	2.1 ml

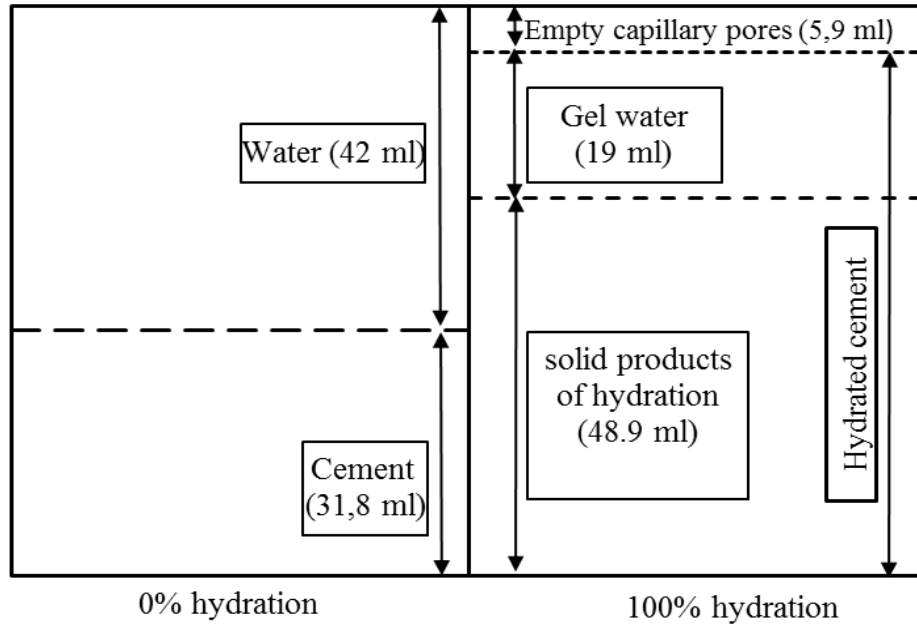


Figure 6-1: Volumetric quantities of water and cement, before and after hydration (Neville, 1995).

Effects of different water/cement ratio on hydration process are shown in Figure 6-2. It can be seen, how the volume of the hydrated cement increases, and how the volume occupied by water is replaced by hydration products.

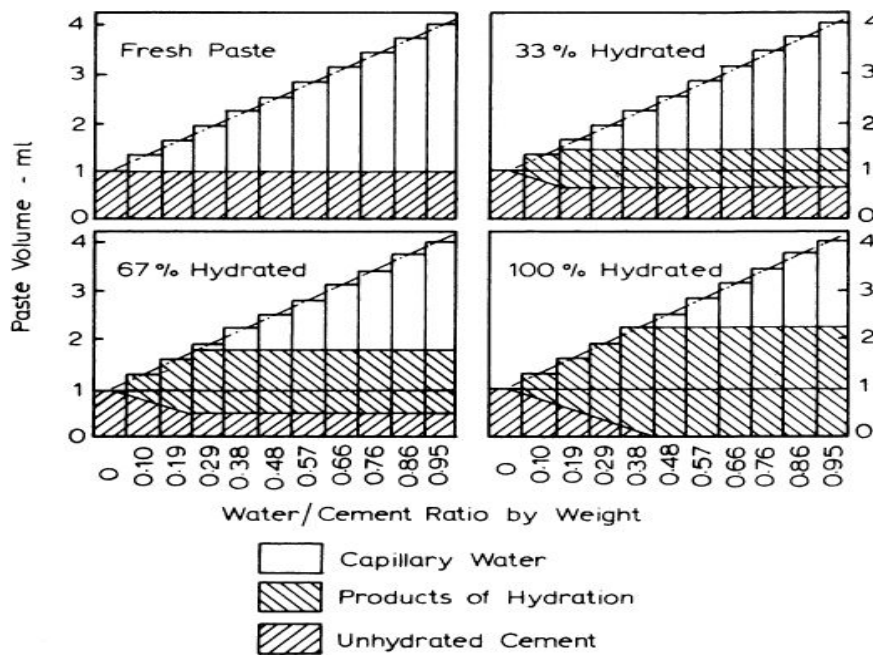


Figure 6-2: The progress of hydration regarding different stages of hydration and water/cement ratios (Neville, 1995).

6.2.3 Effect of cementation on mechanical behaviours of soil-cement mixtures

The number of interparticles contacts between cement bond and the strength of the bond are the main parameters to influence the microstructure of soil-cemented aggregates. An important part of the microstructure is represented by cementing bonds, which usually change the characteristics of cemented soils to characteristics of porous weak rocks (Leroueil & Vaughan, 1990). Also, the small amount of cement significantly increases the strength and the stiffness of soils (Boone & Lutenecker, 1997). Generally, the following parameters of cement are the major issues dealing with the mechanical behaviour of artificially cemented soils (Yun & Santamarina, 2005).

- The cement content.
- Types of the cementing agent.
- The grain size distribution.
- Curing time.
- Density.
- Cementation-stress history.

Ingles & Metcalf (1972) evaluated the effect of cement content on compression strength for several types of soils. They stabilized soil by Portland cement at the constant humidity and curing time. Figure 6-3 represents the effect of cement content on various types of soil strength. It can be observed, by increment the cement content the compressive strength increased for all types of soil.

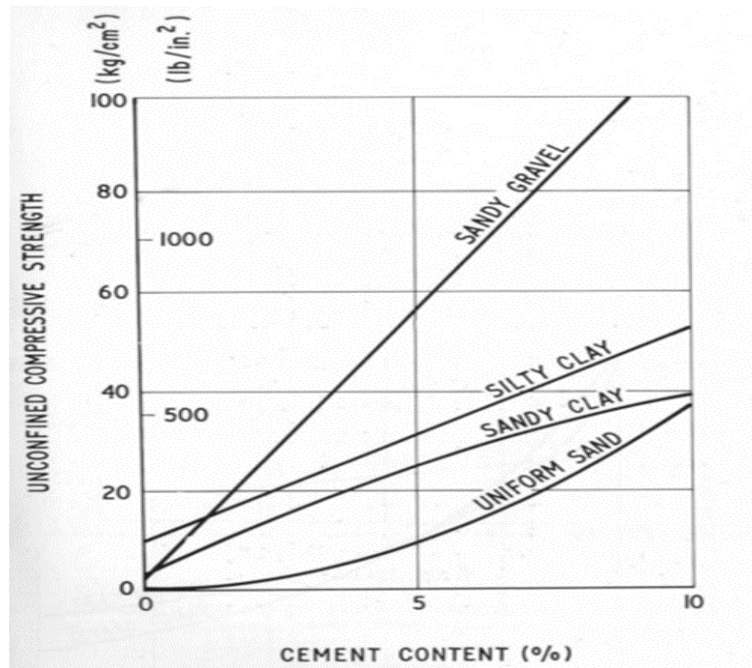


Figure 6-3: Effect of cement content on compression strength for several types of soils stabilized by Portland cement and cured for 7 days at 25 ° C and constant humidity (Ingles & Metcalf 1972).

Also, the resistance compression for different values of dry densities for stabilized clay with a cement content of 10% is depicted in Figure 6-4. The amount of strength increased by an increment of dry density.

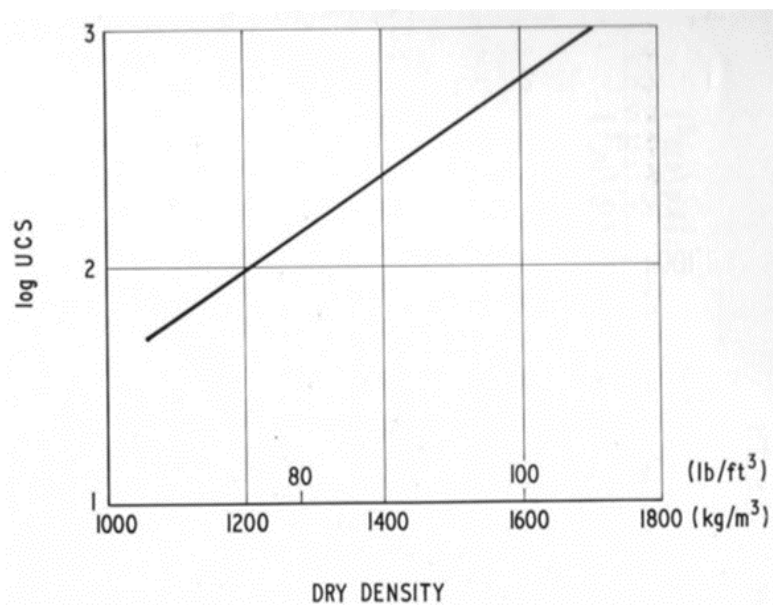


Figure 6-4: Effect of the dry density of mixtures on the resistance compression of stabilized clay with a cement content of 10% (Ingles & Metcalf 1972).

The relationship between the strength of concrete at different ages and fineness of cement are studied by (Neville, 1995). He obtained that, to have a rapid development of strength, high fineness content of cement is required. Finer cement content leads to a stronger reaction with soil aggregates. Also, by increasing the curing time the amount of strength increased. Figure 6-5 illustrates the relationship between the strength of concrete at different ages and fineness of cement (Neville, 1995).

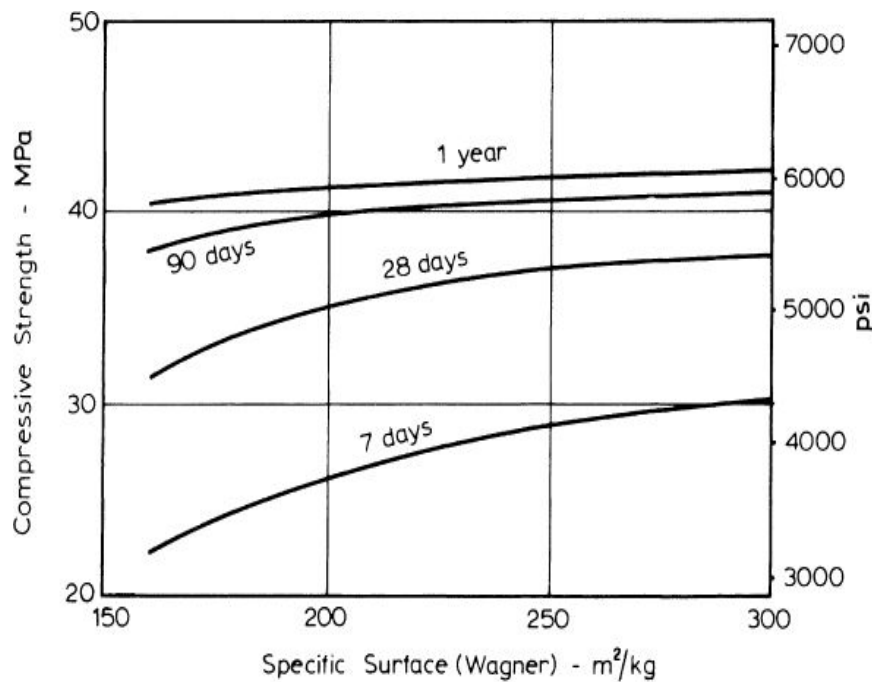


Figure 6-5: The relation between the strength of concrete at different ages and fineness of cement (Neville, 1995).

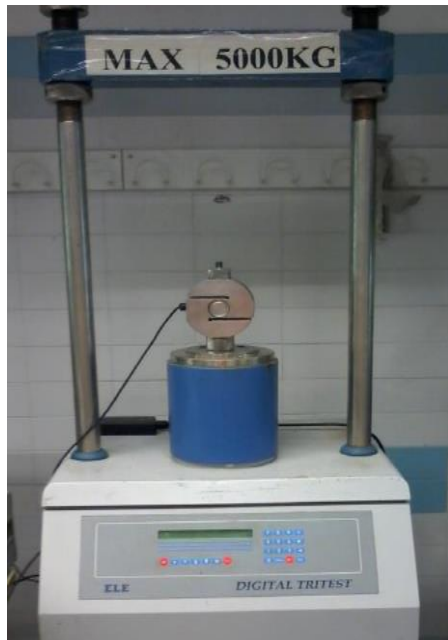
6.3 Artificial samples preparation method and available equipment

In order to have aggregates with different strengths and hydro-mechanical characterization to compare with natural fragments, artificially cemented specimens were created through the addition of a cementing agent to the soil. In this section, the procedure and material to prepare artificial samples and available equipment at UPC Geotechnical Laboratory will be described.

6.3.1 Materials and equipment used

For the purpose of fabricated artificial soil-cemented fragments, samples are prepared by combining available Barcelona silty clay particles less than 2 mm with distilled water and Portland cement. The cement is the Superdragon type of the company Cements Molins.

It is a Portland CEM I 52.5 R, and its physical and chemical properties are described in chapter 3. Static compaction was carried out to compact soil-cement mixtures. The available equipment for static compaction and several cells to provide specimens are described in Figure 6-6 and Figure 6-7, respectively.



(a)



(b)

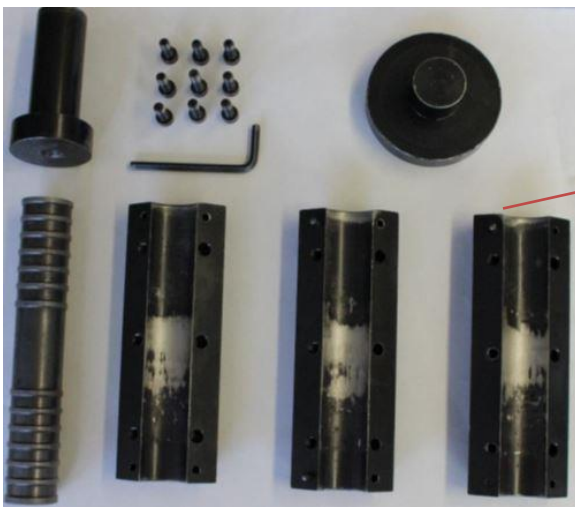


(c)

Figure 6-6: Available static compaction equipment at UPC Geotechnical Laboratory, (a) Tritest 100 press with a capacity of 5 tons, (b) Wykeham France press with a capacity of 5 tons, (c) hydraulic press with a capacity of 50 tons.



Diameter of mould: 33 mm
Height of mould: (variable)



Diameter of mould: 38 mm
Height of mould: (variable)



Diameter of mould: 151 mm
Height of mould: (variable) mm

Figure 6-7: Provided cells and moulds to compact artificial fragments at UPC Geotechnical Laboratory.

According to Figure 6-8, the static compaction machines with capacity of 5 tons (types of a and b) are chosen to compact material with density of 17 kN/m^3 , whereas, in order to fabricate sample with higher density close to 21 kN/m^3 , the machine with high capacity of 50 tons are selected to reach the higher value of density. Figure 6-8 shows the load applied to compact both samples with a low and high value of density at the same ratio of compacted time.

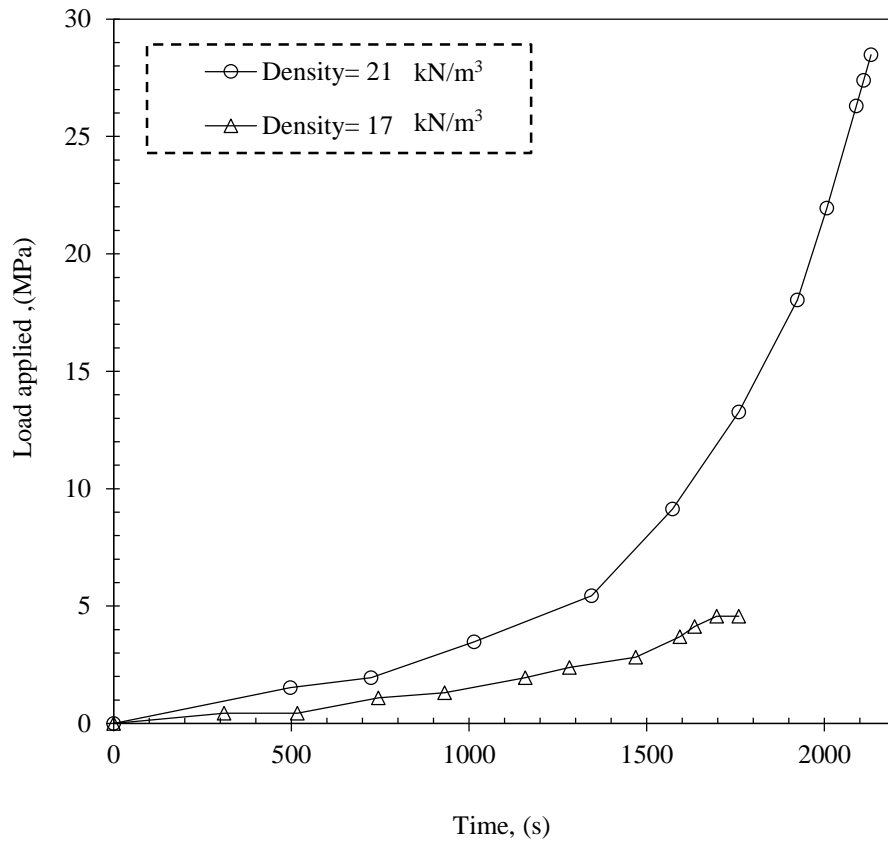


Figure 6-8: Compaction loads versus time for different dry densities of samples.

In this investigation, the unconfined strength test, determination of specific densities by paraffin, tensile strength test, mercury intrusion porosimetry and water retention characterization (WP4) are provided to evaluate the hydro-mechanical behaviour of artificial soil-cemented fragments. The description of each test and equipment are included in chapter 3. Also, the idea to use different cell sizes and static compaction procedure will be described in next section.

6.3.2 Method to prepare artificial soil-cemented samples

In order to have various cement proportions in the soil-cement mixture for a constant dry unit weight in the case of the same volume of mould, the equation 6-1 and equation 6-2 were selected to determine the mass of soil and cement in the mixtures.

$$M_{\text{soil}} = \left(\frac{100}{100+C} \right) M_{\text{total}} \quad \text{Equation 6-1}$$

$$M_{\text{cement}} = \left(\frac{C}{100+C} \right) M_{\text{total}} \quad \text{Equation 6-2}$$

Where;

M_{soil} = Mass of the soil.

M_{cement} = Mass of the cement.

M_{total} = Mass of the soil (M_{soil}) + mass of the cement (M_{cement}).

C= percent of cement.

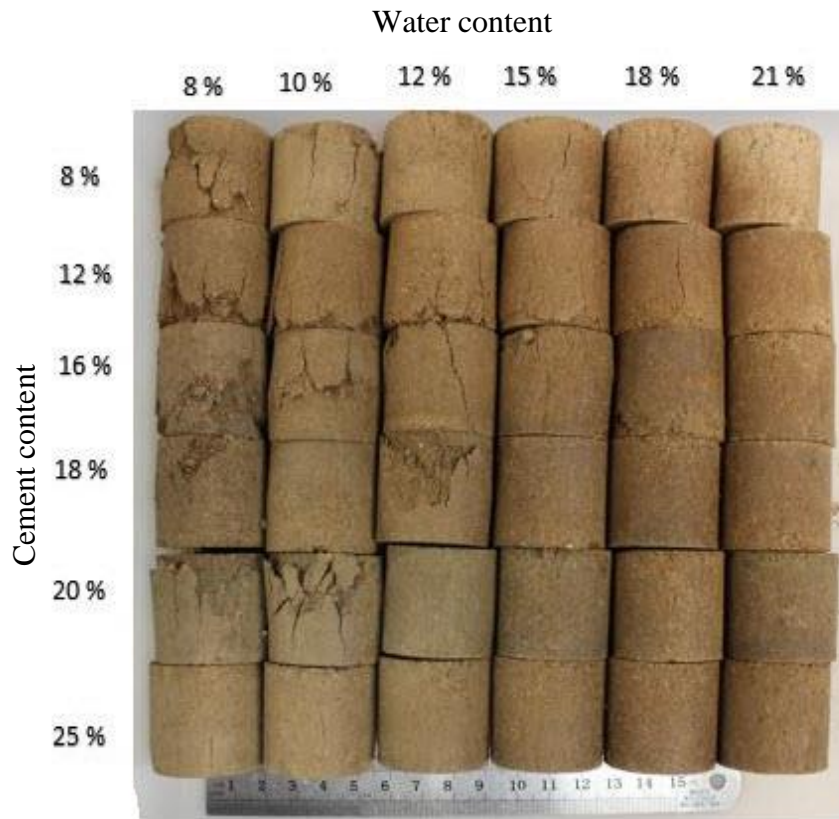
It should be considered that following conditions are provided during the sample preparation:

- During the compaction, the load applied to the mould is controlled by the constant strain (compaction ratios ranged of 0.5 to 1 mm/min are selected as a very slow ratio, to keep water in the system and allow contributed suitable in the mixtures).
- The soil, cement, and water are blended as possible as much to have a homogenous mixture.
- By application of lubricant is tried to reduce the friction between wall and piston during compaction.

6.3.3 Selection of samples for experimental work

At the beginning of the decision to fabricate aggregates with cement and soil, the initial samples were prepared at various cement percents and water contents in a mould with diameter and height of 33 mm. The density was kept constant for all samples equal to 17 kN/m³. The compression tests have been selected to understand the resistance behaviour of total samples for 7 days curing. Figure 6-9 depicts 36 specimens with various cement ratios, water contents, and degree of saturation after the compression test. Moreover, the

amount of water for cement hydration process($M_{w_{ch}}$) were calculated by considering that, the saturation water content for microstructure of the soil fragments is approximately 7.4 %. This water is not combined with cement and will not have effect to the hydration process. The amount of available water for hydration of various specimens are displayed in Table 6-5. The relationship between resistance and available water for hydration are presented in Figure 6-10.



		Water-%					
		8	10	12	15	18	21
		S _r - (%)					
Cement- %	8	36.7	45.9	55.2	69.1	83	96.9
	12	36.4	45.6	54.7	68.5	82.3	96.1
	16	36.1	45.2	54.3	68	81.6	95.3
	18	36	45	54.1	67.7	81.3	94.9
	20	35.8	44.9	53.9	67.5	81	94.6
	25	35.5	44.5	53.5	66.9	80	93.8

Figure 6-9: Specimens with several cement and water contents after the compression.

Table 6-4: The amount of available water for hydration of various specimens.

Mc/Ms (%)	8	12	16	18	20	25
Mw/Ms+c (%)	Mw _{ch} /Mc (%)					
8	16	13	12	11	11	10
10	43	32	26	24	23	20
12	70	50	41	38	35	30
15	110	78	63	57	53	45
18	151	106	84	77	71	60
21	191	134	106	97	89	75

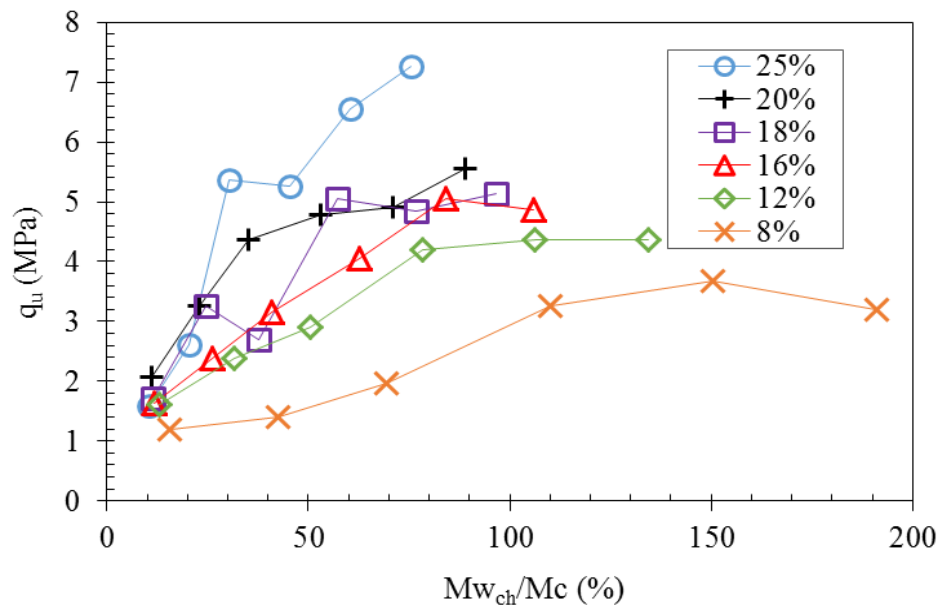


Figure 6-10: The relationship between resistance and available water for hydration of cement-samples with dry density of 17 kN/m³.

According to Figure 6-10 it was decided to select samples with 8 and 25 percent of cement (Ms/Mc) and the available water for hydration of cement (Mw_{ch}/Mc) around 70 % for future experimental work. The 8 and 25 percent represented the specimen with low and high cement content with suitable water for hydration process. It should be noted that the minimum water mass needed for the hydration of cement is 38% compared to that of dry cement (Neville, 1995). It should be considered that the selected specimens are not sufficient to represent the behaviour of artificial fragments. Therefore, 7 more cases are

provided for the constant density of 17 kN/m^3 and degree of saturation 0.85 with low to high cement content as shown in Figure 6-11. It is clear, by increasing in cement/soil ratio the resistance increased. Although the 60% cement content has an erroneous value due to the surface deformation of the sample. Finally, a mass percentage of the cement with respect to the soil of 80% is chosen, as the type of mixture with greater resistance and the specific dry weight of 17 kN / m^3 , but it was decided to take into account a larger degree of saturation ($S_r=95\%$), to ensure the complete saturation.

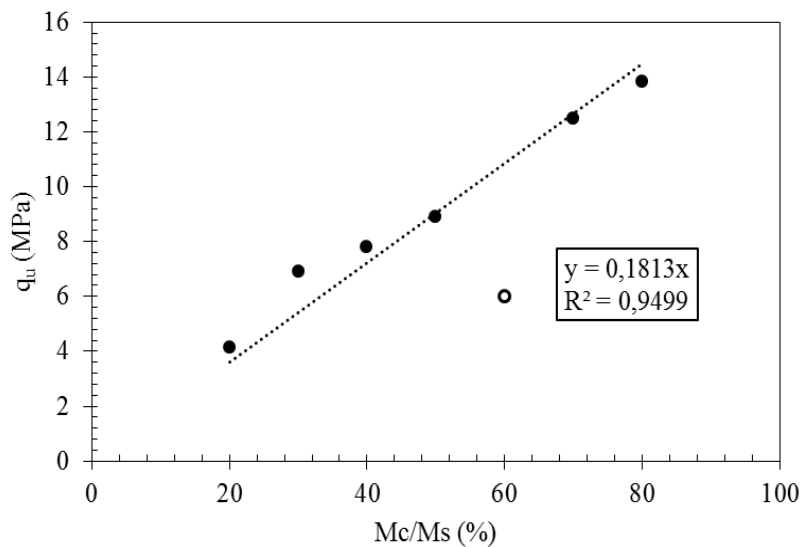

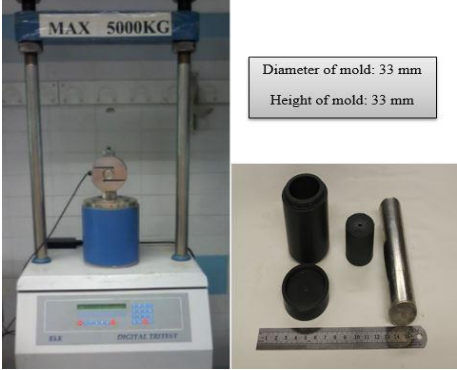

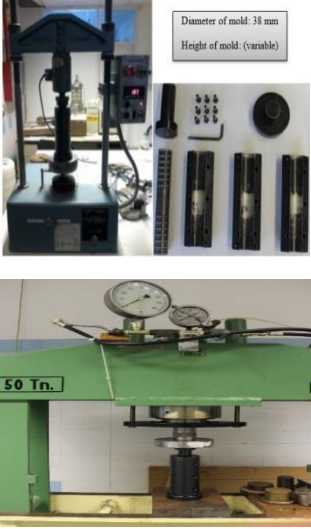




Figure 6-11: Compressive strength of mixtures with a S_r of 85% and different mass ratios between cement and dry soil.

At the end, it was decided to manufacture two more types of samples to compare artificial fragments with natural one. Samples are made with a density of 21 kN/m^3 which are similar to Barcelona silty clay carbonated fragments. A cement content of 2% with a degree of saturation of 80% and a cement content of 4% with a degree of saturation of 90% were chosen for this new density. Thus, finally, five samples with different dosages are selected (17-8, 17-25, 17-80, 21-2, 21-4) to evaluated hydro-mechanical behaviour of soil-cemented samples. The first part of the notation is referred to specific dry density and the second one is the percentage of the mass of the cement over the mass of the dry soil. The mixtures have been made in a mould with a diameter of 38 mm and height of 77 mm. Also, the height of samples can be altered by utilizing the steel pads on top of the mould during compaction. The static compaction has been chosen to compact samples with different dry densities. Table 6-5 demonstrates the selected samples regarding the types of experimental program and equipment.

Table 6-5: Selected samples regarding the types of experimental program and equipment to compact samples.

Sample	Equipment to compact sample (cell + static compaction device)	Experimental work on sample
<p>36 specimens</p> 		<ul style="list-style-type: none"> • Unconfined compression test
<p>17-8, 17-25, 17-80, 21-2, 21-4</p> 		<ul style="list-style-type: none"> • Unconfined compression test • Density analysis by paraffin and pycnometer • Tensile strength • MIP • Suction measurements
<p>21-4</p> 		<ul style="list-style-type: none"> • Experimental work on compacted 'all-one' mixtures

6.4 Fabric of soil cemented fragments

6.4.1 Volumetric phases of samples before and after of cement hydration

Five types of the mixtures have been manufactured to define the volumetric phases of samples before and after of the cement hydration process. The samples are 17-8, 17-25, 17-80, 21-2 and 21-4.

For the purpose of volumetric analysis following conditions (Neville, 1995) and properties were considered:

- The cement as a dry and fine material reacts with water but the effect of hydration velocity on volumetric properties are not specified.
- The water of samples will divide to water that reacts with cement and the water that goes to the microstructure of the soil and the rest of water goes randomly to the pores of the samples in the form of free capillary water.
- The specific gravity of the soil solids has a value between 26.6 and 27 kN/m³.
- The specific density of cement is equal to 31 kN/m³.
- The specific weight of the water is 9.8 kN/m³.
- The minimum ratio of masses between the cement and the water which it reacts (a / c) is 0.38.
- Saturation water content of the microstructure of the silty clay of Barcelona is approximately 0.74 % (w micro=0.74%) (Romero, 2013).
- The hydrated cement has a porosity of about 28 - 34%.
- A portion of the water reacted with the cement does not evaporate at 110 ° C (23% of the dry cement mass).
- The volumetric changes of samples 17-8, 17-21, and 17-80 before and after hydration are displayed in Figure 6-12 and Figure 6-13. Additionally, the volumetric changes of samples 21-2 and 21-4 are presented in Figure 6-14 and Figure 6-15.

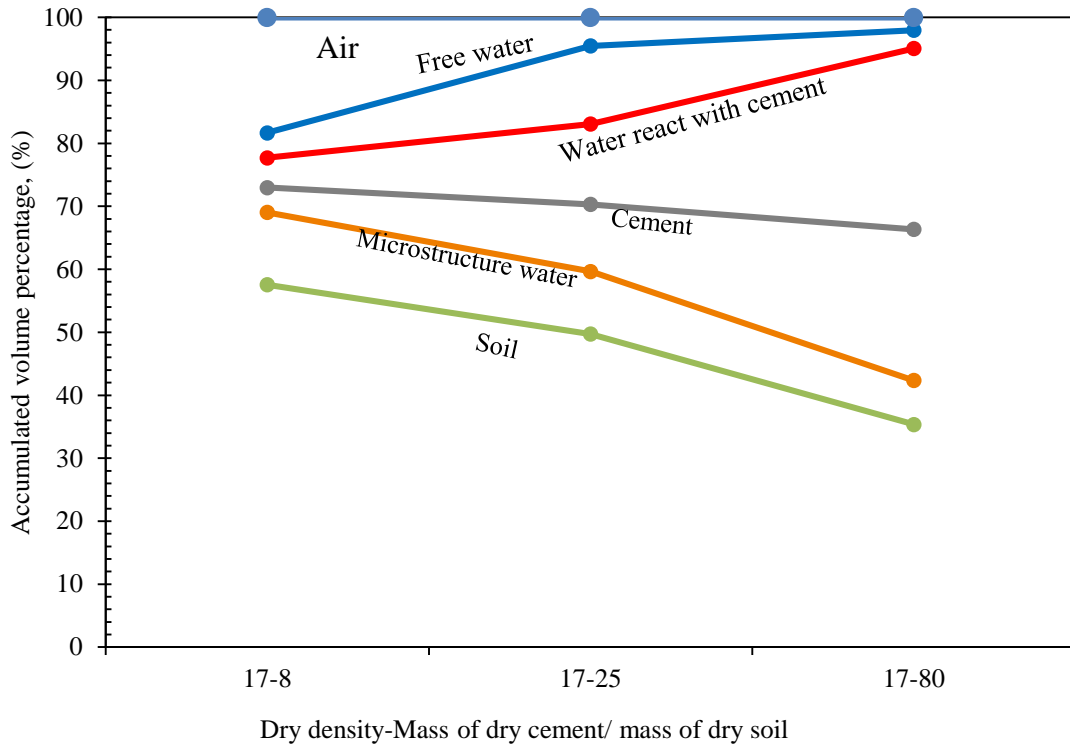


Figure 6-12: Volumetric properties of samples with a density of 17 kN/m³ before hydration.

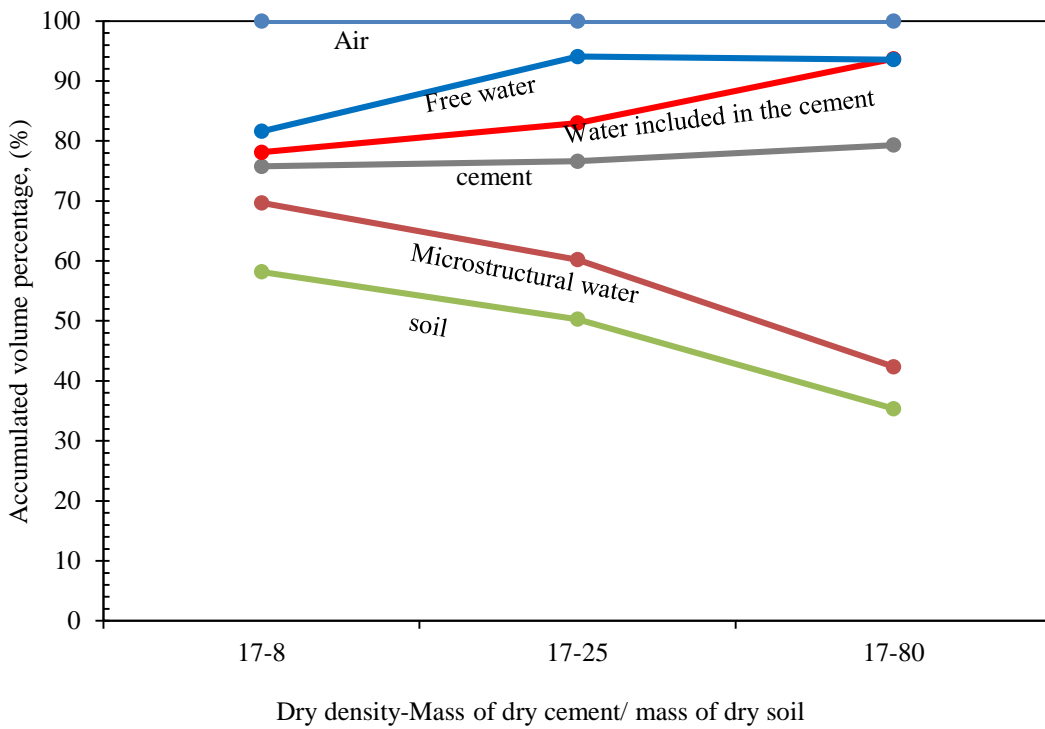


Figure 6-13: Volumetric properties of samples with a density of 17 kN/m³ after hydration.

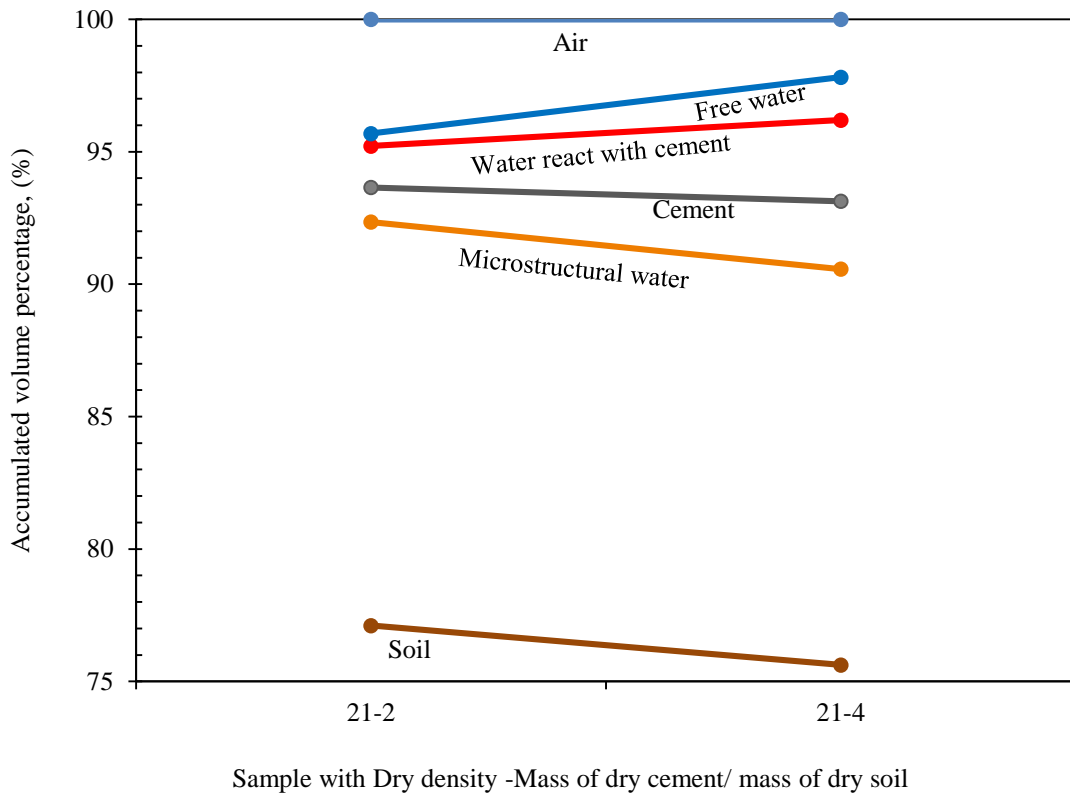


Figure 6-14: Volumetric properties of samples with a density of 21 kN/m³ before hydration.

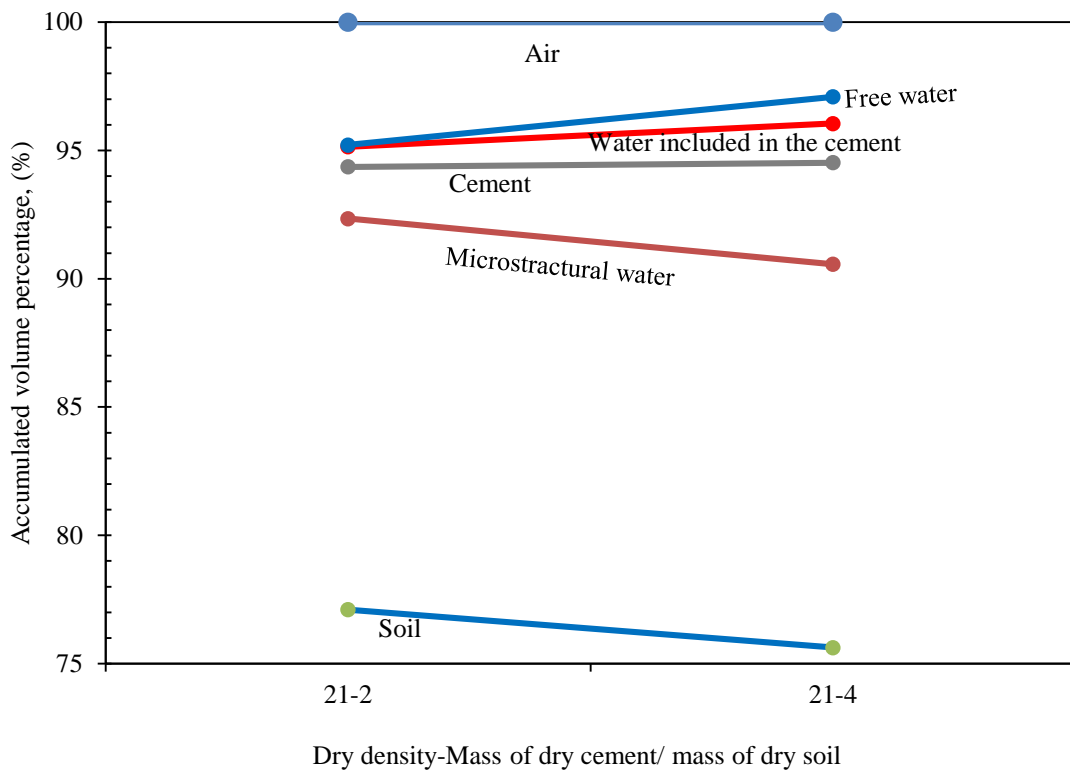


Figure 6-15: Volumetric properties of samples with a density of 21 kN/m³ after hydration.

It has been considered that the cement acts on its own volume, without affecting the volume and properties of the soil. In addition, a porosity of the cement paste is established, and it is separated between the part corresponding to the solids coming from the hydration and that corresponding to the reacted water, included inside the paste or in the capillary pores between crystals of solid and hydrous.

6.4.2 Determination of specific densities by paraffin method

In order to assess the density by paraffin, five samples are selected and compared to densities specified to compact samples before the test. The comparison results are shown in Figure 6-16. The results display that the differences between densities obtain by paraffin and the one that sample is decided to design is considered as admissible and they do not influence the calculation of experimental study.

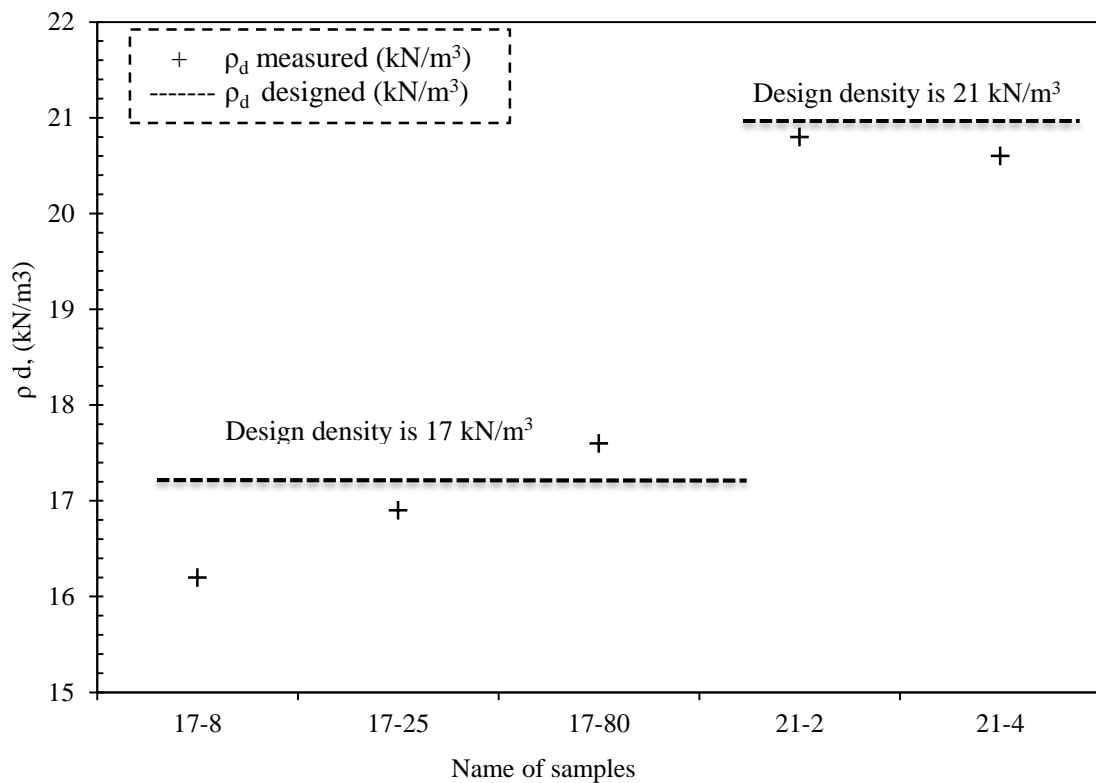


Figure 6-16: Comparison between the dry densities obtained experimentally and the design values proposed.

6.4.3 Microphotography of fragments

In order to do the microphotography, the picture of each sample will be taken by a camera Canon model 600d with lens 18-55 mm under adequate light and micro condition at Geotechnical Laboratory of UPC. The available equipment is shown in Figure 6-17. Reverse ring technique is used to obtained micro photos. The results of microphotography are shown in Figure 6-18 and Figure 6-19. It is clear that the cement is distributed uniformly on the samples.



Figure 6-17: Available microphotography devices available at UPC Geotechnical Laboratory.

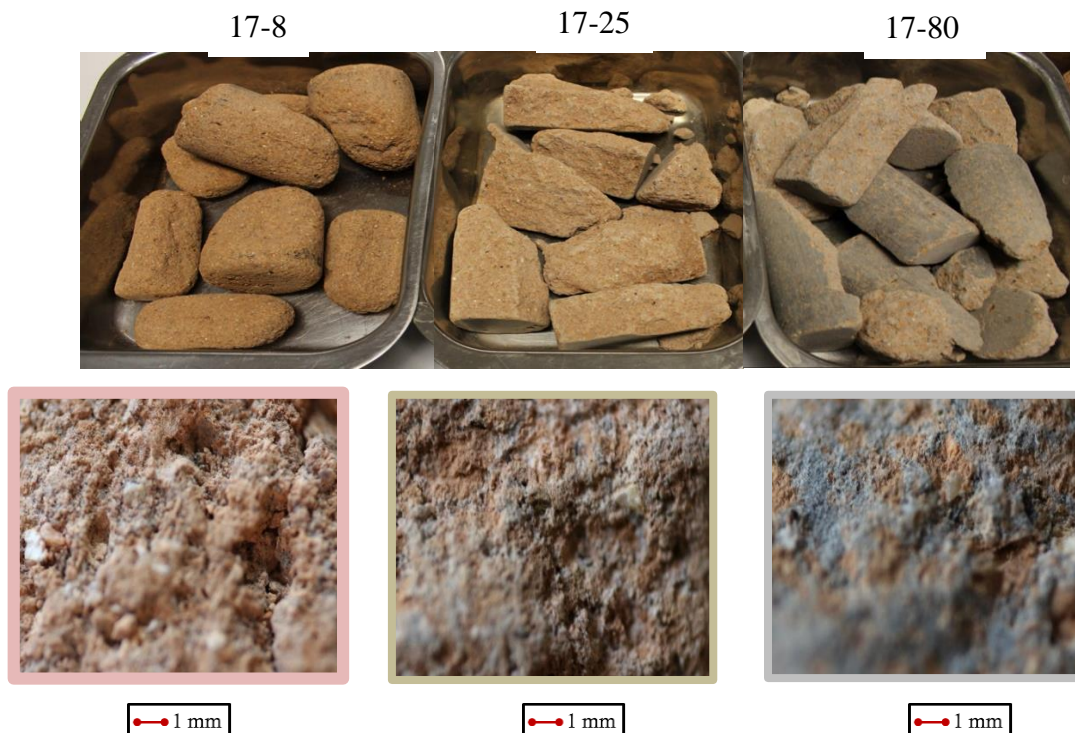


Figure 6-18: Microphotography of samples with density of 17 kN/m^3 .

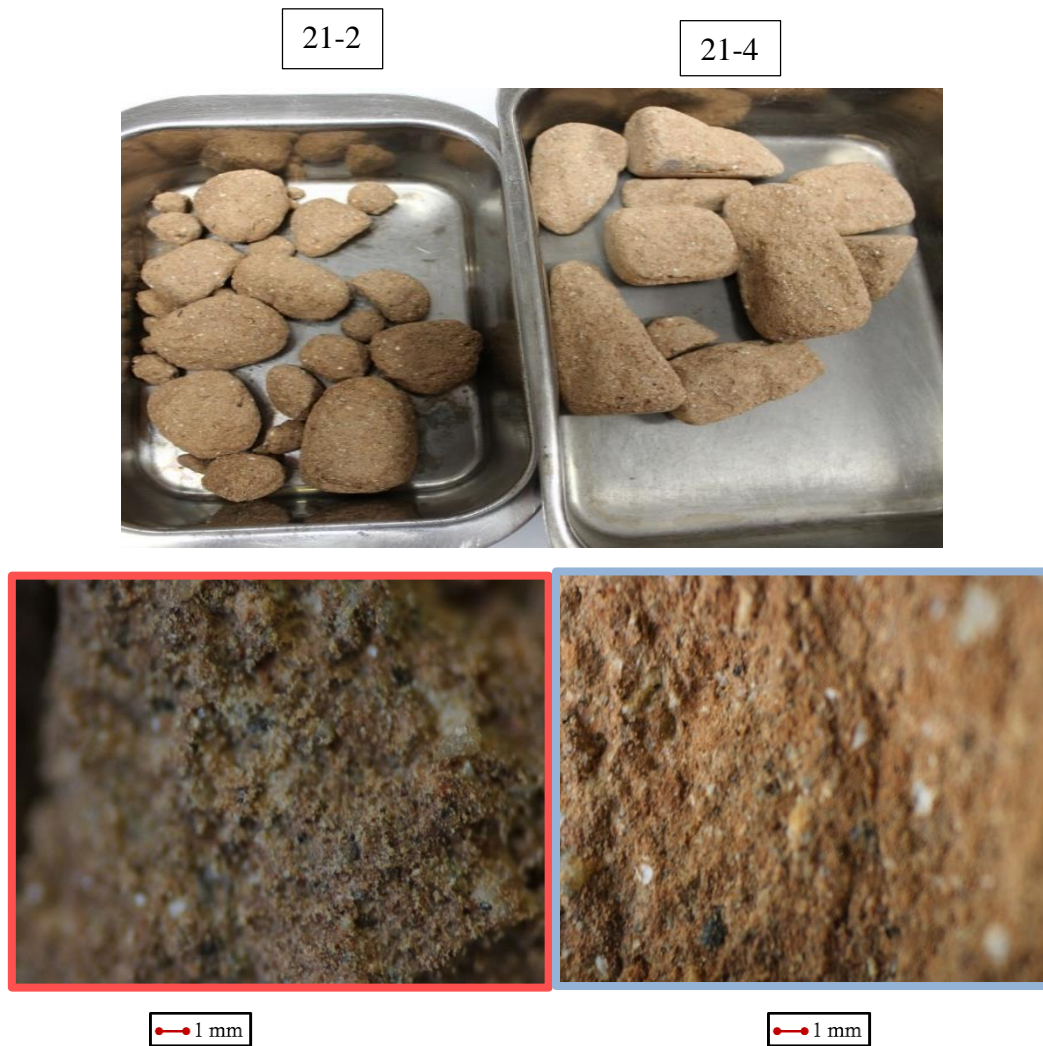


Figure 6-19: Microphotography of samples with density of 21 kN/m^3 .

6.4.4 Pore size distributions

Mercury intrusion porosimetry test has been selected to describe the porosimetry analyses of samples 17-8 and 17-25. Figure 6-20 and Figure 6-21 present the results of mercury intrusion test on both samples, the MIP test analysis of Barcelona silty clay fragments in order to compare by artificial aggregates are displayed in Figure 6-20. It can be seen that, by increasing the cement content the macrostructure of soil and mixture is reduced.

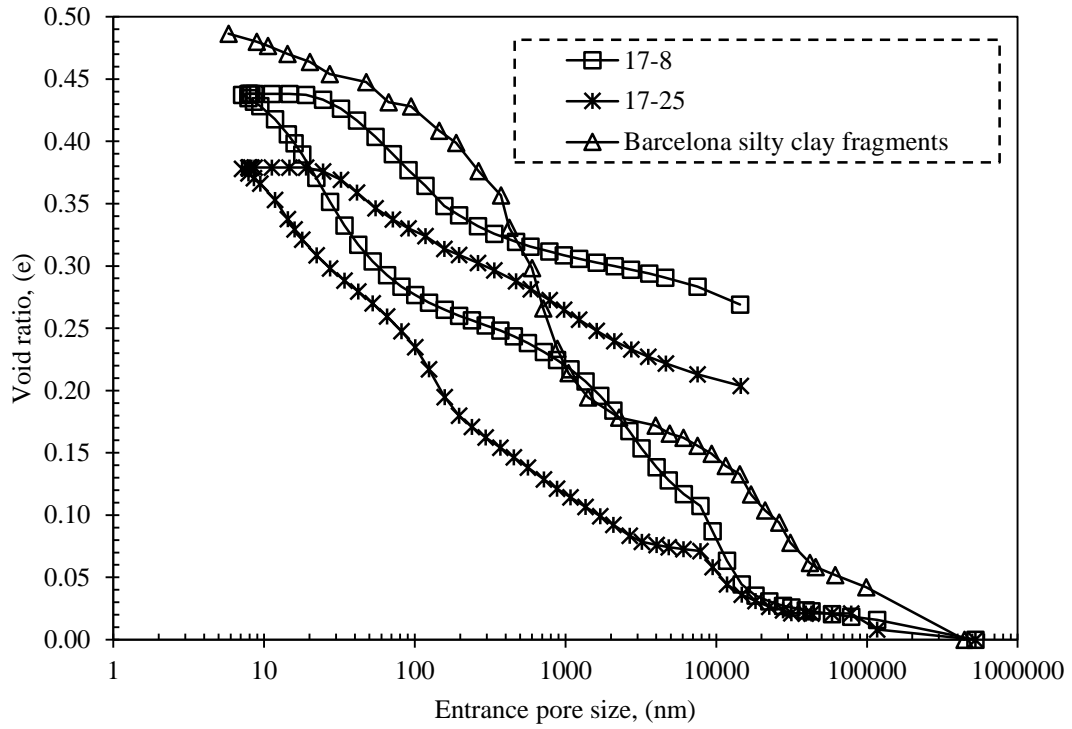


Figure 6-20: MIP results of two samples and comparison with Barcelona fragments.

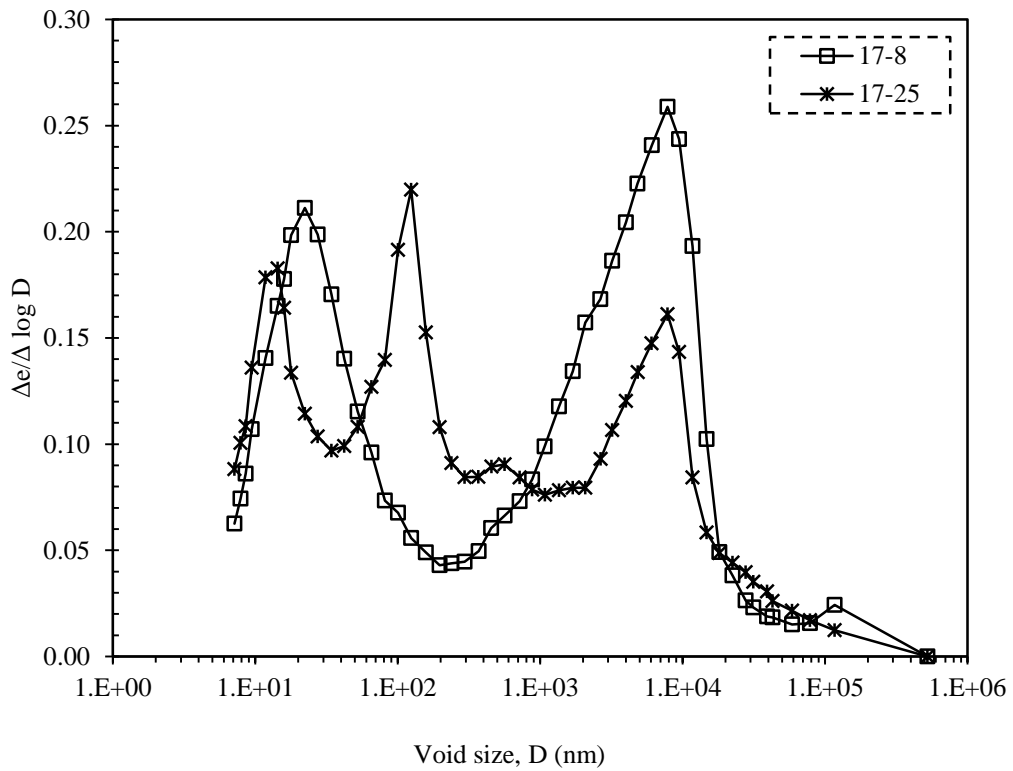


Figure 6-21: MIP results of two samples.

6.5 Mechanical behaviour of artificial samples

6.5.1 Introduction

The unconfined compression related to curing and water content, elastic modulus and tensile strength tests are carried out to assess the mechanical characterization of samples 17-8, 17-25, 17-80, 21-2, and 21-4.

6.5.2 Unconfined compression strength

In order to see the effect of curing time on compressive strength the resistance of samples are evaluated in various times curing to reach the final amount of 30 days. The results are displayed in Figure 6-22. It can be seen that after 7 days curing there was no significant increase occurred in the resistance of the samples, therefore, it is possible to take samples after 7 days curing for future experimental work, in order to well organize the time.

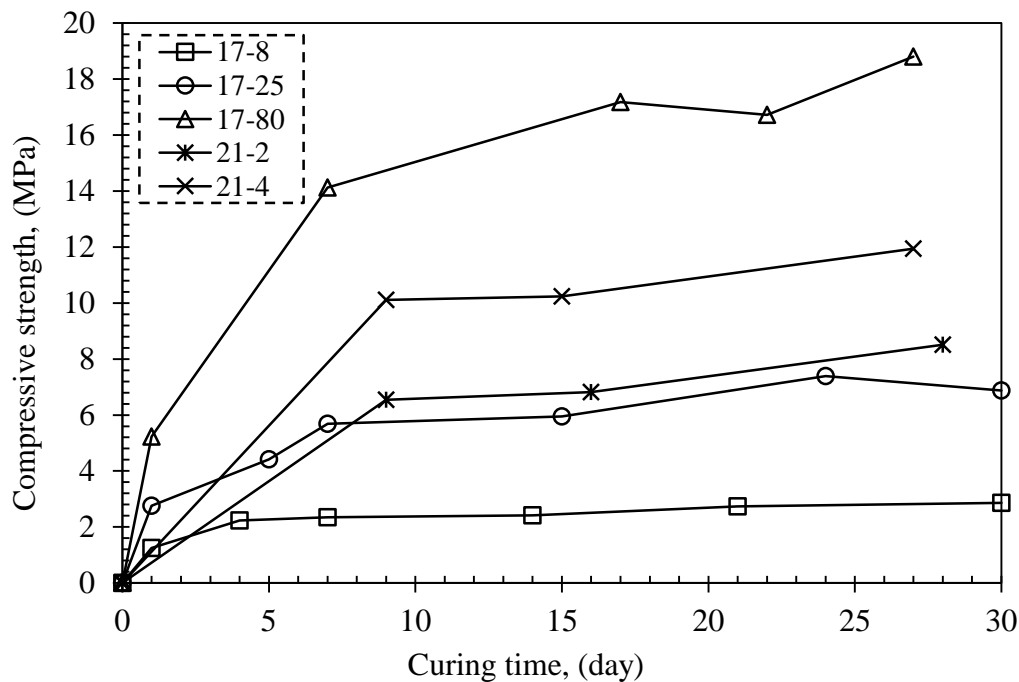


Figure 6-22: Compressive strength versus curing time for different samples.

Additionally, the relationship between of water contents and degree of saturation of each samples on compressive strength are presented in Figure 6-23. The results determined that by increasing the amount of dry density and cement content in specimens the resistance of soil-cemented fragments increased.

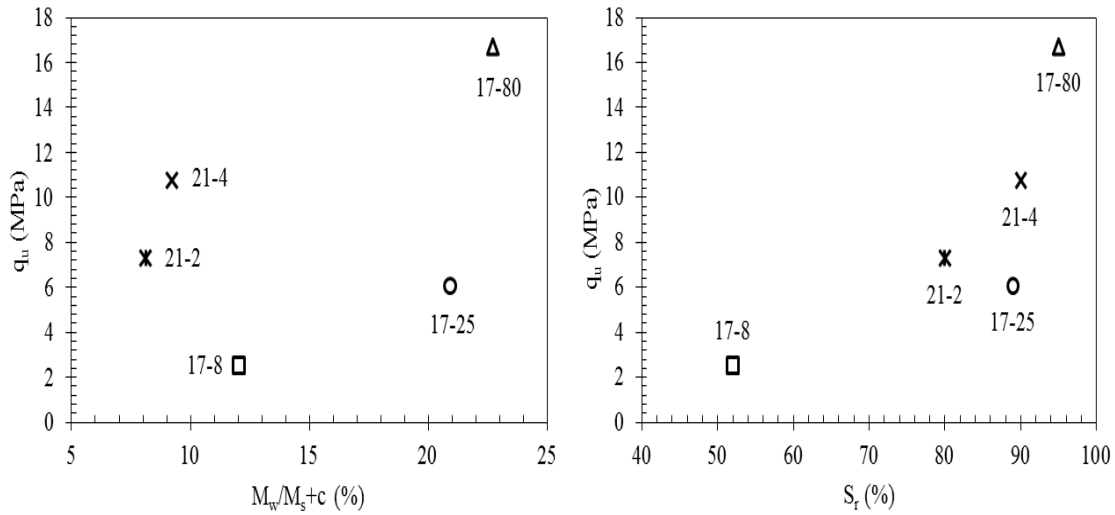


Figure 6-23: relationship between of water contents and degree of saturation with compressive strength.

6.5.3 Elastic modulus

Young modulus of the samples 17-8, 17-25, 17-80, 21-2, and 21-4 is calculated with the data obtained from applied load and vertical deformation of the samples. The values provided by a load cell and a LVDT. The relationship between compression resistance and deformation modulus and slopes are set out in Figure 6-24. Actually, the modulus of all samples are similar for the sample with high cement content.

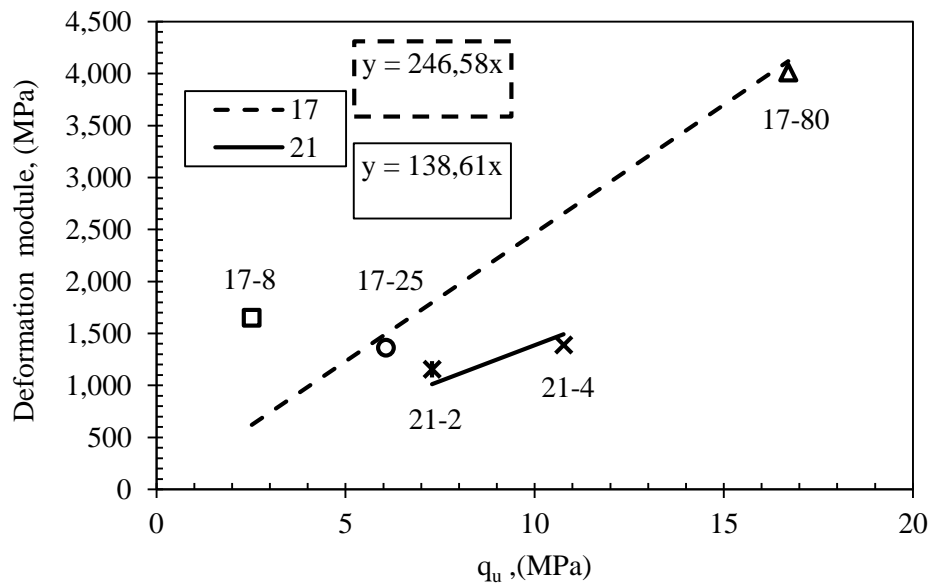


Figure 6-24: The relationship between compression resistance and deformation modulus.

6.5.4 Tensile strength

In this section, the relationship between indirect tensile strength and compressive strength and correlations for samples 17-8, 17-25, 17-80, 21-2, and 21-4 are presented.

The results of the correlation between tensile and compressive strength are displayed in Figure 6-25. It can be seen, tensile strength can be obtained by 13 % and 10 % of compressive strength for samples with a density of 17 kN/m³ and 21 kN/m³, respectively.

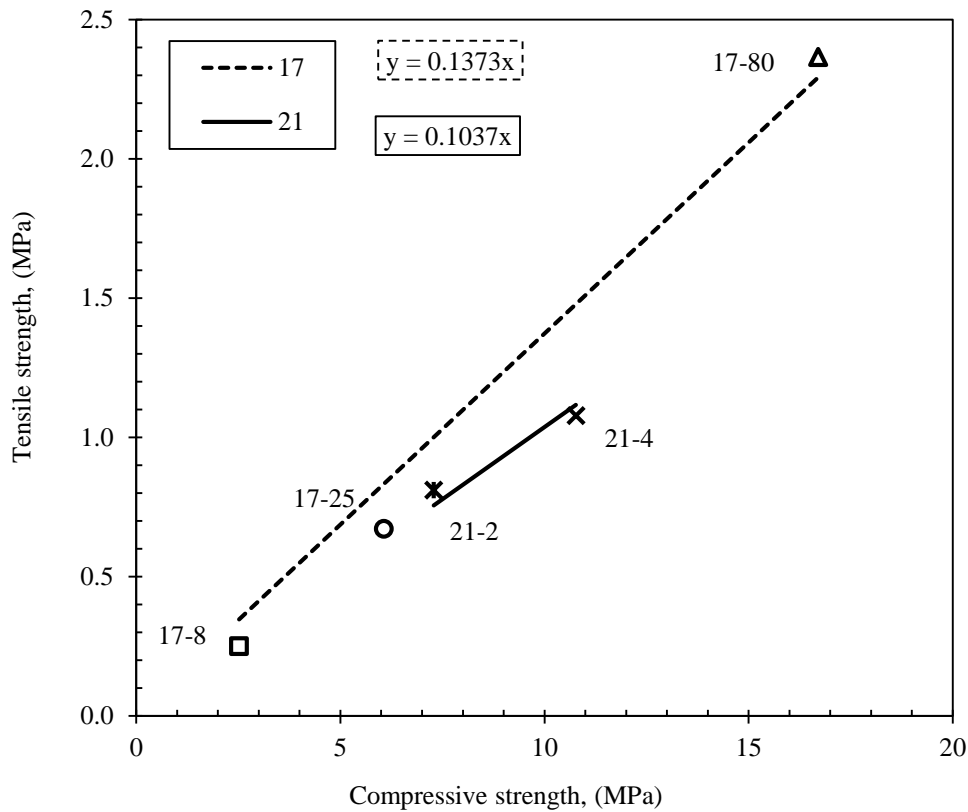


Figure 6-25: Relationship between indirect tensile strength and compressive strength.

In addition, Figure 6-26 provides the combination of resistance results to the mass of cement content respect to the mass of the dry soil. It is apparent that when both resistances are grouped in different axis have linear trend for each density of samples.

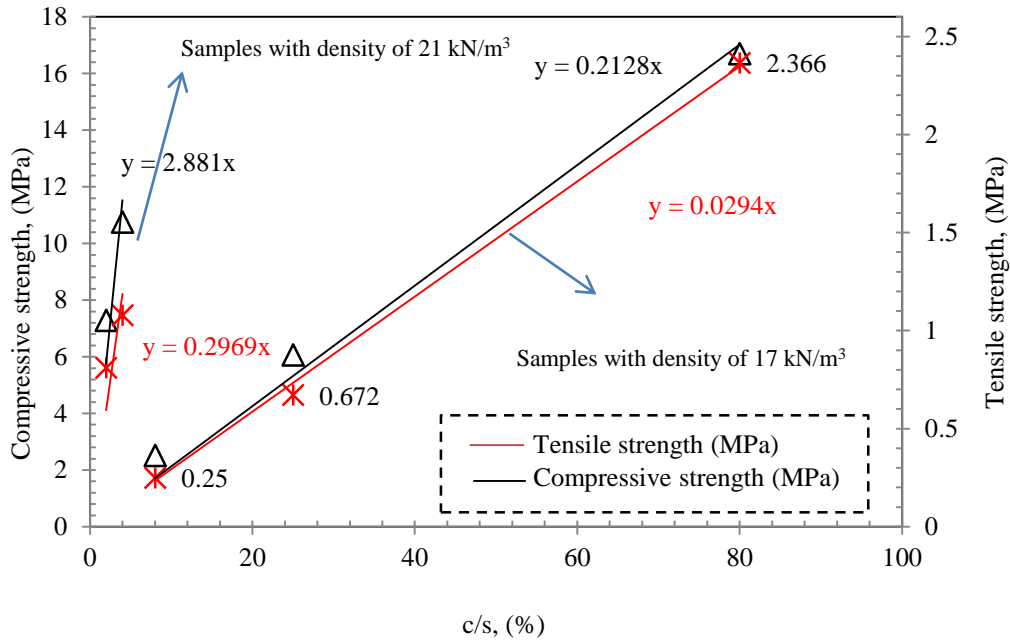


Figure 6-26: Tensile and compressive resistance in case of several cement/soil ratios.

6.6 Water retention curves

A dew point psychrometer was used to determine the behaviour of the retention curve for five different samples (17-8, 17-25, 17-80, 21-2, and 21-4). The results obtained for the drying path are shown in Figure 6-27, in the wetting path it has not been possible to reach maximum saturation due to the limit range of the equipment. When the soil samples are completely dry, the suctions tend to have a values of 1000 MPa, therefore, the lines plotted in Figure 6-27 are an approximation. The effect of dry density (porosity) in the retention characteristics of the samples is clear.

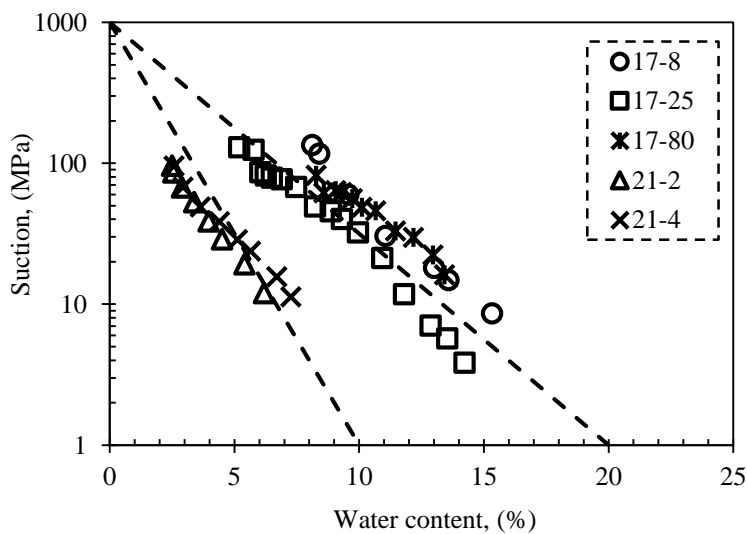


Figure 6-27: Retention curves on drying at different densities and cement/soil ratio.

In addition, fitting parameters of the retention curves in term of degree of saturation the five specimens, according to a single equation, and the Excel Solver tool have been analysed. The adjustments provided according to a logarithmic line and the van Genuchten model (van Genuchten 1980), which can be seen in Figures 6-28 and 6-29, respectively.

Based on logarithmic adjustment values are presented as a function of the degree of saturation as shown in equation 6-1 and equation 6-2.

$$\psi = e^{(A*S_r+B)} \quad \text{Equation 6-1}$$

$$S_r = [\ln(\psi) - B]A \quad \text{Equation 6-2}$$

Where,

Ψ = Suction.

S_r = Degree of saturation.

A and B = Fitting parameters.

According to van Genuchten's model data were fitted based on α and n_v (equation 6-3).

$$S_r = \left[\frac{1}{1+(\alpha*\psi)^{n_v}} \right]^{(1-\frac{1}{n_v})} \quad \text{Equation 6-3}$$

Where,

Ψ = Suction.

S_r = Degree of saturation.

n_v and α = Fitting parameters.

In addition, the value of the degree of saturation was adjusted as a function of saturation water content of approximately 20% for samples with a specific dry weight of 17 kN/m³ and 10% for samples of 21 kN/m³, based on equation 6-4.

$$S_r = \frac{\omega}{\omega_{sat}} \quad \text{Equation 6-4}$$

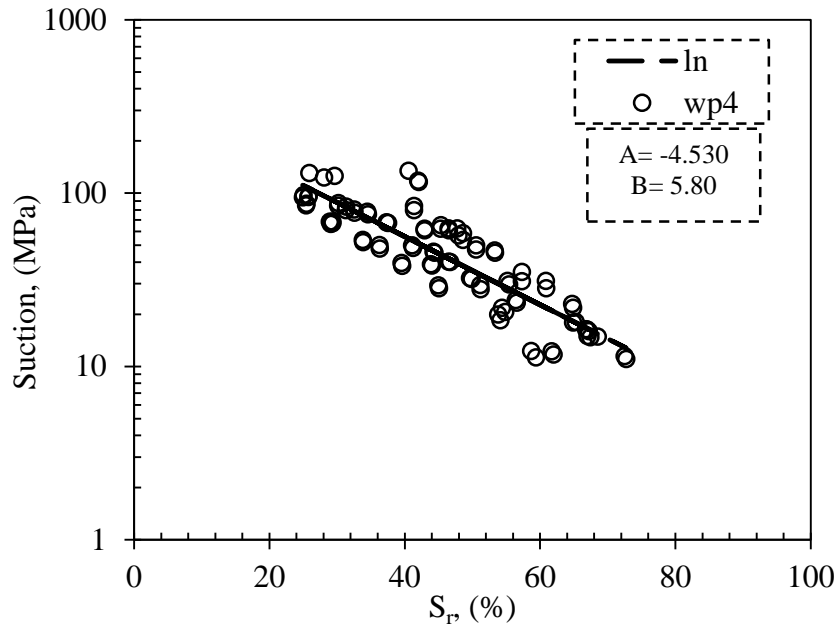


Figure 6-28: Water retention curve by WP4 and logarithmic fitting.

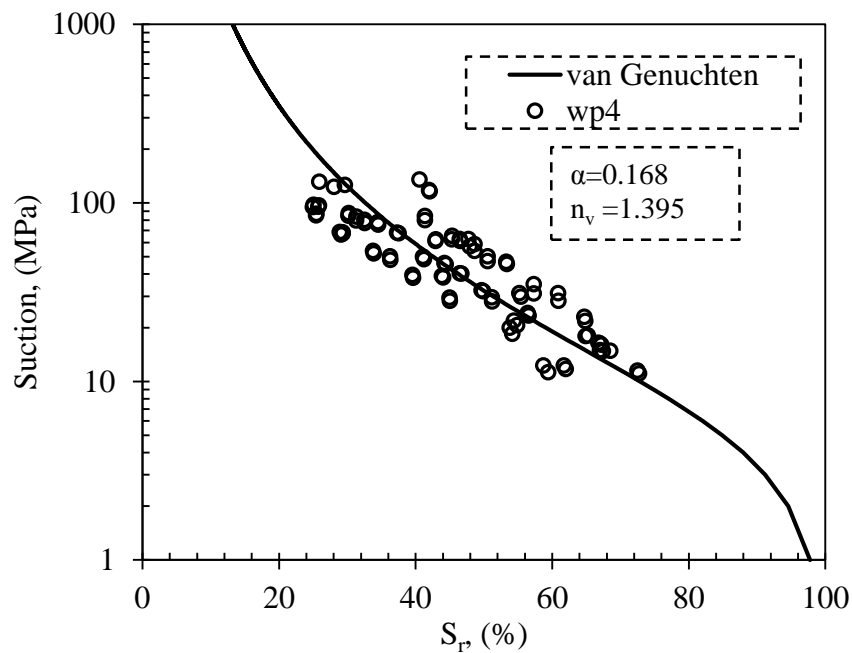


Figure 6-29: Water retention curve by WP4 and van Genuchten fitting.

The water retention curves are affected by dry densities, so the behaviours are divided into their dry densities properties. In addition, by increment, the cement content the pore size and water content decreased causes increasing in suction. In case of the samples 21-2 and 21-4 for the same suction the water content decreased for sample with less cement content. In the case of the dry density of 17 kN/m³ this effect is not clear.

7 Hydro-mechanical tests

7.1 Oedometer test in dry condition

7.1.1 Introduction

The fundamental characteristics of the hydro-mechanical behaviour of samples under oedometric conditions are described in this section. The dynamic compaction energy (596 kJ/m³) was selected to compact material before oedometer test, 10 % of water content added to the matrix part before dynamic compaction. The main properties of various samples after compaction are as follows: (Matrix, $\rho=1.72$ Mg/m³, $e=0.578$ and $S_r=0.430$; FN, $\rho=1.68$ Mg/m³, $e=0.594$ and $S_r=0.309$; FA, $\rho=1.71$ Mg/m³, $e=0.572$ and $S_r=0.354$; FS, $\rho=1.80$ Mg/m³, $e=0.522$ and $S_r=0.383$). The most relevant properties, such as compressibility, preconsolidation pressure, and confined modulus have been established. Breakage and fractal analysis are selected to do a microstructural evaluation of the soil specimens after each test. In addition, the concept of energy dissipation has been analysed during dynamic compaction and oedometer conditions.

7.1.2 Compressibility, preconsolidation pressure, and elastic modulus analysis

At oedometer condition, a total vertical stress of 1.9 MPa was continuously applied to the samples pure matrix, FN, FA, and FS. Experimental results are given as total void ratio and void ratio of the matrix part versus the logarithm of effective vertical pressure (Figure 7-1 and Figure 7-2). The parameters obtained from these curves, the compression index (C_c), swelling index (C_s), and preconsolidation pressure (σ_{pc}) for both global and matrix part are presented in Table 7-1. The preconsolidation pressure relationship with particles' strength in both total mixtures and matrix part is provided in Figure 7-3. As well as, the compression and swell indices are plotted versus the particles' strength as shown in Figure 7-4. The confined elastic modulus (E_m) is calculated during various loading steps and the results are shown dealing with vertical stress and void ratio in Figure 7-5 and Figure 7-6, respectively.

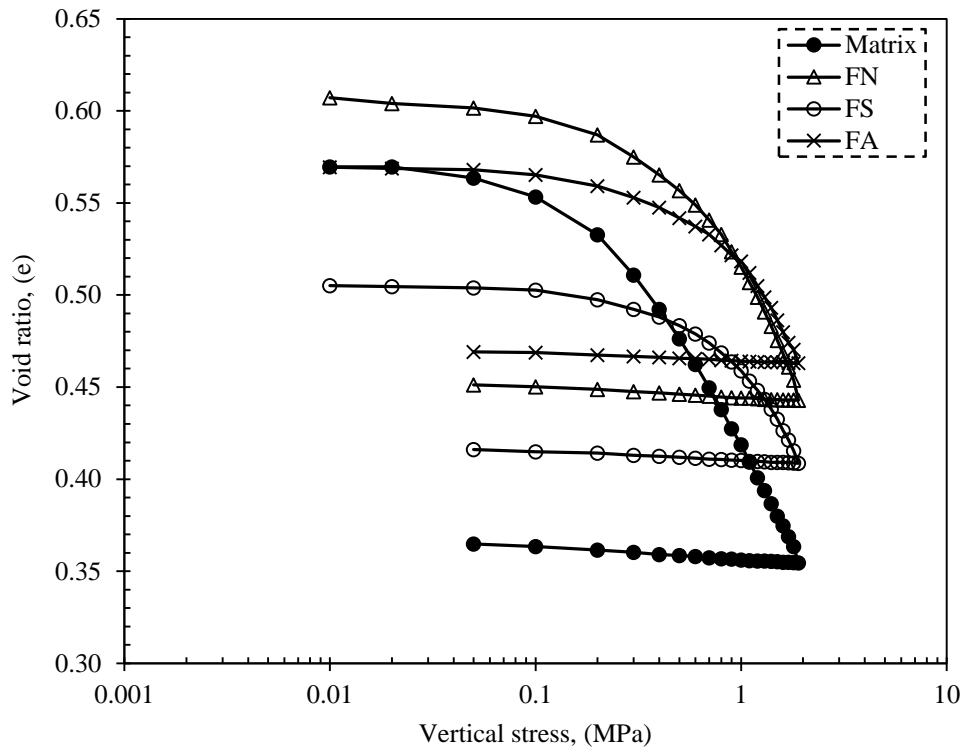


Figure 7-1: Variation of total void ratio in relation to vertical stress (samples loaded up to 1.9 MPa and unloaded up to 0.05 MPa for different types of the mixtures in as compacted conditions).

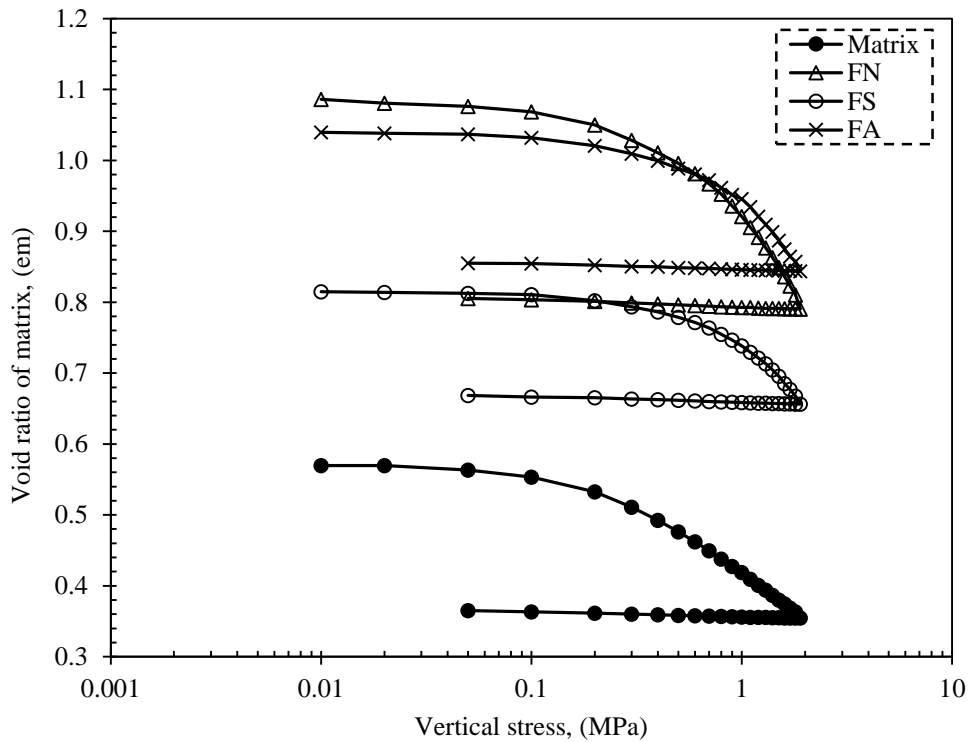


Figure 7-2: Variation of matrix void ratio in relation to vertical stress (samples loaded up to 1.9 MPa and unloaded up to 0.05 MPa for different types of the mixtures in as compacted conditions).

Table 7-1: Data summary of compression index (C_c), swelling index (C_s), preconsolidation pressure (σ_{pc}) for different mixtures.

Type of the mixture	σ_{pc} (Preconsolidation pressure) (kPa)-Total mixture	σ_{pc} (Preconsolidation pressure) (kPa)- Matrix part	C_c	C_s
Matrix	270	270	0.2053	0.0800
FN	550	400	0.2082	0.0060
FA	650	600	0.2000	0.0059
FS	725	610	0.2100	0.0055

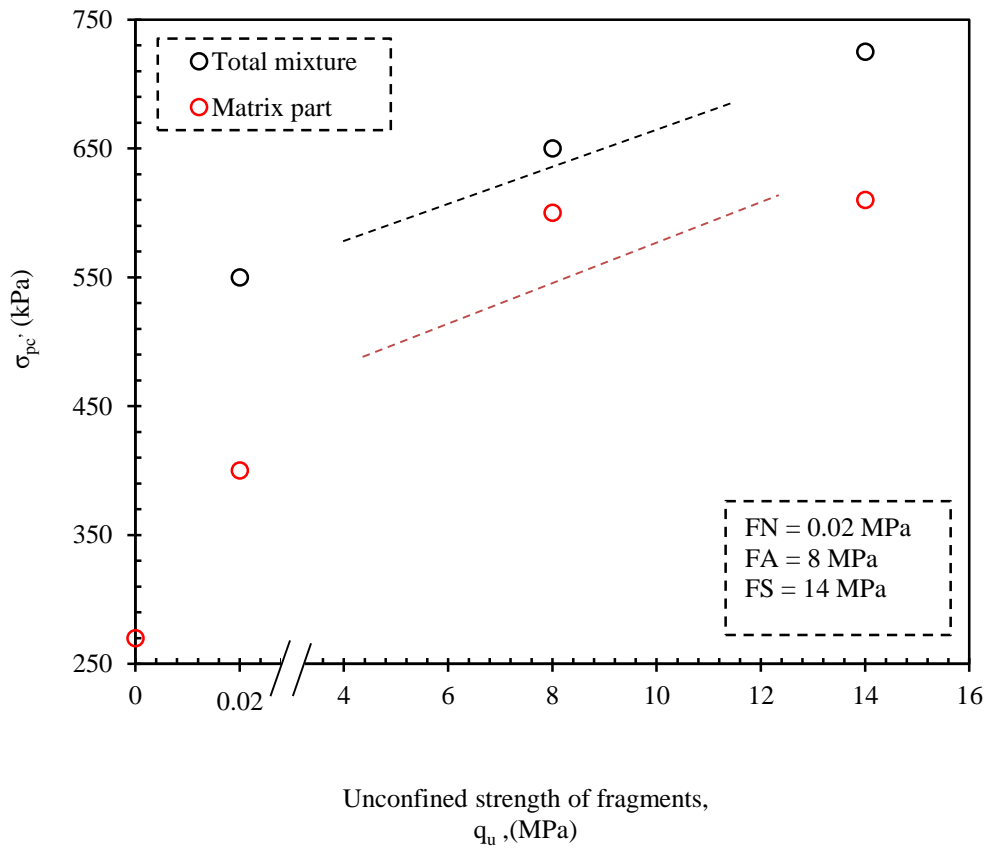


Figure 7-3: Effect of particles' strength on preconsolidation pressure.

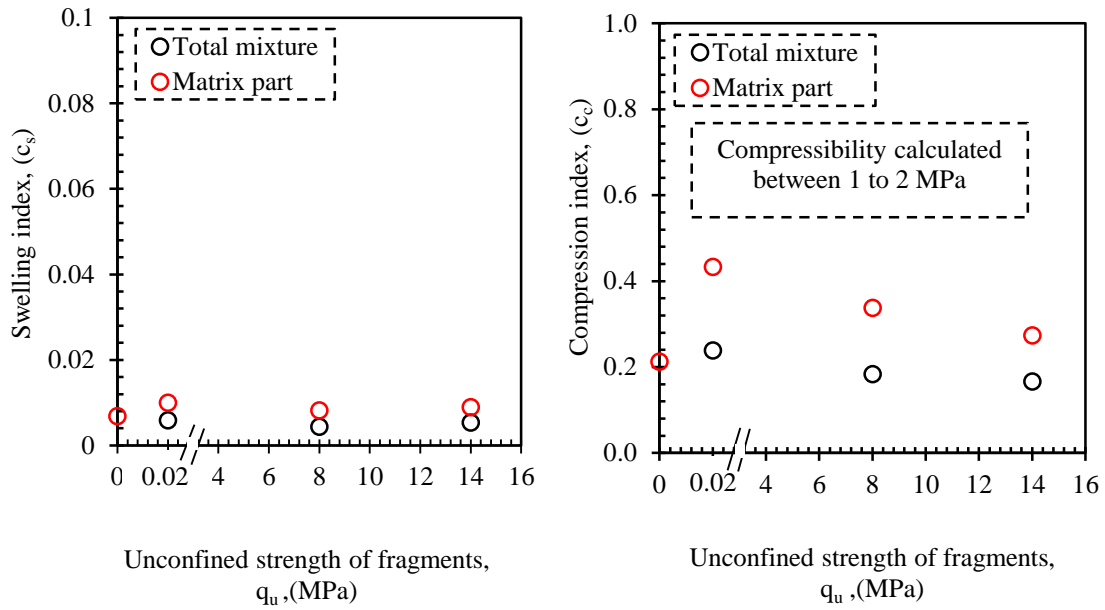


Figure 7-4: Influence of particles' strength on compression (C_c) and swell (C_s) indices.

The results achieved from Table 7-1 and Figure 7-3 reveal that the lowest preconsolidation pressure takes place in the pure matrix (270 kPa). By adding large particles to the mixtures, the value of the preconsolidation pressure increases up to 720 kPa in presence of the slate fragments with heightened strength. It means that the preconsolidation pressure goes up by increasing the strength of the large particles within the mixtures. The increment of preconsolidation versus aggregates' strength has a linear tendency. This behaviour is replicated even in matrix part of the mixtures.

Based on results from Table 7-1 and Figure 7-4, no significant differences were observed between the compression and swelling indices for all types of mixtures. That being said, there was a small change that occurred in both indices by increasing the strength of the fragments.

Figure 7-5, makes it evident that the elastic modulus has a steady tendency in the case of FA and FS (mixtures with high fragment strength) by load increment; however, this value increases by raising the load for FN and M due to the lesser fragments strength. The similar behaviour observed in Figure 7-6, reducing in void ratio raises the modulus of the pure matrix and FN moreover it is steady in FS, and FA.

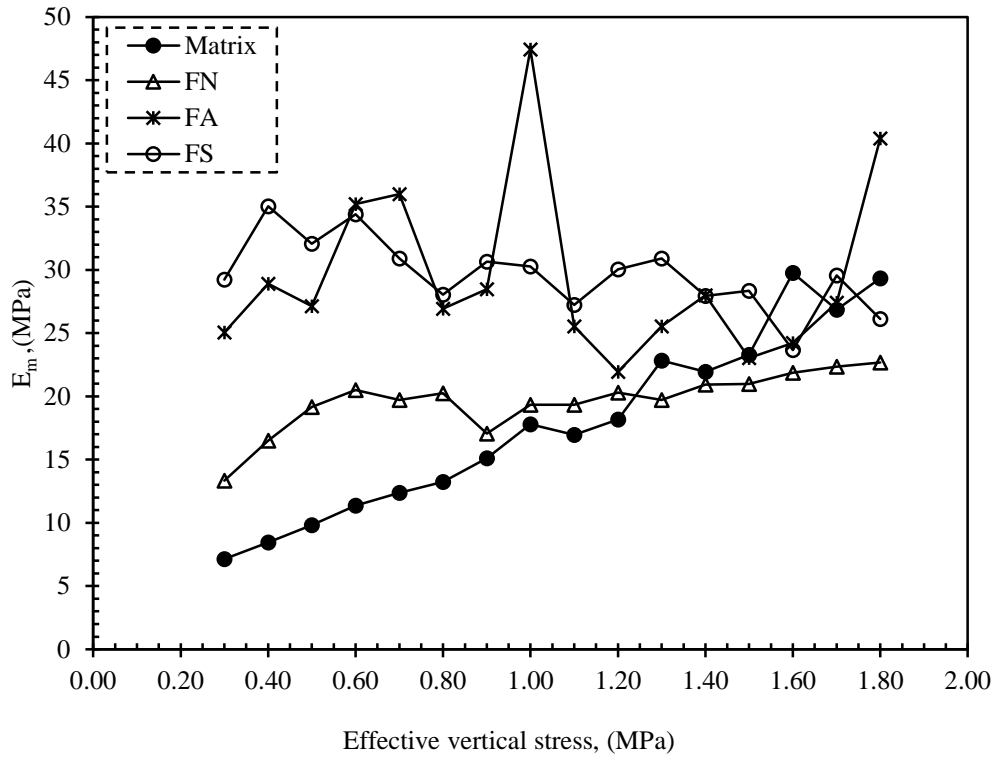


Figure 7-5: Changing of the elastic modulus versus effective vertical stress for different types of the mixtures.

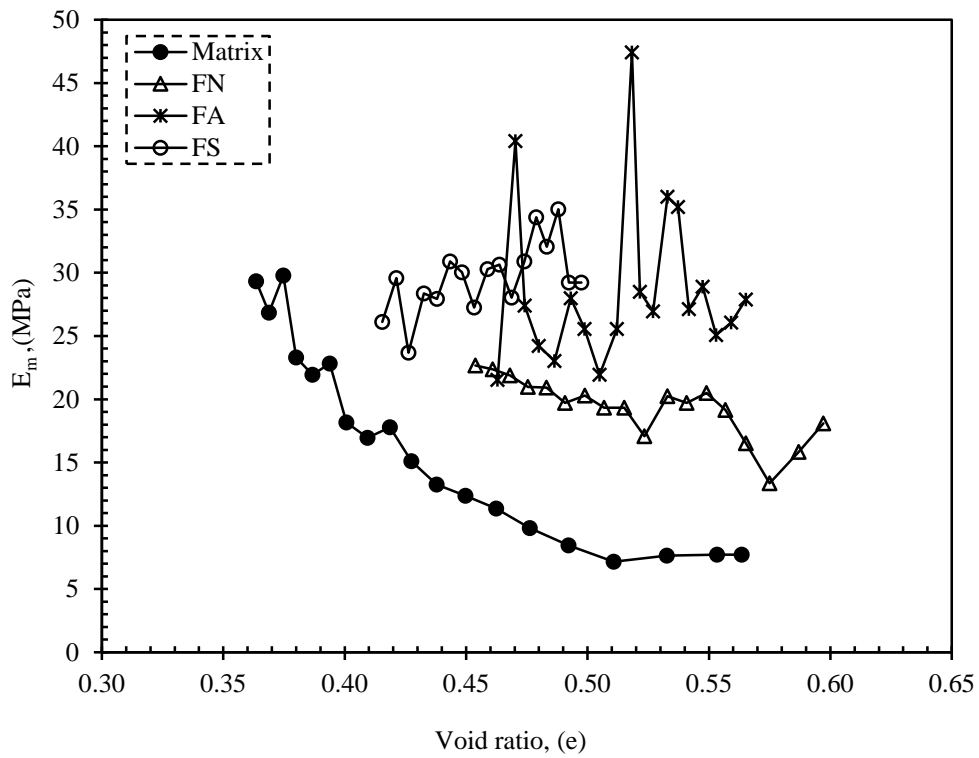


Figure 7-6: Changing of the elastic modulus versus void ratio for different types of the mixtures.

7.1.3 Particle braking mechanism

7.1.3.1 Introduction

The breakage of particles is a key feature that controls the mechanical behaviour of samples. Therefore, Hardin and Marsal indices have obtained after compaction and loading-unloading process. Later, the crushing procedure was evaluated in more detail by concentration on mass of particles retains on each sieve size. The breaking mechanism has been analysed using two techniques; the first analysis is made considering both large and fine content as result of the breaking of particles for various sieve sizes. Next, only large particles have been used to evaluate crushing analysis. The following sections will describe all techniques.

7.1.3.2 Hardin and Marsal breakage indices

To point out breakage mechanism in this investigation, the sieve analysis has been carried out before and after of each test. The analysis has been done for all mixtures (FN, FA, and FS). The grain size distribution curves for all specimens are plotted after dynamic compaction and static compaction under loading-unloading oedometer tests. The grain size distribution curves are depicted in Figure 7-7.

These sieve analysis test highlighted that remarkable differences are observed between grain size distribution before and after each test. Meanwhile, this variation is small between dynamic compaction and static loading-unloading test. Furthermore, to assess these alterations in GSD curves in more detail the Hardin and Marsal indices are calculated and the values are presented in Table 7-2. These values are in good agreements with the changing observed in grain size distribution curves. It can be seen that the highest breakage occurs in FN after oedometer test (Hardin, $Br = 0.492$, Marsal, $Bg = 32.2$), the amount of breakage reduced by 45.55 % and 45.49 % in case of FA and FS, respectively. In addition, the value of ΔBr ($\Delta Br = Br_{L-U} - Br_{A-C}$) shows GSD differences between dynamic compaction and oedometer loading-unloading test among the mixtures. This value is higher in FN due to weak structure of natural fragments. Otherwise, this amount is not significant with FA and FS according to the high stiffness of aggregates ($\Delta Br = 0.141$ for FN, $\Delta Br = 0.059$ for FA, $\Delta Br = 0.046$ for FS). It can be concluded that the strength of the fragments is one of the main parameters in crushing mechanism either in high-stress level or in low stress.

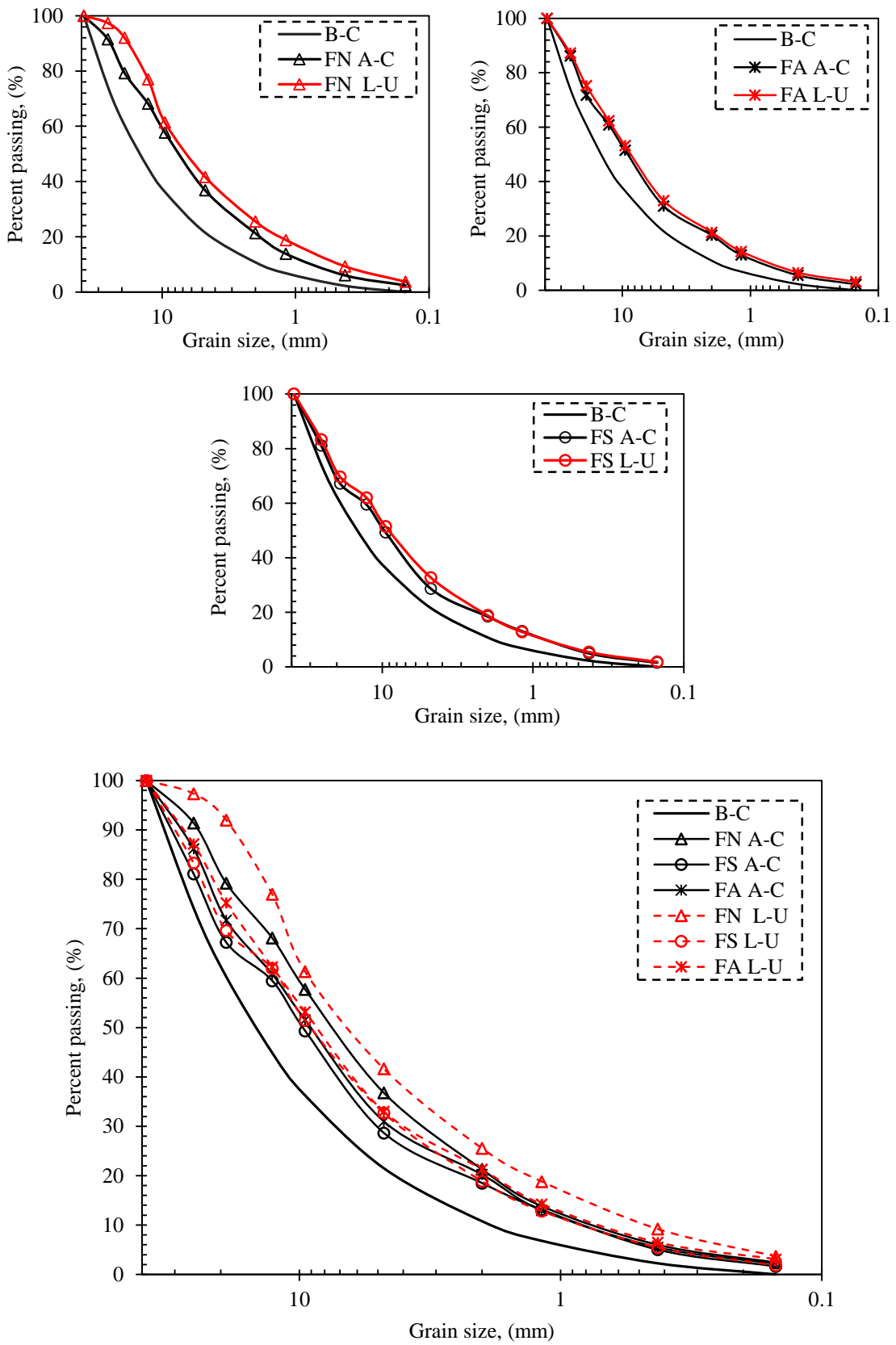


Figure 7-7: Grain size distributions of FN, FA, and FS mixtures after dynamic compaction (A-C) and static compaction under loading-unloading oedometer (L-U) test.

Table 7-2: Data summarizing for breakage indices after dynamic compaction and static loading-unloading oedometer tests.

Type	Bg (Marsal)	Br (Hardin)
B-C	-	-
FN A-C	23.36	0.351
FN L-U	32.20	0.492
FA A-C	17.24	0.238
FA L-U	17.53	0.297
FS A-C	15.96	0.172
FS L-U	17.55	0.218

In order to investigate the crushing indices in more detail, the relationship between accumulated breakage indices and the other parameters such as; total density of the mixture, the unconfined strength of the fragments, volumetric strain, the area of the particles increment, and plastic work, are shown in Figure 7-8 through Figure 7-12, respectively. To enable computing the area of retaining particles for each sieve size after test the following index ΔA^* (cm²/gr) has been used. The index are obtained based on following equation 7-1 (Particle is assumed a sphere):

$$\Delta A^* = \frac{\Delta A}{M} \quad \text{Equation 7-1}$$

Where,

ΔA = Area of particles after compaction - Area of particles before compaction.

M = Mass of total particles related to sieve size.

In addition, plastic work is expressed as work per unit of volume of specimen (stress unit) and is defined equation 7-2:

$$W_p = \sum \sigma' \Delta \varepsilon_v \quad \text{Equation 7-2}$$

Where W_p is the plastic work (MPa), σ' is the average stress, and $\Delta \varepsilon_v$ is the volumetric strain of the samples between two loading steps.

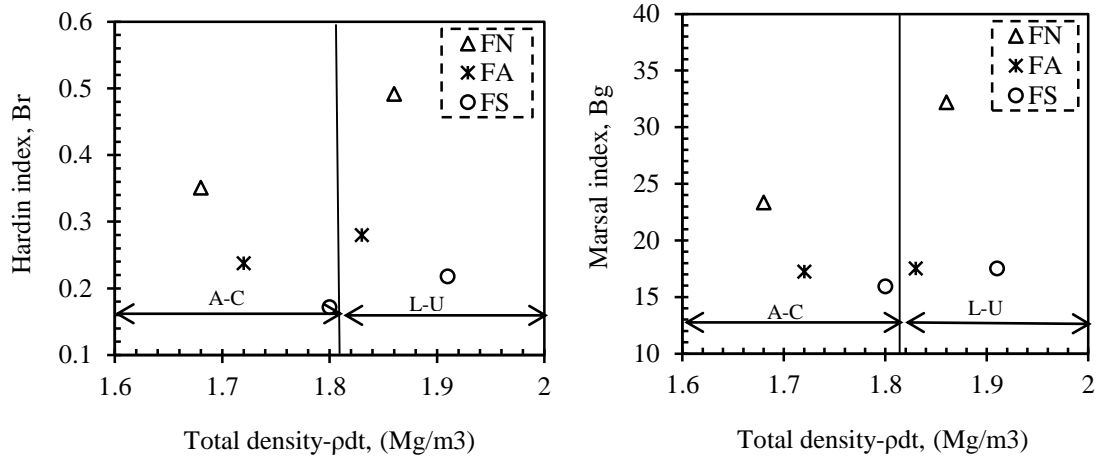


Figure 7-8: Breakage indices versus density of the mixture.

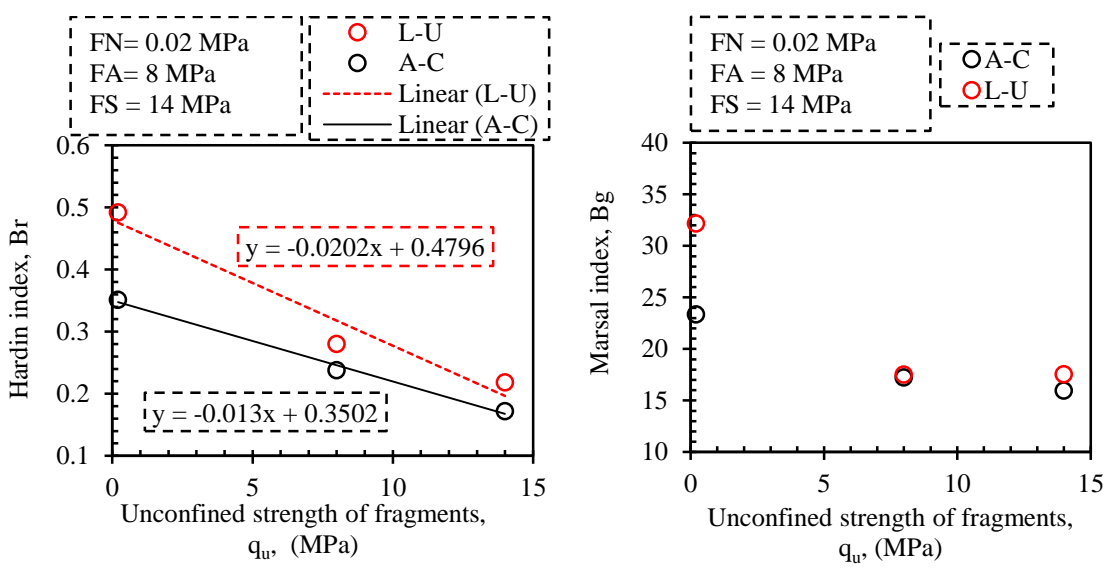


Figure 7-9: Breakage indices versus unconfined strength of fragments.

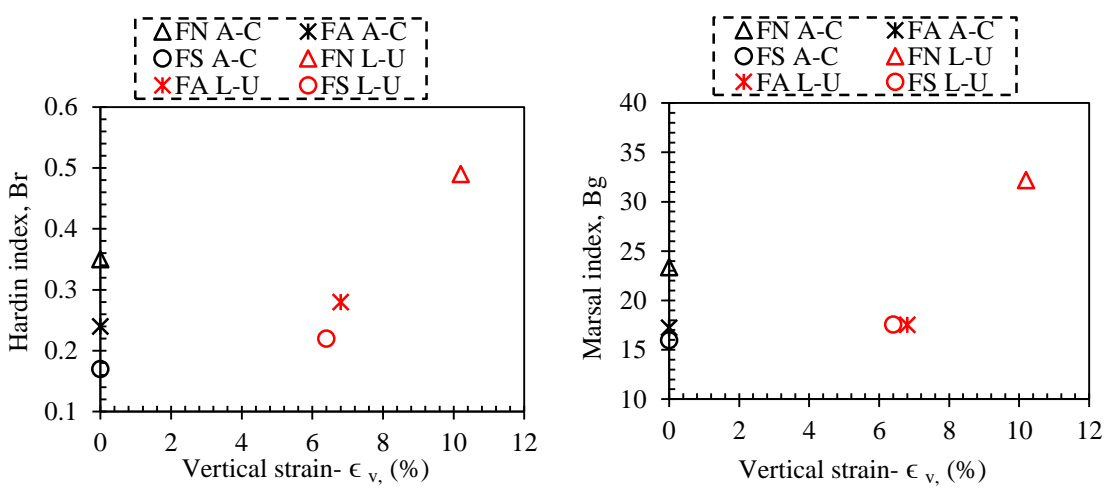


Figure 7-10: Breakage indices versus volumetric strain during L-U process of the samples.

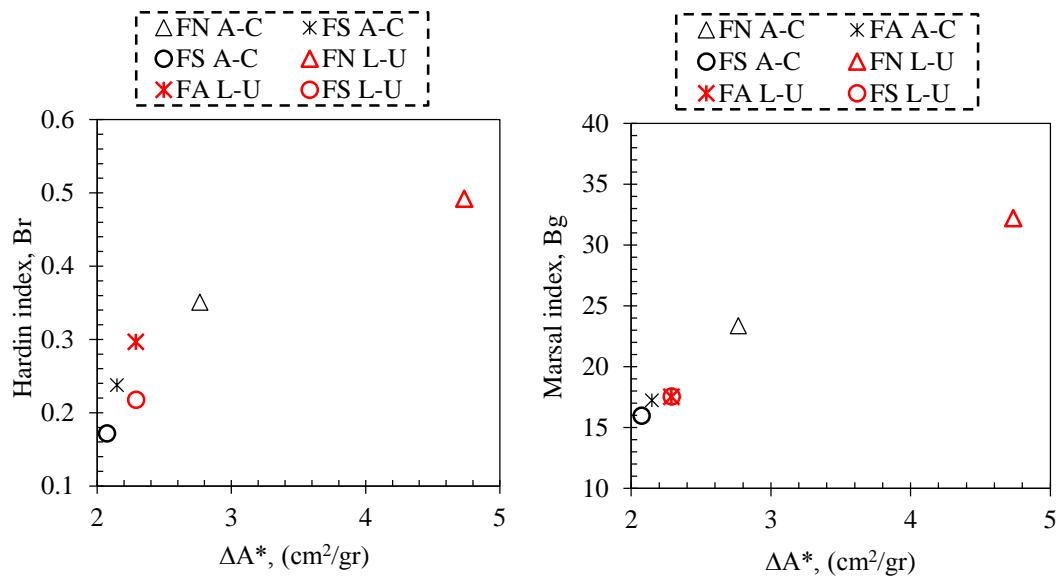


Figure 7-11: Breakage indices versus area of the particles over mass of the samples.

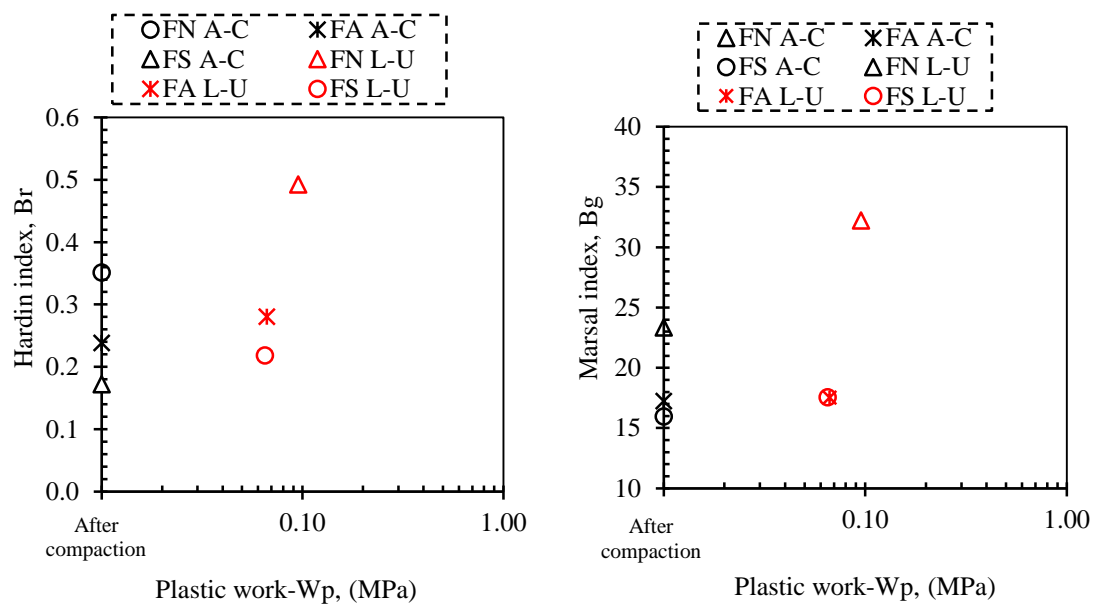


Figure 7-12: Breakage indices versus plastic work.

Based on data obtained from breakage analysis, it is apparent that the Hardin and Marsal breakage indices indicate the same tendencies. The crushing of various strength aggregates is displayed in better conditions in case of utilizing Hardin index. Consequently, the Hardin method is selected to analyse the behaviour observed in the above Figures (Figure 7-8 to Figure 7-12).

The analysis of the crushing results for different mixtures based on Figure 7-8 to Figure 7-12 is discussed below:

- From Figure 7-8, it is observed that due to loading process there is a direct relation between the amount of breakage and the reduction of the density of total mixture. On the other hand, the maximum density corresponds to the fragments with maximum strength. It means that the most part of the compaction energy either in dynamic and static goes to breakage instead of densifying the mixtures. FS shows the highest total density due to less crushing. The same behaviour is detected after compaction and loading-unloading. Moreover, FN because the very weak stiffness in high-stress level (L-U oedometer) shows the density close to artificial fragments. It is clear that the natural aggregates already crushed after compaction and in more stress levels shows better density.
- From Figure 7-9, it can conclude that smaller breakage belongs to larger strength of the fragments in the mixture. As it can be seen, the behaviour of breakage versus particle's strength has a linear tendency and the regression line equation is equal to $y = -0.013x + 0.3502$ and $y = -0.0202x + 0.4796$, in place of after compaction and loading-unloading oedometer, respectively.
- From Figure 7-10, the vertical strain for specimens after compaction is not taken into account. The results after loading-unloading reveal, by increasing the volumetric strain the breakage of particles increases. The highest strain amount is observed in FN ($\epsilon_v = 10.2\%$) which is corresponded to highest breakage ($Br = 0.49$).
- Figure 7-11 analyses the amount of new particle surface created for unit mass during compaction and loading-unloading process. There exist an almost linear correspondence between the Breakage indices and the new particle surface created. So, FN because of highest breakage value shows a larger new area of the particles ($\Delta A^* = 4.1 \text{ cm}^2/\text{gr}$). This amount decreases remarkably by 56 % in presence of slate aggregates (FS).
- From Figure 7-12, it can conclude the observed rate of breakage is practically related to the plastic work at the end of the test. A higher value of plastic work displays the higher amount of breakage.

Alvarado (2017), investigated the crushing behaviour of the slate fragments in various maximum sizes ($D_{max} = 40 \text{ mm}$, $D_{max} = 20 \text{ mm}$, and $D_{max} = 2 \text{ mm}$). The results of breakage were plotted as a function of plastic work. Figure 7-13 illustrates the comparison results of Alvarado (2017) tests with this investigation. It can be seen that there is

consistency between two results. The breakage for slate in the binary mixture has very close behaviour to fragment with 20-40 mm sizes, indicating that the role of the matrix in this case is not very relevant.

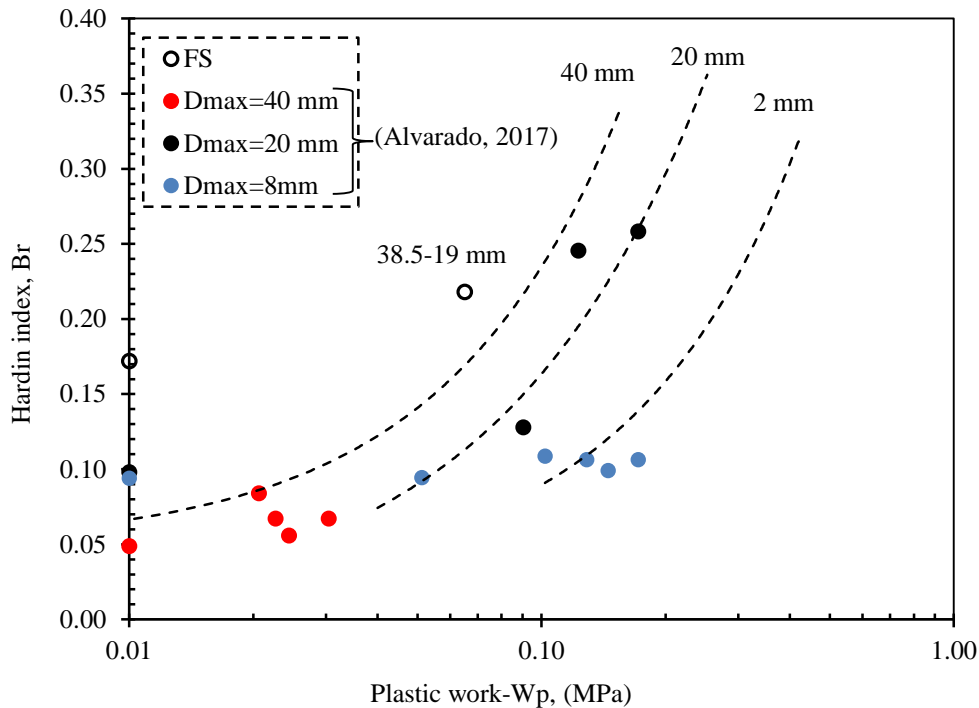


Figure 7-13: Comparison of breakage results for slate aggregates as a function of plastic work.

7.1.3.3 Crushing based on both large and fine content

According to study of Tapias et al. (2016), during the crushing procedure, the two dominant grain size family (11 mm for the coarse part and 0.4 mm for fine size) are observed when the initial grain size was of 20 mm. The Figure 7-14 illustrates the distribution of retained weight at the given sieve size in time evolution under vertical stress of 440 kPa. The largest diameters correspond to particles with a diameter about the half of the initial one and the finest particles have a diameter that ranges between 1/100 and 1/25 of the original size particle.

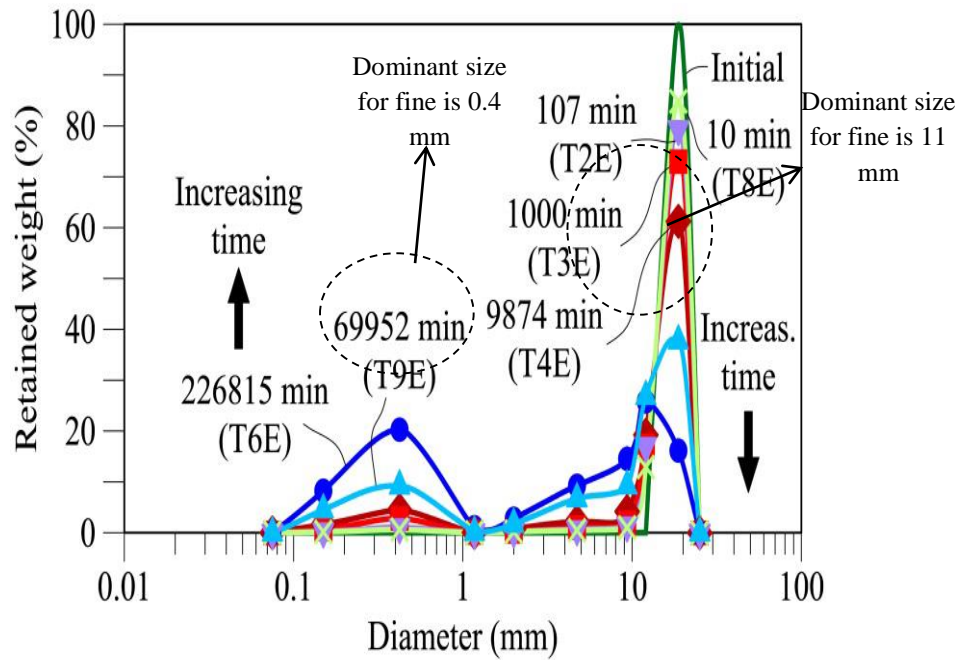


Figure 7-14: Distribution of retained weight at a given sieve size (Tapias et al., 2016).

The breakage analysis with considering both large and fine content consists of the distribution of the particles' mass after test on each sieve size. For the material retained in each sieve (i) with an average diameter D_i , the same breakage rule has been considered. The initial mass (M_i) is divided between a ratio X of fines and $(1-X)$ of large sizes. The value of "X" has been considered the same for all the sieves. In addition, the diameter of the larger particles varies uniformly between D_i and D_i/R and the diameter of the fines ranges uniformly between $D_i/100$ and $D_i/25$. In order to obtain the new grain size distribution curve, the larger particles have been subdivided in three categories corresponding to the diameters ($D_i \times D_1$, $D_i \times D_2$ and $D_i \times D_3$) and the fines has been subdivided in two sizes ($D_i \times D_4$ and $D_i \times D_5$). The first three ($D_i \times D_1$ to $D_i \times D_3$) are belonged to splitting crushing of large aggregates. In splitting mechanism, the particles size made by half size of the particles due to previous sieve size diameters. The sizes $D_i \times D_4$ and $D_i \times D_5$ are associated with comminution crushing regarded to fine particles. The comminution mechanism is the amount of fine generated from origin fragments and the rest of particles after compaction. Figure 7-15 indicates schematically how the particles originally retained in the sieve with average diameter D_i are broken.

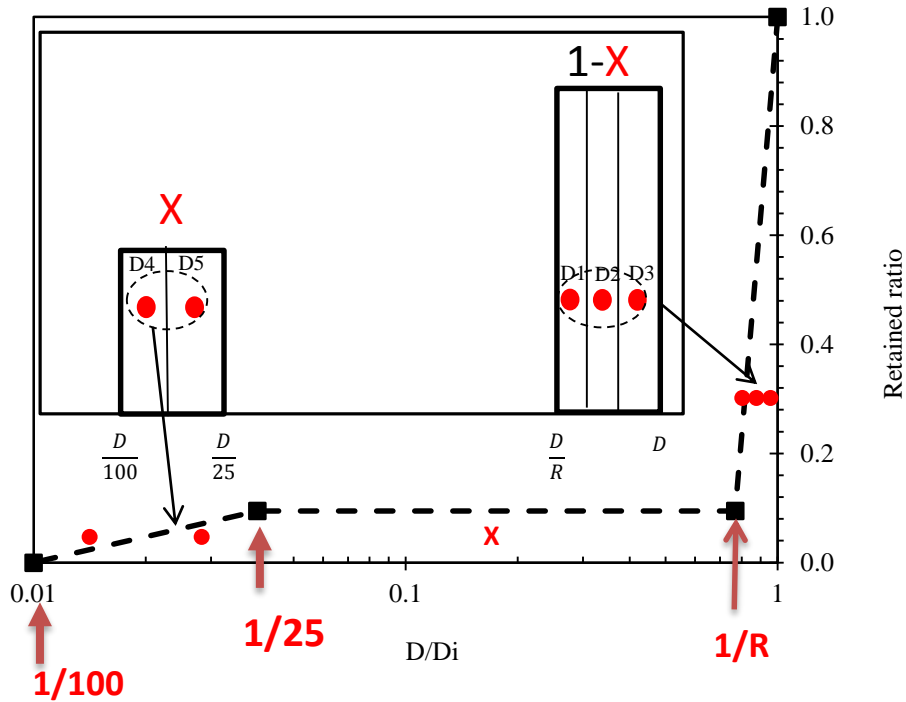


Figure 7-15: The distribution of fine and large particles with various diameters resulting from particles with a diameter D_i .

The diameter and retained mass for each size (D_1 to D_5) are calculated by procedure indicated in the Figure 1-16:

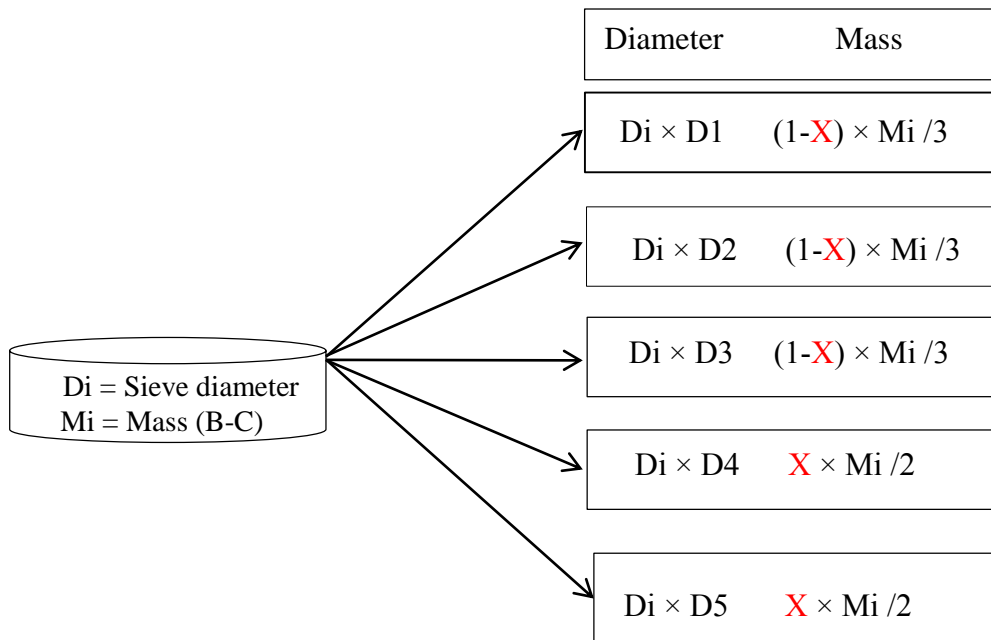


Figure 7-16: Schema of the breakage mechanism considering splitting and comminution crushing.

Where,

$$D1 = R^{-1/6}$$

$$D2 = R^{-3/6}$$

$$D3 = R^{-5/6}$$

$$D4 = (1/100)^{0.25} \times (1/25)^{0.75}$$

$$D5 = (1/100)^{0.75} \times (1/25)^{0.25}$$

Utilizing the data for the total retained mass of each sieve before test and following the breakage mechanism, all retained weight belonged to same diameter after compactions are calculated by above procedure. The total mass of different sieve sizes is obtained by adding all retained weight for same diameter. The procedures are repeated for all mixtures after compaction and loading-unloading oedometer tests. The values of the fine ratio (X) and the larger diameter limit 1/R have been obtained by curve fitting with the experimental results. The value of R is almost the same for all materials and finally a fixed value of R=1.3 has been used for all the materials. Table 7-3 shows the values of the parameter R. This parameter is about 0.08 for all the cases except for the loading-unloading process with artificial and slate fragments where the fine ratio is about 0.04.

The outcomes are shown in Figure 7-17 for all mixtures. It has been found that the assessment between calculated and experimental GSD curves presents a reasonable fit. Therefore, the method is an effective way to evaluate the particle breakage.

Table 7-3: Parameters of breakage model and average errors obtained by curve fitting of the experimental results

	FN ac	FA ac	FS ac	FN LU	FA LU	FS LU
R	1.3	1.3	1.3	1.3	1.3	1.3
X(ratio fines)	0.095	0.076	0.071	0.079	0.049	0.034
Error average (%)	4.01	2.36	2.90	4.01	1.90	2.74

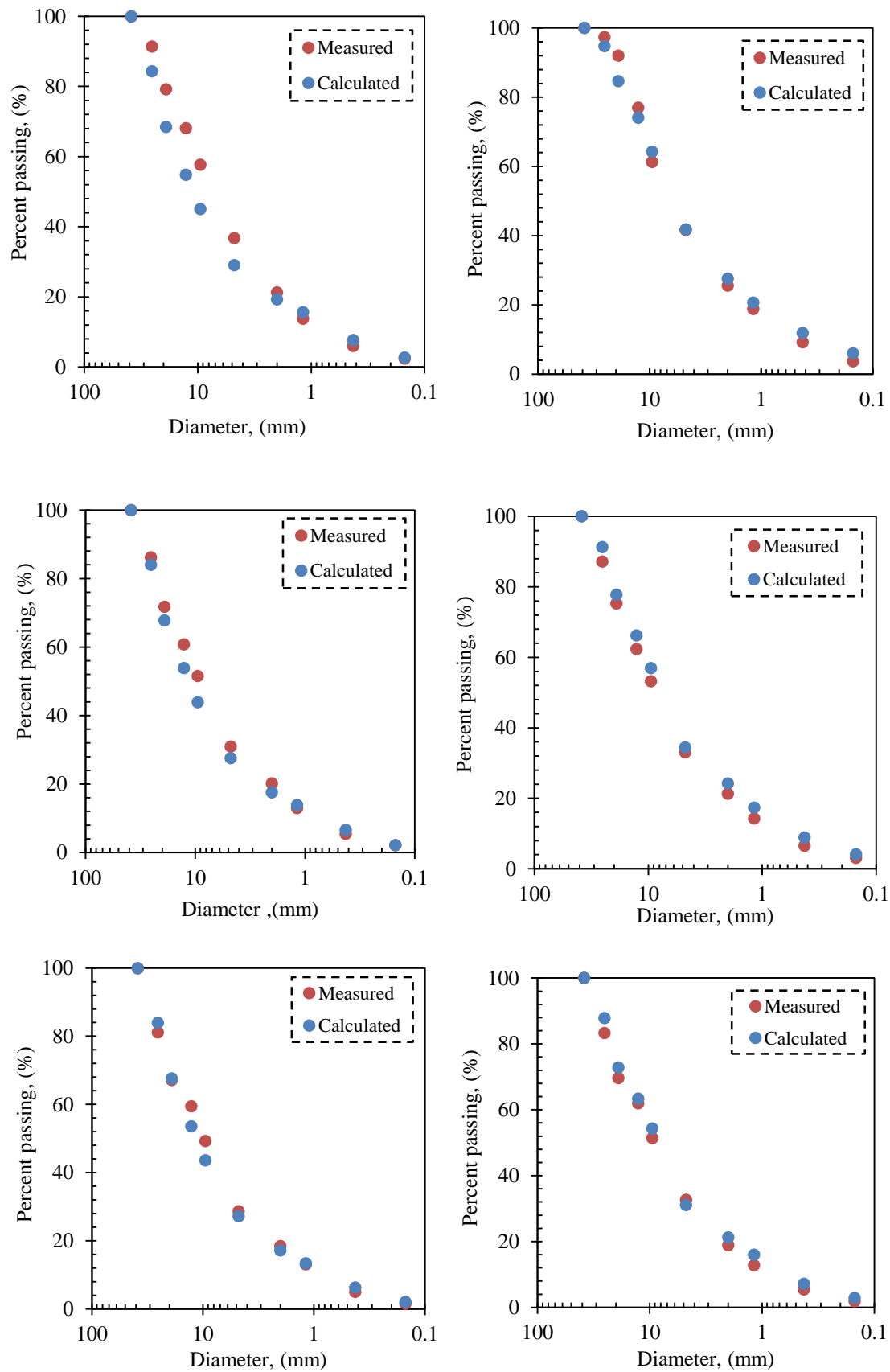


Figure 7-17: Comparison of GSD curve achieved in the experimental and theoretical method.

7.1.3.4 Crushing without considering fine content

The idea of investigating the breakage of large aggregate is designed based on the retained mass of particles obtained after test for the next three sieve number. This model of breakage is more simple than the previous one, and may be justified taking into account that the fine ratios (X) obtained in previous section were very small. Figure 7-18 shows the procedure used to calculate the GSD curves after breaking processes.

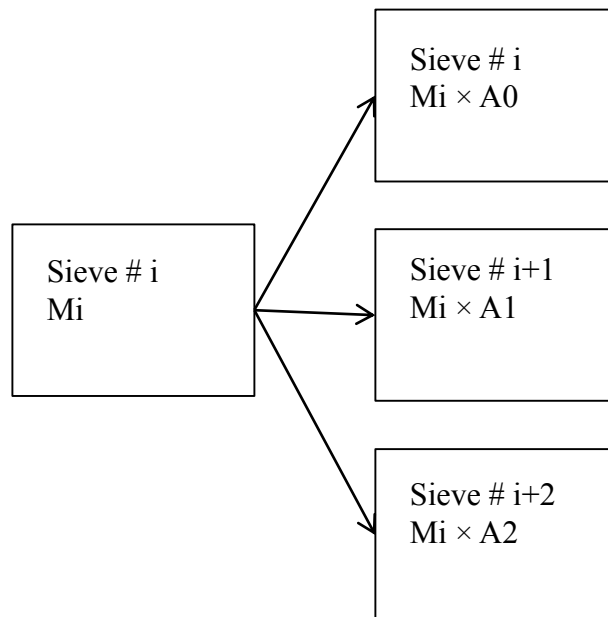


Figure 7-18: Schema of the breakage mechanism without considering comminution crushing.

Where,

M_i = Mass of particles originally retained in sieve size i .

$A_0 = 1 - A_1 - A_2$.

A_1 = Proportion of the mass retains in sieve size $i+1$.

A_2 = Proportion of the mass retains in sieve size $i+2$.

The A_1 and A_2 proportions were estimated for all sieve sizes to minimize the difference between the experimental and theoretical retained mass, afterwards, by using excel solver program the value of A_1 and A_2 are obtained. Table 7-4 depicts the value of A_0 , A_1 , and A_2 for all mixtures.

Table 7-4: The value of A0, A1, and A2 for all specimens after dynamic compaction(A-C) and static loading unloading oedometer (L-U) test.

	FN A-C	FN L-U	FA A-C	FA L-U	FS A-C	FS L-U
A0	0.42	0.6	0.78	0.67	0.91	0.85
A1	0.31	0.24	0.17	0.15	0.03	0.15
A2	0.26	0.16	0.05	0.18	0.07	0

The data of Table 7-4 are plotted in stacked graph form in Figure 7-19.

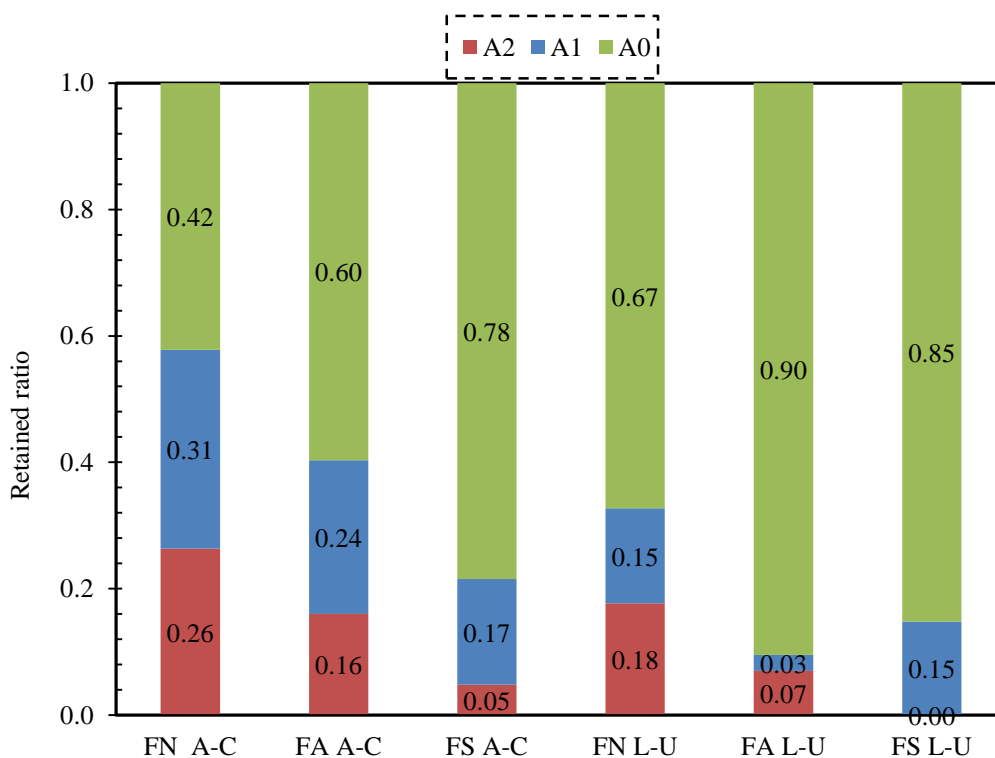


Figure 7-19: Variation of the value A0, A1, and A2 for all mixtures type after compaction and loading-unloading oedometer test.

It appears that the proportion A1 and A2 ratios increased gradually from FS to FN, peaking at around A1=0.31 and A2=0.26 in FN. It means that by increasing the crushing of aggregates more particles go to the next sieve sizes. In addition, a small variation in transferring ratio is observed in loading-unloading part. It is related to the small value of breakage that occurs after loading-unloading in case of comparing with after compaction results, not with initial conditions.

7.1.4 Fractal analysis

The fractal dimension (DF_R) by utilizing the masses of samples is determined depending on the particle size, the type of material selected and the sample mass. Three samples are used (FN, FS and FA) in order to provide the process of fragmentation. The value of DF_R calculated is based on Tyler Wheatcraft (1992) method (as described in state of the art chapter 2).

Figure 7-20 and Figure 7-21, present the relationship of the logarithm of the size ratio (r/r_1) with the logarithm of the mass ratio M/MT for the three types of mixtures after compaction and loading and unloading oedometer test, respectively. The slope of this relation (m) is related to fractal dimension ($DF_R = 3 - m$). The tested samples indicated a good fit to the power law giving very good correlation ($R^2 \geq 95\%$). The values of DF_R are shown in Table 7-5.

Later the relationship between the DF_R and strength of fragment is shown in Figure 7-22. The high value of DF_R indicates that the sample present a large amount of fine particles. Therefore, according to the samples of the three materials, the fractal dimension is still increasing after testing but this amount is greater after loading and unloading oedometer compare with after compaction in all cases. The fragmentation increased by reducing the strength amount of fragment. The largest amount of fragmentation occurred in FN due to the smallest strength among three materials. In conclusion, by increasing the strength of the particles in the mixtures the value of fine reduced because of less breakage happened in particles and the fractal number increased.

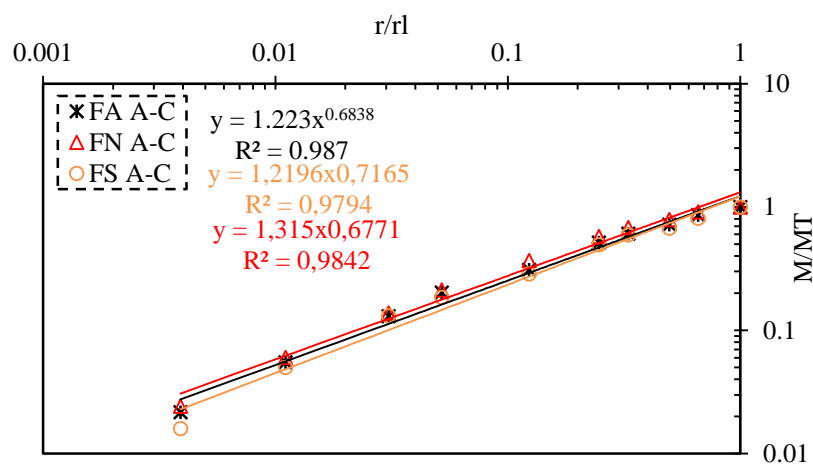


Figure 7-20: Influence of particle size range on the fractal dimension for different mixtures after dynamic compaction test.

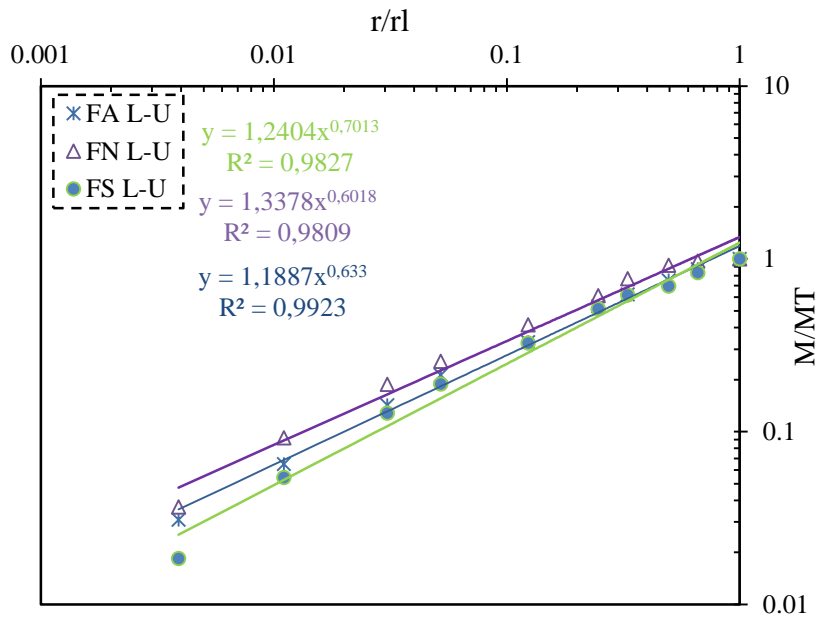


Figure 7-21: Influence of particle size range on the fractal dimension for different mixtures after Loading- unloading oedometer test.

Table 7-5: The value of fractal number for various mixtures.

Soil Type	Equation of $\text{Log}(M/M_T) - \text{Log}(r/r_1)$	$DF_R = \text{Fractal number}$
Origin Before compaction (b-c)	$y = 1,0867x^{0,8188}$ $R^2 = 0,9941$	2.18
FN A-C	$y = 1,315x^{0,6771}$ $R^2 = 0,9842$	2,32
FN L-U	$y = 1,3378x^{0,6018}$ $R^2 = 0,9809$	2,39
FA A-C	$y = 1,223x^{0,6838}$ $R^2 = 0,987$	2.31
FA L-U	$y = 1,1887x^{0,633}$ $R^2 = 0,9923$	2.37
FS A-C	$y = 1,2196x^{0,7165}$ $R^2 = 0,9794$	2,28
FS L-U	$y = 1,2404x^{0,7013}$ $R^2 = 0,9827$	2,29

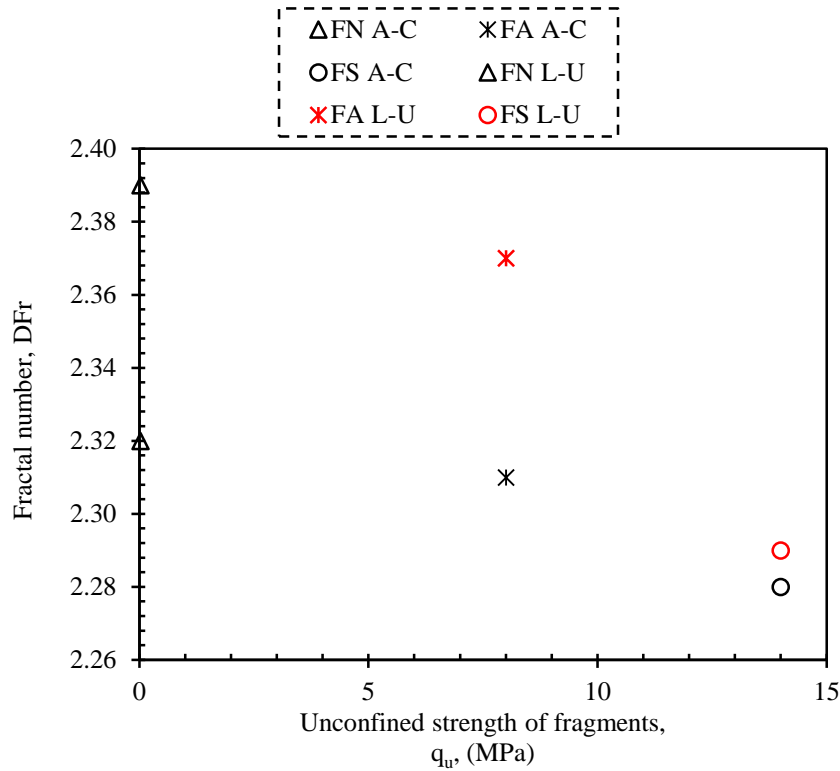


Figure 7-22: Fractal number (DFr) versus unconfined strength of fragments.

7.1.5 Energy dissipation during dynamic compaction and static loading-unloading oedometer test

7.1.5.1 Introduction

To assess energy transferring during dynamic and static compaction following hypothesis are considered:

- The energy that goes to matrix part of the mixtures is equal to energy to densify the matrix part (energy to break the matrix fragments are not considered).
- The energy that goes to large fragments is equal to the energy of the particles breakage.
- The energy lost due to the friction of compaction cell wall is neglected.
- The energy lost by human error is disregarded during experimental work.
- The effect of heating is ignored.

The calculated energy for particle breakage will be higher than the true applied energy due to disregard the effect of friction, human error, and heating. The energy considered is equal to energy for per unit volume, so the unit to describe it is equal to $(\text{kN}\cdot\text{m}/\text{m}^3=\text{kPa})$.

Therefore, the energy dissipation during dynamic and static loading-unloading oedometer will be described for the different mechanisms in next sections.

7.1.5.2 Energy dissipation during dynamic compaction

In order to evaluate the conversion of the energy during dynamic compaction, initially, a series of compaction tests were carried out in the pure matrix. Standard Proctor compaction mould was selected for all cases. Different energies were used to compact pure matrix by changing the blow number of the hammer. The dry densities corresponding to the different blow numbers are shown in Figure 7-23. In addition, Figure 7-24 depicts the dry densities versus compaction energies obtained by several blow numbers.

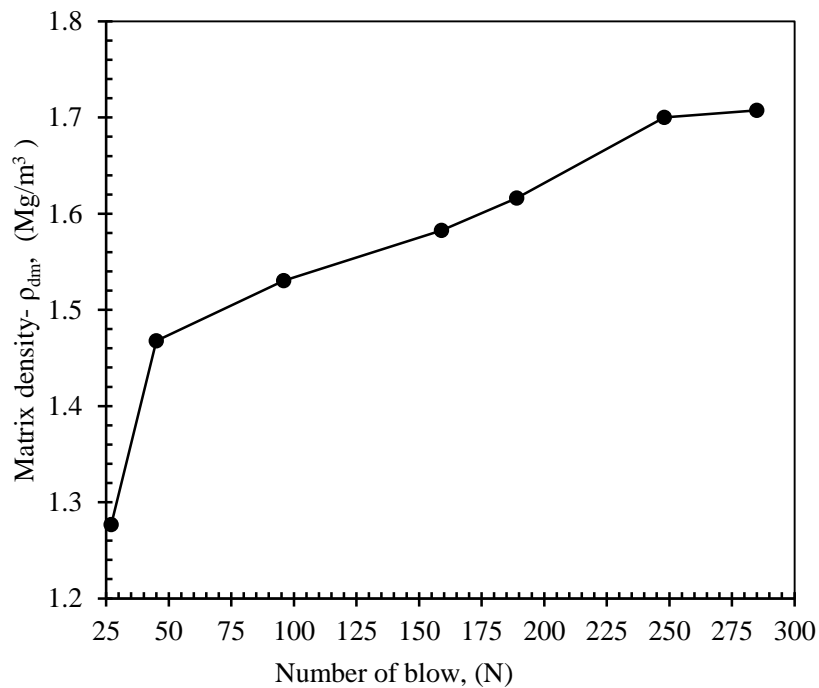


Figure 7-23: Dry density achieved related to different blow numbers in pure matrix.

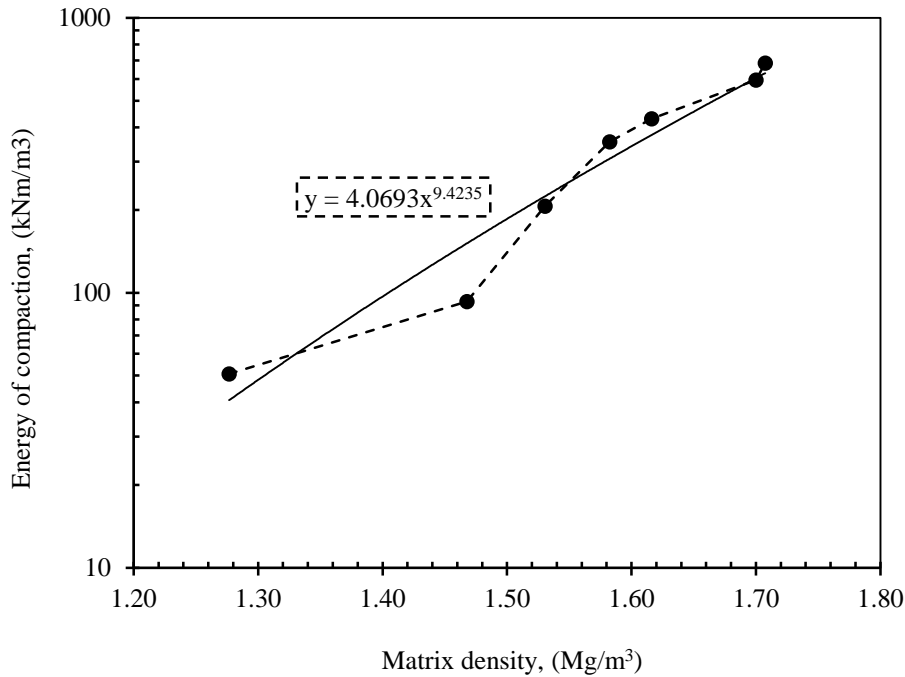


Figure 7-24: Relationship between energy of compaction and the dry density of matrix.

Figure 7-24 reveals that by knowing the density of the matrix in the mixtures (x), the energy necessary to densify the matrix part (Y) may be achieved utilizing the equation $Y=4.0693x^{9.4235}$.

Additionally, the equation 7-3 may be used to specify energy spent in particle breakage when the standard Proctor compaction is done and the dry density of the matrix is known.

$$E_{dt} = E_{dM} + E_{dPb} \quad \text{Equation 7-3}$$

Where,

E_{dt} = Total dynamic energy applied by standard Proctor compaction energy equal to 596 (kN-m/m³) (Energy imparted per unit volume of compacted mixture).

E_{dM} = Dynamic energy that goes to densify matrix per unit volume of compacted mixture (evaluated from the matrix dry density).

E_{dPb} = Dynamic energy that goes to breakage particles per unit volume of compacted mixture).

In addition,

$$E_{dM} = E_M / V = (E_M/V_M) (W_M/W) (\rho_d/\rho_{dM}) \quad \text{Equation 7-4}$$

Where,

E_M = Total compaction energy that goes to the matrix.

V, V_M = Total volumes of mixture and matrix part respectively.

W, W_M = Total weights of mixture and matrix part respectively.

ρ_d, ρ_{dM} = Dry density of mixture and matrix part respectively.

The value of (E_M/V_M) is obtained knowing the dry density of the matrix using the relationship derived from Figure 7-24.

Table 7-6 displays the energy contribution during dynamic compaction for all mixtures (FN, FA, and FS). It can be observed that a large part of the compaction energy goes to the breakage of the particles, especially in the mixtures where the strength of the fragments is low.

Table 7-6: Energy (kPa) distribution through matrix and breakage of the particles in dynamic compaction.

Type of material	Dry density of mixture (Mg/m ³)	Dry density of matrix (Mg/m ³)	Energy to matrix/volume of matrix (kNm/m ³)	Energy to matrix/volume mixture (kNm/m ³)	Energy to breakage /volume mixture (kNm/m ³)	Energy to matrix / Total energy (%)	Energy to breakage / Total energy (%)
FN	1.68	1.28	42	33	563	5.5	94.5
FA	1.72	1.31	52	41	555	6.9	93.1
FS	1.8	1.47	154	113	483	18.9	81.1

7.1.5.3 Energy dissipation during static loading-unloading oedometer test

To know how much energy is consumed to densify matrix under oedometric static compaction, oedometer tests have been done following the same loading path until reach 1.9 MPa on pure matrix. After oedometric test, the applied vertical stress versus volumetric strain relationship can be plotted for pure matrix and mixtures.

Two hypothesis can be made concerning the structure of the compacted soil mixture. In the first case, it can be assumed that an over filled structure exists and the fragments are not deformable (Figure 7-25 and Figure 7-26). For the second case, it is assumed an

interactive-underfilled structure and that the strain in the matrix is the same that the strain in the fragment skeleton (that is the same of the global strain), see Figure 7-27.

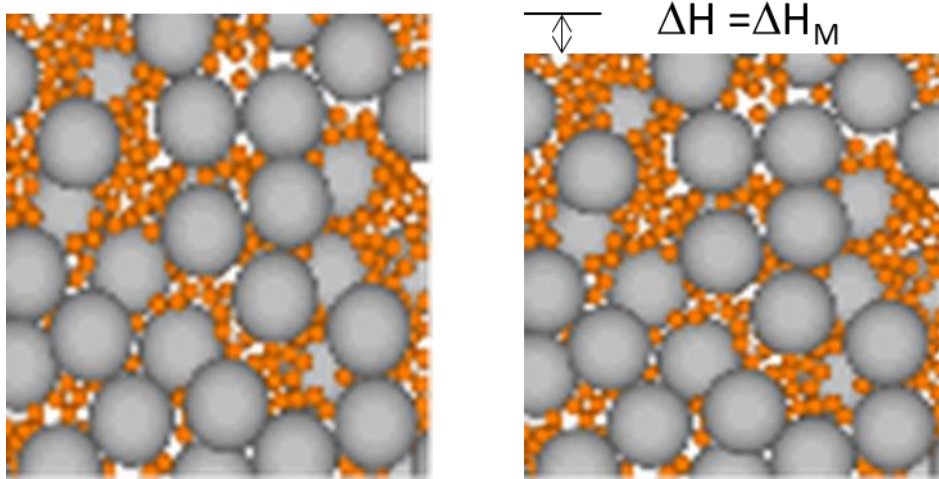


Figure 7-25: Scheme of deformation in the case of rigid fragments ($\Delta H = \Delta H_M$).

If the fragments are considered rigid, the global strain (ε) and matrix strain (ε_M) are obtained as follow (equation 7-5) :

$$\varepsilon = \Delta H/H = (\Delta H_M/H_M) (V_M/V) = \varepsilon_M (W_M/W) (\rho_d/\rho_{dM}) \quad \text{Equation 7-5}$$

Considering the stress-strain relationship for the global mixture and for the matrix sample, the value of the maximum strain in the matrix (ε_M^{\max}) can be evaluated from the maximum strain measured in the oedometer test on the mixture (ε^{\max}) using the equation (7-5). In Figure 7-26 it can be observed that the maximum strain in the mixture is smaller than the maximum strain in the matrix and the stress supported by the matrix is lower than the applied load.

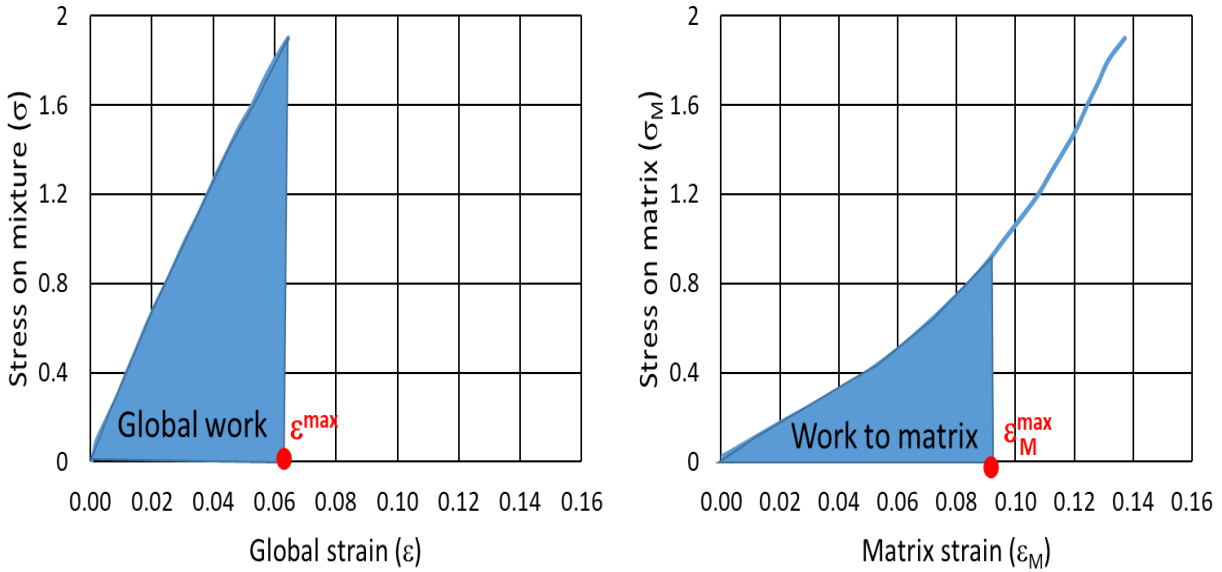


Figure 7-26: Global work and work that goes to the matrix for the oedometric test on FS sample (hypothesis of rigid fragments).

The global and the matrix works per unit of global volume (E_t and E_M) can be calculated according to equation 7-6 and 7-7 respectively:

$$E_t = \int_0^{\varepsilon^{\max}} \sigma \, d\varepsilon \quad \text{Equation 7-6}$$

$$E_M = \left(\frac{V_M}{V}\right) \int_0^{\varepsilon_M^{\max}} \sigma_M \, d\varepsilon_M \quad \text{Equation 7-7}$$

In the second hypothesis, the same strain is considered for the global mixture and matrix part. In consequence, the values of ε_M^{\max} and ε^{\max} are the same and the value of the energy that goes to the matrix per unit of global mixture can be evaluated from equation 7-8.

$$E_M = \left(\frac{V_M}{V}\right) \int_0^{\varepsilon^{\max}} \sigma_M \, d\varepsilon_M \quad \text{Equation 7-8}$$

In Figure 7-27 it is shown that the stress that goes to compress the matrix is small in relation to the applied stress. This is due to the small stiffness of the matrix in comparison to the rigidity of fragment skeleton.

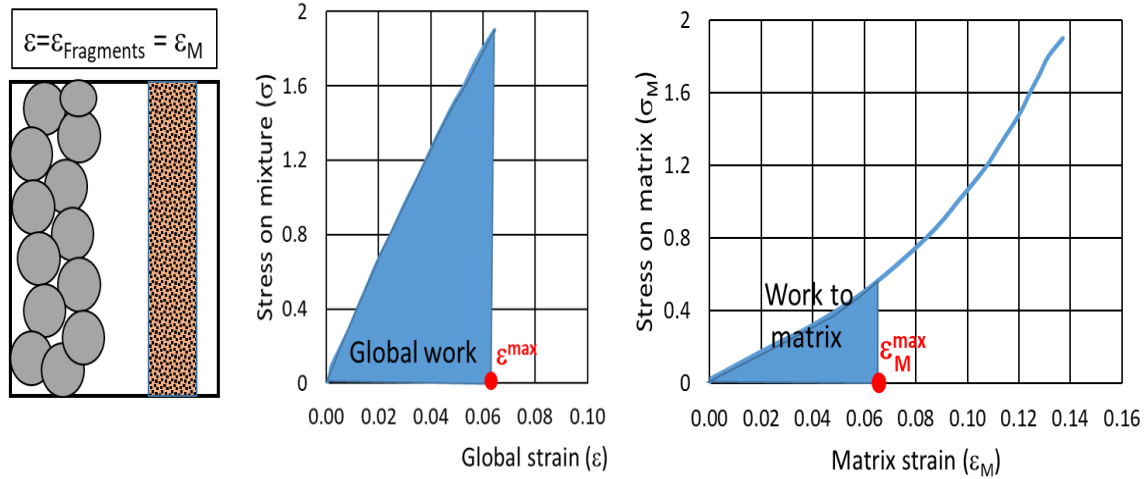


Figure 7-27: Global work and work that goes to the matrix for the oedometric test on FS sample (hypothesis of same strain in matrix and global mixture).

The energy that does not go to compress the matrix is spent in the breakage of the fragments and in the compression of fragments skeleton. Table 7-7 displays the energy contribution during static compaction oedometer tests for all mixtures (FN, FA, and FS). Taking into account that the amount of matrix particles is of 60% of the mixture, the second hypothesis may be more adequate because the structure of the binary mixture is interactive-underfilled. In this case, an important part of the applied energy goes to deform the skeleton formed by the fragments and to fragment breakage. The energy that goes to the fragments increase with the stiffness of the fragments.

Table 7-7: Energy (kPa) distribution through matrix and breakage of the particles in static loading oedometer compaction.

Type of material	Hypothesis	Maximum strain in the matrix (%)	Energy to matrix/ volume mixture (kNm/m ³)	Energy to fragments/ volume mixture (kNm/m ³)	Energy to matrix / Total energy (%)	Energy to fragments / Total energy (%)
FN	1	12.7	62	31	67.0	33.0
	2	10.2	38	54	41.5	58.5
FA	1	8.6	24	42	36.3	63.7
	2	6.8	12	55	17.6	82.4
FS	1	9.2	25	40	39.1	60.9
	2	6.4	10	65	13.8	86.2

Based on data obtained from Table 7-6 and Table 7-7 (second hypothesis), the relationship between Hardin breakage index and energy goes to fragments are presented in Figure 7-28. It appears, there is a good match between Hardin breakage index and energy that goes to particles. In fact, high amount of energy shows higher breakage value, an average value for the ratio $\Delta Br/\Delta Energy$ of $0.0027 \text{ m}^3/\text{kNm}$ has been obtained.

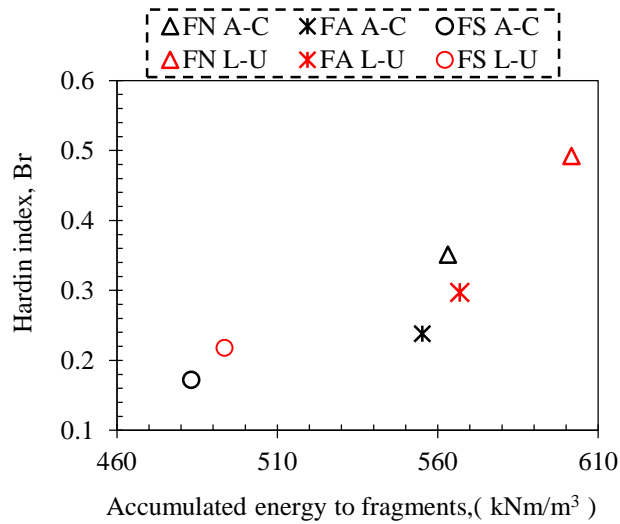


Figure 7-28: Relationship between Hardin breakage index and accumulated energy goes to fragments for various types of mixture.

In addition, the ratio of the differences in Harding breakage index after dynamic and static oedometer test over energy that goes to fragments may be related to the accumulated global strain in the oedometer. This relationship is shown in Figure 7-29. The effect of the strain is not significant, for the three materials an average value of for the ratio $\Delta Br/\Delta Energy$ of $0.0044 \text{ m}^3/\text{kNm}$ can be considered.

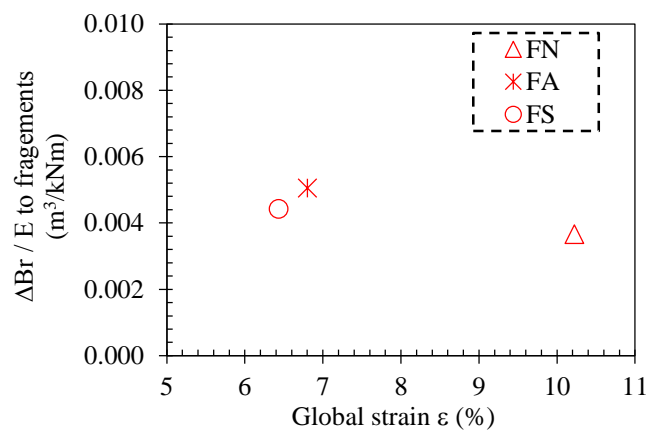


Figure 7-29: Ratio of breakage/energy to fragments as a function of accumulated strain.

7.2 Oedometer tests with saturation process at different vertical stresses

7.2.1 Introduction

The hydraulic and mechanical properties of compacted 'all-one' material with the same 10 % water content in the matrix part are investigated for various types of material under 0.075 and 1 MPa saturated conditions. (At 0.075 MPa saturation- Matrix, $\rho=1.72 \text{ Mg/m}^3$, $e=0.578$ and $S_r=0.430$; FN, $\rho=1.68 \text{ Mg/m}^3$, $e=0.594$ and $S_r=0.309$; FA, $\rho=1.71 \text{ Mg/m}^3$, $e=0.572$ and $S_r=0.354$; FS, $\rho=1.80 \text{ Mg/m}^3$, $e=0.524$ and $S_r=0.31$; At 1 MPa saturation- Matrix, $\rho=1.72 \text{ Mg/m}^3$, $e=0.571$ and $S_r=0.435$; FN, $\rho=1.68 \text{ Mg/m}^3$, $e=0.600$ and $S_r=0.306$; FA, $\rho=1.71 \text{ Mg/m}^3$, $e=0.570$ and $S_r=0.355$; FS, $\rho=1.80 \text{ Mg/m}^3$, $e=0.500$ and $S_r=0.357$). Various types of mixture FN, FA, FS, and pure matrix are evaluated under two oedometer conditions. At the first oedometer test, materials are loaded statically to the vertical stress of 1 MPa, and then fully saturated by imbibition with distilled water for 48 hours under the same vertical stress. Later material was loaded up to 2 MPa and unloaded up to 0.05 MPa. In the second test, materials are saturated at the beginning of the test under a load of 0.075 MPa, and then loaded up to 2 MPa and unloaded up to 0.05 MPa.

The results obtained from the oedometer tests were analysed considering these parameters: compressibility, collapse deformation, oedometric modulus, creep, and the direct and indirect permeability measurements. The parameters mentioned are the main factors to consider in the design of several constructions such as a dam, embankment, and etc.

7.2.2 Compressibility analysis

The compressibility of samples under different conditions is represented by plotting volumetric strain against the logarithm of vertical stress. as shown in Figure 7-30. It can be seen that the highest volumetric strain is around 20.21 % that occurs in the pure matrix in saturation at 1 MPa oedometric conditions. This amount is reduced by 57.14 %, 40.82 %, and 17.67 % correspond to FS, FA, and FN, respectively. It means that by increasing the strength of the fragments in global mixtures the volumetric strains are lower when are compared to the strains of pure matrix. The same behaviour is observed in saturation at 0.075 MPa. In all cases, for each type of fragment, the samples saturated under 0.075 MPa or 1 MPa reach similar strains after the collapse.

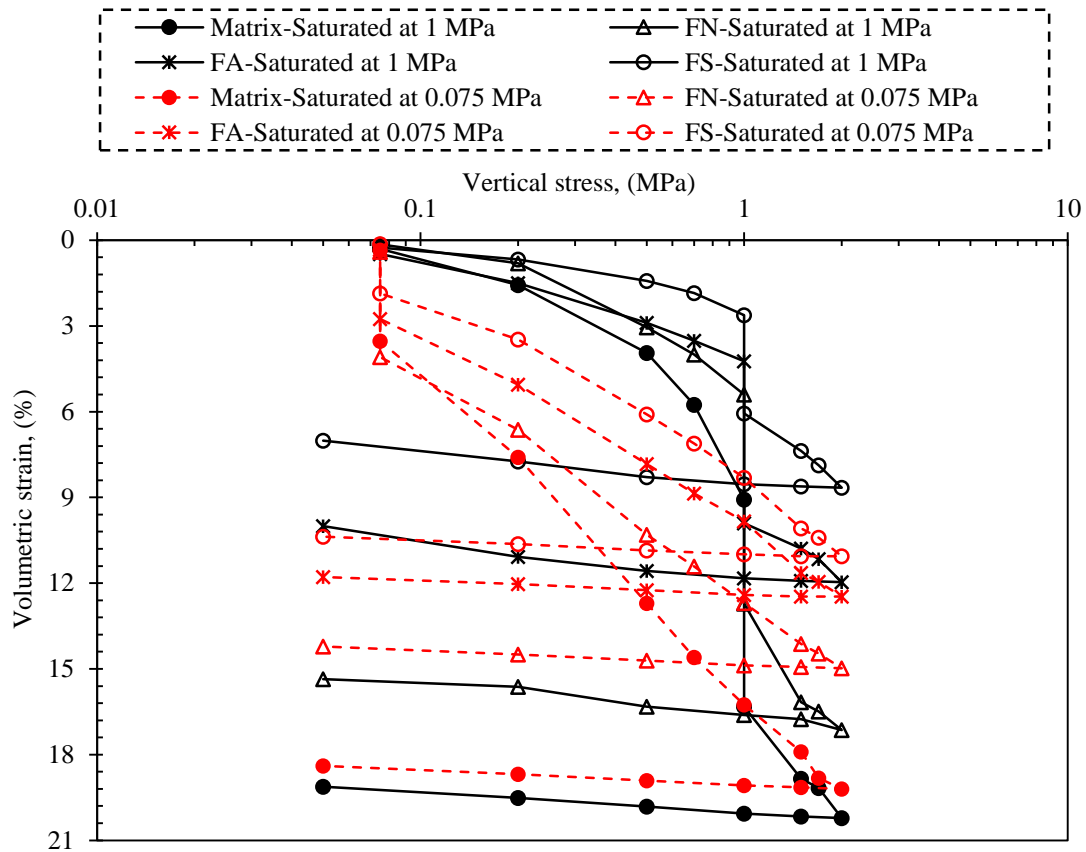


Figure 7-30: Volumetric strain versus vertical effective stress in all mixtures.

In the case of dry condition, as discussed in the previous section, the changing in volumetric strain can be related to the breakage of the fragments, but in the saturated conditions the formation of clay aggregates make impossible to perform the sieve analysis needed to obtain breakage indices. After the tests, two types of behaviour are observed in saturation samples. In the first group that includes pure matrix and natural clay fragments (FN), in addition to the effect of breakage, water acts making less hard the internal bonds and fragments to become softer. This means that water disrupts fragments physically and causes more deformation. On the other hand, in the second group that contained artificially fragments (FA) and slate (FS), the granular particles dose not lose the internal bonds and deformation regarded to deformation of the matrix part and the rearrangement of the large fragments. Figure 7-31 shows the effect of water on the structure of different samples. It is clear that in dry condition fragments break and is easy to distinguish, but in presence of water, the internal bonds of matrix part in all mixtures and aggregates of natural fragments are destroyed.

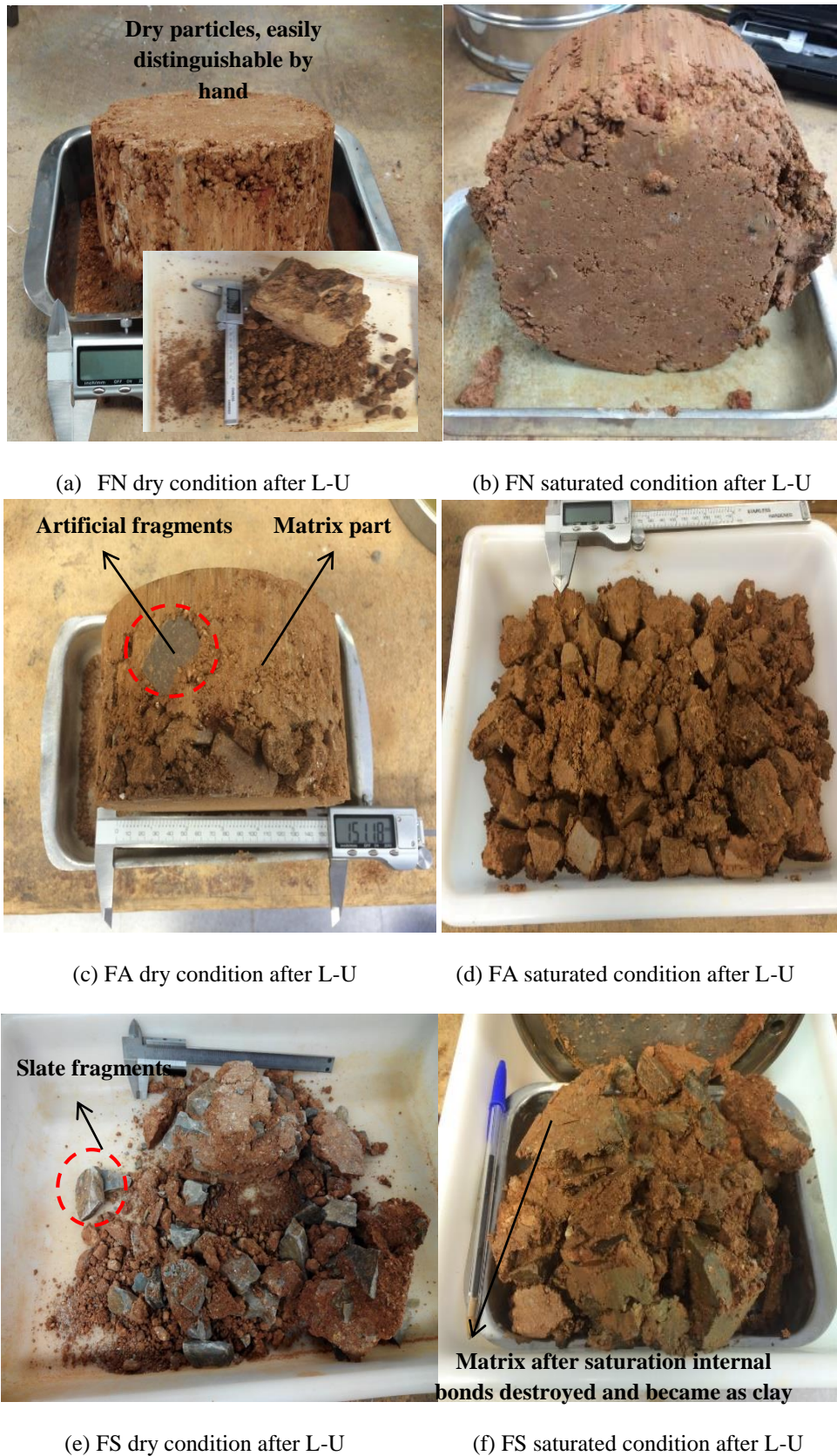


Figure 7-31: Structural changes of various samples under dry and wet conditions after L-U oedometer conditions.

In order to assess the compression and swell index, the relationship between void ratio and the logarithm of pressure for the four types of mixtures both global mixture and matrix part are presented in Figure 7-32 to Figure 7-35.

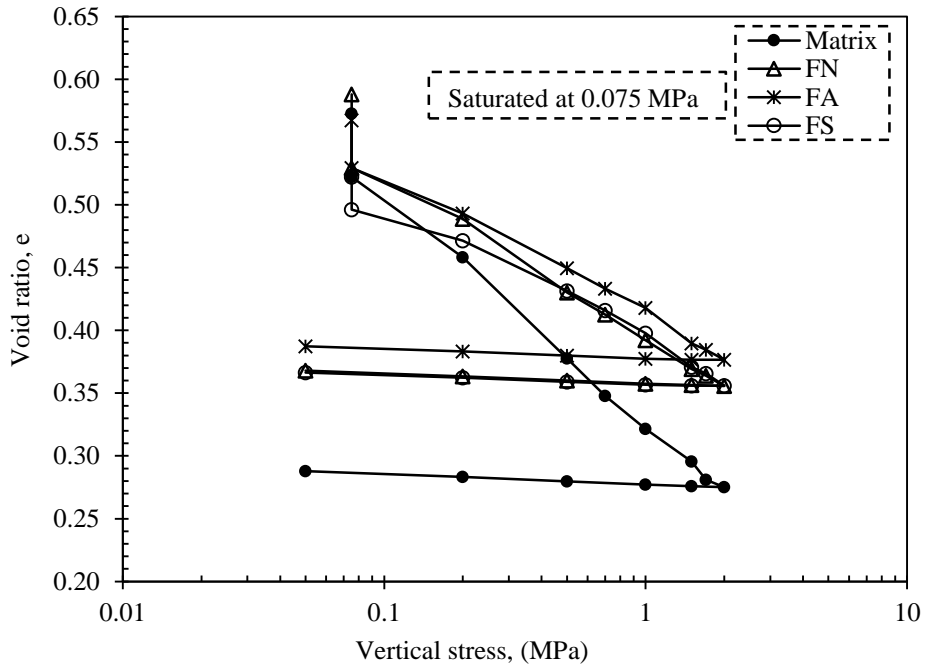


Figure 7-32: Results of the oedometric tests performed for all the materials in global mixtures (saturation under 0.075 MPa).

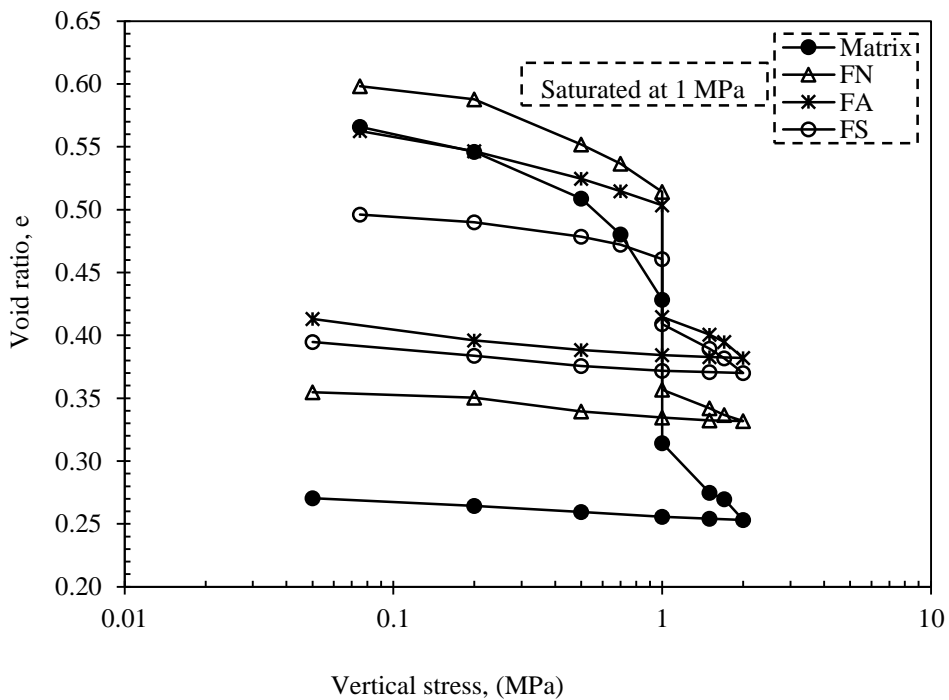


Figure 7-33: Results of the oedometric tests performed for all the materials in global mixtures (saturation under 1 MPa).

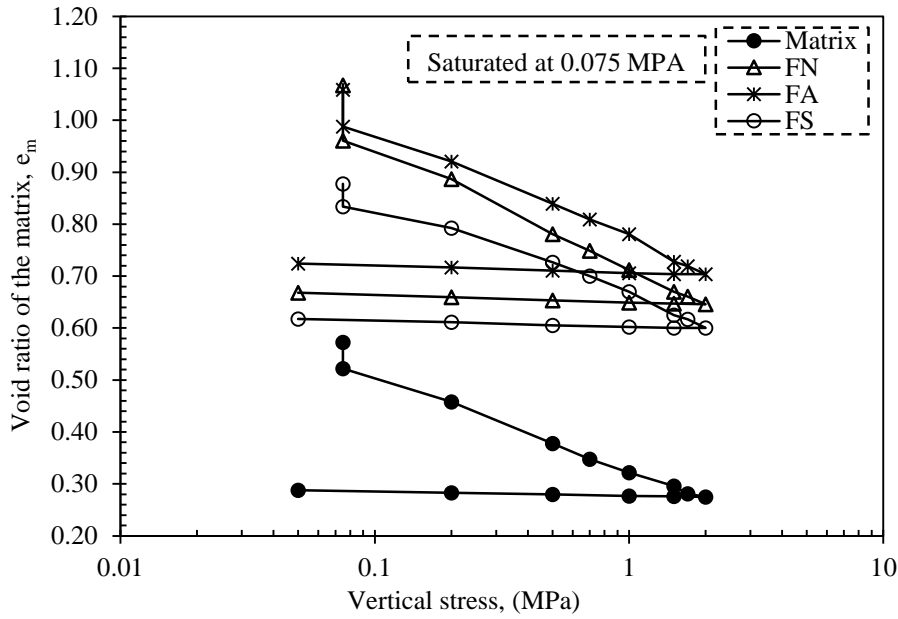


Figure 7-34: Results of the oedometric tests performed for all the materials in matrix part (saturation under 0.075 MPa).

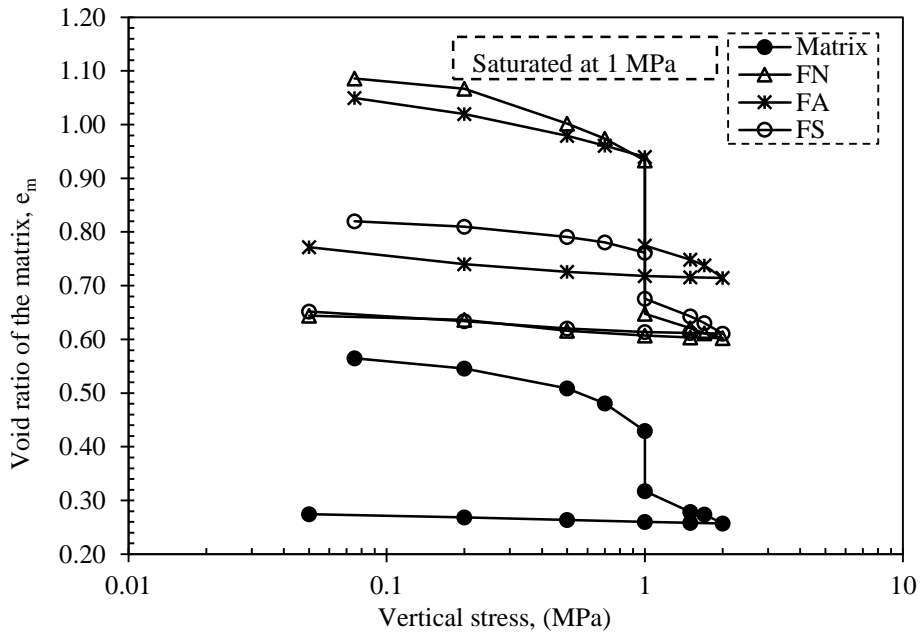
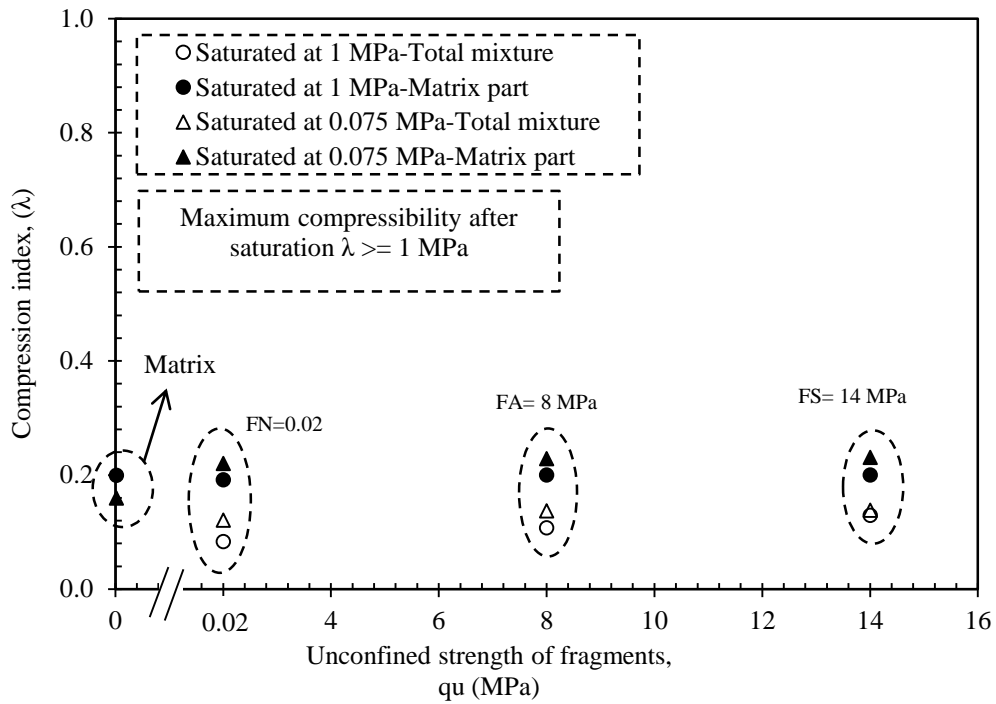


Figure 7-35: Results of the oedometric tests performed for all the materials in matrix part (saturation under 1 MPa).

It is clear that the shape of all curves is concave down before saturation, however, after saturation the behaviours tends to be linear. The compressibility and swelling indices are displayed versus the strength of the fragments in Figure 7-36 and Figure 7-37. In order to compare These values in all curves the compressibility was calculated between 1 and 2 MPa of vertical stresses.



. Figure 7-36: Comparison of compressibility index in respect to unconfined strength of the fragments.

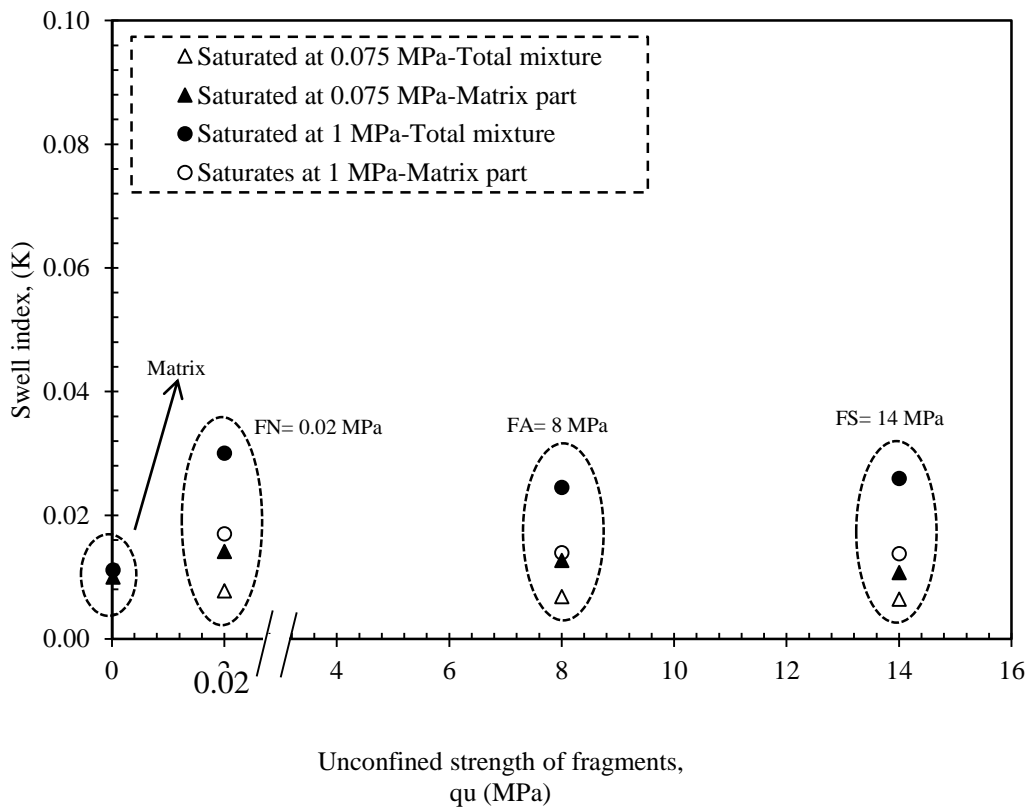


Figure 7-37: Comparison of compressibility index in respect to unconfined strength of the fragments

Looking at above figures, it is apparent that by increasing the strength of the fragments small variation of compressibility observed. Moreover, these values are higher in matrix part of the mixture than a global mixture. In addition, the compression index of the matrix part is almost the same for all mixtures. As well as the similar behaviour is detected in the rebounded index.

7.2.3 Collapse deformation analysis

The collapse deformations are evaluated for all mixtures under two vertical loads. Firstly, the evolutions of the all samples during the loading up to saturated load and wetting process are presented in Table 7-8 to Table 7-15.

Table 7-8: The evolution of the pure matrix during the loading and wetting process at 0.075 MPa.

Step	Vertical stress σ'_v (MPa)	Strain ε_v (%)	e	S_r	ρ_d (Mg/m ³)
Initial	0	0	0.578	0.430	1.71
Loading	0.075	0.344	0.572	0.434	1.72
Saturation	0.075	3.535	0.522	1.000	1.77

Table 7-9: The evolution of the FN mixture during the loading and wetting process at 0.075 MPa.

Step	Vertical stress σ'_v (MPa)	Strain ε_v (%)	e	S_r	ρ_d (Mg/m ³)	$\rho_{dmatrix}$ (Mg/m ³)
Initial	0	0	0.594	0.309	1.69	1.29
Loading	0.075	0.407	0.588	0.312	1.70	1.30
Saturation	0.075	4.089	0.529	1.000	1.77	1.37

Table 7-10: The evolution of the FA mixture during the loading and wetting process at 0.075 MPa.

Step	Vertical stress σ'_v (MPa)	Strain ε_v (%)	e	S_r	ρ_d (Mg/m ³)	$\rho_{dmatrix}$ (Mg/m ³)
Initial	0	0	0.572	0.354	1.72	1.31
Loading	0.075	0.327	0.567	0.357	1.72	1.31
Saturation	0.075	2.754	0.529	1.000	1.77	1.36

Table 7-11: The evolution of the FS during the loading and wetting process at 0.075 MPa.

Step	Vertical stress σ'_v (MPa)	Strain ε_v (%)	e	S_r	ρ_d (Mg/m ³)	$\rho_{dmatrix}$ (Mg/m ³)
Initial	0	0	0.524	0.361	1.77	1.44
Loading	0.075	0.136	0.5223	0.383	1.77	1.44
Saturation	0.075	1.856	0.4961	1.000	1.81	1.47

Table 7-12: The evolution of the pure matrix during the loading and wetting process at 1 MPa.

Step	Vertical stress σ'_v (MPa)	Strain ε_v (%)	e	S_r	ρ_d (Mg/m ³)
Initial	0	0	0.571	0.435	1.72
Loading	1	8.923	0.428	0.580	1.89
Saturation	1	16.063	0.314	1.000	2.05

Table 7-13: The evolution of the FN mixture during the loading and wetting process at 1 MPa.

Step	Vertical stress σ'_v (MPa)	Strain ε_v (%)	e	S_r	ρ_d (Mg/m ³)	$\rho_{dmatrix}$ (Mg/m ³)
Initial	0	0	0.600	0.306	1.69	1.29
Loading	1	5.397	0.514	0.357	1.78	1.39
Saturation	1	12.714	0.357	1.000	1.99	1.63

Table 7-14: The evolution of the FA mixture during the loading and wetting process at 1 MPa.

Step	Vertical stress σ'_v (MPa)	Strain ε_v (%)	e	S_r	ρ_d (Mg/m ³)	$\rho_{dmatrix}$ (Mg/m ³)
Initial	0	0	0.5700	0.355	1.72	1.31
Loading	1	4.233	0.503	0.402	1.80	1.39
Saturation	1	9.898	0.414	1.000	1.91	1.52

Table 7-15: The evolution of the FS mixture during the loading and wetting process at 1 MPa.

Step	Vertical stress σ'_v (MPa)	Strain ϵ_v (%)	e	S_r	ρ_d (Mg/m ³)	$\rho_{dmatrix}$ (Mg/m ³)
Initial	0	0	0.5000	0.357	1.80	1.47
Loading	1	2.623	0.460	0.387	1.85	1.52
Saturation	1	6.060	0.409	1.000	1.92	1.60

Table 7-16 displays the comparison of collapse deformation in both matrix and global mixtures. It is clear that the value of collapse deformation in matrix part is higher than in global mixture for all samples. This is because the fragments are slightly deformed when saturated while the matrix has a greater collapse. When the global collapse is measured, both the deformation of the fragments and the matrix are taken into account.

Table 7-16: Summary of the collapse deformation in both matrix and global part of the various mixtures.

Collapse deformation ($\Delta e/1+e_0$), (%)				
Conditions	Pure matrix	FN	FA	FS
Saturated at 0.075 MPa-Total mixture	3.19	3.68	2.43	1.72
Saturated at 0.075 MPa-Matrix part	3.19	5.13	3.43	2.32
Saturated at 1 MPa-Total mixture	7.14	9.83	5.67	3.44
Saturated at 1 MPa-Matrix part	7.14	13.66	8.02	4.69

The data affected the collapse deformation are presented in Table 7-17 for both saturated conditions.

Table 7-17: Parameters related to collapse deformation under two vertical loads.

Type of mixture	Saturated at 0.075 MPa			Saturated at 1 MPa		
	Collapse deformation %	S _r Before collapse	ρ _d (Mg/m ³) before collapse	Collapse deformation %	S _r before collapse	ρ _d (Mg/m ³) before collapse
FN	3.69	0.312	1.70	10.39	0.357	1.78
Matrix	3.20	0.434	1.72	7.98	0.508	1.89
FA	2.43	0.357	1.72	5.91	0.402	1.8
FS	1.72	0.383	1.77	3.53	0.387	1.85

In the case of pure matrix and saturation under 0.075 MPa, 3.2 % of collapse occurred, moreover, the FA and FS mixtures decrease this amount by 24 % and 46 %, respectively. It should be considered that by saturation samples at 1 MPa collapse deformation increases compare to saturation at lowest load conditions. The value revealed from the pure matrix, in this case, is equal to 7.98 % which is reduced with FA and FS by 25 % and 56 %, respectively. It is apparent that by changing some parts of the pure matrix and utilizing large fragments to cover all-one mixture concept the collapse deformation reduces. However, it should be considered that the strength and structure of fragments play an important role, because in the case of FN with natural particles and low strength the water acts on interparticle and destroyed the bonds that cause more collapse than the pure matrix. Therefore, in all-one mixtures, strength and microstructure of large particles are the main factors to understanding the collapse behaviour.

At this time, in order to investigate different specimens with a variation of void ratio, dry density, vertical stress, and strength of the fragments, the following expression is proposed to calculate collapse deformation based on above parameters.

$$\text{Calculated } collapse = \alpha q_u^a \ln\left(\frac{\sigma_v}{1kPa}\right)^b e^c \quad \text{Equation 7-9}$$

Where,

q_u= Unconfined strength of fragments.

σ_v= Vertical stress at saturation condition.

e = Void ratio before the collapse.

α , a , b , and c = Fitting parameters.

The calculated and measured collapses using the fitted parameters are shown in Figure 7-38.

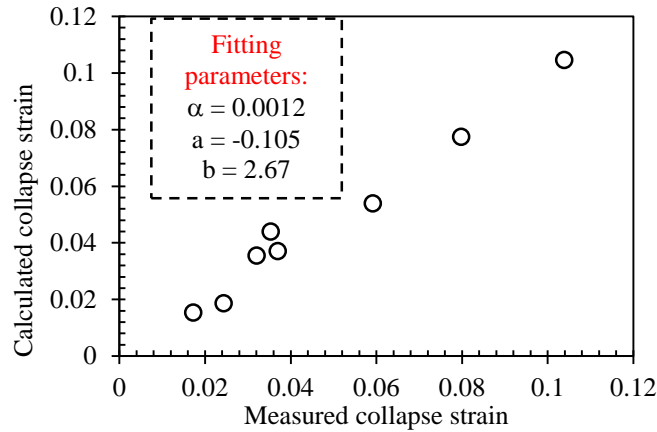


Figure 7-38: Comparison of measured and calculated collapse.

In order to assess the collapse strain associated with the strength of the fragments, the variation of collapse strain is calculated based on strength for the same stresses and dry densities of the mixtures. The results are illustrated in Figure 7-39.

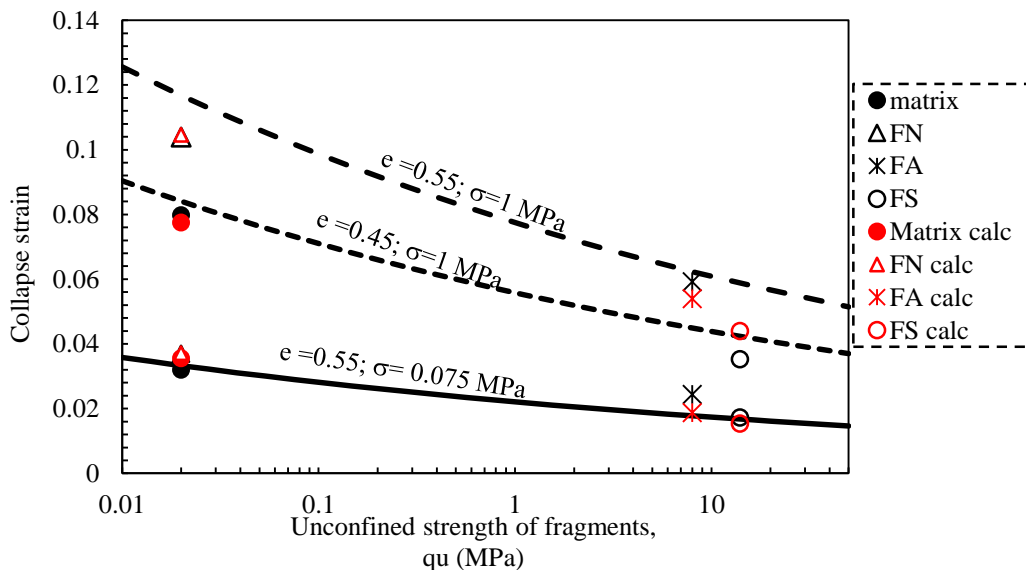


Figure 7-39: Evolution of collapse strain dealing with unconfined strength of fragments for various void ratio and saturation oedometer conditions.

In Figure 7-39 for the same void ratio, there is a clear trend of decreasing in collapse strain by increasing the strength of the fragments in global mixture. These performances detected for the same void ratio and vertical stresses. For the same strength and void ratio of the mixtures, collapse strain rises when the stress at saturation conditions increases. Additionally, the collapse strain is evaluated by variation of void ratio before collapse for the same stresses and strength of the fragments. Figure 7-40 depicts the results for collapse deformation versus different void ratios of mixtures.

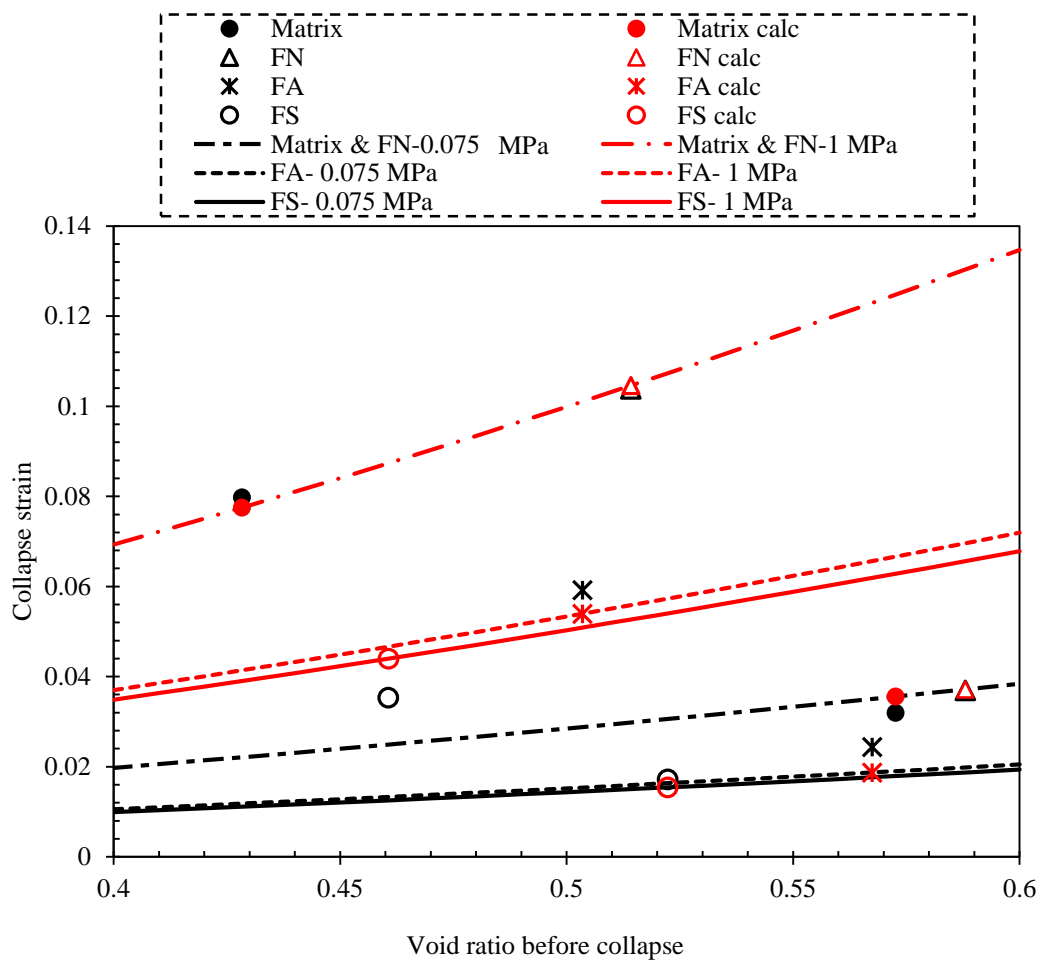


Figure 7-40: Evolution of collapse strain dealing with void ratio for various fragments' strength and saturation loads.

It is clear that at the same saturated load by decreasing the void ratio in total mixtures the amount of collapse strain reduced. The lowest collapse observed in the highest particles' strength. The same mixtures show larger collapse even with smaller amount of void ratio. In general, all the mixtures saturated under 1 MPa displays more collapse strain than those saturated at 0.075 MPa.

7.2.4 Oedometer modulus analysis

The oedometer modulus has been evaluated for all materials under two oedometer stress path both in saturated and dry conditions. The varying of modulus is assessed in different loading steps. Figure 7-41 depicts the experimental and calculated modulus related to samples saturation at 1 MPa. As it can be seen, on dry side the modulus increases due to the increment of vertical stress. The highest modulus is associated with slate and artificial fragments because of more rigidity of fragments. On the other hand, the lowest occurs in matrix.

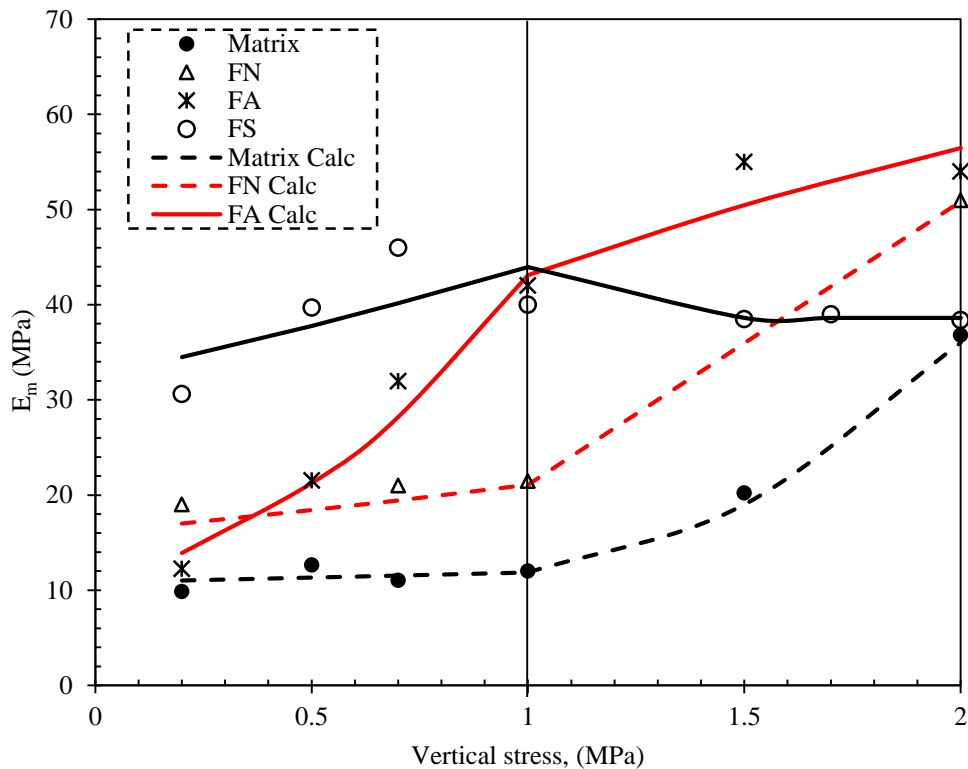


Figure 7-41: Oedometer modulus vs vertical stress in dry and saturated conditions.

In case of saturation at 0.075 MPa, the modulus values are presented in Figure 7-42. From this data, it can be seen that because of constant compressibility index of the mixture the modulus displays a linear tendency. Also, the vertical stress increment is the main factor to increase the modulus of different materials. Again, the highest and lowest modulus is related to FS and matrix, respectively that can be associated with the stiffness of the particles.

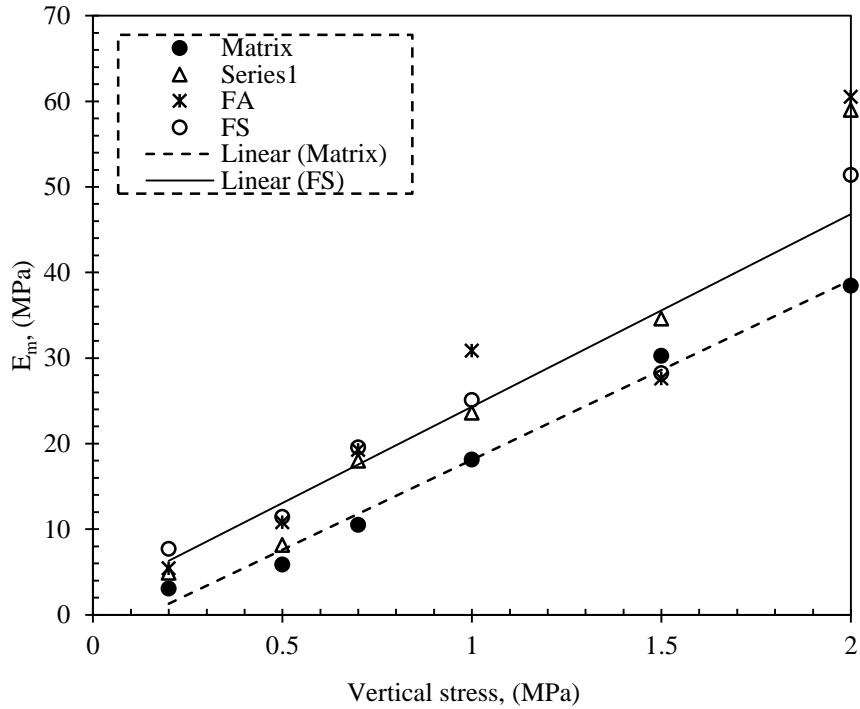


Figure 7-42: Oedometric modulus vs vertical stress in saturated conditions.

7.2.5 Creep analysis

In this section creep deformation of all specimens are investigated during loading and wetting process. The secondary consolidation is calculated between 6000 s to 9000s in the samples saturated at 1 MPa. The time is 6000s to 12000s in case of samples saturated at 0.075 MPa. The results are presented in Figure 7-43 and Figure 7-44. Generally, several parameters can affect the creep behaviour such as: mineral composition, stress level, stress history, drainage condition, and soil structure. In these tests, the results revealed that in all cases, the stress increment increases creep rate. During the time periods specified above the secondary consolidation of natural (FN) and matrix is higher than artificial (FA) and slate (FS) mixtures. The reason can be related to the very fast decomposition of the structure of natural and matrix particles which is easy to break. Moreover, it is a challenge to predict exactly creep deformation by this test. The rearrangements and breakage of slate and artificial fragments can be influenced the creep in the long time period.

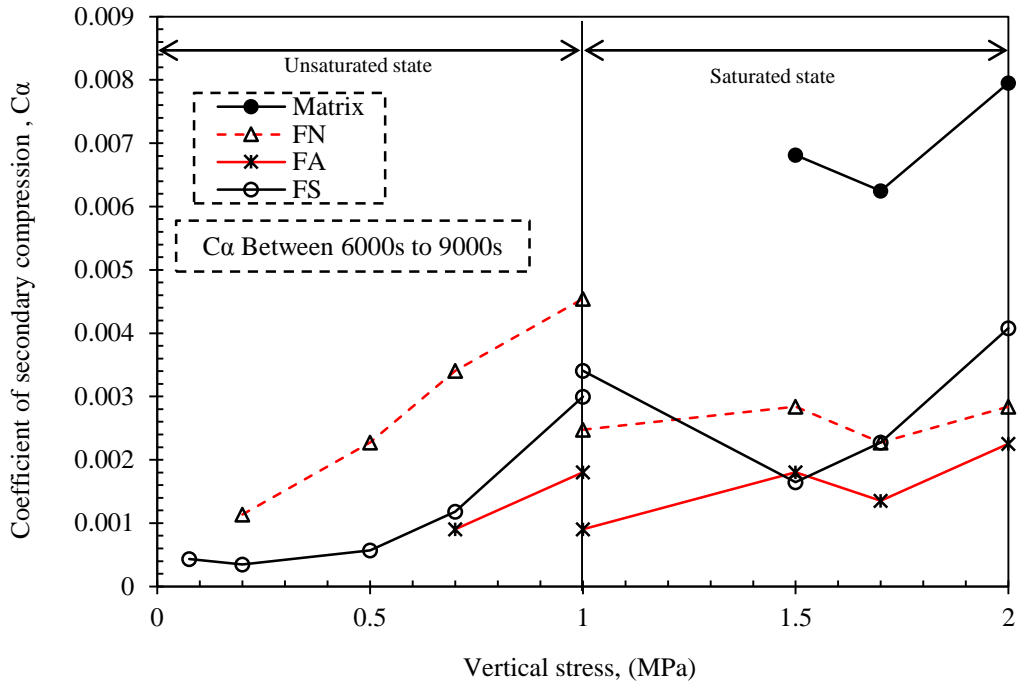


Figure 7-43: Secondary consolidation coefficient $C\alpha$ versus vertical stress. Samples are saturated at 1 MPa.

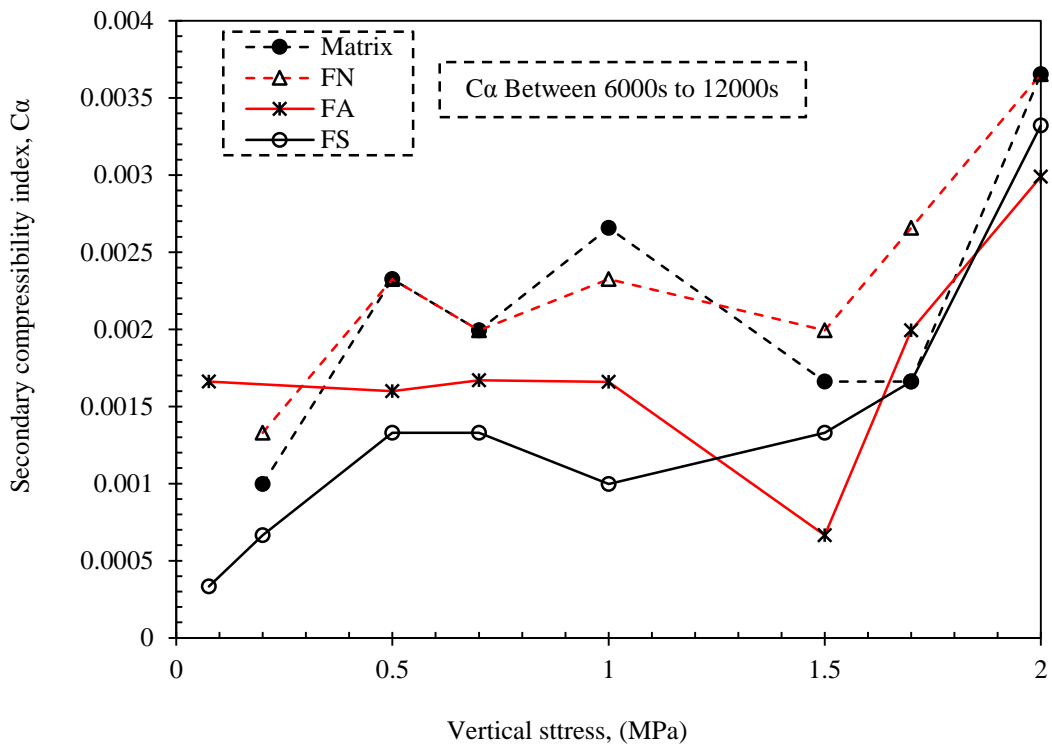


Figure 7-44: Secondary consolidation coefficient $C\alpha$ versus vertical stress. Samples are saturated at 0.075 MPa.

7.2.6 Direct and indirect permeability measurements

The water permeability was measured for all samples (FN, FA, FS, and pure matrix) in both direct and indirect methods during and after saturation conditions. In the direct method, permeability obtained by a process described in methodology chapter for the samples under a constant vertical stress in a saturation state. In indirect method, time evolution of soil deformation has been interpreted using a non-linear curve-fitting algorithm, in order to determine the different conventional parameters used in consolidation analysis following Terzaghi's theory (Das. 1983). The vertical displacement under an effective stress increment $\Delta(\sigma_v - u_w)$ can be theoretically expressed as:

$$d = d_0 + \frac{2h}{E_k} \delta(\sigma_v - u_w) \bar{U}(t, C_v) + 2hC_\alpha \log(t/t_{90}) \quad \text{Equation 7-10}$$

Where, d_0 is the initial compression mainly due to the equipment deformability, $2h$ the mean thickness of the specimen, E_k the drained constrained modulus of elasticity, $\bar{U}(t, C_v)$ the average degree of consolidation that is a function of time t and the coefficient of consolidation C_v (Lambe and Whitman. 1979; Das. 1983b), C_α the coefficient of secondary consolidation, and t_{90} the time required for 90% of average consolidation.

Later based on data obtained by fitting consolidation curve, saturated water permeability values k_{ws} can be indirectly estimated from consolidation data, according to the equation 7-11 that is based on Terzaghi's theory of the rate of consolidation (Das. 1983).

$$K_{ws} = \frac{C_v * \gamma_w}{E_k} \quad \text{Equation 7-11}$$

Where $\gamma_w = 9.8 \text{ kN/m}^3$ is the unit weight of water.

In fact, fitting consolidation curve has been done for all samples with various vertical stresses, nevertheless here to show an example only the fitted consolidation curves for vertical stress between 1.7 to 2 MPa are depicted in Figure 7-45 for all samples.

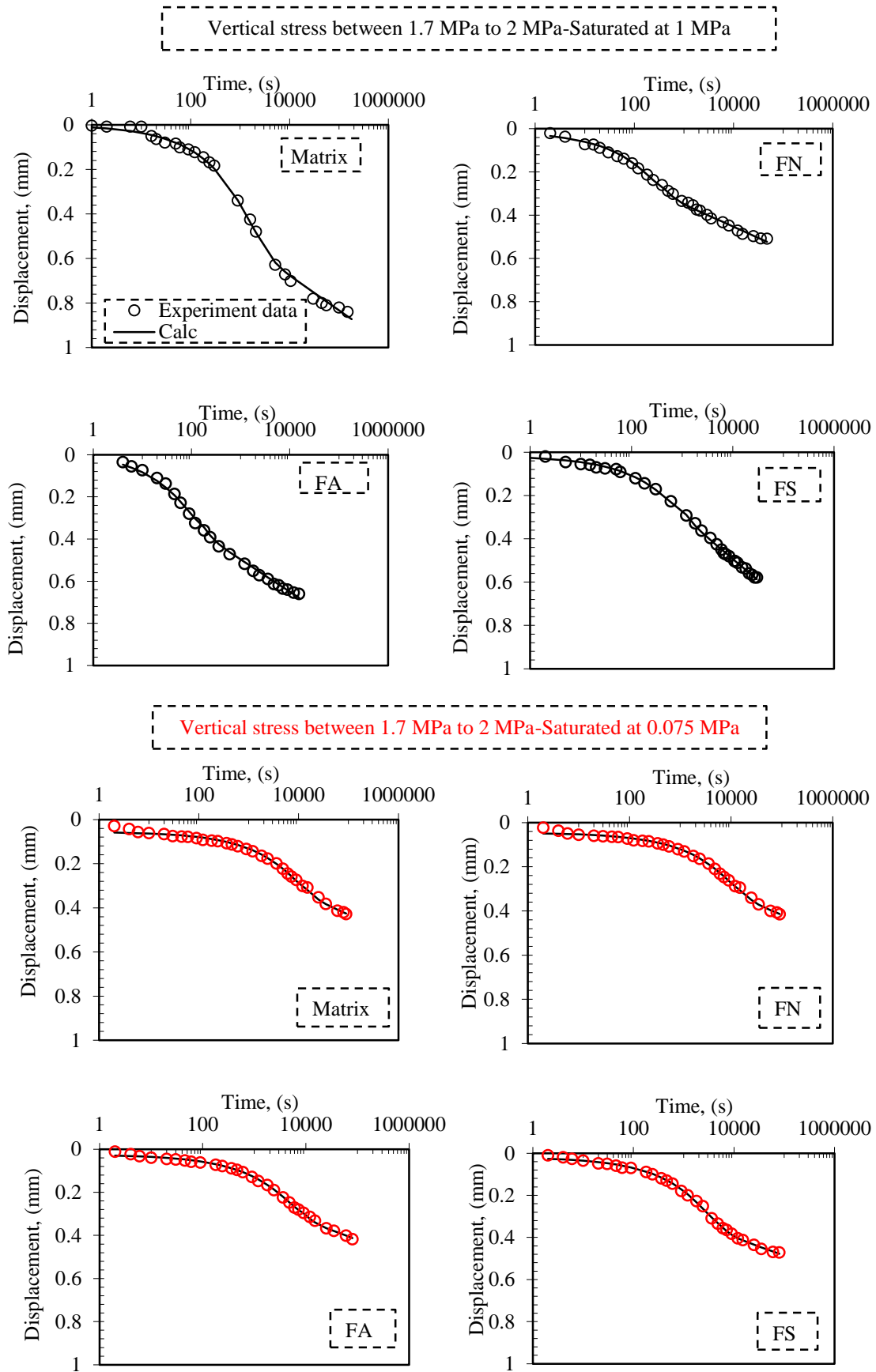


Figure 7-45: Fitted consolidation curves for vertical stress between 1.7 to 2 MPa for all samples.

To evaluate the effect of vertical stress on the saturated permeability, Figure 7-46 and Figure 7-47 provide the permeability results under (including samples saturated under a vertical effective stress of 0.075 MPa, and 1 MPa). The data obtained from consolidation back-analysis and direct measurements at saturated load are presented.

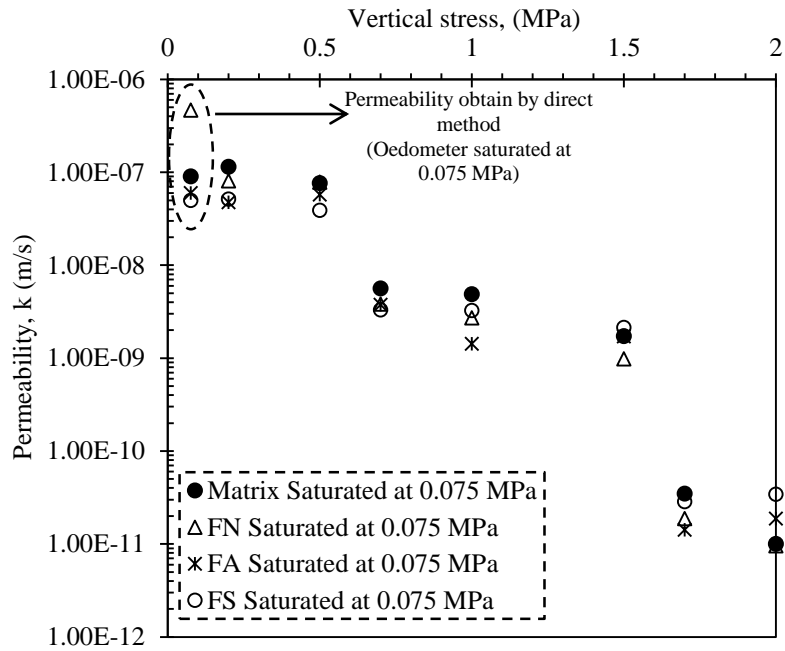


Figure 7-46: Permeability vs vertical stress. Samples saturated at 0.075 MPa.

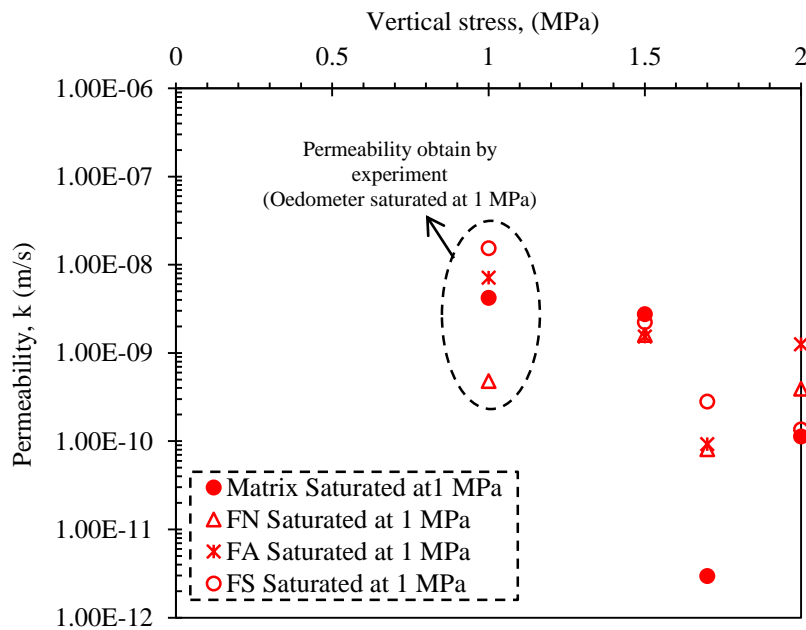


Figure 7-47: Permeability vs vertical stress. Samples saturated at 1 MPa.

Generally, It is clear that the permeability reduced during the increment of vertical stress. It has been found that from Figure 7-46, at the first saturated load the FN with natural fragments displays the higher amount of permeability equal to 4.68×10^{-7} m/s. This value decreases to 9×10^{-8} , 6×10^{-8} , and 5×10^{-8} m/s corresponding to matrix, FA, and FS, respectively. Because at the load of 0.075 MPa the specimens are directly saturated after compacted by standard Proctor energy, therefore the lowest initial dry density of the FN ($\rho_d = 1.69 \text{ Mg/m}^3$) is a reason for high permeability. The values of initial dry densities for the matrix, FA, and FS are 1.71, 1.72, and 1.8 Mg/m^3 . Meanwhile, permeability declined by increasing the load and at the end of loading step the lowest amounts are with respect to matrix and FN. In fact, at high-stress level and saturated state, water and stress applied destroy their granular structure. The aggregate material becomes a clayey soil, which is in accordance with the permeability value measured is about 10^{-12} m/s for clayey materials. Nevertheless FS, and FA has no clay in their aggregates, thus have no high water absorption capacity and therefore its final permeability is probably higher than those of FN and matrix.

In the case of saturated at 1 MPa, similar behaviour of permeability at the first saturated loaded are not observed compared with saturated at 0.075 MPa. The high values of densities are the reason to obtain the same behaviour of the permeability in all stresses after saturation at high stress.

In addition, the water permeability tests are plotted as a function of void ratios for all mixtures (Figure 7-48). The higher the void ratio reduction, the higher is the permeability reduction.

Finally, the permeability is presented through the void ratio of the matrix compared with pure matrix. The obtained permeability dealing with matrix void ratio is depicted in Figure 7-49. The low value of the permeability of the fragments forces the water to find ways through the matrix avoiding passing through the fragments. This implies an increase of the tortuosity and a decrease of permeability.

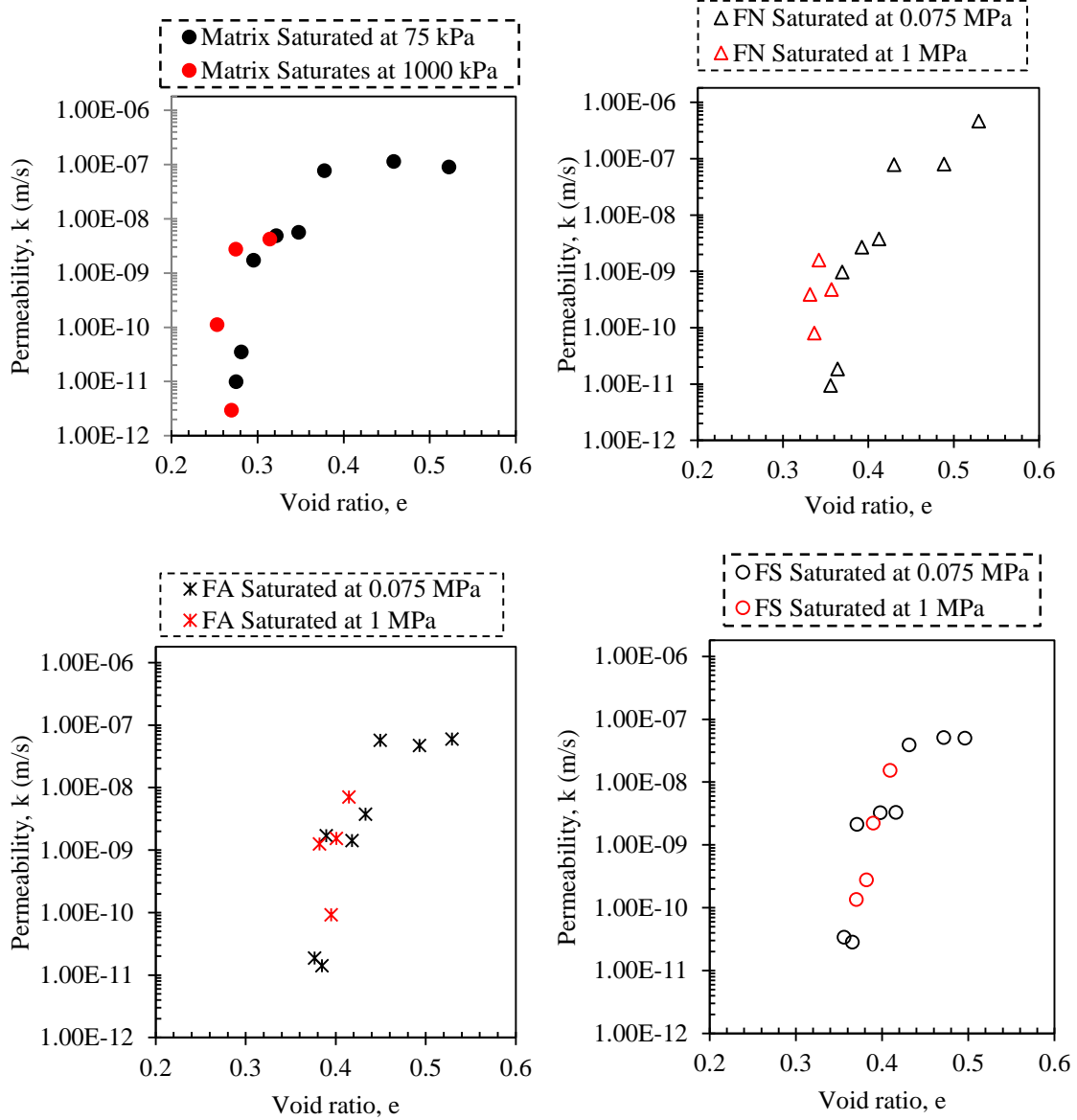


Figure 7-48: The permeability in respect to the variation of void ratio under to saturation condition for all types of mixtures.

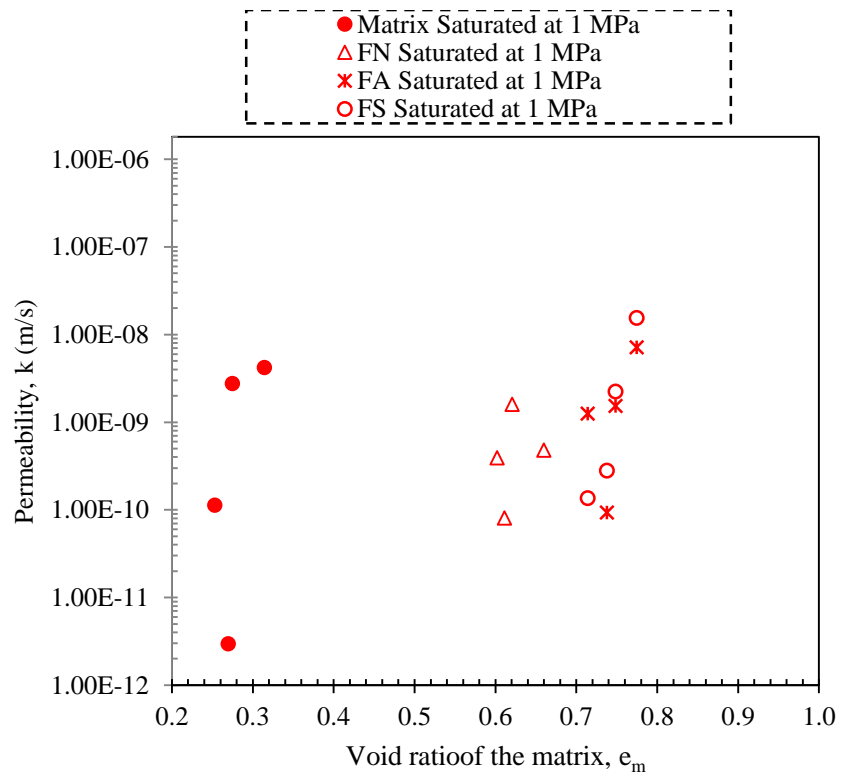
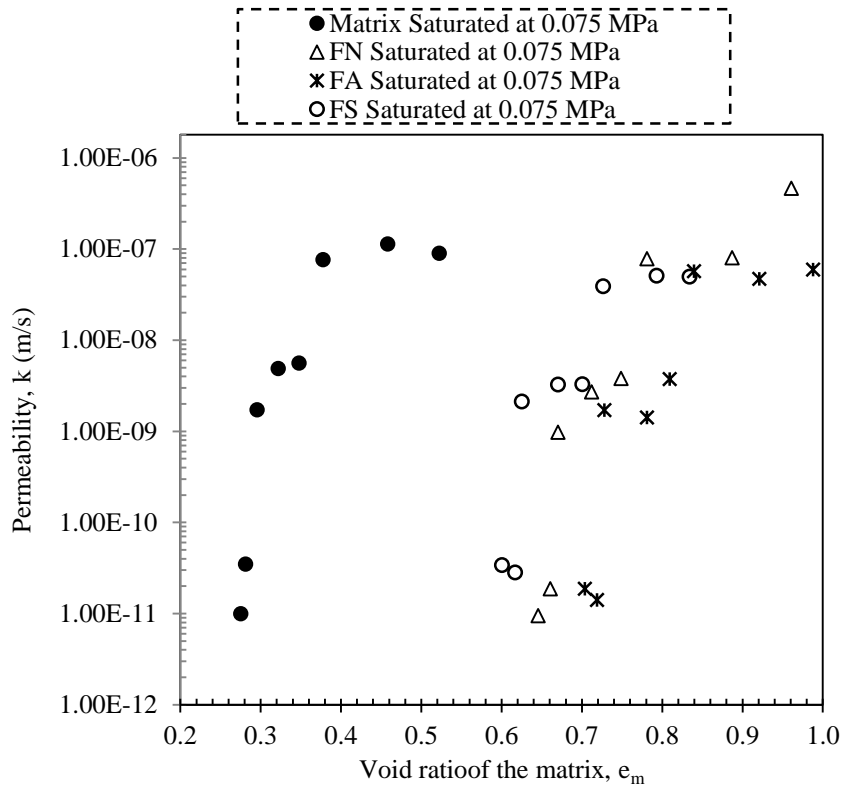


Figure 7-49: The permeability in respect to the variation of matrix void ratio under to saturation condition for all types of mixtures

7.3 Water retention curve and suction equalization

To assess water retention curve, fragments are selected after loading-unloading saturated conditions test. The WP4 device used to measure suction values in the range between 1 to 100 MPa. The water retention curve (WRC) in drying path is presented in Figure 7-50 for FN, FA, and FS. It was fitted by equation 7-7 (van Genuchten, 1980), where S_e is the saturation degree at the current liquid pressure, P_l , P_g is the gas pressure, P and λ are fitting parameters. The parameter P is related with the air entry values of the soil mixtures.

$$S_e = 1 + \left[\left(\frac{P_g - P_l}{P} \right)^{\frac{\lambda}{1-\lambda}} \right]^{-\lambda} \quad \text{Equation 7-12}$$

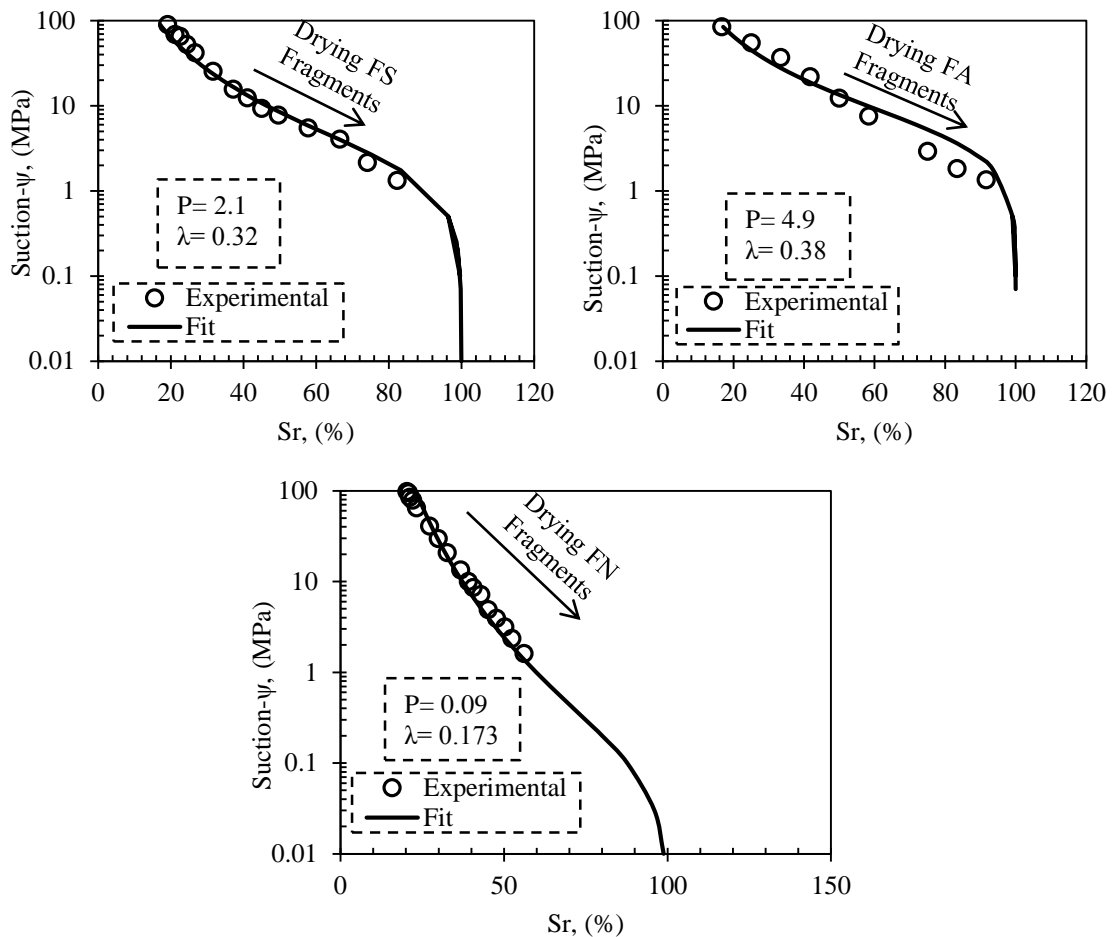
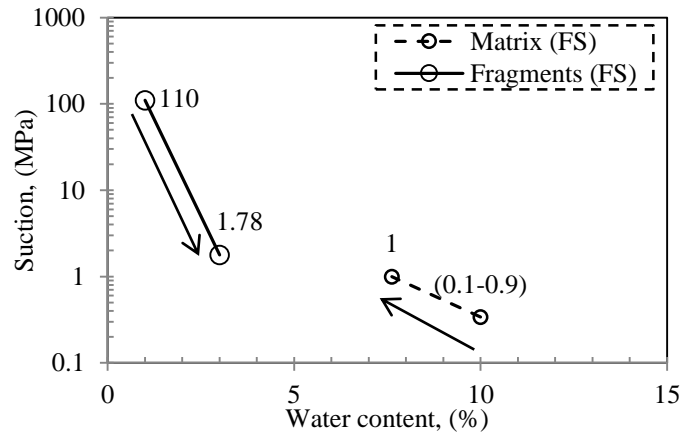


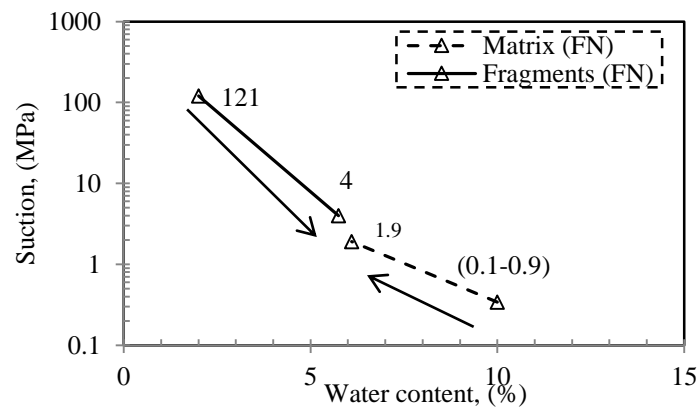
Figure 7-50: Water retention curve of the fragments dealing with the degree of saturation, drying paths.

To investigate the equalization of the initial suctions in the fragments and the matrix, the transference of water from the matrix to the fragments was measured. The suction of the

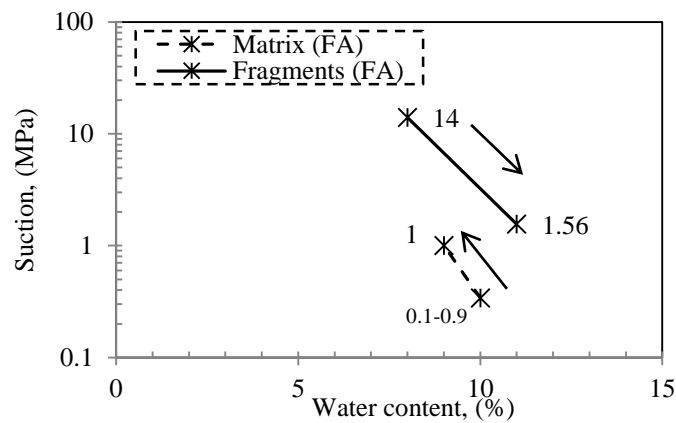
matrix and the fragments was measured before and after the test for all samples. The data are shown in Figure 7-51. It reveals that the suction reaches equilibrium conditions at values near 1MPa after each test between the matrix part and large fragments.



(a)



(b)



(c)

Figure 7-51: Suction equilibration during oedometer saturation condition.

7.4 Collapse comparison

The ‘all-one’ mixture utilized in the structure of Albagés dam originated due to the excavation of argillite and sandstones from the Oligocene epoch. As a construction material, the material constituted mainly by argillite and sandstone is the dominant material of the project. The dry density of the all-one material is around 2.1 Mg/m^3 after in situ compaction conditions with a water content of 10%. It has a liquid limit of 30% and a plasticity index of 13.6%. Here the strength properties of sandstone and argillite are presented.

Figure 7-52 shows the simple compression tests results by Romero, (2004). It can be seen that the average resistance of sandstone material is 15-26 MPa. The sandstone material behave like a medium quality rock. The argillite are softer than sandstone.

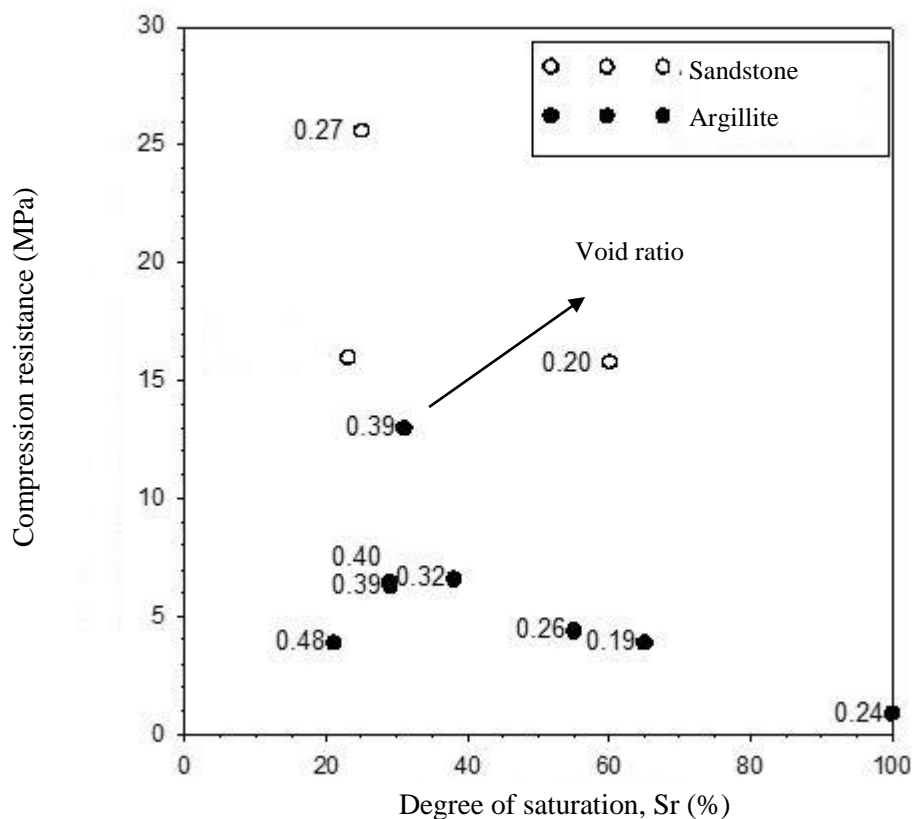


Figure 7-52: Results of compression test versus degree of saturation for sandstone and argillite with various void ratios.

In order to compare the collapsibility results of all-one material in the construction of the Albagés dam with this investigation, a normalised collapse analysis can be done taking into account the following relations:

$$\Delta \mathcal{E} = \frac{\lambda - k}{1 + e_1} \ln \frac{\sigma}{\sigma^*} \quad \text{Equation 7-13}$$

$$\lambda^* = \lambda - k \quad \text{Equation 7-14}$$

$$\Delta \mathcal{E} = \frac{\lambda^*}{1 + e_1} \ln \frac{\sigma}{\sigma^*} \quad \text{Equation 7-15}$$

$$e_1 = a - \lambda^* \ln \sigma^* \quad \text{Equation 7-16}$$

$$\varepsilon_0 = \frac{a - e_1}{1 + e_1} \quad \text{Equation 7-17}$$

$$\frac{\Delta \mathcal{E} - \varepsilon_0}{\ln \sigma} = \frac{\lambda^*}{1 + e_1} \quad \text{Equation 7-18}$$

In base of the preceding formulation, the collapse strain can be normalized using the natural logarithm of the vertical stress ($\Delta \mathcal{E} / \ln \sigma$). The results of normalized collapse strain for various material with different strengths are plotted versus the void ratio before collapse (Figure 7-53). The normalized collapse of the sandstone aggregate of Albagés dam results slightly higher than the collapse measured in the binary mixtures tested in this work.

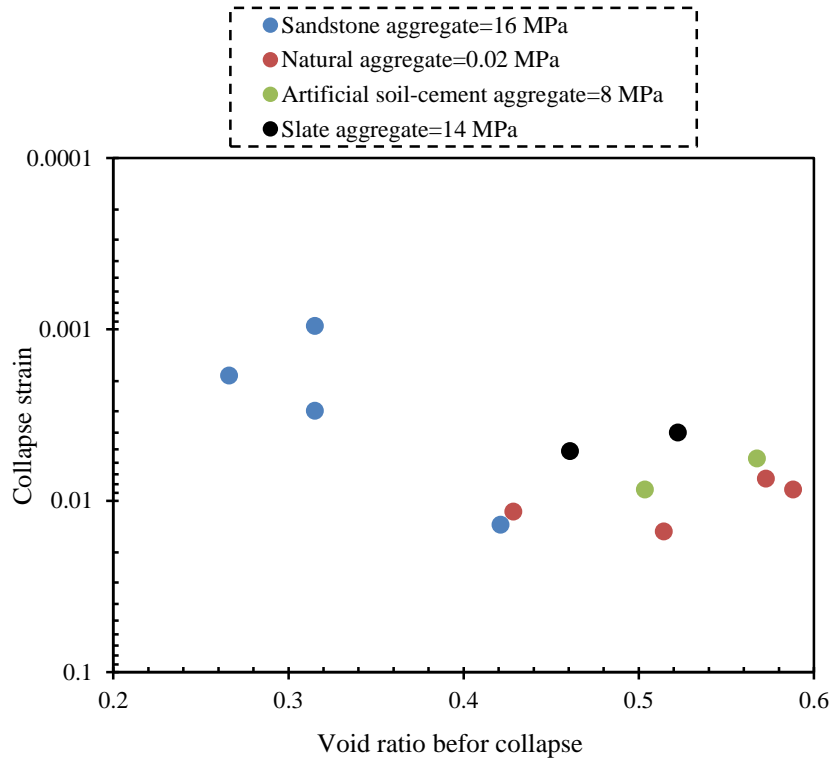


Figure 7-53: The results of normalized collapse strain for various material with different strengths are plotted versus the void ratio before collapse.

It is clear that, the behaviour of collapse strain is in respect to void ratio and strength of the fragments, the lowest collapse occurred in material of dam due to high strength of the fragments and lower void ratio.

8 Summary, concluding remarks and future investigations

8.1 Summary

This experimental study has tried to contribute to improve our understanding of the knowledge of ‘all-one’ materials as granular binary mixtures formed by large fragments and a finer matrix component. Emphasis has been placed in the influence of the properties of the fragments (unconfined shear strength) and the void ratio of the finer matrix to explain the hydro-mechanical behaviour of these mixtures.

Four main parts have been followed in the thesis to perform the experimental research. The first section is performed to explore binary mixture properties with various proportions of fragments. This part allowed obtaining a matrix proportion able to fill nearly all inter-fragments voids and to ensure good compaction properties. In the next section, the behaviour of an in situ compacted ‘all-one’ mixture used in the construction of Albagés dam (Lleida, Spain) is studied as an example of material used in a real case. The third part involved the fabrication of soil-cemented artificial fragments with different uniaxial compressive strengths that allows bridging the gap between low-strength and high-strength fragments. Finally, in the last part, the experimental results of hydro-mechanical tests including loading / unloading cycles under saturated and unsaturated conditions, as well as soaking tests at constant vertical stress, have been evaluated. The microstructural changes along different stress paths are discussed in terms of breakage of the fragments and void ratio changes of the matrix material.

8.2 Concluding remarks

Some of the most important conclusions obtained during this investigation are presented and discussed below.

The ‘all-one’ materials are formed during excavation of natural materials including soil and rock components with different ranges of particle sizes. These complex materials can be studied as binary mixtures formed by large fragments and a finer matrix.

In these mixtures it is important to determine a reference grain size distribution curve to allow the fabrication under laboratory conditions and to cover the range between rockfill particles and soils. Fuller and Thompson (1907) grain size distribution curve was the first

approach to follow. Nevertheless, this grain size distribution was only concentrating on the maximum particle sizes (fragments), but not on the fine particles (matrix). For this reason, another approach was used to prepare the material based on a modified curve following Funk and Dinger (1987), who proposed a grading curve based on both maximum and minimum sizes. Therefore, by using Funk and Dinger approach it was possible to prepare different mixtures with various proportions of fine matrix and large fragments.

The amount of fragments is an important issue to control the behaviour of binary mixtures. By varying the proportions, the behaviour of binary mixtures is controlled by fines, coarse aggregates or both (transition zone). Based on the study of Vallejo (2011), the transition zone can be defined based on the minimum porosity attained after compaction of the binary mixtures with different fine contents. When small proportions of fine particles are mixed with coarse aggregates, fine particles will partially fill the voids between granular fragments, originating a decrease in void ratio until they fill all voids (minimum porosity corresponding to the transition zone). After that, void ratio starts to increase by increasing the amount of fine particles, in which fragments are 'floating' in the matrix. In this research study, the transition zone was obtained at a range of 75 to 85% of matrix content (mass basis) in granular mixtures. Using a proportion of fines slightly lower than that of the transition zone, the mixture behaves as an interactive-underfilled packing structure (López, 2016), and the behaviour is mainly controlled by both the density of the fine matrix and the strength of large aggregates. To achieve this type of mixture, 40 % of granular fragments between 19 to 38.5 mm and a 60% of the fine particles between 19 to 0.15 mm have been selected to perform the hydro-mechanical tests. This way, the matrix proportion will be able to nearly fill all inter-fragments voids and still ensure good compaction properties.

To study the compaction behaviour of the binary mixtures, dynamic compaction using the standard Proctor energy was selected. A new hammer (diameter: 30 mm and height: 305 mm) was developed to increase the number of blows needed to reach the specified energy and to simulate the sheepsfoot roller as a dynamic field compaction. It was decided to compact sample on dry side of the optimum by adding 10 % of water content to the matrix part (at this water content the matrix developed an aggregated structure with dominant macropores between aggregates and micropores inside aggregates).

Before doing the preliminary tests on compacted ‘all-one’ mixtures, a real case study of in situ compacted ‘all-one’ used as shoulder material in the Albagés dam has been considered. The H-M behaviour of the ‘all-one’ material of the Albagés dam was evaluated and main results are listed below:

- At the beginning of compaction procedure, the material started from a distribution curve that was more close to a uniform rockfill material, but during compaction particle breakage occurred tending to a more extended grain size distribution GSD curve (‘all-one’ material). This was observed by comparing the GSD curve before and after field compaction. The field compaction induced no significant changes with depth of the compaction layer. The compaction helped in creating a structure, which was better than the original material not only by densifying it but also creating an extended GSD with better contacts between grains.
- The ‘all-one’ material presented low collapse deformations on soaking. This was confirmed when plotting the normalised collapse results (deformation over vertical stress) of the compacted core material (silty clay) and the ‘all-one’ mixture with the initial void ratio (before collapse). This was a consequence of the extended GSD, in which matrix particles protected larger fragments.
- Despite the good mechanical behaviour, the ‘all-one’ mixture did not display a high permeability (around 10^{-9} m/s), which justified the decision of using a different external upstream shoulder material (coarser material).

One of the objectives of this thesis was to understand how the strength of the fragments and the void ratio of the matrix were controlling specific hydro-mechanical behavioural features of the mixtures.

To reach this objective different types of fragments were used in the binary mixtures. Two different fragment strengths were used with natural materials, namely the natural carbonated fragments with unconfined compression strength of $q_u = 0.02$ MPa and slate fragments with $q_u = 14$ MPa. To bridge the gap between the aforementioned values, artificially prepared fragments were fabricated at $q_u = 8$ MPa. A methodology to fabricate these artificial fragments have been described.

The main H-M behaviour of ‘all-one’ mixtures were evaluated after dynamic compaction using loading-unloading oedometer tests. After dynamic compaction on dry side of the

compaction curve, it was expected to reach a higher value of density in ‘all-one’ mixtures when compared to pure matrix. However, it was observed that the increase in dry density by using ‘all-one’ materials was not only related to the use of large fragments, but also to the strength and microstructure of the fragments. The ‘all-one’ mixture with high value of strength (slate fragments) increased the total value of dry density. Nevertheless, in the case of natural carbonated fragments with weak particles, the total dry density decreased compared to pure matrix. It was clear that some part of the applied energy was transferred to break aggregates instead of densifying the matrix. The energy transferred between fragments and matrix part will be discussed later.

Compacted mixtures were evaluated on loading-unloading oedometer paths on both dry and saturated conditions. At dry conditions, a total vertical stress of 1.9 MPa was continuously applied to the samples and then unloaded to 0.05 MPa. The main results are listed below:

- **Preconsolidation stress:** The increment of preconsolidation stress versus fragment strength (unconfined compression strength) has a linear tendency. It means that the preconsolidation pressure increases by increasing the strength of the large particles within the mixture.
- **Compression (post-yield) and swelling (pre-yield) indices:** No remarkable differences were observed between the compression and swelling indices for all types of mixtures. When the value of compression and swelling indices are evaluated with respect to void ratio of the matrix, the amount of these indices show higher values than those obtained dealing with total mixture void ratio.
- **Elastic constrained modulus:** In case of fragments with high strength the elastic modulus has a relatively constant value with stress increment. Whereas, in case of pure matrix and weak fragments the value of modulus increases by raising the stress. The all-one mixture with high strength of the fragments shows the highest stiffness.

After dynamic compaction and oedometer tests on mixtures at constant water content conditions some changes were observed in grain size distribution due to breakage of the particles. The sieve analysis has been used to detect these differences. The behaviour analysis of samples before and after tests is considered based on particle breakage, fractal analysis, and energy dissipation during compaction. Hardin index and Tyler Wheatcraft

method have been selected to evaluate the breakage and fragmentation in ‘all-one’ mixtures, respectively. In addition, the applied energy to particle breakage during compaction and loading process have been calculated based on the compaction curve of pure matrix and stress-strain curve of loading-unloading tests, respectively. The main conclusions extracted from the experimental results are:

- It can be seen, the behaviour of breakage (measured as Hardin index) versus particle strength has a negative linear tendency. Smaller breakage are associated with higher strengths of the fragments in the mixture.
- There exists an almost linear correspondence between the Hardin breakage index and the new surface of particles created.
- The higher values of plastic work input (per unit volume), the higher amount of particle breakage.
- The change in GSD has been analysed using two methods. The first one considers both the splitting and comminution crushing mechanisms and from its results, it can be concluded that splitting crushing of large fragments is the dominant particle breakage mechanism in the mixtures. Less than 10% can be attributed to comminution. In fact, there is no significant changes observed for fines after the compaction. Based on this, the second method of analysis only takes into account splitting crushing. For the two methods, it has been found that calculated and experimental GSD curves present a reasonable agreement. Therefore, both methods are effective ways to evaluate the particle breakage.
- The fragmentation increased by reducing the strength of fragments. By increasing the strength of the particles in the mixtures, the value of fine reduced because of less breakage happened in particles and the fractal number increased.

By knowing the density of the matrix in the mixtures, the energy necessary to densify the matrix part was estimated and an expression proposed to link matrix dry density and transferred energy to the matrix component. This procedure was used to estimate the percentage of dynamic compaction energy that was transferred to breakage of fragments. It appeared that 94.5 % of dynamic compaction was transferred to breakage of the natural

fragments. When using slate fragments, 81.1 % of the compaction energy is transferred to breakage.

In the case of static loading unloading oedometer, two hypothesis are considered based on structure of compacted soil. The first case, it can be assumed that an over filled structure exists and the fragments are not deformable. For the second case, it is assumed an interactive underfilled structure and that the strain in the matrix is the same that the strain in the fragment skeleton. The second hypothesis may be more adequate because the structure of the binary mixture is interactive underfilled. In this case, an important part of the applied energy goes to deform the skeleton formed by the fragments and to fragment breakage. The energy that goes to the fragments increase with the stiffness of the fragments. There is a good match between Hardin breakage index and energy that goes to particles. In fact, high amount of energy shows higher breakage value, an average value for the ratio $\Delta Br/\Delta Energy$ of $0.0027 \text{ m}^3/\text{kNm}$ has been obtained. In addition, the ratio of the differences in Harding breakage index after dynamic and static oedometer test over energy that goes to fragments may be related to the accumulated global strain in the oedometer. The effect of the strain is not significant, for the tree material an average value of for the ratio $\Delta Br/\Delta Energy$ of $0.0044 \text{ m}^3/\text{kNm}$ can be considered.

The hydraulic behaviour of compacted ‘all-one’ mixture has been examined under saturated oedometer conditions. Two different stress paths have been followed. In the first path, compacted mixtures were statically loaded to a vertical stress of 1 MPa, and then fully saturated by imbibition with distilled water for 48 hours under the same vertical stress. Later, the material was loaded up to 2 MPa and unloaded up to 0.05 MPa. In the second path, materials are saturated at the beginning of the test under a load of 0.075 MPa, and then loaded up to 2 MPa and unloaded up to 0.05 MPa. The main results obtained are listed below:

- **Compressibility:** Under saturated conditions the strength and microstructure of the fragments are the main dominant issue regarding compressibility. After the tests, two types of behaviour have been observed in saturated samples. In the first group that includes pure matrix and natural clay fragments, in addition to the effect of breakage, water acts inducing softening of the internal bonds and the broken fragments become softer. This means that water disrupts fragments physically and causes more deformation. On the other hand, in the second group

that contained artificially fragments and slate fragments, the granular particles with higher strength do not lose the internal bonds and deformation is associated more with the deformation of the matrix part and the rearrangement of the large fragments.

- **Collapsibility:** When compared to equivalent void ratio, some benefit is obtained when considering the strength of the fragment. High-strength fragments show less collapse deformation on soaking. In general, all the mixtures saturated under 1 MPa display more collapse strain than those saturated at 0.075 MPa.
- **Permeability:** Permeability is mainly dominated by the void ratio of the matrix. No important changes have been detected when using the fragments with different strength properties. When comparing mixture permeability to pure matrix at equivalent void ratio, the tortuosity in addition to other phenomena induces the mixture permeability to decrease (flow follows a more tortuous path in the matrix).

To sum up, in the case of ‘all-one’ mixtures with high strength fragments as fill material in engineering construction, some benefits are observed compared to pure soil as follows:

- To reduce water demand in field compaction and to optimise the cost.
- To reach better dry density compared to pure soil.
- To reduce the collapsibility and the compressibility on loading.

Nevertheless, the permeability is one of the disadvantages in using ‘all-one’ mixtures.

The microstructure and strength of the fragments plays an important role in the behaviour of ‘all-one’ mixtures. No important benefit can be observed when using ‘all-one’ mixture with low strength fragments (natural cemented coarse aggregates).

8.3 Future investigations

The following further researches are proposed:

- To extend the experimental programme to study the behaviour along cyclic wetting and drying paths, as well cooling and heating cycles.

- To analyse the long-term deformation behaviour using different proportions and quality of fragments.
- To extend the current study with other proportions of fragments.
- To perform some numerical simulations to analyse local transfers of water between fragments and matrix. To perform a parallel experimental programme to compare these local transfers with simulated result.

9 References

- Alonso, E. E., Pinyol, N., & Alonso, M. (2016). Análisis tenso deformacional elastoplástico de la construcción de la presa de l'Albagès, *Barcelona* (In Spanish).
- Alonso, E. E., Gens, A., & Hight, D. W. (1987). Special problem soils: general report. *9th European Conference of Soil Mechanics and Foundation Engineering, Dublin, 3*, 1087-1146.
- Alonso, E. E., Romero, E., Gens, A., & Mata, C., (2004). *Proyecto original. Informe geotécnico. Análisis de estabilidad y tensodeformacional de la presa*. Anejo. No. 13, Barcelona, (In Spanish).
- Alvarado, C. (2017). Comportamiento hidro-mecánico de agregados gruesos. PhD thesis, *Universitat Politècnica de Catalunya, Barcelona* (In spanish).
- Andreasen, A.H.M. & Andersen, J. (1930).Über die Beziehung zwischen Kornabstufung und Zwischenraum in Produkten aus losen Körnern (mit einigen Experimenten). *Colloid & Polymer Science*, 50 (3), 217-228.
- Barden, L. (1965). Consolidation of compacted and unsaturated clays. *Géotechnique*, 15(3), 267-286.
- Barden, L. (1974). Consolidation of clays compacted “dry” and “wet” of optimum water content, *Géotechnique*, 24(4), 605–625.
- Barden, L. & Sides, G. R. (1970). Engineering behaviour and structure of compacted clay. *Journal of soil mechanics, ASCE*, 96, 1171-1200.
- Barrera, M. (2002). Barrera, M. (2002). Estudio experimental del comportamiento hidromecánico de suelos colapsables. PhD thesis, *Universitat Politècnica de Catalunya, Barcelona* (In spanish).
- Belkhatir, M., Arab, A., & Schanz, T. (2011). Laboratory study on the liquefaction resistance of sand-silt mixtures: effect of grading characteristics. *Granular Matter*, 13(5), 599-609.
- Blackwelder, E. (1920). The Origin of the Central Kansas Oil Domes. *Bulletin of the American Association of Petroleum Geologists*, 4(1), 89-94.
- Boone, S. J., & Lutenecker, A. J. (1997). Carbonates and cementation of glacially derived cohesive soils in New York State and southern Ontario. *Canadian Geotechnical Journal*, 34, 534-550.
- Brouwers, H.J.H. and Radix, H.J. (2005) Self-Compacting Concrete: Theoretical and experimental study. *Cement and Concrete Research*, 35, 2116-2136.

- Buenfil, C. M., Romero, E., Lloret, A., & Gens, A. (2004). Experimental study on the hydromechanical behaviour of a silty clay. *Proc. 2nd International Workshop on Unsaturated Soils*, Anacapri, 15-29.
- Buenfil, C. M. (2007). Caracterización experimental del comportamiento hidromecánico de una arcilla compactada. PhD thesis, *Universitat Politècnica de Catalunya, Barcelona (In spanish)*.
- Cardoso, R., Naves, E. M. D., Alonso, E. E. (2012). Experimental behaviour of compacted marls. *Géotechnique*, 62(11), 999-1012.
- Cardoso, R., Romero, E., Lima, A. and Ferrari A. (2007). A comparative study of soil suction measurement using two different high-range psy-chrometers. *Proc. 2nd Int. Conf. Mechanics of Unsaturated Soils. Weimar, T. Schanz (ed.). Springer-Verlag, Berlin*, 79-93.
- Carvalho, C. J., Nunes, P. M., Berberian, D. & Ferriera, E. S.,(1987). Influencia del liquida saturacion en el colapsibilidad. *Congress panamericano de mexicana. Colombia (in Spanish)*.
- Collins, K., & McGown, A. (1974). The form and function of microfabric features in a variety of natural soilsThe behavior of granular soils at elevated stress. *Géotechnique*, 24(2), 223-254.
- Coop, M. R., & Lee, I. K. (1993). The behavior of granular soils at elevated stress. *Predictive soil mechanics: proceedings of the Worth memorial symposium held at St Catherine's College, London, England: Thomas Telford Limited*. 186-198.
- Cox, D.W. (1978). Volume change of compacted clay fill. *Clay fill, London, ICE*: 79-86.
- Cuccovillo, T. & Coop, M. R. (1999). On the mechanics of structured sands. *Géotechnique*, 49(6), 741-760.
- Das, B.M. (1983b). Advanced soil mechanics. *Hemisphere Publishing Corporation, Washington*.
- Decagon Devices, Inc. (2003). WP4 Water Dewpoint Potentiometer. *Operator's Manual, Version 2.2. Decagon Devices, Inc., Pullman (www.decagon.com)*.
- Delage, P., Audiger, M., Cui, Y. J., & Howat, M. (1996). Microstructure of a compacted silt. *Canadian Geotechnical Journal*, 33(1), 150-158.
- Doddiah, D., Bhat, H. S., Somasekhar, P. V., Sosalegowda, H. B., & Ranganath, K. N. (1969). Shear characteristics of soil-gravel mixtures. *Journal of the Indian National Society of Soil Mechanics and Foundations Engineering*, 8(1), 57-66.
- Einav, I. (2007). Breakage mechanics: Part I: Theory. *Journal of the Mechanics and Physics of Solids*, 55(6), 1274-1297.

- Feda, J. (2002). Simulation of behaviour of undisturbed soil samples. *Geotechnika*, 1, 3-5.
- Funk, J.E., Dinger, D.R. (1980). Coal Grinding and Particle Size Distribution Studies for Coal-Water Slurries at High Solids Content. *Final Report, Empire State Electric Energy Research Corporation (ESEERCO)*.
- Fragaszy, R. J., Su, J., Siddiqi, F. H., & Ho, C. (1992). Modeling strength of sandy gravel. *Journal of Geotechnical Engineering*, 118(6), 920-935.
- Fonseca, J. (2011). The evolution of morphology and fabric of a sand during shearing. *PhD thesis, Imperial College London*.
- Fredlund, D. & Rahardjo, H. (1993). Soil mechanics for unsaturated soils. London, UK: Wiley.
- Fuller, W. B., & Thompson, S. E. (1907). the laws of proportioning concrete. *Journal of Transportation*, 59, 67-143.
- Indraratna, B., Lackenby, J., & Christie, D. (2005). Effect of confining pressure on the degradation of ballast under cyclic loading. *Géotechnique*, 55(4), 325-328.
- Ingles G. O., Metcalf, B. J. (1972). *Soil stabilization. Principles and Practice*. Sydney - Melbourne - Brisbane: Butterworths.
- Garas, V.Y. & Kurtis, K.E. (2008) Assessment of methods for optimising ternary blended concrete containing metakaolin. *Magazine of Concrete Research*, 60 (7), 499-510.
- Gens, A., Alonso, E. E., Suriol, J., & Lloret, A. (1995). Effect of structure on the volumetric behaviour of a compacted soil. *Proc. 1st International Conference on Unsaturated Soils, Paris,1*, 83-88.
- Grimal, C. A. (2010). Influencia de la forma de las partículas en la compresibilidad de las escolleras. PhD thesis, *Universitat Politècnica de Catalunya, Barcelona (In spanish)*.
- Hagerty, M., Hite, D., Ullrich, C., & Hagerty, D. (1993). One-Dimensional high-pressure compression of granular media. *Journal of Geotechnical Engineering*, 119(1), 1-18.
- Hardin, B. O. (1985). Crushing of soil particles. *Geotechnical Testing Journal*, 14(3), 296-308.
- Hardin, B. O. (1978). The nature of stress-strain behaviour for soils. *Geotechnical Engineering Division Specialty Conference, June 19-21, 1978, Pasadena, California, ASCE*, 3-90.
- Hazen, A. (1911). "Discussion of Dam on Sand Foundation, by A. c. Koenig" Transaction ASCE, New York, N.Y., Vol. 73.

- Holtz, W. G., & Gibbs, H. S. (1956). Triaxial shear tests on previous gravelly soils. *Triaxial shear tests on previous gravelly soils*, 82(1), 1-22.
- Hunger, M. (2010). An integral Design Concept for Ecological Self-Compacting Concrete. Bouwkunde. *PhD Thesis. Eindhoven: Eindhoven University of Technology*.
- Kamruzzaman, A. H. M., Chew, S. H. & Lee, F. H. (2009). Structuration and destructuration behavior of cement-treated Singapore marine clay. *Journal of Geotechnical Geoenvironmental Engineering*, 135 (4), 573-589.
- Kuerbis, R., Nagussey, D., & Vaid, Y. P. (1988). Effect of gradation and fines content on the undrained response of sand. *Proc. Hyd. Fill. Struc. Geotech. Spec*, 21, 330-345.
- Kumar, S.V. and Santhanam, M. (2003). Particle packing theories and their application in concrete mixture proportioning: A review. *The Indian Concrete Journal*, 77 (9), 1324-1331.
- Lade, P. V., Yamamuro, J. A., & Bopp, P. A. (1996). Significance of particle crushing in granular materials. *Journal of Geotechnical Engineering*, 122, 309-316.
- Lambe, T. W. (1958). The Structure of Compacted Clay. *Journal of the Soil Mechanic and Foundation*, 84, 10-34.
- Lambe, T. W., & Whitman, R. V. (1969). *Soil mechanics*. New York, USA: Wiley.
- Lawton, E. C., Fragaszy, R. J. & Hardcastle, J. H. (1989). Collapse of compacted clayey sand. *Journal Geotechnical Engineering, ASCE* 115(9), 1252-1267.
- Lee, K. L., & Farhoomand, I. (1967). Compressibility and crushing of granular soil in anisotropic triaxial compression. *Canadian Geotechnical Journal*, 5(1), 68-86.
- Lee, X., & Zhang, L. M. (2009). Characteristics of dual structure pore size distribution of soil. *Canadian Geotechnical Journal*, 46(2), 129-141.
- Leroueil, S., & Vaughan, P. R. (1990). The general and congruent effects of structure in natural. *Géotechnique*, 4(3), 467-488.
- Leslie, D. D. (1963). Large Scale Triaxial Tests on Gravelly Soils. *Proceeding of the 2nd Pan-American Conference on Soil Mechanics and Foundation Engineering, Brazil*, 1, 181-202.
- Lopez, R. D., Silfwerbrand, J., & Jelagin, D. (2016). Force transmission and soil fabric of binary granular mixtures. *Géotechnique*, 66(7), 578-583.
- Marsal, R. J. (1967). Large scale testing of rockfill materials. *Journal of the Soil Mechanics and Foundations Division*, 93, 27-43.

- Marsal, R. J., & Fuentes de la Rosa, A. (1976). Mechanical properties of rockfill–soil mixtures. *In Transactions of the 12th International Congress on Large Dams Mexico City., 1*, 179-209.
- Marsal, R. J. (1965) .Discussion of Shear Strength. *proceedings of 6th International conference on Soil Mechanics and Foundation Engineering, Vol. 3, pp. 310-316.*
- Mauricio., B. B. (2002) Estudio experimental del comportamiento hidro-mecánico de suelos colapsables, PhD thesis, Universitat Politècnica de Catalunya, Barcelona (In spanish).
- McDowell, G. R. & De Bono, J. P. (2013). On the micro mechanics of one-dimensional normal compression. *Géotechnique, 63(11)*, 895-906.
- McGown, A., & Collins, K. (1975). The microfabric of some expansive and collapsing soils. *Proc. 5th Panamerican Conf. Soil Mech. Found. Engng, 1*, pp. 323-332. Buenos Aires.
- Mekkiyah, H., & Al-Khazragie, A. (2015). Behavior of clay soil mixed with fine sand during consolidation. *Applied Research Journal.1(8)*,437-443.
- Mitchell J.K. (1993). Fundamentals of soils behaviour. *Second edition. John Wiley & Sons*, New York.
- M. Industrial, Certificado de análisis. Cemento Portland Super Dragon. EN 197-1 - CEM I 52,5 R, 2014.
- Minh, N., & Cheng, Y. (2014). A micromechanical study of the equivalent granular void ratio of soil mixtures using DEM. *Geomechanics from Micro to Macro, 1*, 219.
- Monroy, R., Zdravkovic, L., & Ridley, A. (2010). Evolution of microstructure in compacted London clay during wetting and loading. *Géotechnique, 60(2)*, 105-119.
- Neville, A. M. (1995). *Properties of Concrete* (Fourth Edition ed.). Edinburgh, England.
- Nonell, X. A. (2016). Fabricación de clastos artificiales en laboratorio y el estudio de sus propiedades hidromecánicas. Master thesis, Universitat Politècnica de Catalunya, Barcelona (In spanish).
- Oldecop, L. A., Alonso, E. E. (2001). A model for rockfill compressibility. *Géotechnique, 51(2)*.127-139.
- Peronius, N. & Sweeting, T.J. (1985). On the correlation of minimum porosity with particle size distribution. *Powder Technology, 42*. 113-121.
- Pinyol, N. M. & Alonso, E. E. (2017). Modelling the construction of an instrumented earth dam. The relevance of compaction. *9th workshop on Code-Bright users, Barcelona, Spain.*

- PG3, Spanish standard for road construction for earthworks. ‘All-one’ or in Spanish ‘*Todo uno*’ *Capítulo III: Rellenos.- Artículo 333*, 196-204.
- Yessenia E. P. D. (2011). Thermo-Hydro-Mechanical behaviour of Ypresian clay. *Master thesis, Universitat Politècnica de Catalunya, Barcelona (In spanish)*.
- Romero, E. (2004). Presa de l’Albagès. Ensayos sobre materiales del cuerpo de la presa y de la cimentación. Barcelona.
- Romero, E. (2013). A microstructural insight into compacted clayey soils and their hydraulic properties. *Engineering Geology*, 165, 3-19.
- Romero, E., & Simms, P. (2008). Microstructure investigations in unsaturated soils. A review with special attention to mercury intrusion porosimetry and environmental scanning electron microscopy. *Geotechnical Geology Engineering*, 26(6), 705-772.
- Romero, E., Della Vecchia, G., & Jommi, C. (2011). An insight into the water retention properties of compacted clayey soils. *Géotechnique*, 61(4), 313-328.
- Rotta, G. V., Consoli, N. C., Prietto, P. D. M., Coop, M. R. & Graham, J. (2003). Isotropic yielding in an artificially cemented soil cured under stress. *Géotechnique*, 53(5), 493-501.
- Rowe, P. W. (1954). A stress-strain theory for cohesionless soil with applications to earth pressures at rest and moving walls. *Géotechnique*, 4(2), 70-88.
- Satyanaga, A., Rahardjo, H., Leong, E. C., & Wang, J. Y.(2013). Water characteristic curve of soil with bimodal grain-size distribution. *Computer and geotechnique*, 48, 51-61.
- Sanderson, V. (2011). Microstructure and its effects on compaction in Barcelona silty-clays. Tesina de especialidad. PhD thesis, Universitat Politècnica de Catalunya, Barcelona (In spanish).
- Santucci de Magistris, F., & Tatsuoka, F. (2004). Effects of moulding water content on the stress–strain behaviour of a compacted silty sand. *Soils Foundations*, 44(2), 85-101.
- Seed, H. B., & Chan, M. A. (1959). Structure and Strength Characteristics of Compacted Clays. *Journal of Soil Mechanics and Foundations Division*, 85, 87-128.
- Shergold, F. A. (1954). A Study of the Crushing and Wear of Surface-Dressing Chippings under Rolling and Light Traffic, Research Note No. RN/2298/FAS.B.P, p.397.
- Suriol, J., & Lloret, A. (2007). Cambios en la estructura de suelos compactados frente a humedecimiento y secado. *Ingenieri’a Civil*, 147, 7-76 (In Spanish).

- Suriol, J., Gens, A., & Alonso, E. E. (1996). Behaviour of compacted soils in suction controlled oedometer. *Proc. 2nd International Conference on Unsaturated Soils, Beijing I*, 443-463.
- Tapias, M., Alonso, E. E., & Gili, J. (2016). Compressibility, grain breakage and time-dependent behavior of gap-graded aggregates of sugar cubes. *Soils and Foundations*, 56(5), 805-817.
- Tatsouka, F. (2015). Compaction characteristics and physical properties of compacted soil controlled by the degree of saturation, Keynote Lecture, Deformation characteristics of geomaterials, *Proc. of 6th International Conference on Deformation Characteristics of Geomaterials, Buenos Aires*, 40-78.
- Tyler, S. W., & Wheatcraft, S. W. (1989). Application of Fractal Mathematics to Soil Water Retention Estimation. *Soil Science Society of America Journal*, 53(4), 987-996.
- Vallejo, L. E. (2011). Interpretation of the limits in shear strength in binary granular mixtures. *Canadian Geotechnical Journal*, 38(5), 1097-1104.
- Vallejo, L. E. (2001). Interpretation of the limits in shear strength in binary granular mixtures. *Canadian Geotechnical Journal*. 38(5), 1097-1104.
- Vallejo, L., & Lobo-Guerrero, S. (2012). The shear strength of granular materials containing dispersed oversized particles: DEM analysis. *International Journal of Geotechnical Engineering*, 6(3), 371-380.
- Vallejo, L., Lobo-Guerrero, S. & Chik, Z. (2005). A network of fractal force chains and their effect in granular materials under compression. *Fractals in Engineering. Springer London*.
- Vasileva, A. A., Mikheev, V. V., & Lobanova, G. L. (1971). How the strength of gravelly soils depend on the type of state of the sand filling the pores. *soil Mechanics and Foundation Engineering*, 8(3), 167-171.
- Vaughan, P. R. (1985). Mechanical and hydraulic properties of in-situ soils. General Report. *Sess. 2 Proc. 1st International Conference in Geomechanics in Tropical Lateritic and saprolitic Soils. Brasilia, Comisión Federal de Electricidad, México City*, 3, 61- 71.
- Vaughan, P. R. (1994). Criteria for the use of weak and weathered rock for embankment fill, and its compaction control. *XIII ICSMFE*. New Dehli, India.
- Van Genuchten, M.T. (1980). A closed form equation for prediction the hydraulic conductivity of unsaturated soils. *Soil. Sci.Soc.Am.* 44, 379-392.

- Vogt, C. and Lagerblad, B. (2006). Ultrafine particles to save cement and improve concrete properties. *Advances in cement and concrete X. July 2-7*, Davos, Switzerland.
- Yun, T. S., & Santamarina, J. C. (2005). Decementation, softening, and collapse: changes in small-strain shear stiffness in k_0 loading. *Journal of Geotechnical and Geoenvironmental Engineering*, 131(3), 350-358.
- Zhang, X., & Baudet, B. A. (2013). Particle breakage in gap-graded soil. *Géotechnique Letter*, 3(2), 72-77.